ARTIFICIAL CHEMICAL AGEING OF ATMOSPHERIC AEROSOL

By

SUAD SAID AL KINDI

A thesis submitted to
The University of Birmingham
For the degree of
DOCTOR OF PHILOSOPHY

School of Geography, Earth and Environmental Sciences
The University of Birmingham
November 2014

ABSTRACT

An aerosol chemical ageing (ACA) system has been developed for artificially processing atmospheric particles. A system in which an aerosol flow tube is coupled to a scanning mobility particle sizer (SMPS) and an aerosol time-of-flight mass spectrometer (ATOFMS) has been constructed to study the heterogeneous reaction between two oxidants, ozone (O_3) and the hydroxyl radical (OH), and three organic aerosol proxies: oleic acid (OL), maleic acid (MA) and bis(2-ethylhexyl)sebacate. The ACA system operates under conditions equivalent to ambient processing times of 1 and 20 days with respect to ozone and OH, respectively.

The study provides new data on the ageing process of organic aerosol proxies. Physical characterisation of aged particles is consistence with the formation of volatile products resulting in an appreciable decrease in particle size and mass. The chemical study, however, shows that the properties of the aged particles are sensitive to the identities of the oxidant and organic material, the particle size and the oxidation environment. Oxidation of OL aerosol with O_3 shows extensive formation of oligomeric products and is found to be relative humidity and particle size dependent. A variation in the composition of aged OL particles as a function of their size is reported. However, oxidation of OL aerosol with OH radicals reveals a different mechanism with no measured high molecular weight products. The studies of both particulate organic acids, OL and MA, have shown the formation of highly oxygenated compounds composed mainly of peroxide, carboxylic acid, ketone or aldehyde functionalities, but higher oligomers could not be detected in the case of MA, indicating differences in the reaction pathways of MA and OL. The applicability of the ageing technique has been tested on real atmospheric particles, but, it is concluded that extrapolating these laboratory procedures to investigate the ambient air may be challenging due to the complexity of the atmospheric composition, and the rapidity of compositional changes real atmosphere.

To everyone who strives to keep our planet Earth a safe, clean and beautiful place to live.

Suad
November 18, 2014

ACKNOWLEDGEMENTS

It is with immense gratitude that I acknowledge the meaningful contributions of people to whom I am greatly indebted in writing this thesis. First and foremost; I wish to express my sincerest appreciation to my supervisors, Professor Roy Harrison and Dr William Bloss, for their continuous support and kind advice over the past five years. They have given me a unique opportunity to grow as an independent research scientist. The trust, freedom, and above all the foundation to study and explore new ideas, have maintained an amazingly enjoyable work environment. The professional guidance, useful recommendations, and critical comments of Professor Roy Harrison have contributed enormously to the success of this thesis. It is truly an honour to work with him leading, shaping and guiding the direction of my research. Dr William Bloss has been a tremendous mentor for me since the early phases of my study; initially, when I was reading my Masters courses, and during my research project later on. His valuable advice, constructive suggestions in the lab and field as well as the modelling studies, have been priceless. I am deeply grateful for his willingness to patiently listen to my questions and generously sharing with me his vast knowledge, experience and time.

Dr Francis Pope, who joined the supervisory team halfway through my work, has offered another invaluable layer of expertise. His careful and insightful suggestions have been a great help, particularly relating to the chemical study of the research. His willingness to review and evaluate the results chapters of this thesis has helped me to coordinate my project, especially in improving the standard of the results discussion.

I have benefited immeasurably from my laboratory partners; the past and present members of the Wolfson lab. Dr. Kathleen Faloon and Dr. Juan Najera have both enlightened me with the first glance of atmospheric simulation research. I am extremely grateful for their unconditional help and support. Dr. Johanna Gietl has been particularly helpful in guiding me to operate the ATOFMS. However, the ATOFMS could never have worked efficiently without the huge efforts of Dr. David Beddows. He has fascinated me with his capability and professionalism in maintaining the ATOFMS system and has always helped with many urgent matters I have encountered.

The support and assistance of Richard Johnson in the lab and site measurements have been indispensable and were beyond the call of duty, and I thank him for that. I also thank James Peart for taking time out of his busy schedule in addressing wide range of matters related to equipment transport, field experimental settings, printing and binding issues. All the people in the workshop, Bioscience store and the glass blower (Stephen Williams) were genuinely nice and deserve a huge ‘thank you’ for their unlimited help in various practical matters related to my experimental settings that otherwise I would not have been able to accomplish.

I would like also to thank the efficient laboratory managers, Gillian Kingston and Eimear Orgill, for constantly providing a safe and secure working environment. Mary Harding and Gretchel Coldicott have played key roles in coordinating the progress of so many students in our school, and I am thankful for their support during my course of study.

I would like to take this time to thank the generous support of the Omani Government: the Ministry of Higher Education and the Ministry of Manpower for funding this study and for the 5 years fully paid study leave, respectively. This study was partially-funded by NERC and I would like to thank them for their contribution. I would also like to thank the University of Birmingham for providing all the necessary facilities and resources to produce and complete this thesis. It was a wonderful, productive and life changing experience to be here for the past five years.

My hearty thanks go to Khalid Al Salami, my husband. Words cannot express how grateful I am for all the sacrifices he has made on my behalf, the biggest of which was for him to be away from our family for five years. I thank him so much for doing his best just to make us happy and to support us in all our needs. The presence of my three sons: Al Azwar, Shadhan, and Al Yaqdhan during my study has been a source of happiness and joy in some scientific dark days and made the years I spent here in the UK such an incredible journey. I am so proud to call them my sons. I would like also to extend my thanks to my beloved family and in-laws: my mother, father, mother in-law and father in-law, for their continuing support, faith, encouragement and prayers throughout my study. I have to especially thank my sister Yusra and her husband Mohammed Al Kindi for their endless help and unconditional support. Big thanks also to the most supportive brothers ever (and their families): Abdul Munim, Abdul Bari, Mohammed, Ibraheem, Khalid, Musa, Jamal, Abdullah and Abdul Kareem. I am ever so grateful for their support, greeting calls, visits, and very warm welcomes during my summer vacation in Oman and UAE.

It has been very nice to always come to a clean tidy fresh home after a long working day in the lab. In this regard, I value all the hard work of Kumari Manukonda, in making the house a wonderful home for us, looking after my sons and in giving me relaxing evenings and weekends to spend with my children.

A special mention for Norman and his wife Sheela, our next door neighbours. Sadly, our late dear Norman, to whom I owe a sincere gratitude, is no longer here with us today. Knowing that he kept an eye on us, looked after my children whenever I was occupied, took care of our house whenever we were away, certainly put my mind at rest at all times for more than four years. His kindness has truly inspired us, for he was more than a neighbour and he will forever stay in our hearts.

Many friends have cheered and supported me to strive towards my goal in every way. I must say a special ‘thank you’ to Aisha Al Wishahi, whom I consider to be my best friend, for being there to listen, bearing the brunt of the frustrations, and sharing the joy of the successes. I wish to give Eun-Hwa Jang my best thanks for sharing her stories with me, giving me her time when I needed it and for being such a good friend. I also owe a special thanks to Pallavi Pant for the effort she has put in arranging formal and friendly group meetings and for keeping our group updated with the recent scientific findings in our area of interest. I cannot forget to thank my previous research colleagues Dr Salim Alam, Dr Shana Saha and Dr Vivien Bright for their encouragement and help. For all the current and newer friends and members at the school of Geography, Earth and Environmental Sciences: Adobi Okam, Ajit Singh**,** Barbara Hernandez, Fang, Forough Jafary, Hao Huang, Ian Keyte, Jian Zhong, Lami Karimatu Abdullahi, Lubna Al-Saadi, Mariam Al-Adba, Massmiliano Mascelloni, Mathew Taiwo, Nicholas Davidson Paul Sanderson, Tara Rasoul and Van Tuan Vuthank you for the very friendly chatting times, keep your enthusiasm as much as possible, enjoy the wonderful experience, and I will definitely miss you all!

(Please accept my apologies if I have forgotten anyone)

TABLE OF CONTENTS

LIST OF TABLES

LIST OF FIGURES

LIST OF SCHEMES

CHAPTER 1 INTRODUCTION

1.1 General overview

Climate change and improvement of air quality are the most issues facing the international community. In spite all the significant progress made over the past decades in understanding the causes and the implications of our changing environment, many aspects of the global atmospheric system remain uncertain and not fully understood.

At present time, atmospheric aerosols are recognized to play an important role in atmospheric chemistry, climate, visibility, and human health (Kroll and Seinfeld, 2008; Calvello et al., 2010; Lyamani et al., 2010; Rengarajan et al., 2011; Zeng et al., 2013). Scientists have made appreciable developments and improvements in understanding sources, formation mechanisms, physical and chemical transformations of atmospheric organic aerosol (OA). Nevertheless, the composition, hygroscopicity and reactivity of secondary organic aerosol on the troposphere remain poorly characterized (Carlton et al., 2009; Hallquist, 2009; Slowik et al., 2010). The large discrepancies, as much as an order of magnitude (Carlton et al., 2009), associated with the estimated fluxes of OA are thought to arise largely due to the poor understanding of the formation mechanism of the secondary organic aerosol (SOA) from their precursors (Rengarajan et al., 2011). This is because OA is part of a complex atmospheric system with hundreds of different compounds, both natural and anthropogenic, covering a wide range of chemical and thermodynamic properties (Saxena and Hildemann, 1996; Ghorai et al., 2014).

1.2 Atmospheric aerosols

Atmospheric aerosols can be defined as "suspensions of small solid and/or liquid particles in air that have negligible terminal fall speeds" (Wallace and Hobbs, 2006). The aerosol range in size from a few nanometers to several hundred micrometers (John, 1986; Zahardis et al., 2011). Both inorganic and organic compounds can transfer between the gas and the particle phase (Topping et al., 2011). The organic material make up a substantial fraction of the total mass of fine aerosols (Zahardis et al., 2011), accounting in the lower troposphere for 20–50% of aerosol mass at continental midlatitudes (Putaud et al., 2004) and up to 90% in tropical forested area (Roberts et al., 2001; Kanakidou et al., 2005; Zhang et al., 2007; Carlton et al., 2009; Hildebrandt et al., 2010).

Environmental issues related to particulate matter (PM) intensified after the industrial revolution in many countries including European countries and many parts of the United States (Donahue et al., 2009). Researchers began to consider the atmospheric processing of the OA in the early 1950s when Haagen-Smit, in 1952, discussed the formation of the aerosol from atmospheric processing of ring compounds having a double bond in the ring. The study emphasized aerosols formation as a result of atmospheric oxidation of organic compounds, such as cyclohexene and dicyclopentadiene, which caused ring opening, increased polarity and decreased volatility (Haagen-Smit, 1952). Also in 1952, Mader et al characterized the chemical composition of organic aerosols. They were shown to contain significant amounts of oxygenated and peroxidized organic substances and their quantities per unit volume of air differed from day to day, depending on the degree of pollution (Mader et al., 1952). The first study of atmospherically processed OA goes back to the 1960 with Went who proposed that the partial

oxidation of volatile organic carbon emitted directly by plants could lead to molecular condensation of organic vapour to macromolecules resulting in the formation of SOA (Went, 1960).

Two decades later, in 1980s, systematic laboratory studies proved that the oxidation of organic vapours can create products with low volatility and that their subsequent condensation to the particulate phase is a second important pathway for the formation of atmospheric organic PM (Kamens et al., 1981; Tao and McMurry, 1989). Since then, most researchers consider SOA as the most important organic aerosol component and laboratory work focused on studying the organic vapours precursors that led to their formation (Kanakidou et al., 2005).

1.3 Primary organic aerosols versus secondary organic aerosols

POA is emitted directly to the atmosphere from biogenic sources such as terrestrial (e.g., pollen, soil dust, and plant debris) and marine sources, as well as anthropogenic sources, primarily related to combustion processes including burning of fossil fuels, cooking, domestic heating, and deforestation practices (Petters et al., 2006; Zahardis et al., 2011). By contrast, SOA is formed in the atmosphere as the oxidation products of certain volatile organic compounds (VOCs) or via condensation of VOCs on preexisting aerosols or formation of new aerosol (nucleation).

Studies of SOA formation based on biogenic and anthropogenic VOC fluxes, show that SOA globally dominates over the POA (Tsigaridis and Kanakidou, 2007; Rengarajan et al., 2011; Lambe et al., 2013) and estimates of SOA suggest the dominance of biogenic VOCs source over several industrial and automobile emission sources (Hallquist, 2009).

Common constituents of POA include mono-carboxylic acids, alkanes, terpenoids and polycyclic aromatic hydrocarbons (PAH) (Fraser et al., 1999). POA are generally composed of

non-polar high molecular weight hydrocarbons and are hydrophobic (Saxena and Hildemann, 1996). However, SOA generally contain more multi-functional oxygenated compounds, such as poly-carboxylic acids (Blando et al., 1998).

Recently, Zhang et al. (2007) showed that the separation of POA from SOA depends on the location and period of interest. More recently, Donahue et al. (2009) reported that POA dominated during the relatively clean days in heavily polluted areas such as Los Angeles, while SOA built up and dominated during the most polluted periods, which combined stagnant conditions and high photochemical activity.

1.4 Sources of organic aerosol

1.4.1 Natural sources

Natural emissions of VOCs from plants and vegetation are responsible for the majority of SOA formation on a global scale. For example biogenic isoprene (2-methyl-1,3-butadiene, C_5H_8) is the most abundant biogenic VOC (excluding methane) and it is thought to contribute significantly to SOA formation (Seinfeld and Pandis, 2006). Smoke and ash particles injected directly into the air from forest fires are a major source of organic compounds.

1.4.2 Anthropogenic sources

The global input of particles into the atmosphere from anthropogenic activities is ~20% (by mass) of that from natural sources (Wallace and Hobbs, 2006). Emissions of hydrocarbons attributed to human activities arise primarily from fuel combustion and industrial processes. Most SOA originate from biogenic precursors, however, those biogenic precursors require atmospheric processing via photooxidants whose levels are clearly strengthened by human activities. Thus,

most biogenic SOA are considered to be anthropogenic by origin (Rogge et al., 1993b; Saxena and Hildemann, 1996; Kanakidou et al., 2005; Kroll and Seinfeld, 2008).

1.5 Health impacts

Concerns over the human health effects of fine PM constitute the most important element in formulating the national ambient air quality standard (Charron et al., 2013). The long term health hazard impact of the PM is one of the major reasons for studying the OA. Aerosols, both natural and anthropogenic, create serious challenges for people with asthma or other lung problems (Jeannet et al., 2014), and children growing up in heavily polluted cities have lowered lung function. Very fine particulates can penetrate deep into the lungs. The finest particles can also leave the lungs to enter the bloodstream and affect other parts of the body, especially as carcinogens. Other health impacts involve cardiovascular functions, and allergic diseases (Fuzzi et al., 2006).

1.6 Removal processes

Although efforts have continued for decades to measure and model aerosol sinks, the removal pathways of organic aerosols remains a major uncertainty (Petters et al., 2006). The two major mechanisms for the removal of the atmospheric aerosols are dry and wet deposition (Lang et al., 2002; Zhang and Vet, 2006). Dry deposition is the process in which aerosol particles are taken up by the Earth's surface where they are adsorbed by the vegetative canopy's surfaces, leaf stomata, underlying soil, water, ice and snow surfaces. The rate of the dry deposition depends on the climate (e.g temperature, and wind direction and frequency (Lang et al., 2002)), the nature of the surface, and the physical/chemical properties of the particles (Wesely and Hicks, 2000). Wet

deposition (or precipitation scavenging) is classified into two categories: in-cloud scavenging (e.g nucleation) and below-cloud scavenging. In both cases, particles first have to be incorporated into hydrometeors, such as rain, snow, fog, or clouds, and then delivered to the surface via precipitation (Lang et al., 2002). The rate of removal of particles by wet deposition depends strongly on their hydrophilicity, which influences their ability to act as cloud condensation nuclei (CCN) (Kanakidou et al., 2005).

Dry deposition is ineffective at removing POA from the atmosphere especially those originated from combustion processes because they are generally very small (number mode diameters < 0.1 μm) (Seinfeld and Pandis, 2006). Studies, models and observations, indicate that wet deposition is responsible for 70–85% of the tropospheric sink for OA mass (Pöschl, 2005). It follows that a portion of hydrophobic OA must be rendered hydrophilic, and thereby capable of being scavenged by cloud droplet nucleation followed by precipitation (Petters et al., 2006).

1.7 Physical and chemical properties

1.7.1 Size distribution

The size distribution of atmospheric aerosols is a key element in understanding and managing aerosol sources, formation, growth mechanisms, environmental impacts, health effects, visibility, and climate (Stanier et al., 2004b; Lan et al., 2011). The concentration of atmospheric aerosols, depending upon factors such as location, atmospheric conditions, annual and diurnal cycles and presence of local sources, varies between 10^7 to 10^8 particles per cm^3 with their diameters span between few nanometers to around 100 μm (Seinfeld and Pandis, 2006). Particles are classified into coarse (>2.5 μm), generated primarily from mechanical processes, fine (<2.5 μm), and ultrafine or nano (<0.1 μm) particles, consisting of transient nuclei or Aitken nuclei originating

from natural and anthropogenic sources (Hsieh et al., 2009). Figure 1.1 shows some of these processes, along with the three sizes ranges where high aerosol number concentrations are often observed.

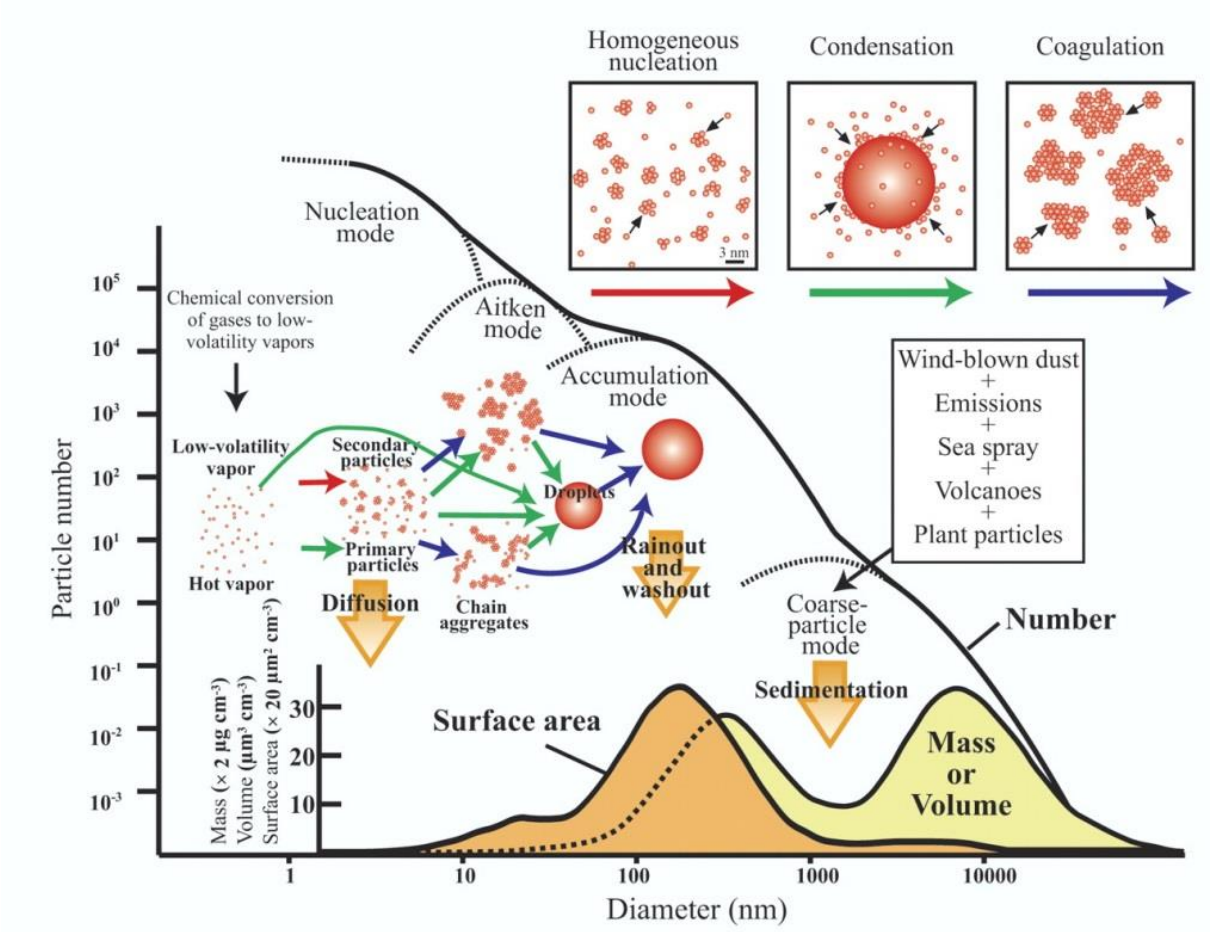

Figure 1. 1 Idealized schematic of the size distribution of particles in the atmosphere. Modes, sources, and removal mechanisms are indicated (Cheng et al., 2008).

1.7.2 Scattering and absorption of light

Because aerosols are tiny objects with sizes typically around 100 nm, they affect the Earth's radiative balance directly by absorbing and scattering a significant fraction of incoming solar radiation back to space and thus they impact the Earth's climate by their optical properties (Wallace and Hobbs, 2006; Tsigaridis and Kanakidou, 2007; Alexander Kokhanovsky, 2008; Laj

et al., 2009; Lyamani et al., 2010). Aerosols affect Earth's radiative balance indirectly by acting as CCN and changing the microphysical properties of clouds (Takemura and Nakajima, 2001). As a result, aerosols markedly affect the radiative balance in Earth's atmosphere and play a central role in climate (Hallquist, 2009). However, the aerosol radiative forcing remains a problem with a medium-low level of scientific understanding due to the strong unhomogeneity of aerosol sources and the high spatial and temporal variability of aerosol properties in the atmosphere (Ming et al., 2005; Calvello et al., 2010; Ghorai et al., 2014).

1.7.3 Chemical composition

The composition of OA is an important quantitative element to consider in atmospheric science. This is because the composition of the particles is a key fundamental factor in determining their properties such as the interaction with incident light, their physiological damage, and the ability to form CCN (Heard, 2006). Due to the complexity of ambient aerosols, they may have various chemical and physical properties in variable proportions and states of mixing (Chang et al., 2010).

SOA formed from the oxidation of VOCs generally consist of six or more carbon atoms (Pankow, 2007; Kroll and Seinfeld, 2008; Chan et al., 2009; Vivanco et al., 2011). This is because oxidation product must have vapour pressures that are sufficiently low to enable them to partition into the aerosol phase (Kroll and Seinfeld, 2008). Recently, field studies in urban areas have indicated the dominance of oxygenated species in OA, of which a major fraction is likely to be secondary in nature (Zhang et al., 2007). Other investigators proved that OA in heavily polluted areas is much more oxygenated than expected (Alfarra et al., 2004; Zhang et al., 2005).

The fact that oxidation of VOCs can create products with low volatility was further emphasized by laboratory studies. Aromatic hydrocarbon pollutants from anthropogenic sources,

such as benzene, toluene, ethylbenzene, and xylene constitute an important fraction of total VOCs. Toluene is the most abundant aromatic hydrocarbon. Hao and co-workers investigated constituents of SOA evolved from toluene-photooxidation reaction in a smog chamber (HAO et al., 2006). The study provided some important compositions of SOA such as aldehyde, ketone and carboxylic acid compounds. In a detailed study of gas-particle partitioning showed that photooxidation products of isoprene and 1,3,5-trimethylbenzene are dicarbonyls, in particular, glyoxal and methylglyoxal with no single carbonyl moiety were observed (Healy et al., 2008).

Currently, further complexity to the overall mechanistic picture of SOA is thought to be composed of polymers and oligomers, formed through particle phase heterogeneous reactions (Kalberer et al., 2006; Kroll and Seinfeld, 2008). Experimentally, oligomers and oligoesters were shown to be common component of SOA as heterogeneous and particle-phase reactions products (Kalberer et al., 2004; Szmigielski et al., 2007). Polymers in SOA formed from organic nitrates, carboxylic acids, acetals and hemiacetals via the heterogeneous reactions are reported in a number of studies (Hastings et al., 2005; Barsanti and Pankow, 2006; Surratt et al., 2006; Kroll and Seinfeld, 2008; Camredon et al., 2010; Vivanco et al., 2011).

1.7.4 Volatility

SOA is characterized by its low volatility as a result of high oxygen contents. Generally volatility and oxygen to carbon ratio (O:C) are inversely correlated. Volatility is important because it regulates whether a compound is present as a vapour or as a condensed matter. This in turn determines whether a substance is more likely to be subject to chemical transformations by gas- or condensed phase reactions. The atmospheric lifetimes and fates of different species are strongly affected by their volatilities because the rates of reaction with atmospheric oxidants and

rates of removal by wet and dry deposition depend largely on the phase of a species (Jimenez et al., 2009).

Studies identify two types of SOA that differ in volatility and O:C and thus have distinct physicochemical properties. Low-volatility SOA is strongly correlated with nonvolatile secondary species and has a high O:C, consistent with regional, heavily aged OA. Semi-volatile SOA has a higher correlation with semivolatile species and a lower O:C, consistent with less photochemically aged OA (Valorso et al., 2011).

1.7.5 Hygroscopicity

Hygroscopicity is the ability to take up water as the ambient relative humidity rises (Whitten et al., 2009). The amount of water vapour absorbed by aerosols is one of the most important factor affecting the particle size and phase and therefore influences many physicochemical characteristics of the aerosol such as the radiative properties of the atmosphere (Vesna et al., 2009; Pope et al., 2010b), atmospheric lifetime, chemical reactivity and the ability to serve as a CCN (Varutbangkul et al., 2006). Figure 1.2 illustrates the effect of ambient relative humidity and temperature on the phase state, viscosity, and diffusivity of atmospheric organic aerosol particle (physical transformation). To date, several laboratory studies on the hygroscopicity of SOA have been performed (Virkkula et al., 1999; Prenni et al., 2003; Gysel et al., 2004; Lee and Chan, 2007; Vesna et al., 2008; Khalizov et al., 2009; Pope et al., 2010a**;** Pope et al., 2010b; Schwier et al., 2011; Topping et al., 2011; Hosny et al., 2013; Shrestha et al., 2013; Ghorai et al., 2014), however, less is known about the aerosol growth with humidity.

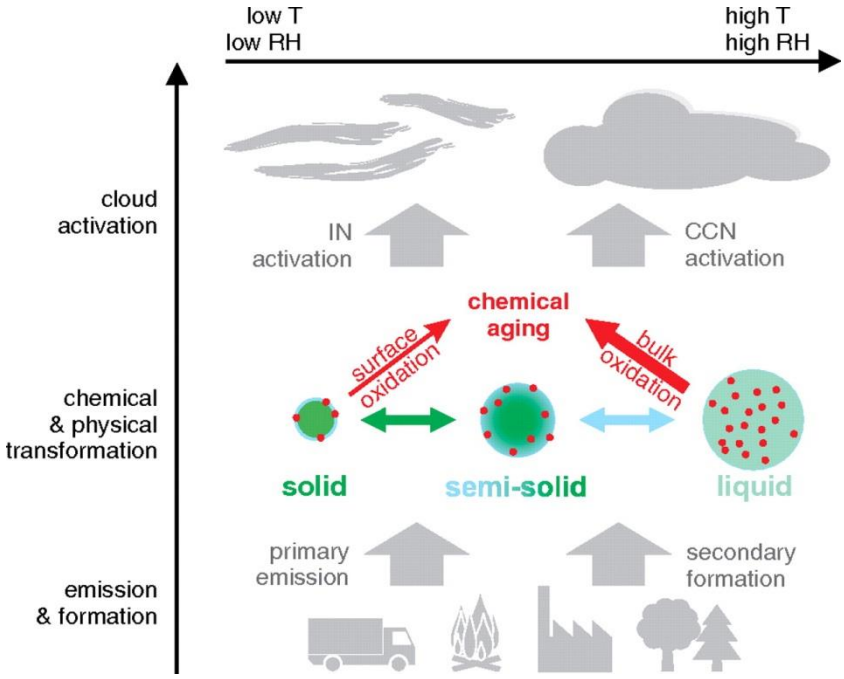

Figure 1. 2 Effect of ambient relative humidity and temperature on the phase state, viscosity, and diffusivity (Shiraiwa et al., 2011)

In a detailed investigation of factors affecting the hygroscopicity of SOA, Varutbangkul et al. (2006) concluded that the temporal variation of hygroscopicity of SOA is probably a result of two competing effects. The first being the oxidation of organic products into more polar and thus more hygroscopic species. This is consistent with the fact that the hygroscopicity of particulate organic matter increases in close correlation with its degree of oxidation (Andreae, 2009; Jimenez et al., 2009). The second is the oxidation to form higher-molecular weight might result in less hydrophilic oligomers (Varutbangkul et al., 2006) and therefore less hygroscopicity.

A good understanding of aerosol role in climate forcing involves also the deliquescence point, the relative humidity where the aerosol goes from a solid dry phase to an aqueous or mixed solid-aqueous phase. This is because different aerosols phases have very different properties and very different effects on climate such as the difference in the activity of these phases in the

scattering of radiation. Solution droplets are considerably larger in size than crystalline particles, and thus they are more efficient in scattering visible wavelength (Martin, 2000).

Various authors studied the ability of a mixture of inorganic and organic aerosols to absorb water and found a slight depression in the deliquescence point with relative to pure inorganic aerosols (Prenni et al., 2003; Brooks et al., 2004).

1.7.6 Theory of formation of SOA

Several pathways for the formation of SOA in the atmosphere have been identified including gas-phase reaction, particle-phase reaction, multiphase reaction, and multigenerational chemistry. Multigenerational chemistry has received attention recently because it is the least understood (Rudich, 2003; Petters et al., 2006; Kroll and Seinfeld, 2008).

1.7.6.1 Gas-phase reaction

The gas-phase reaction is initiated by the reaction of a strong atmospheric oxidizer such as the hydroxyl radical (OH), ozone (O_3) or the nitrate radical (NO_3) with VOCs (Kroll and Seinfeld, 2008). The most important of these in terms of its reactivity is the OH (Monks, 2005). The markedly studied aspect of VOCs degradation is the OH-initiated chemistry, for which a simplified schematic is shown in scheme 1.1. For unsaturated hydrocarbon, the OH initial oxidation step occurs predominantly by addition mechanism so that the first-generation products generally contain two (or more) polar oxygenated functional groups. This leads to the generation of a set of less volatile and more water soluble organic products such as aldehyde (−C(=O)H), ketone (−C(=O)−), alcohol (−OH), nitrate ($-ONO_2$), peroxyacyl nitrate ($-C(=O)OONO_2$), carboxylic acid (−C(=O)OH), hydroperoxide (−OOH) and percarboxylic acid (−C(=O)OOH) groups. Further oxidation may introduce additional functional groups, such that the "second-

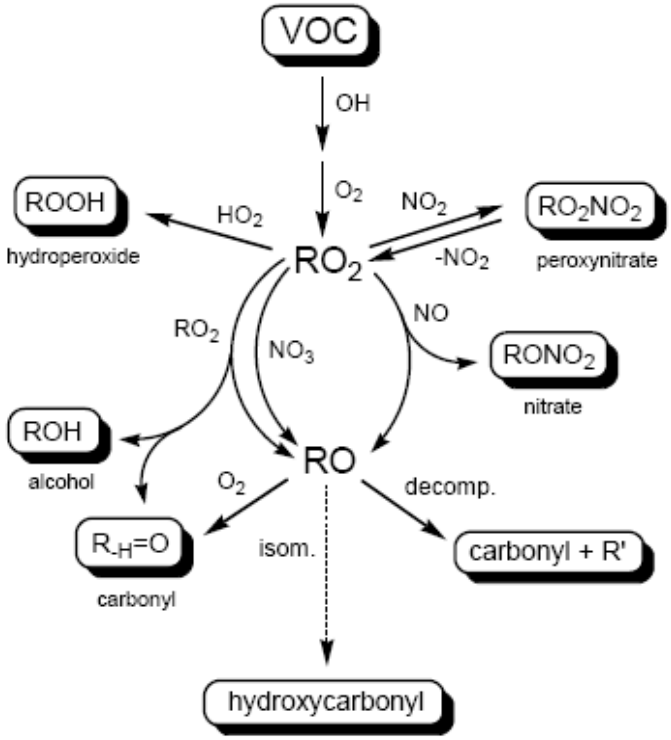

Scheme 1. 1 Simplified schematic of the OH-initiated degradation of generic VOCs to form first-generation products (Source: Hallquist, 2009).

generation" set of products (and subsequent generations) may be of even lower volatility and higher solubility (Hallquist, 2009). However, a radical can initiate oxidation by abstracting a hydrogen atom from a C-H bond of a saturated hydrocarbon. In this case, the organic products and their volatilities are unaffected by the identity of the radical (Kroll and Seinfeld, 2008). This is because hydrogen abstraction does not involve the addition of a functional group from the radical rather the ultimate oxidation product depends on the consecutive reactions following the hydrogen abstraction and the species involved in these reactions.

1.7.6.2 Particle-phase reactions

Particle-phase reaction is the reaction between the organic compounds in the condensed phase such that their chemical properties and volatility are affected (Kroll and Seinfeld, 2008). In the

past decade there has been substantial progress in understanding the chemistry of particle-phase reactions which potentially could convert POA to SOA on time scales shorter than the days-to-weeks estimated for condensation and coagulation processes (Kanakidou et al., 2005; Petters et al., 2006). The particle-phase reaction includes both heterogeneous and multiphase reactions (Ravishankara, 1997).

Some studies emphasize the continuous formation of low volatility components of SOA even after the completion of gas phase chemistry (Tobias and Ziemann, 2000; Dommen et al., 2006; Paulson et al., 2006). Several studies have also shown that species in SOA have high vapour pressures, such that condensation as the mechanism to the particle phase is precluded (Forstner et al., 1997; Kalberer et al., 2000; Jang et al., 2003; Kroll and Seinfeld, 2008).

1.7.6.3 Multiphase reaction

Multiphase reaction is the reaction of a gas-phase molecule with an aerosol solid particle or liquid droplet. The heterogeneous reaction (HR) rigorously ascribes the reaction takes place at the interface between two different phases. However, in atmospheric chemistry, HR term is broadly used to describe reactions taking place at the surface or inside a droplet. It also includes gas molecules uptake into a droplet (Guy et al., 1999).

1.7.6.4 Multigenerational chemistry

Multigenerational or multiple generations of oxidation is a continuous chemical evolution of more or less volatile organic compounds occur in the gas or particle phases until all OC is oxidized to CO_2, or is removed from the atmosphere by physical processes (wet or dry deposition) (Kroll and Seinfeld, 2008; Shiraiwa et al., 2014). This chemical evolution occurs in a

number of oxidation steps or "generation number" of products (Altieri et al., 2008). Ng et al emphasized a substantial growth after the complete consumption of the parent hydrocarbon which indicates an additional rate-limiting step to SOA formation. Others showed that measurements of gas-phase intermediates strongly suggest additional steps of oxidations in the formation of SOA (Kroll and Seinfeld, 2008). Kinetic studies of aromatic compounds oxidation forming SOA also suggests multiple oxidation steps are involved in the SOA formation (Ng et al., 2007).

Field and laboratory evidence on SOA formed from isoprene (2-methyl-1,3-butadiene, C_5H_8), the largest global atmospheric emissions of all non-methane VOCs (~600 Tg yr^{-1}) (Guenther et al., 2006), showed multiple oxidation steps in SOA formation (Fan and Zhang, 2004; Carlton et al., 2009). The first-generation products of isoprene oxidation reaction with OH are volatile compounds and thus are not expected to partition directly into the particle phase (Pandis et al., 1991; Fan and Zhang, 2004; Kroll and Seinfeld, 2008). Few products from the first-generation products have been studied (Orlando et al., 1999) and shown that they are oxidized to a second-generation products characterized with smaller, semivolatile, multifunctional, water-soluble compounds (Paulot et al., 2009), and therefore can contribute to SOA via absorptive partitioning into the particle phase (Carlton et al., 2009).

1.8 Literature review on the heterogeneous reaction of oleic acid and ozone

The oxidative addition reaction of ozone to the unsaturated carbon-carbon double bond is defined as ozonolysis (Bailey, 1958; Zahardis and Petrucci, 2007). The Oleic Acid-Ozone Heterogeneous Reaction system (OL-O_3 HR) has emerged as an ideal model system to study ozone processing of abundant and ubiquitous monounsaturated fatty acids in the troposphere (Hearn and Smith, 2004;

Ziemann, 2005; Gonzalez-Labrada et al., 2007; McNeill et al., 2007; Zahardis and Petrucci, 2007; Vesna et al., 2008; Sage et al., 2009; Pfrang et al., 2011; Lee et al., 2012). The mechanism of the heterogeneous reaction between OL and O_3 is similar to that of alkenes detailed first by Weiss (Weiss, 1905) and simplified into step mechanisms by others (Criegee, 1975; Bailey and Ferrell, 1978; Calvert et al., 2000). The initial step in this reaction is the addition of ozone molecule across the unsaturated double bond of OL forming unstable primary ozonide (POZ) (Scheme 1.2). Subsequently, the POZ decomposes by the cleavage of the C-C bond and one of the two O-O bonds following two possible reaction routes depending on which O-O bond breaks. Each reaction route consists of an aldehyde and an excited criegee intermediate (ECI), a biradical. In reaction route 1, nonanal (NN) and ECI1 are formed; the ECI1 can isomerize to form stabilized azelaic acid (AA), a cyclic acyloxy hydroperoxide (CAHP), or octanoic acid (OcA) and carbon dioxide (Gonzalez-Labrada, Schmidt et al. 2007). Alternatively, ECI1 is scavenged via a

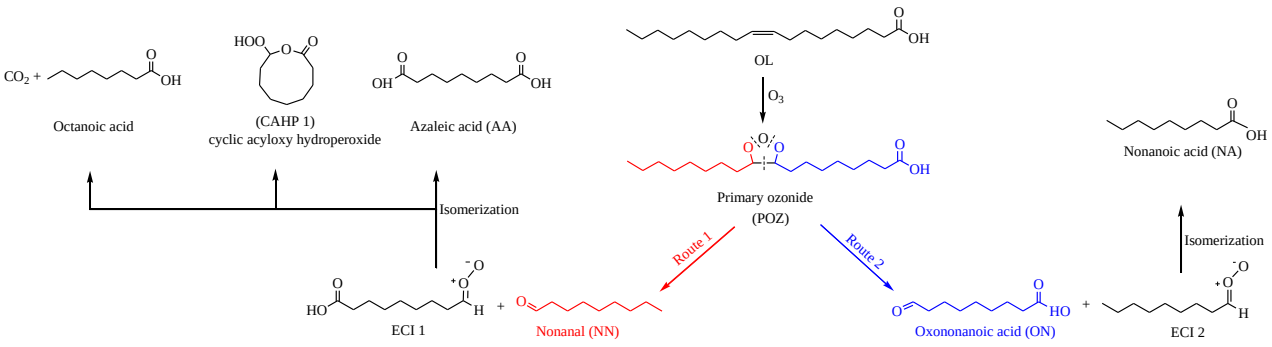

Scheme 1. 2 Mechanism and primary products of OL-O_3 HR.

"secondary chemistry"; numerous association reactions with its respective aldehydes, carboxylic fragment, OL double bond, solvents or self-reactions. This secondary chemistry arises primarily from the reactivity of ECIs (Zahardis and Petrucci 2006). Similarly, in reaction route 2, 9-oxononanoic acid (ON) and excited criegee intermediate 2 (ECI2) are formed, the ECI2

decomposes by forming stabilized nonanoic acid (NA), or scavenged via similar pathways as described above for ECI 1. The principle reaction products of OL ozonolysis are thus NN, AA, ON, and NA.

1.8.1 Criegee intermediates

Mechanisms for the formation of Criegee intermediates (CIs) via ozonolysis were first proposed by Criegee and others (Criegee, 1948; Criegee, 1953; Meinwald, 1955). The electronic structures of the CI have been debated considerably in the literature over whether they are zwitterions or biradicals (Bailey, 1958; Criegee, 1975; Harding and Goddard, 1978; Cremer et al., 1993; Zahardis and Petrucci, 2007; Johnson and Marston, 2008). Based on the reactivity trend of the CIs resultant from ozonolysis reaction in solutions, Criegee depicted them as zwitterions (Criegee, 1975). However, other researchers used computational evidence to calculate the energy difference between zwitterion and biradical forms and found that CIs have significant biradical characters (Goddard et al., 1973; Wadt and Goddard, 1975; Harding and Goddard, 1978; Bunnelle, 1991). More recently, a study of the dielectric constant effect of the solution on the CI resonance indicated an increase in the zwitterion character as the dielectric constant of the solvent increases (Parrondo et al., 1995). At the time of this write-up, Kalinowski and Räsänen simulated the electronic states of the simplest CI, CH_2OO, and their study indicated a significant role of combined biradical and zwitterionic features (Kalinowski et al., 2014). The distilled conclusion of the conflict in the electronic structure of CIs is that CIs are best represented as a resonance structure between the zwitterion and the biradical structure (Zahardis and Petrucci, 2007).Scheme 1.3 displays the electronic resonance structures of the CI.

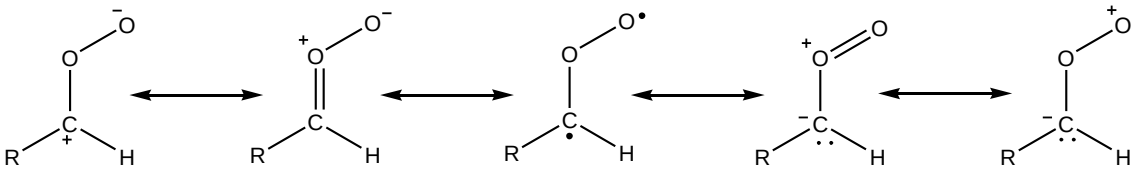

Scheme 1. 3 Resonance structure between zwitterion and the biradical of CI.

In the gas phase, CIs are short-lived species (Horie and Moortgat, 1991) rapidly rearrange to their corresponding carboxylic acids (Bunnelle, 1991). However, due to the solvent cage effect, the presence of CI in the condensed phase increases their life time and thus their probability to recombine with their corresponding carbonyl compounds to form secondary ozonides (SOZ) (Neeb et al., 1998; Moise and Rudich, 2002; Zahardis et al., 2005), hence the molecular rearrangement analogous to gas phase becomes less important (Katrib et al., 2004). The following reactions summarize possible fates of CI formed as a result of the attack of gaseous O_3 on an unsaturated substance in the pure or solution liquid phase (Bailey, 1958; Atkinson and Carter, 1984; Zahardis and Petrucci, 2007):

A) 1,3-dipolar cycloaddition of CI with one of the formed carbonyl products to form SOZ and polymeric ozonides:

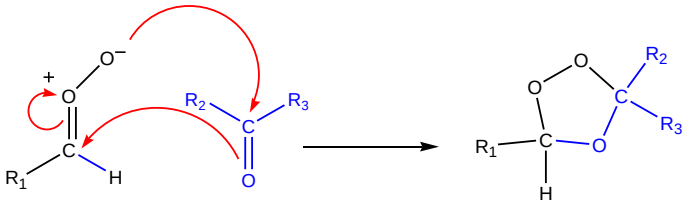

R1. 1

B) 1,3-dipolar cycloaddition of CI with other CI to form geminal diperoxide and polymeric peroxide:

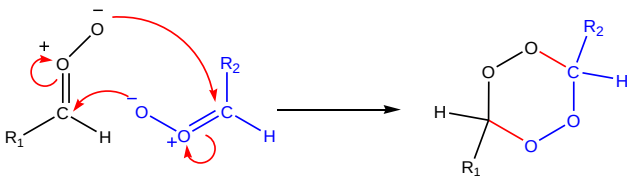

R1. 2

C) Addition to an acid:

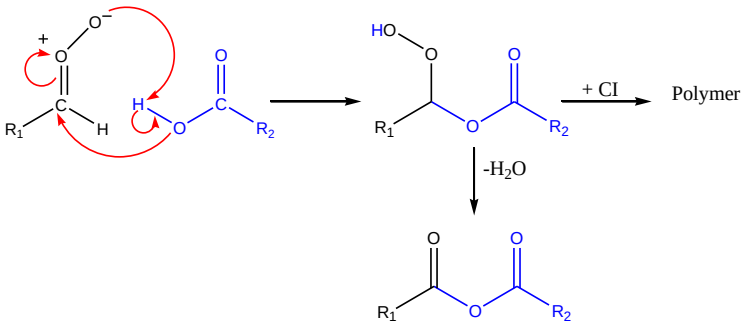

R1. 3

D) Addition to an alkene:

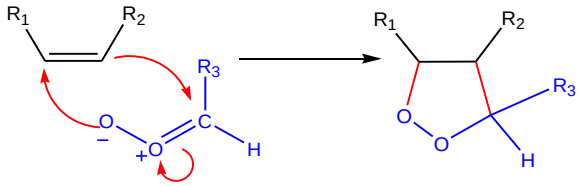

R1. 4

E) CI can react with protic solvent to form hydroperoxides:

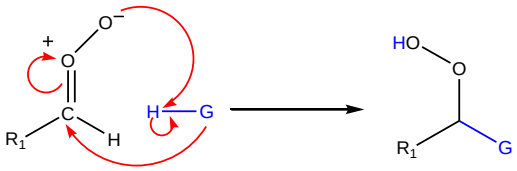

R1. 5

G= OH, OR, or OCOR

F) CI can rearrange to form stable products:

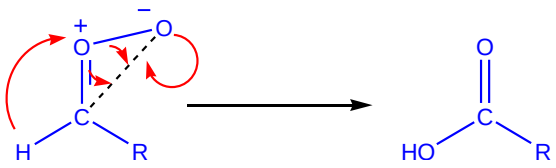

R1. 6

1.8.2 Reaction pathways and products of OL-O_3 HR

The four primary lower molecular weight products of the OL-O_3 HR, AA, NN, NA, ON have been reportedly observed in related studies as fragmented molecular ions (de Gouw and Lovejoy, 1998; Moise and Rudich, 2002; Morris et al., 2002; Smith et al., 2002b; Katrib et al., 2004; Thornberry and Abbatt, 2004). Few studies have reported the detection of the OL-O_3 HR primary products as unfragmented molecular ions using chemical ionization mass spectrometry (CIMS) (Hearn and Smith, 2004; Zahardis et al., 2005), field-induced droplet ionization (FIDI) (Grimm et al., 2006) and direct analysis in real time mass spectrometry (DART-MS) (Nah et al., 2013).

Katrib and coworkers studied the OL-O_3 HR of OL layers coats (2-30 nm) on inert polystyrene latex cores using an aerosol mass spectrometer and scanning mobility particle sizer. They determined the yields of the reaction products in the particle-phase for ON as a major product, while AA and NA occur as minor products, and other unidentified organic molecules. They assumed the observed evaporation to be the result of the formation of volatile NN as it was not detected in the particle phase. The formation of the organic molecules in their study was hypothesized to the reaction between CI and OL. Their proposed reaction mechanism (scheme 1.4) for the formation of these compounds is the addition of the CIs (precursor to AA and NA) across the double bond of OL to form a C_{27} peroxides which can cleave to yield the primary products. However, according to their gas-phase study, the reaction of the NA precursor with OL

is less favoured. The increase in the layer thickness of the OL appears to have no effect on AA yield but it did increase and decrease ON and other unidentified organic compounds yields, respectively (Katrib et al., 2004).

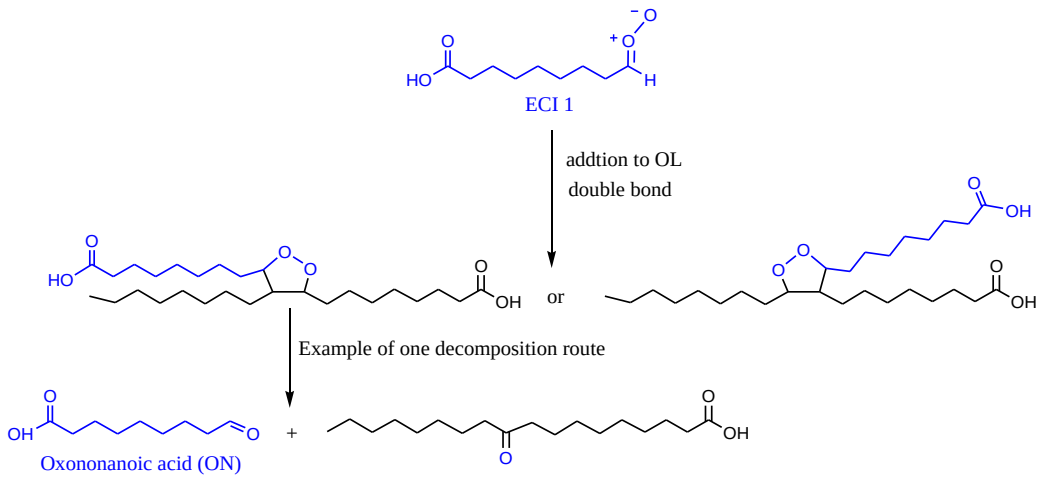

Scheme 1. 4 Example of a proposed condensed-phase reaction pathway between a CI1 and OL, by Katrib et al, 2004.

Hearn and Smith (2004) utilized aerosol chemical ionization mass spectrometry to study the OL-O_3 HR of pure ploydisperse particles. They found the four primary products to exist in the reacted particle phase. NN was detected in both particle and gas phases. AA was detected at a very low yield, while NN and ON were observed at larger yields than other products which they suggested the involvement of the CIs as a secondary route for their formation. In addition to the four primary products of the reaction, Hearn and Smith were the first to observe and identify a fifth product for this reaction, 9-oxooctadecanoic acid (Molecular Weight, MW, 298) at a small yield. They also believed that this product is formed via secondary reactions (Hearn and Smith, 2004).

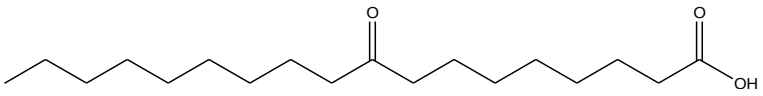

9-oxooctadecanoic acid (MW 298)

In addition to the direct observations of all major predicted products of the OL-O_3 HR in the particle phase, products of 1,3-dipolar cycloaddition such as SOZs and cyclic geminal diperoxides were first observed and reported by Zahardis and coworkers (Zahardis et al., 2005). OL particles were generated by nebulizing OL solution prepared in water/ethanol mixture. The chemical makeup of aged OL particles was followed by photoelectron resonance capture ionization mass spectrometry (PERCI-MS). The reported relative product yields in their study did not agree with others works (de Gouw and Lovejoy, 1998; Moise and Rudich, 2002; Morris et al., 2002; Katrib et al., 2004; Thornberry and Abbatt, 2004). The relatively volatile NN and ON were observed in higher yields than previously reported. Additionally, a high relative yield of AA has never been reported for similar reaction system which they attributed it to the high detection efficiency of PERCI-MS for dicarboxylic acid moiety. The mechanism for the formation of the 1,3-dipolar cycloaddition products was first proposed by Katrib and coworkers (Katrib et al., 2004) while their decomposition products were first observed by Hearn and smith (Hearn and Smith, 2004).

Following this development, studies then began to closely represent the complex matrix of ambient atmospheric particles to account for the importance of reaction conditions such as solvent, alkene identity and concentration. Zahardis and coworkers studied OL-O_3 HR using olive oil samples containing OL prepared in either ethanol or ethanol/water mixture and

aerosolized using a nebulizer. They reported the detection of five and six member oxygen-containing rings as fragmented molecular ions. Their proposed mechanism for the formation of these compounds is self-reaction of CIs and reaction of CI with aldehydes (Zahardis et al., 2005).

Ziemann used pure and mixed oleic acid particles to investigate the kinetics, reaction products, and mechanisms of OL-O_3 HR. He utilized a thermal desorption particle beam mass spectrometry (TDPBMS) and TDPBMS coupled to high performance liquid chromatography (HPLC). The reaction major products are ON, SOZs, α-acyloxyalkyl hydroperoxides (AAHP). AA was observed as minor product while NN and NA were not observed presumably because of their volatility to remain in particles. The study did not give evidence for the formation of higher molecular weight oligomers and their absence was attributed to their low formation yields and to the limitation of the technique. If present in the reaction matrix, aldehydes and organic acids were expected to react with AAHP to form bis(a-acyloxy-a-alkyl) peroxides. The study provided extensive reaction mechanism for more predicted reaction products for OL-O_3 HR (Ziemann, 2005).

Zahardis et al (2006) reported in their study a high molecular mass of unfragmented polyanhydride product detected at 963 Da by PERCI-MS. OL particle phase was generated by nebulizing OL in a water/ethanol mixture. The proposed pathway for this formation is via the addition of four CIs to one OL molecule.

Reynolds et al (2006) used Tandem mass spectrometry to study OL-O_3 HR system of OL solution prepared in ethyl acetate and bubbled with O_3 gas. All four primary products were observed in addition to a complex mixture of high molecular weight with m/z of up to 1000 Daltons. The identified high molecular weight compounds included SOZ, cyclic diperoxides, and linear AAHPs. One important conclusion of this study was oligomerization process is time

dependent. Ozonized samples were stored at 4 °C and were analyzed 1 week and 3 months after being oxidized by ozone. The result showed higher masses oligomers are more evident in aged ozonized samples.

Lee and Chan (2007) investigated the heterogeneous reaction of single levitated particles of OL with ozone using an electrodynamic balance (EDB) coupled with Raman spectroscopy. The study revealed no effect of ozone concentration on the reaction pathways and products formation. The oxidation products detected in the condensed phase were found to be more hygroscopic than the parent hydrophobic molecules.

The study by Hung and Ariya (2007) provided qualitative evidences for reaction pathways involving CIs. Attenuated total reflectance Fourier transform infrared spectroscopy (ATR-FT-IR) was utilized to monitor the heterogeneous reaction of OL droplets and aqueous OL/sodium-chloride mixed droplets with ozone. The high-mass species were identified by a Fourier transform ion cyclotron resonance mass spectrometer (FT-ICR-MS). A total of 13 organic molecules were identified and found to be composed mainly of AA and NA possibly formed via propagation reaction of AA and NA precursors. Additionally, the ozone consumed during the reaction was found to be 30 ±2% of total OL which supports the hypothesis of secondary reactions via CIs.

McNeill and co-workers (2007) studied the oxidation of aqueous particles of oleate mixed with inorganic salts. They employed aerosol flow tube and a photochemical reaction chamber coupled to chemical ionisation mass spectrometry (CIMS). ON was the most abundant oxidation product than NA and AA while NN was not detected. The oxidation reaction was concluded to occur at the particle surface for the reaction conditions and particle composition under the study.

The effect of the relative humidity on the particle reactivity OL-O_3 HR was explored via a number of laboratory studies (Asad et al., 2005; Vesna et al., 2008; Vesna et al., 2009; Lee et al., 2012). The water up take by a thin film of pure and processed OL was investigated by Asad et al using a quartz crystal microbalance. The change in the infrared spectra of pure and processed films was monitored using a Fourier transform infrared spectroscopy (FTIR) microscope. The study showed that the amount of water taken up by a processed OL film was 4 times that of pure OL film. The spectra were found to be consistent with the formation of an oxygenated polymeric product (Asad et al., 2005).

The hygroscopic growth factor, the change in particles diameter as a result of water uptake, of OL and other unsaturated fatty acid aerosols, arachidonic acid, was measured as a function of humidity and O_3 by Vesna et al. The study was performed on particles with size diameters between 20 and 250 nm at a humidity range of 10% to 95%. Particles were characterized using hygroscopicity tandem differential mobility analyzer (H-TDMA). As oppose to arachidonic acid particles, the study indicates that the growth factor of OL particles was very low and remained invariant to the ozonolysis conditions (Vesna et al., 2008).

In a detailed quantitative study of products formation in both, gas and particle phases at five different relative humidities (0%, 26%, 45%,70% and 81%), Vesna and coworkers characterized pure (at a geometric mean diameter of 78 nm) and processed OL particles using SMPS and an off-line gas chromatography mass spectrometry (GC–MS). They reported an increase in the product yields with increasing relative humidity. The most pronounced change in the product yields and distribution was between 0% and 26% RH. However, the peroxides yield was found to decrease as the humidity increased which was attributed to the reduction in the

peroxide precursors, CIs, by reaction with water to form hydroxyhydroperoxides (Vesna et al., 2009).

Very recent studies provided a comparison on ozonolysis reaction schemes and products for three unsaturated organic aerosol systems: oleic, maleic and arachidonic acid (Pope et al., 2010b; Gallimore et al., 2011b; Lee et al., 2012). While ozonolysis of OL particles showed independency on humidity, maleic and arachidonic acids showed distinct behavior at humid conditions. The authors explained their observations by the effect of the particle phase and the solubility of both the acids and the corresponding oxidation products on water. The liquid phase of OL droplets makes easy and comparable diffusion of O_3 to the bulk of the droplet at all relative humidity conditions. Additionally, the low solubility of OL and its oxidation products in water limits the effect of the humidity on the ozonolysis process. However, solid maleic and arachidonic acids droplets liquefy at high relative humidity thus increasing O_3 diffusivity into the bulk of the particle hence allowing oxidation process for the entire particle. On the other hand, the relatively high water solubility of maleic and arachidonic acids and their corresponding oxidation products significantly enhance the ozonolysis process at humid conditions (Lee et al., 2012).

The major finding in Lee and coworkers study of OL-O_3 HR using pure OL particles was that reactions of CIs in OL-O_3 HR system with other primary ozonolysis products leads to the formation of high molecular masses of oligomers (up to 1000 Da and more). CIs and ON were observed to be most abundant monomeric units (Lee et al., 2012).

The change in the viscosity of OL particles was demonstrated recently using Fluorescence Lifetime Imaging Microscopy (FLIM). The observed increase in the viscosity of OL particles and

the reaction dependent changes in viscosity during ozonolysis were taken as an indication of the formation of oxidation products with higher viscosity than the OL precursor (Hosny et al., 2013).

To sum up, the OL-O_3 HR is a popular model system for studying atmospheric oxidation of organic particles. Methods vary in the way the condensed phase of OL is presented from solution, coated tubes, coated cores, pure and internal mixed single, mono and polydispers particles. Most employed methodologies rely on mass spectral detection to follow the chemical makeup of the processed condensed phase or gas phase and most products in these studies are reported as fragmented molecular ions. Studies have strongly suggested secondary chemistry involving CIs leading to the formation of high molecular weight compounds characterized by low volatility and high hydrophilicity than the parent OL. Although studies have explored the effects of the droplet state, OL and ozone concentrations, aging process time, on the oxidation products or products distribution, no studies have explicitly focused on products distribution and mechanism of a processed pure polydisperse OL aerosol as a function of particle size using real online physical and chemical analysis. This study is the first to demonstrate a link between the particle size and reaction mechanism of OL aerosol. Finer particles may be hydrophilic arising from the complete oxidation of the organic material in the particles and the formation of early generation of oxidation products. However, observed product in large particles suggests the hydrophobicity of larger particles.

1.9 Objectives of the study

The overall aim of the study is to investigate the HR between OA and oxidants. The specific objectives of this study are to (1) construct a setup for the preparation and ageing of OA, in which generated OA are subjected to elevated levels of oxidants such as ozone, OH and HO_2 achieving exposures equivalent to several days in the atmosphere, in a matter of minutes, (2) determine the

change in chemical and physical properties of aged organic aerosol using a range of instruments and (3) examine the applicability of the technique on real ambient atmospheric particles.

Chapter 2 details the development of the experimental procedures to generate, oxidise and characterise organic aerosol. The fundamental aspects of the SMPS and the ATOFMS techniques are discussed in chapter 3 whereas the approach and the implementation of the PEroxyl Radical Chemical Amplifier (PERCA) in measuring HO_x levels is explained in chapter 4. Chapter 5 discusses the characterisation of the developed artificial chemical ageing system. Chapter 6 reports the results of the physical and chemical characterisation of laboratory generated OA employing SMPS and ATOFMS. A study of the reaction kinetics of OL-O_3 HR system is presented in Chapter 7. The feasibility of the developed technique in artificially processing real atmospheric particles is discussed in chapter 8. Finally, chapter 9 contains the main conclusions of the present work in addition to atmospheric implications and future directions.

CHAPTER 2 GENERAL EXPERIMENTAL METHODOLOGY

2.1 Introduction

This chapter outlines the general experimental methodology used in this study. Methods of atmospheric simulation are described and a detailed description of the approach followed in this research is given. The development of the Aerosol Chemical Ageing (ACA) system is discussed. This includes the generation of reactants, characterization of flow tube reactor and monitoring equipment. The operating conditions of the ACA including relative humidity, temperature, pressure, levels of particles and oxidants, species residence time in the system are summarized at the end of this chapter.

2.1.1 Atmospheric simulation

One of the most invaluable tools to study and understand the physicochemical transformations associated with local, regional, and global scale pollution is to simulate the atmosphere and atmospheric conditions. Air pollution has been simulated extensively using outdoor and indoor simulation chambers and aerosol flow tubes.

Although smog chambers have proven to be an essential tool for developing, evaluating, and advance understanding of chemical and physical transformations in the atmosphere, uncertainties in characterization, variability, background effects, and chamber contamination remains challenging.

Laboratory flow tube reactors have been employed to investigate the chemistry of inorganic particles as early as 1950s, but their application to organic surfaces and particles is relatively recent (Lambe et al., 2010). Flow tube reactors range in size from 0.001–0.01m^3 providing

shorter residence time in the range of seconds to minutes equivalent to hours in a smog chamber and to 1-2 weeks in real ambient atmosphere. Flow tube reactors operate with higher oxidants concentrations and exposure. Two main types of flow tube reactors have been employed to study chemical and physical transformations of atmospheric aerosols: the coated wall flow tubes (CFT) and aerosol flow tubes (AFT) reactors. The main difference between the CFT and AFT is the way the condensed phase of interest is presented to react with oxidants. In CFT the condensed phase of interest is coated onto the walls of the flow tube and the reactant gas is injected to the system, whereas in AFT the condensed phase of interest is in the form of particles which are generated artificially and flowed with the reactant gases to the AFT. In CFT studies oxidant decay is typically monitored while in AFT studies the loss of the condensed phase maybe monitored either for monodisperse or polydisperse particles. Flow tube reactors, however, are imperfect in simulating the chemistry of semivolatile organics because particle growth and composition are influenced by the tube walls that can also cause particle loss (Ziemann, 2010). However, AFTs are inexpensive and easy to use. They provide faster reaction time (seconds to few minutes), maintain better oxidation efficiency for OA under oxidation conditions that can be better controlled (e.g. oxidant concentration, contamination and wall interaction) (Lambe et al., 2010). The AFT is the deployed approach in this study. A typical experimental setup consists of an AFT, a source of aerosol, a source of oxidants, a gas line for introducing the reactants into the AFT, and characterization equipment.

2.1.2 Atmospheric particles proxies

To date, most particle studies focusing on kinetics, product evolution, and reaction mechanism of HR have utilized pure particles, internally mixed particles and coatings of the condensed phase

on seeds of salts or inert latex spheres (Katrib et al., 2004; Hearn et al., 2005; Hung et al., 2005; Zahardis and Petrucci, 2006). A number of organic compounds have been studied as model systems for chemical ageing of organic aerosols such as arachidonic acid, linoleic acid, linolenic acid, maleic acid, succinic, glutaric, pyruvic, malonic (Shende and Levec, 1999; Miñambres et al., 2013) palmitic acid, oleic acid, bis(2-ethylhexyl) sebacate, squalane hexacosane, hopanes, steranes and n-alkanes (Che et al., 2009).

In this study, bis(2-ethylhexyl) sebacate (BES), *cis*-9-octadecenoic acid (Oleic acid, OL), and *cis*-butenedioic acid (maleic acid, MA), were chosen as primary atmospheric proxies for artificial chemical ageing process. These species were selected as (i) they are frequently found in the natural environment, (ii) they are of the size range – and hence physic-chemical properties - appropriate for primary emissions, and (iii) they have been used previously as "model" compounds for the study of atmospheric oxidation. In more detail: compounds of this type were found on the surfaces of natural bodies of water (Shende and Levec, 1999; Vlasenko et al., 2008). The carbon number of OL and BES compounds is within the range typically found in primary particles such as those hydrocarbons found in diesel lubricating oil, a major component of heavy-duty diesel emissions (Sakurai et al., 2003). BES and OL particles are liquid at room temperature eliminating complications of particle shape on particle analysis. The low vapour pressures (BES, 2.8×10^{-6} Pa at 25°C and OL, 1.9×10^{-6} Pa at 25°C (George et al., 2007; Cappa et al., 2008)) minimizes possible gas-phase reactions with oxidants and maximizes heterogeneous kinetics (surface and bulk particle processes). OL, a long-chain fatty acid, was selected as a model aerosol system for unsaturated carboxylic acids. It has been used frequently as atmospheric proxy in a number of studies (Katrib et al., 2004; Tedetti et al., 2007; Zahardis and Petrucci, 2007; Vesna et al., 2009; Hosny et al., 2013). BES is chemically reduced as compared to OL. Unlike OL and

BES, MA, is solid and readily soluble in water. It is a small unsaturated di-carboxylic acid. MA has been found in ambient particles at a considerable concentration (Shende and Levec, 1999; Oliviero et al., 2001) and it appears as a major intermediate in aromatic pollutant oxidation pathways such as the oxidation of phenol (Devlin and Harris, 1984; Shende and Levec, 1999).

2.2 Aerosol Chemical Ageing (ACA) system

The experimental set-up is mainly composed of a gas supply, purification and controlling systems, an aerosol generator, oxidants creation system, AFT, and monitoring instruments.

2.2.1 Gas supply and purification system

Synthetic air, nitrogen (N_2) (99.9% stated purity), oxygen (O_2), carbon monoxide (CO) (research grade), nitric oxide (NO) (NO/N_2 mixture 600 ppm), and nitrogen dioxide gases (NO_2) (NO_2/N_2 mixture 0.89 ppm), were supplied by BOC and purified as follows:

Synthetic air, N_2, CO, and NO_2 lines were purified by passing through charcoal traps (Grace Discovery Science, Efficiency<20 ppb) to remove hydrocarbon impurities. Traces of water were removed from the N_2 and synthetic air lines using a silica trap (Sigma-Aldrich, Molecular Sieve 5A Moisture Trap) so that no radicals were created unless the water bubbler was in use. NO gas was purified by passing through ferrous sulphate trap to selectively reduce traces of NO_2 to NO so that no NO_2 is introduced in the system (unless created).

2.2.2 Mass flow controllers (MFCs)

The gas-phase streams flowing through the system were introduced at constant rates controlled by newly purchased mass flow controllers (Brooks Instruments; Model SLA5850S). The software was IGI systems (LAB Interface 130410, v1.0). The mass flow of the gases was

displayed in terms of the volume of the gas and expressed either in units of standard litres per minute (slm) or standard cubic centimetres per minute (sccm). The accuracy of the new MFCs over the entire flow range was tested by calibrating them using a dry flow standard meter (Gillibrator, Defender 510 Volumetric Primary Flow Standard, Model 510-M and 510-L). The flow in the MFC to be calibrated was varied over its entire working range and the dry flow standard meter was attached to the exit of the MFC to record the actual set flow. The recorded actual flows were corrected for the differences in temperature between the calibration in the factory and the operating temperature during the calibration using the following formula:

$$V_1 = V_2(T_1 / T_2)(P_2 / P_1)$$

Eq 2. 1

where V_1 and V_2 are the corrected flow at the standard temperature and pressure and the actual flow during the calibration, respectively. T_1 and T_2 are the standard temperature at which the factory calibrated the MFC and the temperature during the calibration, respectively. P_1 and P_2 are the standard pressure at which the factory calibrated the MFC and the pressure during the calibration, respectively. MFC calibration is performed whenever the MFC is cleaned, repaired, replaced, or reinstalled for ambient experiments after being used for laboratory experiments or vice versa. A typical calibration curve of an MFC is presented in Appendix B, figure B-1

2.2.3 Chemicals and reagents

For particles generation, liquid BES, $C_{26}H_{50}O_4$, (M 426.67), (>97.0%), and OL, $C_{18}H_{34}O_2$, (M 282.47) (>99.0%), were obtained from Sigma-Aldrich while solid MA, (M 116.07) (>99.0%) was obtained from Fisher Scientific and were used as received without further purification. Liquid methyl oleate (MOL), $C_{19}H_{36}O_2$, (M 296), (99%), is the analogue ester to OL (used in this study

to emphasis the cyclisation mechanism in the OL oxidation reaction products) was obtained from Sigma-Aldrich and was used as received. Iron sulphate heptahydrate ($FeSO_4.7H_2O$) used to purify nitric oxide (NO) line was of analytical reagent grade purchased from Fisher Scientific and was used as received.

Luminol solution used in the chemiluminescence detection of NO_2 was obtained from Drummond Technology and was of chemically pure grade (Luminol II Solution) used without further purification.

Butanol used in optical particle detection was of laboratory reagent grade, obtained from Fisher scientific and used as received.

ATOFMS size calibration was accomplished using polystyrene latex spheres suspension (PSL, size 0.3, 0.4, 0.56, 0.7, 0.9, 1.3, 2, and 2.5 μm in diameter) and were supplied by Duke Scientific and used as received. Chemicals for ATOFMS mass calibration, ICP Multi-Element standard solutions were used: standard A (900 μg/ml: Ba, Pb, Li, K, Na & V in 5% HNO_3) and standard B (900 μg/ml: Ag and Mo in 5% HNO_3) were obtained from AccuStandard and were used as purchased without further purifications. Compounds used in ATOFMS mass data interpretation include azelaic acid (98%), nonanal (95%), nonanoic acid (96%) and 4-oxononanoic acid (95%) were purchased from Sigma-Aldrich and were used as received without further purification.

The cationic laser dye, Bis[5-amino-9-(diethylamino)benzo[a]phenoxazin-7-ium] sulfate, Nile Blue Sulphate (NBS), (M 733), used to modify the spectroscopic properties of OL particles was purchased from Fisher Scientific and used as received. Methanol solvent was of laboratory reagent grade, obtained from Fisher scientific and used as received.

2.2.4 Tubing and connections

All connections were made of Polytetrafluoroethylene (PTFE) or stainless steel and all tubing for gas-phase species was PTFE and has an outer diameter (o.d.) of 6 mm. Tubing used to introduce or monitor aerosol in the system was antistatic tube (GRIMM AEROSOL, antistatic flexible tube) and has an internal diameter (i.d) of 4 mm.

2.2.5 The Aerosol Flow Tube reactor (AFT)

The AFTs reactor consists of one set of Pyrex cylindrical tubes that is 10 cm in internal diameter and either 20, 50, or 100 cm long corresponding to a reactor volume of 1.6 l for AFT 1, 3.9 l for AFT 2, and 7.9 l for AFT 3, respectively. The cylindrical tube is closed on both sides by aluminium flanges which are fitted with stainless steel inlets and outlets for the entrance and exit of dry or wet air, O_3 loaded air, and aerosols. The reactor is held in a vertical orientation in an aluminum frame. A hygrometer probe (Rotronic, hygropalm) inside the AFT is used to monitor the temperature and the relative humidity. The PEroxy Radical Chemical Amplifier (PERCA), O_3 monitor, SMPS and ATOFMS sampling outlets are located immediately downstream of the AFT.

2.2.5.1 Flow through the AFT

The flow in a circular tube can be divided into two different types, laminar and turbulent flows, depending on the physical characteristics of the flowing fluid. In a laminar flow molecules of the fluid are moving in straight lines with variable velocities resulting in a laminae movement i.e. moving in numerous layers without much mixing between the layers. This is because molecules at the centre of the tube move faster at approximately twice the mean velocity of the molecules at the wall of the tube which are almost stationary due to the resistance between the fluid and the

tube wall that opposes the flow. The resulting velocity profile of a fully-developed laminar flow is parabolic.

Turbulent flow is opposite of the laminar flow, where molecules of a fluid move with high velocities which fluctuate with time causing considerable chaotic mixing between layers at each point in the tube. The difference between the laminar and the turbulent flows is represented by Figure 2.1. Reynolds number (Re), a dimensionless number established by Osborne Reynolds, is used to characterize and quantify laminar and turbulent flows and is given as:

$$\mathrm{Re} = \frac{D\upsilon\rho}{\eta}$$

Eq 2. 2

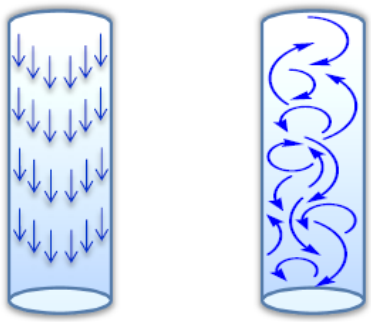

(a) **(b)**

Figure 2. 1 Types of flows in a circular tube: (a) laminar and (b) turbulent.

where D is the diameter of the circular tube in m, υ is the velocity of flow in m/s, ρ is the density of the carrier gas in Kg m^{-3}, and η is the viscosity of the carrier gas in Pa s.

Experimental observations have shown that for Re below 2100 the flow is considered as laminar flow and above that value the flow is turbulent (Bird et al., 2007). In the ACA system the velocity of the flow in AFT 3 was 0.74 cm s^{-1}, the diameter of the AFT is 10 cm, the density of

the air is 1.195 Kg m^{-3}, and the viscosity of the air is 1.82 x 10^{-5} Pa s (both at 20°C and atmospheric pressure) (Kaye and Laby, 1995). The calculated Re, 48.8, meets the conditions of the laminar flow. However, the build-up of the parabolic profile of the laminar flow in a flow tube requires the flow to travel a distance before the laminar flow conditions are established. This distance is called the entrance length, *Le*, and it is determined using the diameter of the flow tube, D, and Re, (Bird et al., 2007):

$$Le = 0.035DRe \qquad \text{Eq 2. 3}$$

The established entrance length, Le, for this system was 17.1 cm, which may be compared with the total lengths of the reactor tube set.

2.2.5.2 Residence time in the AFT

Experimentally, the residence time (τ) in the ACA system was measured at the established conditions of oxidation by monitoring the change in the ozone (O_3) mixing ratio in the system. Ozone was generated or terminated by alternatively switching the UV lamp on or off, respectively, and delivered to the AFT as described previously. Figure 2.2 shows the raw data obtained from the O_3 monitor for a series of three experimental trials each consists of two parts. The first part being a positive response where the concentration of O_3 changes from 0 to maximum level at ~21 ppm. In the graph this corresponds to time intervals labelled as 'On'. The second part being a negative response where O_3 level is regulated back from maximum concentration at ~21 ppm minimum level at 0 ppm. In the graph this corresponds to time intervals labelled as 'Off'. The relative difference between measured τ (147 s) and calculated τ (135 s) for the AFT 3 is 9% suggesting a satisfied agreement between the measured and the plug flows.

For data analysis, only the time corresponds to the beginning of the O_3 concentration fall event from maxima to the time O_3 concentration reaches 0 ppm is considered. Normalizing and integrating the area under these curves yields the measured τ, which was found to be 147 (± 0.6) s. The theoretical τ, was calculated based on the universal mathematical equation as follows:

τ=volume of the system/flow rate through the system

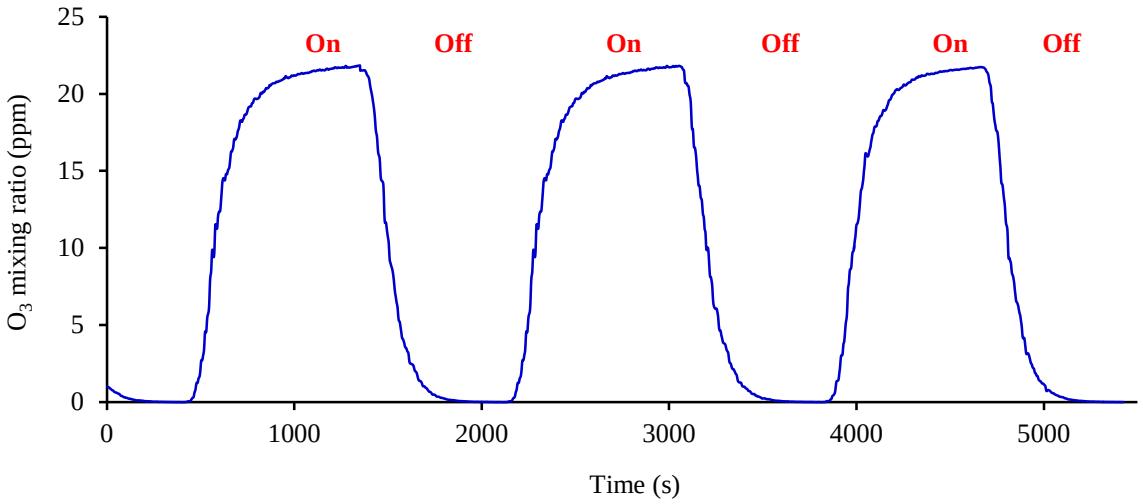

Figure 2. 2 Ozone monitor response to switching on and off the ozone generator.

2.2.6 Preparation of the reactants

2.2.6.1 Generation of organic aerosol

To date, studies conducted on organic aerosol formation, kinetics, and reaction mechanisms have made the use of wide range of generation methods. Condensation of liquid vapour phase and mechanical dispersion are the two main techniques of generating organic aerosol. In this study both approaches were used in order to meet both optimum generation conditions (particles number concentration and diameter), particles residence time, and better instrumental detection for the techniques deployed in the study; the SMPS and the ATOFMS.

Condensation of liquid vapour

Condensation or nucleation of liquid vapour is the formation of new particles from a continuous phase, can occur heterogeneously in which a gas nucleates on foreign nuclei such as aerosol particles, ions or surfaces. Nucleation of liquid vapour can also occur homogenously i.e. self-nucleation, in which a vapour deposits on its own clusters or embryos without the presence of foreign substances serving as nucleation sites.

Homogenous nucleation of liquid BES and OL

For the physical characterisation of organic aerosol using the SMPS, liquid BES or OL particles were generated by homogeneous nucleation of pure vapour of the liquid organic compounds. The diagram of the experimental setup for the homogeneous nucleation of BES and OL aerosols is shown schematically in Figure 2.3.

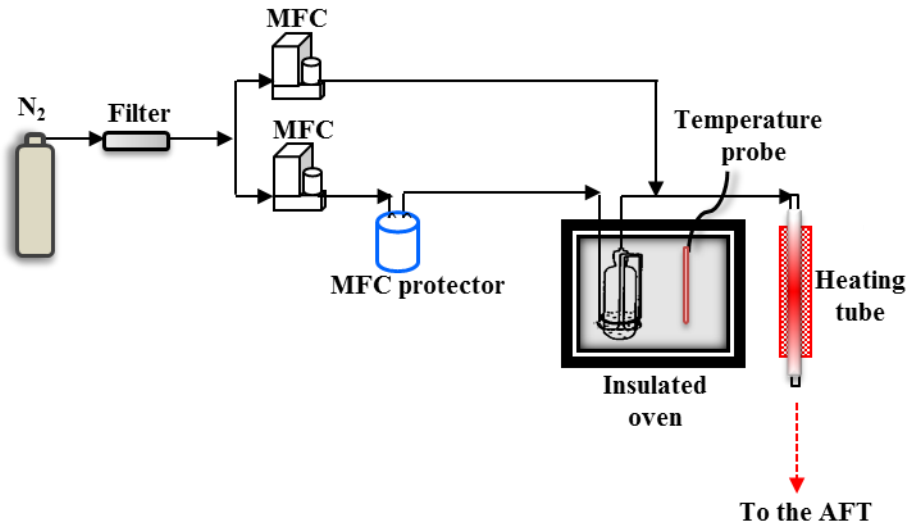

Figure 2. 3 The experimental setup for the homogeneous nucleation of BES and OL aerosols.

The low-volatile liquid, BES or OL, was heated in a Pyrex vessel in an insulated thermostatted oven to create a pure vapour at an elevated constant temperature of 140°C or

120°C, respectively, to maintain a uniform concentration of the liquid vapour. A flow of 0.5 slm N_2 was bubbled through the high-boiling liquids to produce a spray of liquid droplets before being diluted immediately after leaving the oven with a second flow of N_2, 0.5 slm. The N_2 flows were always kept at constant conditions to maintain constant number concentration of nuclei. The aerosol flow then passed directly at ambient temperature to a reheating tube set at 200°C to homogenize aerosol formation (Richard, 2006). The temperature of the system was controlled to maintain constant heating and was kept well below the boiling point of BES (256°C), and OL (360°C) (Bokis et al., 1999) in order to prevent pyrolysis of organic compounds, i.e. charring may occur in an oxidative environment at these temperatures (Philippin et al., 2004). The resulting aerosol stream was transferred via an antistatic tube at ambient temperature to the inlet of the AFT. These operating conditions were capable of producing aerosols size distribution with a geometric standard deviation, σ_g, of 1.1-1.3, a median aerodynamic diameter close to 300-450 nm and a number concentration of particles in the range of 10^6-10^7 particles cm^{-3}. The produced particle size and concentrations were controlled by varying the proportions of N_2 flow through the bubbling vessel and the N_2 dilution flow, the temperature of the bubbling vessel containing the high boiling liquid, and the temperature of the heating tube. Characterization study of the factors affecting particles generation via vaporization-condensation methods has been discussed in chapter 5, section 5.2.2.

Aerosols generation by liquid atomization

Liquid atomization or nebulization is the generation of liquid droplets by means of dispersing a liquid into a gas stream from a bulk reservoir of pure liquid or from a bulk of a solution prepared from solid or liquid substance (Richard, 2006). Droplets generated from a bulk solution can be

further dried by evaporating the liquid solvent to leave the nonvolatile solid or liquid residual of the material under investigation. In this work, a constant output atomizer (TSI, Model 3076) was used to generate organic aerosol prior their physical and chemical characterization. Figure 2.4 illustrates the atomizer operation principle.

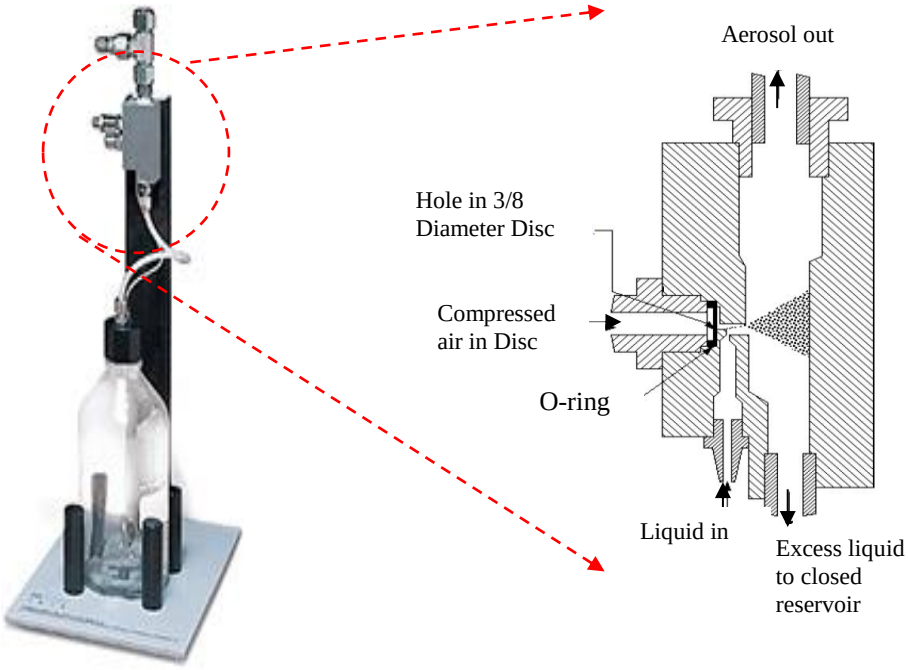

Figure 2. 4 A schematic diagram of the TSI constant output atomizer (Model 3076) (TSI 2008).

Generally, a solution of interest at a certain concentration is prepared in a solvent and placed in the atomizer bottle (1 L in volume). A high velocity jet of air is formed by sending a purified dry air to a small orifice. The liquid from the bottle is supplied to the atomization area through a solution inlet via the capillary action. A polydisperse liquid aerosol is formed when the high velocity air jet impinges the liquid in the atomization area with larger droplets impacting on

the back wall of the atomizer and dripping back to the atomizer bottle. While smaller droplets travel out of the atomizer through the aerosol outlet with the dry stream of the air.

Generation of MA aerosols using liquid atomization

A solution of MA (0.1 M) was prepared by dissolving 11.6 g of the acid powder in 1 L of deionised water. The solution was made to a polydisperse aerosol using a constant output atomiser (TSI, Model 3076). The flow rate to the atomiser was kept constant at 3 slm to meet the minimum flow requirement of the atomiser. Subsequently, the aerosol output flow was split in to two flows by means of a valve, 1 slm was either passed directly to the AFT for wet oxidation or passed through a series of 2 silica gel diffusion dryers (TSI: Model 3062) prior the entry to the AFT for investigating dry oxidation of MA particles. The reminder of the flow was sent to the vent. Figure 2.5 sumarises the generation process of MA aerosol.

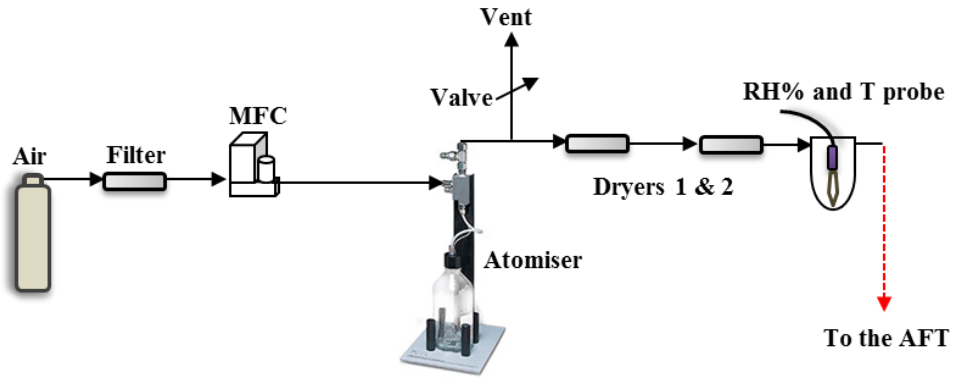

Figure 2. 5 Typical experimental setup for the liquid atomization of MA, standards and optically modified BES and OL aerosols.

Aerosol generation by atomization gave a size distribution of a σ_g of 1.4-1.8, a median diameter close to 200-400 nm and a number concentration of particles in the range of 10^6-10^7 particles cm^{-3}.

Generation of optically modified aerosols using liquid atomisation

In this study, standards (AA, NA, and NN), pure and processed OL, MOL and BES liquid particles generated via homogeneous nucleation method have shown poor absorption of the laser desorption ionization (LDI) pulse at 266 nm and thus have not met the detection criteria of ATOFMS. To measure the chemical composition of non-absorbing particles by the ATOFMS, the spectroscopic properties of the generated particles were modified by adding a cationic laser dye, NBS, at a low concentration ($5x10^{-5}$ M) to OL (0.15 M), MOL (0.15 M), BES (0.2 M) and standards (0.15 M) solutions matrices prepared in methanol to serve as energy capture for the laser desorption ionisation energy (Figure 2.5). The prepared solutions were then atomized as describe above for MA aerosol. Under the experimental condition of this study, methanol is expected to evaporate after drying the aerosol stream using the two silica gel diffusion dryers as explained above (Figure 2.5). Morris et al (2002) measured the amount of residual methanol in pure OL polydisperse aerosols (mobility diameter at the high end of the size distribution is >500 nm), produced using the same constant output atomizer (TSI Model 3076) from a solution of OL in methanol, dried using a silica gel diffusion, at atmospheric pressure and found that only 2% by weight of methanol was left in the particles.

Measurement of NBS absorbance spectrum

The suitability of the laser dye (NBS) as a chromophore for absorbing the LDI energy at 266 nm was investigated by measuring the absorbance spectrum of the NBS. The measurement was conducted was using a dilute solution of NBS (4.6 μM) and was recorded on a JENWAY UV/VIS spectrophotometer (model 6800). 10×100 mm quartz cells (kromatek, ES Quartz Glass 190nm – 2500 nm) (100 mm path length) were used in the measurements. The reference cell contained the pure solvent, methanol, used in preparing NBS solution. Appendix B, figure B-2,

illustrates the structure and the characteristic absorption spectrum of NBS. The absorption spectrum shows distinct peaks at 624 and at 276 nm and a minor peak at 325 nm. Wavelengths (below 276 nm) are capable of capturing the LDI energy in the ATOFMS system and thus detection of organic aerosol doped with NBS was achieved.

2.2.6.2 Generation of ozone

Ozone was generated by irradiating a known flow of either synthetic air or pure oxygen entering three glass vessels connected in series each containing a mercury UV pen-ray lamp (Ultra-Violet Products Ltd., $\lambda = 184.9$ nm) before being diluted in a second known flow of synthetic air:

$$O_2 + h\nu\,(184.9\text{ nm}) \longrightarrow 2O \qquad \text{R2. 1}$$

$$O + O_2 + M \longrightarrow O_3 + M \qquad \text{R2. 2}$$

The ozone mixing ratio was controlled by the gas stream (air or oxygen) flowing to the ozone generator vessels, the ratio of the amount of gas flow through the ozone generator vessels and the air used to dilute the flow, and the number of lamps involved in the photolysis in a reproducible manner. Low mixing ratio of ozone was maintained by involving only one UV lamp partially covered with aluminium foil in the photolysis and the use of synthetic air as a feed gas. High level of ozone was produced by involving more than one UV lamp and/or the use of oxygen as a feed gas. Section 5.6 characterises the efficiency of ozone production from synthetic air and pure oxygen feed gases in the ACA system. The ozone loaded air then enters the AFT through an upstream inlet. Sufficient time was allowed for the concentration inside the AFT to reach steady state by monitoring the stability in the concentration of ozone inside the AFT.

2.2.6.3 Creation of radicals

Radicals, OH and HO_2 (collectively known as HO_x), were created in-situ by the reaction of water vapour in the ambient flow with singlet atomic oxygen O (^{1}D) in the AFT reactor. The water vapour is produced by passing a flow of synthetic air through two water bubblers connected in series and containing deionized water to the AFT at atmospheric pressure. The relative humidity was controlled by the relative amount of the air flows through the bubbler and the dry air used to dilute the flow. O (^{1}D) was generated in the AFT from the photolysis of O_3 loaded air at 254 nm using a mercury UV pen-ray lamp (Ultra-Violet Products Ltd., λ = 184.9 nm) positioned vertically inside the AFT reactor and treated by a shielding tube (Melles 254 nm 5 nm) to filter out 184.9 nm light for two reasons. Firstly, to avoid light interactions of 184.9 nm with the created atmosphere components including aerosol so that any physical or chemical changes can be accounted solely for radicals oxidation. Secondly, to prevent further production of O_3 from O_2 photolysis so that all O_3 entering the reactor is from the O_3 generator source and all HO_x are generated via singlet atomic oxygen O (^{1}D) chemistry. Subsequently, O (^{1}D) reacts with water vapour to form a pair of hydroxyl radicals (OH), which initiate oxidation of the particles. The following equations summarise the creation of OH radical in the AFT:

$$O_3 + h\nu\ (245\ nm) \longrightarrow O(^1D) + O_2 \qquad \text{R2. 3}$$

$$O(^1D) + H_2O \longrightarrow 2OH \qquad \text{R2. 4}$$

This fraction of O (^{1}D) atoms that produces OH depends on concentration of H_2O. However, the bulk of O (^{1}D) atoms collides with N_2 or O_2 and quenched to ground state oxygen atoms:

$$O(^1D) + N_2 \longrightarrow O(^3P) + N_2$$ R2. 5

$$O(^1D) + O_2 \longrightarrow O(^3P) + O_2$$ R2. 6

O_3 reacts with OH and leads to the production HO_2:

$$OH + O_3 \longrightarrow HO_2 + O_2$$ R2. 7

An explanatory experimental investigation supported with a theoretical study of radical chemistry in the ACA system has been described in chapter 4.

2.2.7 Monitoring instruments

2.2.7.1 Scaning mobility particle sizer (SMPS)

To follow changes in the particle size distribution during the course of the oxidation with O_3 and radicals, scanning mobility particle sizer (including electrostatic classifier (TSI model 3080), neutralizer (TSI model 3076), a long differential mobility analyzer (LDMA, Model 3081, TSI Inc.) and a condensation particle counter CPC (3022A)) operating at 3 L/min and 0.3 L/min for sheath and aerosol flows, respectively, was used to monitor the aerosol number and size distribution. Particle densities of 0.891, 0.914, 1.59, 1.03 (Gomez et al., 1986) and 1.2 g cm^{-3} (Morawska et al., 1999) were used for estimating number, mass, volume of OL, BES, dry MA, wet MA and ambient particles, respectively. Size distribution data were recorded and analysed using TSI AIM software v 8.1. Aerosols were monitored in one size scan every 3 minutes for a size range of 15.1-667 nm before and after exposure to oxidants to monitor changes in number, diameter, mass, volume and surface area of aerosols. For each experimental setting, a minimum

of 10 size scans were produced, averaged, plotted and errors were displayed whenever they showed signify magnitudes. The SMPS approach in measuring particle size distribution has been described in detail in chapter 3.

2.2.7.2 Aerosol Time of Flight Mass Spectrometry (ATOFMS)

The Aerosol Time of Flight Mass Spectrometry (ATOFMS) (TSI, model 3800) is an on-line aerosol instrument used to measure physical and chemical characteristic of both artificial and ambient aerosol before and after chemical processing. The ATOFMS instrumentation, advantages implementation and limitation have been discussed in chapter 3.

ATOFMS particle size calibration

The particle sizing region of the ATOFMS was calibrated by nebulizing polystyrene latex spheres (PSL), ranging in size from 0.2 to 2.5 μm in diameter. A series of PSL suspensions (0.2, 0.3, 0.4, 0.56, 0.7, 1.3, 2, and 2.5 μm in diameter) was prepared in deionised water (20 drops in 1 l) and nebulised using a constant output atomiser (TSI: Model 3076) at a constant flow of 3 slm. The output of the nebulizer was sent through a diffusion dryer (TSI: Model 3062) to ensure that the particles were dry prior to entry into the ATOFMS sampling inlet at 0.3 slm and the rest of the flow was sent to the vent. A calibration curve was then created based on the relationship between the measured velocity of the nebulised PSL particles in the sizing chamber and their particle size. A typical size calibration curve is presented in Appendix B, Figure B-3.

ATOFMS particle mass calibration

The mass spectrometer was calibrated using similar procedure as described above but by nebulising different standard ions solutions (NO_3, Ba, Pb, Li, K, Na, V, Ag, Mo, and NO_3),

substances involved in this study: OL, MA and NBS, and ambient carbon clusters. The obtained time of flight of peaks was correlated to the molecular weight of the substance. A calibration curve was then created based on the relationship between the measured velocity of the nebulised liquid particles in the mass spectrometer region and their mass fragments. The ATOFMS mass response was calibrated up to 563 Da, and thus m/z values reported beyond this limit have been calibrated using identified higher molecular weight products peaks which best fit line to the mass calibration data in the MS analyse software. Typical positive and negative ion mass calibration curves are presented in Appendix B, Figure B-4 and B-5 respectively.

Detection sensitivity of ATOFMS

To test the relative sensitivity of the ATOFMS towards OL, NN, AA, NA and 4-ON a standard mixture solution containing OL, NN, AA, NA, and 4-ON at an equimolar concentration and traces of the laser dye NBS was prepared in methanol. The standard mixture solution was aerolized using liquid atomisation as described above.

2.2.7.3 Ozone Monitor

The ozone level was measured using ozone monitor (2B Technologies, Model 205) sampling through 50 cm length tube that ran from the AFT outlet directly to monitor. The monitor is a dual beam ozone monitor, 2B 205, in which simultaneous measurements of UV light intensity at wavelength of 254 nm, I_0, for ozone-scrubbed air and I for unscrubbed air are made. Ozone concentration is then calculated for each cell using Beer-Lambert Law:

$$C_{O_3} = \frac{1}{\sigma l} \ln\left(\frac{I_0}{I}\right)$$

Eq 2. 4

where σ is the absorption cross section for O_3 at 254 nm, which is $1.15x10^{-17}$ molecule^{-1} cm^2 (Daumont et al., 1992), *l* is the path length of the absorption cells, which is 15 cm. The two values of C_{O3} are averaged and obtained via both serial output. The limit of detection ranges from 1 ppbv to an upper limit of 100 ppmv. The generated ozone was in the range of 0.01-100 ppm.

2.2.7.4 Peroxy radical chemical amplifier (PERCA)

The PERCA was deployed in this study to measure the absolute concentration of HO_x in the ACA system. Details of the experimental measurements of HO_x using PERCA and the theoretical study of the oxidation environment in the ACA system have been described in chapter 4. Typically measured HO_x in the ACA system was in the range $(8.0\pm0.4)\times10^9$ to $(1.2\pm0.6)\times10^{10}$ molecules cm^{-3} corresponds to an exposure range of 1.2×10^{12} to 1.8×10^{12} molecules cm^{-3} s. Assuming an average ambient OH concentration of 1.5×10^6 molecules cm^{-3} (Mao et al., 2009), this laboratory exposure is equivalent to 9.3-20.1 days of ambient atmospheric oxidation.

2.3 Artificial chemical ageing of laboratory generated aerosol

Figure 2.6 displays a typical experimental set-up of the artificial chemical ageing of laboratory generated aerosol. In all laboratory experiments the ACA system was prepared by thorough cleaning the AFT and tubing, testing the purity of individual gas streams using the monitoring instruments, checking stability of the gas flows and oxidant levels. Then typical flows of aerosol (1 slm), ozone loaded air (0.5 slm) and dry or wet dilution (2 slm) were introduced to the AFT. Whenever nitrogen flow was used in generating aerosol such as in homogeneous nucleation of OL and BES, a flow of oxygen was added to the dry or wet flow in a portion such that the final air mixture in the AFT mimics the ambient atmosphere. These flows were initially studied and optimised for optimum generation of reactants, oxidation conditions and instrumentation

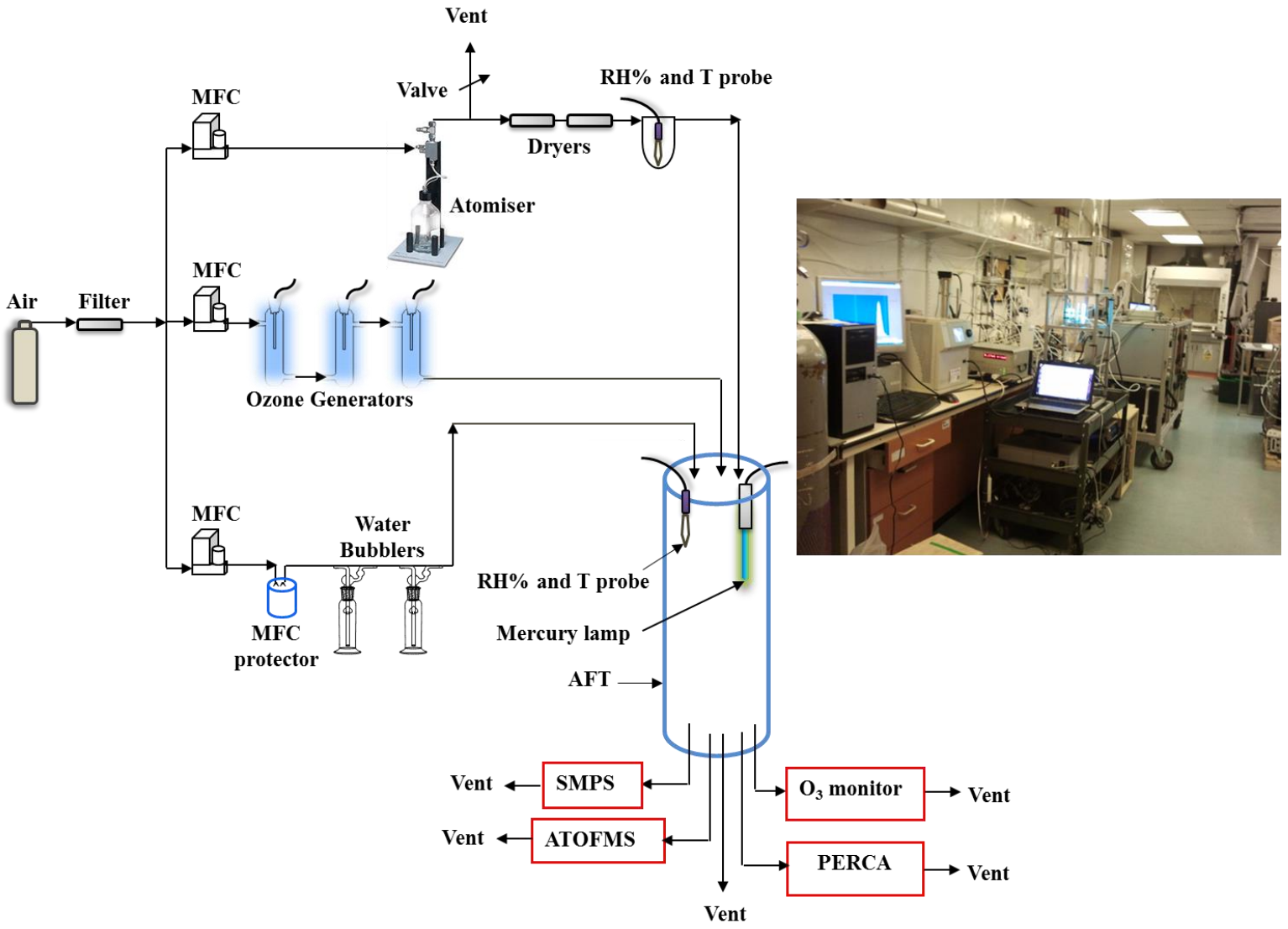

Figure 2. 6 Experimental setup for the heterogeneous oxidation of laboratory generated aerosol.

detection (details of ACA system characterization has been discussed in chapter 5). The concentration of generated particles number was as high as 10^6-10^7 particles cm^{-3} and aerosol was sampled directly from the AFT for analysis by the SMPS and the ATOFMS.

Reactions of generated aerosol with ozone at dry (RH 0.5±0.02) or wet (RH 65.0±0.2%) condition was initiated by turning on the UV lamp of the ozone generator (184.9 nm) to generate ozone at ≥ 20 ppm. However, reaction of aerosol with HO_x radicals was progressed by turning on the UV lamp in the AFT reactor (254 nm) at 65.0 ±0.2% relative humidity while the UV lamp of the ozone generator kept on and partially covered with aluminum foil such that low ozone levels ~100 ppb is produced. This operating procedure was established experimentally and showed to produce maximum HO_x concentration at $(1.2\pm0.6)\times10^{10}$ molecules cm^{-3}. Chapter 4 explains the oxidation environment and optimisation of the oxidation conditions of the ACA system.

The produced SOA was analysed continuously by the SMPS and the ATOFMS which were connected directly to the AFT. The sampling typically starts 5 minutes post turning on or off the UV lights for detection of processed or unprocessed aerosol, respectively. Another 5 minutes sampling period is also run for each new sample before data collection to prevent contamination from a previous sample. 30 minutes averaged measurements of the unreacted and reacted particles were characterised.

The effect of additional residence time within the sampling and characterizing systems was also assessed. Compared to the reaction time in the AFT (147 s), the calculated residence time of the aerosol in the sampling tubes (<2 s), SMPS (<1 s) (von Hessberg et al., 2009) was negligible. However, for ATOFMS system the additional measured residence time is in order of ~10 s (observed from the time the sampling inlet of the ATOFMS was connected with the sampling

tube to the time the first signal appeared in the mass spectrometer). Moreover, the successive pressure drop which reaches an operating pressure of 10^{-7} Torr within the ATOFMS sampling chambers ensures ultimate oxidant removal from the aerosol stream. Therefore the heterogeneous reaction of particles is considered to be terminated at the early stages of the sampling nozzle. The ATOFMS instrumentation and operating conditions are explained in chapter 3

2.4 Artificial chemical ageing of real ambient particles

Following the development, characterization and deployment of the ACA system to process artificial aerosol, the applicability of the ageing system was examined on real atmospheric particles. Measurements of processed and unprocessed ambient aerosol particles by ATOFMS and SMPS were conducted in September 2012 and March 2013. The sampling site was on the University of Birmingham campus and the ACA system including the AFT, ozone monitor, SMPS, and ATOFMS were installed inside a mobile laboratory. The mobile laboratory was a blank car (Ford Transit, Jumbo van-based carrier) adapted for science research by the University of Birmingham. The sampling inlet was mounted on the floor of the rooftop of the mobile laboratory and was made up of a copper pipe and swagelok fittings. Figure 2.7 shows a schematic diagram of ACA instrumental set-up as deployed for artificial ageing of the ambient particles.

Outdoor ambient particles were initially used to evaluate the performance of the instrument. Then air was drawn through AFT before entering the monitoring instruments; the ATOFMS, SMPS and the ozone monitor. The monitoring instruments were attached to the AFT outlets for direct sampling of processed and unprocessed aerosols. The sampling rate for both the ATOFMS and the SMPS was 0.3 l min^{-1} while that of ozone monitor was 1.5 l min^{-1}. The oxidation process of ambient particles was carried out in a similar fashion to that of laboratory generated particles

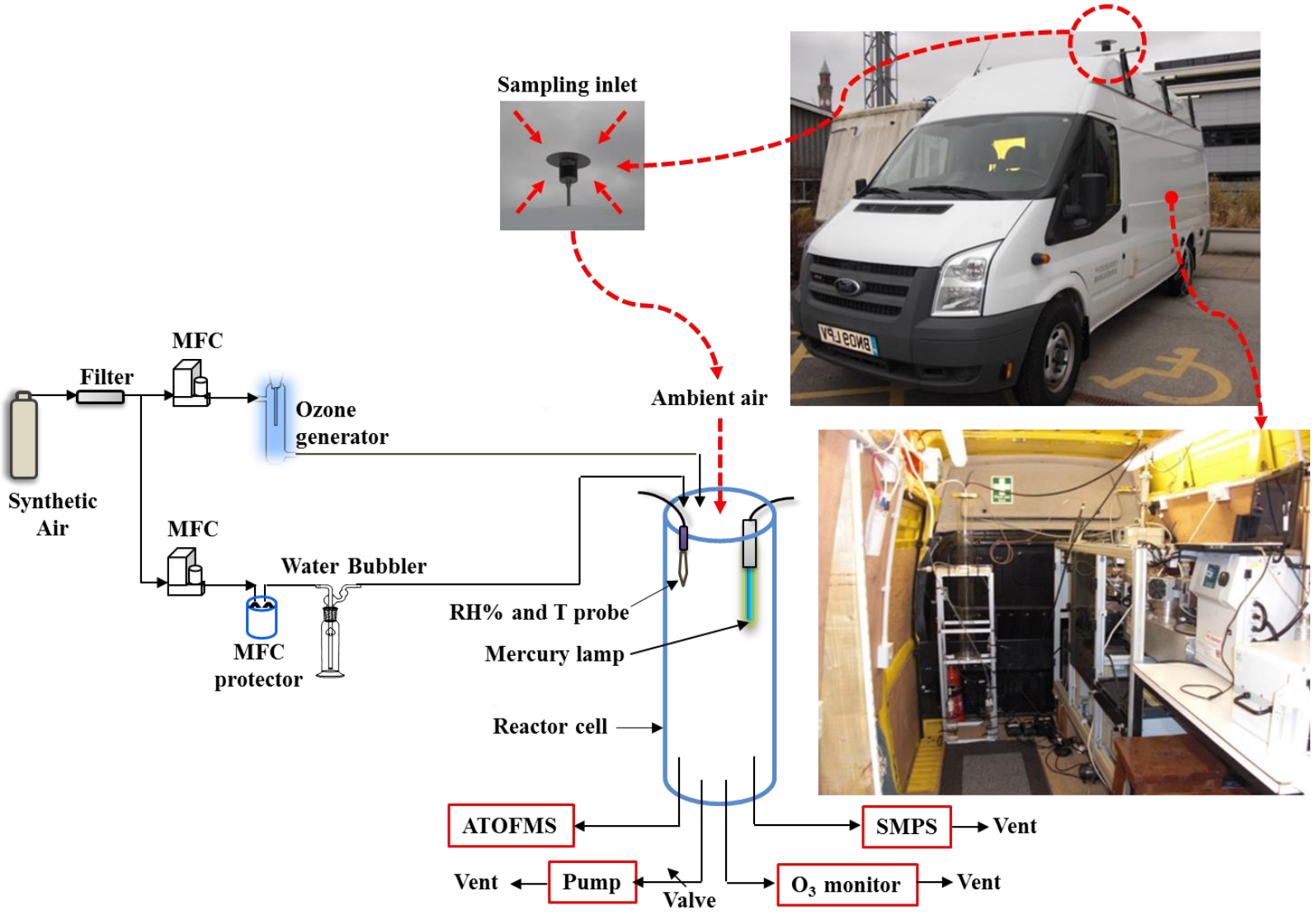

Figure 2. 7 Experimental setup for the heterogeneous oxidation of ambient aerosol.

described above. To maintain a residence time of 147 s for ambient particle in the AFT, analogous to laboratory oxidation time, a pump was connected directly to the AFT outlet and a constant suction was made at 1.4 l min^{-1} by means of a valve.

2.5 Summary

The ACA system is a real-time flow reactor aging system for organic aerosol with real-time characterisation of particles and oxidants. It monitors the physical and the chemical changes of particles exposed to intense levels of oxidants. The ACA system is composed of the AFT, aerosol and oxidant generators, and monitoring instruments, ATOFMS and SMPS. The system operates at atmospheric pressure and temperature with plug residence time ranges from ~20 to 135 seconds. The generation techniques of aerosol vary including homogeneous nucleation of the liquid vapour and mechanical dispersion of material solution giving a number concentration of particles up to 10^6-10^7 particles cm^{-3}. The oxidant, ozone, produced externally via photolysis of pure air or oxygen and loaded to the AFT, production levels ranges from tens ppb up to 100 ppm. However, the oxidant HO_x are generated in-situ and their typical measured levels ranges from $(8.0\pm0.4)\times10^9$ to $(1.2\pm0.6)\times10^{10}$ molecules cm^{-3} corresponds to an exposure range of 1.2×10^{12} to 1.8×10^{12} molecules cm^{-3} s. This laboratory exposure is equivalent to 9.3-20.1 days of ambient atmospheric oxidation.

CHAPTER 3 REAL TIME PHYSICAL AND CHEMICAL CHARACTERIZATION OF AEROSOL

3.1 Introduction

Advanced understanding of the sources, physiochemical transformations, evaluation and composition of ambient aerosol requires real time investigation of aerosols size and chemical composition. Methods of measurements that are sensitive, selective, accurate with good time resolution are an essential element to elucidate atmospheric processes involved in the formation and the fate of atmospheric particles (Finlayson-Pitts and Pitts Jr, 2000a).

This chapter describes the online analysis of atmospheric aerosol using the SMPS and ATOFMS. The fundamental aspects of the SMPS and ATOFMS techniques, advantages and limitations associated with their methodologies, and implementation of ATOFMS to the developed ACA system are discussed.

3.2 Online methods

Real time measurements of the particle size distribution and chemical composition of individual aerosol particles provide useful information such as the nature of the source of the particle size, ageing process, ability to distinguish between internally and externally mixed particle components, temporal resolution and particle's environmental and biological effects (Prather et al., 1994; Hatch et al., 2011b; Laskin et al., 2012). Particle size measurement has been the subject of research and development for over three decades. There are many instruments for particle size distribution measurement each using a particular physical phenomenon to define the size including laser diffraction, dynamic light scattering, electrical mobility and image analysis. Each of these techniques generates results using standard statistical calculations.

The chemical online analysis of atmospheric aerosols have been developed for more than two decades using desorption ionization mass spectrometry (Hoffmann et al., 2011). The general principle is that airborne particles are rapidly introduced into the instrument, where they are vaporized and ionized (Laskin et al., 2012). The ionized particles are then analysed using mass spectrometry. Real time approaches overcomes the limitations associated with classical offline measurements such as volatilization of semi-volatile compounds and adsorption of organic gases on collection sampler's materials during sampling, storage and multi-analytical procedure steps.

3.3 Scanninig Mobility Particle Sizer (SMPS)

The SMPS is commonly used to measure the size distributions of particles based on their electrical mobility. In principle, the smallest aerosol particle could be defined as that containing two molecules (Seinfeld and Pandis, 2006). Thus, aerosol distribution could be described by the number concentration of each cluster, i.e. the concentration of particles per cm^3 of air containing a number of molecules. However, a more complete description of the aerosol size distribution would include the size of each particle. This involves dividing particle size range into discrete intervals and estimation of the number of particles in each size intervals. Various instruments have been used to measure particle size distributions. The established setup of an SMPS system consists of an impactor, a neutralizer, a Differential Mobility Analyser (DMA), and a Condensation Particle Counter (CPC).

3.3.1 The impactor

The aerosol first enters the impactor which is mounted outside the electrostatic classifier. The impactor removes particles above a known particle size that is beyond the measurement range. This is done to prevent errors in the data analysis and to avoid contamination of the SMPS

system. The principle of the impactor is based on particle inertia. That is, when an accelerated stream of aerosol in a narrow throat changes firmly in direction, particles with less inertia can follow, whereas large particles are collected in impaction plates. This is explained in Figure 3.1.

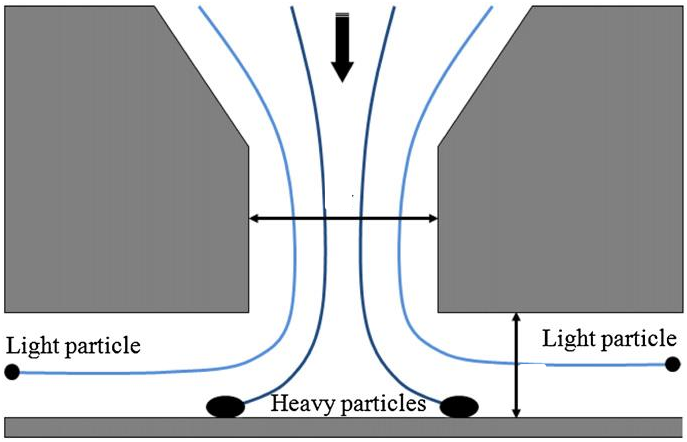

Figure 3. 1 A schematic of a typical impactor showing large particles collected on the impaction plate while small particles follow aerosol stream (Schrobenhauser et al., 2014).

In this study, the mode diameter of generated particles was around 300 nm. The use of an impactor of a nozzle diameter of 0.0508 cm that removes particles of a diameter greater than 1 µm was investigated. It was realised that measuring the size distribution of the generated particles with and without the impactor has no discernible effect.

3.3.2 Electrostatic classifier

The aerosol stream then enters a radioactive Krypton-85 (Kr-85) bipolar charger (or neutralizer) shown in Figure 3.2, which exposes the aerosol particles to high stream of beta radiation. Particles undergo frequent collisions with bipolar ions resulting in a prompt state of an equilibrium charge: particles carrying no charge, a single positive charge, a single negative

charge or multiple of both positive and negative charges. Aerosol then passes from the neutralizer into the DMA.

3.3.3 Differential Mobility Analyser

The differential mobility analyzer (DMA) have been used largely in many applications involving measuring and classifying sub-micrometer airborne particles (Chen et al., 1998; Heard, 2006). The DMA, developed first by Knutson and Whitby in 1975 (Knutson and Whitby, 1975; Finlayson-Pitts and Pitts Jr, 2000a; Willeke, 2001) and later commercialized by TSI Inc (Chen and Pui, 1997). It separates and classifies particles based on their electrical mobility. As it seen in Figure 3.2, a DMA consists of a cylinder contains a negatively charged central rod for the generation of the electrical field between the cylinder walls and the rod.

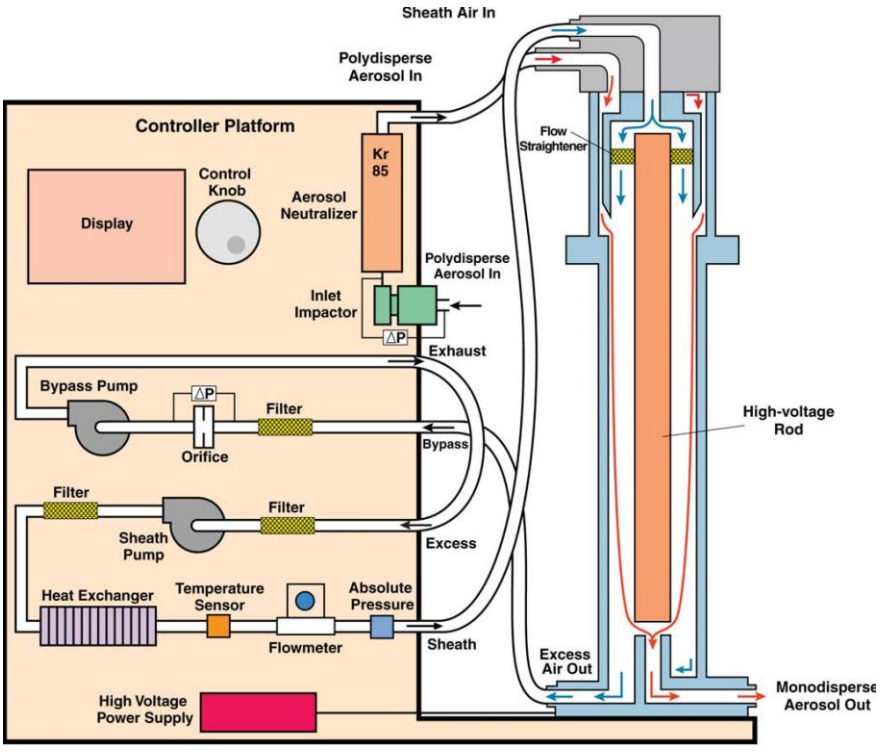

Figure 3. 2 Schematic diagram illustrating the principles of the electrostatic classifier and the DMA (TSI, 2008).

Neutralised aerosol enters the DMA and move towards the central rod with a velocity characteristic to their electrical mobility. A laminar carrier sheath flow (particles free flow) through the classification region is established and particles are subjected to electric field that crosses the carrier flow transversally. Charged particles arriving the classification region develop a series of trajectories depending on the electrical mobility of the particles. Particles with a high electrical mobility impact sooner at the upper portion of the rod and are removed from the gas stream whereas particles with a low electrical mobility are precipitated farther downstream the lower portion of the rod or are discharged by the excess sheath flow. Particles that do not reach the rod before the air flow passes out the electric field pass through to the CPC and are measured. Only particles within a narrow range of electrical mobility exit through the output slit based at the bottom of the collector rod as a monodisperse air flow. The mobility of particle exiting through the slit is determined by the particles size, charge, central rod voltage, DMA geometry, and flow within the DMA. The magnitude of the voltage applied to the DMA limits the size range which can be scanned by a single DMA.

3.3.4 Condensation Particle Counter

The monodisperse aerosol exiting the DMA is transferred to a particle sensor to determine the particle concentration such as a condensation particle counter (CPC). The theory of which is based on a simple optical detection after a supersaturated vapour condenses onto the particles and resulting in grown larger optically detectable droplets.

In brief, particles laden air passes through a saturator and becomes saturated by a heated liquid-soaked wick which is in contact with a working fluid, usually butanol. The saturated air passes through a vertical condenser tube, cooled by means of a thermoelectric device, becoming

supersaturated and causing particles to grow into larger droplets. These droplets are then passed through a nozzle into the optical detector and are counted. Particle number concentration is established by counting individual pulses of the scattered light in the optical detector. Figure 3.3 summarizes the CPC operation concept.

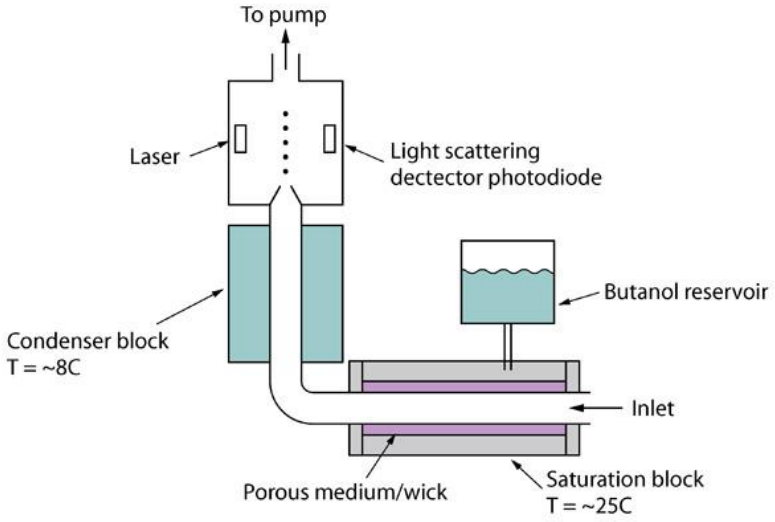

Figure 3. 3 Schematic of a Condensation Particle Counter (CPC).

The minimum particle size which can be measured by a CPC is determined by the supersaturation achieved which depends on the temperature difference between the saturator and the condenser. Particles do not experience the same supersaturation as every droplet size has a certain supersaturation which maintains its grown droplet size making the efficiency of the counter substantially decreases at smaller sizes. In this study, the CPC model (3022A, TSI Inc.) is capable of detecting particles as small as 7 nm (Faloon, 2011). Note that ultrafine particles of 10 nm in diameter size approach molecular clusters and contain ~ 10^4 molecules (Finlayson-Pitts and Pitts Jr, 2000a).

3.3.5 SMPS limitation

The primary limitation of the SMPS system associated with the low detection efficiency of the small size particles (McMurry, 2000). This is because in the SMPS approach the charging efficiency of particles decreases as their size decreases. Conversely, near the upper measurement limit multiple charging of particles occurs. Large particles of a given mobility contain one, two or multiple charges which causes over counting of large size particles (TSI, 2008).

Aerosol particles are sensitive to changing temperature and relative humidity (Stanier et al., 2004a). Water contents in particles exist in equilibrium with the vapour phase under sub saturated conditions making particle size humidity dependent (Martin, 2000). Wet air samples introduces uncertainty in the measurements as butanol in the CPC reservoir continuously absorbs water from the sampled air thus diluting the butanol and results in underestimation of particles counts (Agarwal and Sem, 1980). The induced error by the humidity is minimised by replacing the butanol in the CPC reservoir with fresh volumes regularly and whenever the system is operated under humid condition.

In addition, the diameter of a particle containing soluble species at humid condition is much larger than that measured at dry condition, while a particle with insoluble constituents is much less sensitive to relative humidity. Similarly, some species such as nitrate are very sensitive to changes in temperature while other species show no temperature dependency (Pradeep Kumar et al., 2003).

3.4 Aerosol time of flight mass spectrometer (ATOFMS)

For the past four decades substantial efforts have gone into developing in situ real-time size and composition analysis of airborne particles (Myers and Fite, 1975; Davis, 1977; Allen and Gould,

1981; Stoffels, 1981; Sinha et al., 1982; Sinha, 1984; Giggy et al., 1989; Kievit et al., 1992; Hinz et al., 1994; Prather et al., 1994; Hinz et al., 1996; Liu et al., 1997; Thomson et al., 1997). However, the major advance came when Prather and co-workers introduced the first analytical technique for simultaneous particle size and composition measurement of individual particles in real time (Prather et al., 1994). This technique, the Aerosol Time of Flight Mass Spectrometer (ATOFMS), was commercialized later from TSI, Inc.

ATOFMS has a very high time resolution, it reduces the possibility of artifacts associated with many other analytical techniques, requires of ~6 orders of magnitude less sample than traditional techniques, and requires no separation of the sample constituents (Aiken et al., 2008). The deployment of ATOFMS in field measurements is one essential reason for the advances in atmospheric analytical chemistry in recent years (Hoffmann et al., 2011). ATOFMS has been extensively used in different environments to provide online information of the aerodynamic diameter of the chemically distinct particle types (Gard et al., 1997; Guazzotti et al., 2001; Spencer and Prather, 2006; Pratt and Prather, 2009; Svane et al., 2009; Bi et al., 2011). The capability of the ATOFMS has proven to be very well suited in examining refractory species (Angelino et al., 2001; Moffet et al., 2004; Gaston et al., 2010) and further our understanding in wide areas including environmental monitoring (Koester and Moulik, 2005; Spencer et al., 2008; Hatch et al., 2011b; Hatch et al., 2011a; Dall'Osto and Harrison, 2012; Rosenfeld et al., 2014), characterization of bio-mass burning (Ranjit et al., 2010; Healy et al., 2012; Rosenfeld et al., 2014), fuel exhaust measurements (Sodeman et al., 2005; Healy et al., 2012), emission from smoke stacks (Anderson et al., 2007), industrial hygiene (Healy et al., 2009), pharmaceutical applications (New et al., 2008), contamination in tobacco smoke (Morrical et al., 1998; Yadav et al., 2004) and public health studies (Shandilya and Kumar, 2010).

3.4.1 Operating principles of ATOFMS instrument

The ATOFMS (Model 3800) deployed in this study samples particles in the range of 100 to 3000 nm. ATOFMS instrument is composed of the following major regions: particles sampling region, particles sizing region, particle desorption ionization region and the mass spectrometry region. Figure 3.4 depicts a schematic of the transportable ATOFMS instrument.

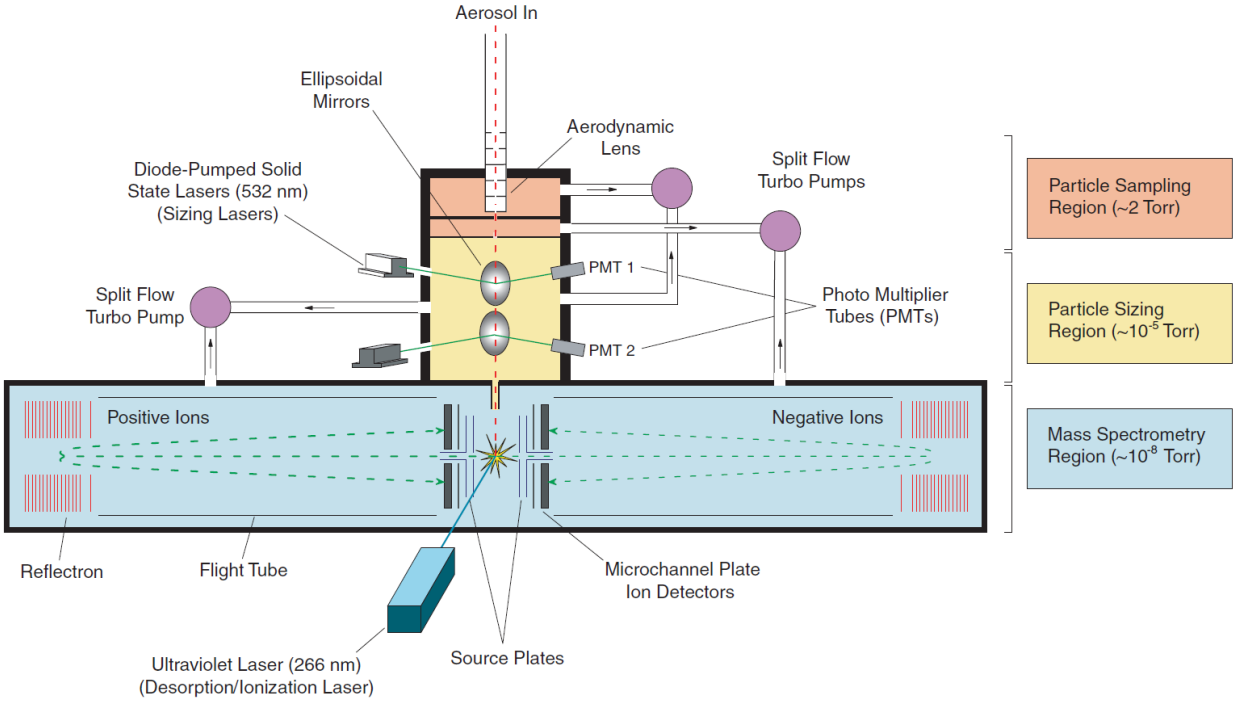

Figure 3. 4 Schematic diagram of Aerosol Time-of-Flight Mass Spectrometry instrument (Allen, 2005).

3.4.1.1 Particles sampling region

Aerosols are drawn directly at atmospheric pressure (760 torr) through an initial flow limiting orifice into a series (typically 5-6) of aerodynamic focusing lenses (AFL) with a significant pressure drop across each lens. This AFL technology, shown in Figure 3.5 , has been used since it

was invented by Liu (Liu et al., 1995) to separate particles from the gas phase based on the difference in the inertia of the carrier gas and particles (Wang and McMurry, 2006). The pressure drop across the AFL results in gas and particles expansions through the expansion nozzle and the

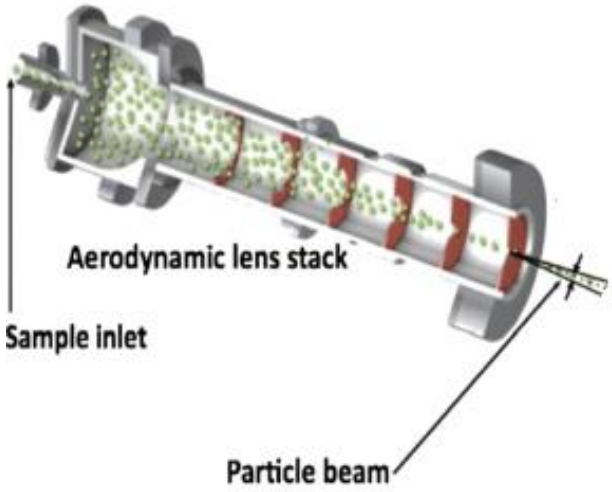

Figure 3. 5 Principle of aerodynamic particles lens (Spence et al., 2012).

skimmers where gas molecules are pumped away while particles are focused into narrow particle beams. The pressure in the first vacuum stage of the sampling region is about 2 torr at which particles of different sizes are accelerated and travel with terminal velocities characteristic of their aerodynamic diameter. The aerodynamic diameter is the diameter of the unit density (ρ=1 g cm^3) of a sphere that has the same settling velocity as the particle. Therefore, smaller particles reach a higher speed than larger particles.

3.4.1.2 Particles sizing region

Particles that are not removed by the skimmers in the sampling region passes through two continuous wave laser beams (532 nm) separated by a known distance of 6 cm (Song et al., 1999). The light scattered from the first laser is detected by a photomultiplier. As particles travel,

they encounter and scatter the light beam from the second laser which is also detected. The delay time between the two pulses of the scattered light is used to determine the velocities of individual particles and hence their aerodynamic diameter size. This delay time is also used to trigger the LDI located further downstream at the laser desorption and ionisation region.

3.4.1.3 Desorption and ionization region

The desorption ionization event is started by a pulse from a laser (LDI). The LDI fires light pulses that intercept the particles at the exact time they should arrive to the optical line of sight. Ionisation is achieved using a high-energy pulsed Nd:YAG laser at 266 nm which ablates and ionizes molecules from the particle. Laser ablation involves a laser beam subjected at the material sample causing an amount of it to be removed and vaporized prior the spectroscopic analysis techniques. For solids or liquids, the task is to generate a vapour, which represents a chemical composition that is almost identical to original sample, a technique first used to ionise and detect single particles by Sinha (1984). The equivalent photon energy for the LDI at 266 nm is 4.66 eV (Schneider and Lippert, 2010). Organic compounds can be ablated and ionised directly by UV laser pulses at relatively low laser fluences; for example, the C–H chemical bonding requires an energy of 3.5 eV to break (She et al., 1999).

The distinct advantages of the LDI in aerosol analysis include high vaporization and ionization efficiency that requires no sample preparation, no artifacts from preceding particles such as those associated with surface ionization techniques and it suits a range of analysis including relatively nonvolatile substances, organic, inorganic and thermally labile compounds (Suess and Prather, 1999).

3.4.1.4 Particles spectrometer region

The LDI is coupled with a dual polarity time-of-flight mass spectrometer which is evacuated to a pressure of ~10-7 torr and obtain positive and negative ion information on individual particles (Spencer and Prather, 2006; Hatch et al., 2011b). The generated ions from the particle are directed to the positive and negative polarity time-of-flight mass spectrometers. They are then separated based on their velocities. Ions with different m/z will possess different velocities and will reach the detector at different times. The detected ions produce signals of a complete positive and negative ion mass spectrum of the desorbed and ionised species from each particle as a function of time since the start of the ionisation process by the LDI. Particles for which mass spectra are measured are referred to as hit, those particles for which sized, but not a mass spectrum, are measured are missed (Wood and Prather, 1998; Allen et al., 2006).

The transformation of the transit time into particle size and m/z ratio of the ionised species is accomplished by size and mass calibrating the instrument with laboratory-generated particles of known size and with particles of known composition. ATOFMS size and mass calibrations have been described in section 2.2.7.2.

3.4.2 ATOFMS limitations

Although much have been learnt from elemental and molecular analysis of ATOFMS technique, ATOFMS still have some unpromising limitations in characterizing aerosols. The LDI process continues to present the major challenges in ATOFMS methodology due to the sensitivity of the desorption and ion formation to particular conditions making independent quantification by ATOFMS quite elusive (Thomson et al., 1997; Suess and Prather, 1999; Finlayson-Pitts and Pitts Jr, 2000a; Kane et al., 2002; Allen et al., 2006; Reinard and Johnston, 2008). To date,

quantitative chemical analysis on aerosols using ion mass spectra produced by LDI has had limited success (Gross et al., 2000; Fergenson et al., 2001; Bhave et al., 2002; Sullivan and Prather, 2005). Variables that influence particles desorption and ionisation process include the shot-to-shot variations in power density which results in poor reproducibility of laser power density absorbed from one particle to another. The optical characteristics of the sample matrix i.e. substances with better absorption properties at the LDI wavelength (266 nm) are likely to be most measurable. The relative intensities of both sodium and potassium provided from ATOFMS analysis elucidate an inherent high sensitivity toward alkali metals (Suess and Prather, 1999). Examples from the present study of recorded mass spectra in which sodium and potassium display are presented in chapter 8.

Although the LDI technique is less harsher than other traditional ionization methodology (suchlike electron impact), it may still produce extensive fragmentation of molecules from a single compound. The fragmentation comes from the multiphoton process when high laser energy is used (Finlayson-Pitts and Pitts Jr, 2000a; Sullivan and Prather, 2005) making organic constituents of complex organic aerosol extremely indistinguishable. On the other hand, fragmentation patterns in the mass spectra are different for the same molecule i.e. no standard type of spectrum is obtained from the LDI for a particular compound, which serves a serious limitation in interpreting the spectrum. These differences could be caused by the particles matrix effect that produces different ionization and fragmentation patterns of the same species. Measuring organic compounds at the molecular level is thus obstructed by the complex mixture of organic compounds in a single particle as well as the fragility of these chemicals (Sullivan and Prather, 2005; Nash et al., 2006; Murphy, 2007; Fang et al., 2011a; Fang et al., 2011b).

3.4.3 Implementation of ATOFMS to the ACA system

Despite all the limitations outlined above, nevertheless ATOFMS in the present study produced meaningful results particularly in ageing laboratory generated aerosols. The ATOFMS which has previously been deployed largely for providing qualitative information in studying ambient aerosol, was an important part of this project for both qualitative and semi quantitative analysis of laboratory generated aerosol aged under controlled experimental conditions. For this study, the ATOFMS provided valuable information on:

- Changes in particle chemical composition as a result of oxidation.
- The effect of time on the heterogeneous reaction.
- The effect of relative humidity on the identity of the oxidation products.
- Components distribution of aged polydisperse aerosol as a function of particles size.
- Reaction probability between O_3 and OL particles.

The makeup of the ageing process was possible to follow by improving the detection process. For example, pure OL droplets are essentially transparent to the laser incident radiation and have been shown to poorly absorb the LDI pulse at 266 nm. As the physical and chemical properties of the particles matrix, in particular the absorption phenomenon, plays a central role in the ablation process (Schneider and Lippert, 2010), the generated particles was optically modified by the addition of the laser dye, NBS, to the particles (section 2.4.1.1). This modification resulted in a remarkable enhancement in ATOFMS detection of the modified particles apparently by maximising the desorption ionisation probability of the pulsed laser. Factors influencing the LDI efficiency and corresponding applications are beyond the scope of this study. However, the spectroscopic analysis of ATOFMS data (chapter 6) indicates unexpectedly large etching depths

from the measured particles. It is possible that the addition of the NBS laser dye has significantly altered the physical and the chemical properties of the generated particles (Tajalli et al., 2008; Cui et al., 2011). NBS molecules absorb effectively within the lasing wavelength of the LDI laser (NBS absorption spectrum and molecular structure are presented in appendix B, Figure B-2). This effective energy absorption could have induced a rapid rise in the surface temperature of the particles thus causing superheating of the liquid at the surface and deeper to the bulk of the particles (Chen et al., 2006b). Consequently large molecular clusters from the ablated particles were evaporated and ejected off the particles. It is also possible that the laser incidence to highly absorbing liquid sphere particles caused explosive vaporization (She et al., 1999) of the particles which impart enough energy to desorb and ionise both the surface and the core of the particles (Heller et al., 1999; Vogel and Venugopalan, 2003; Brown and Arnold, 2010). This is consistent with the highly ionised molecules of NBS (Huang et al., 1999; Tajalli et al., 2008) which produce polar environment that increases the thermal conductivity and the heat storage capacity of the liquid, the effect is more significant when it comes to nanoscale systems (Nieto de Castro et al., 2009).

Although ATOFMS data do not directly reflect the quantitative composition of the measured aerosol (Gross et al., 2000; Fergenson et al., 2001; Bhave et al., 2002; Sullivan and Prather, 2005; Allen et al., 2006; Dall'Osto et al., 2006), relative peak intensities can be advantageous when particles constitution within a measured sample has not changed considerably (Gard et al., 1998; Finlayson-Pitts and Pitts Jr, 2000a). In this sense, ATOFMS was set up in a study to follow the heterogeneous reaction between chloride and nitrate in individual ambient sea-salt particles by monitoring the change in the relative intensities of chloride and nitrate species. The study showed a strong inverse correlation between chloride and nitrate in single

particles. The observed behaviour was consistent with the well-known heterogeneous reaction between gaseous species of nitrogen oxide such as (HNO_3 and N_2O_5) with NaCl to produce gaseous HCl and solid $NaNO_3$ (Gard et al., 1998). In this study, the use of ATOFMS as a semi-quantifiable approach for artificially processed generated particles as a function of particles size (chapter 6, section 6.2.3) is justifiable because individual laboratory based particles are far less complex than atmospheric aerosol (Allen, 2004) as they are oxidised under experimentally controlled conditions. Moreover, ATOFMS information on particle number and the abundance of different species by particle size are possible with high time resolution (Dall'Osto and Harrison, 2012). Most importantly, the relative intensity of the oxidation major products in the case of OL heterogeneous reaction was studied and results were used to correct signals of reacted particles (chapter 6, section 6.2.2.2 and 6.2.3.1, respectively).

However the application of the study to real ambient particles was found to be very challenging as interrelated variables were not stable over the course of the experiment and thus patterns in the produced mass spectra of exposed and unexposed particles to oxidants were difficult to follow (chapter 8).

To allow easier interpretation of the mass spectra, fragmentation was kept at minimum using reduced laser energy (Sullivan and Prather, 2005; Dall'Osto and Harrison, 2012). In the current study, the LDI laser fluence of the ATOFMS was kept very low (0.4–0.8 mJ per pulse) as compared to other related studies (1.3–1.6 mJ) (Dall'Osto and Harrison, 2012) (Silva and Prather, 2000). This allowed us to identify molecular weights of organic compounds as molecular ions with less molecular fragmentation of processed and unprocessed particles as shall be illustrated in chapter 6. However, fragment ions of the starting material and oxidation products in the particles were observed in some mass spectra.

3.5 Summary

This chapter presented the principles and the applicability of the real time techniques deployed for this study, the SMPS and the ATOFMS. Areas of concern that have a potential impact on the detectability of the ATOFMS technique have been outlined. Some of these are related to the techniques fundamentals, while others are specific to the identity of the atmospheric proxies used in this study. The implementation of ATOFMS to follow the chemical changes of laboratory generated required improving the detection technique of the LDI by optically modifying the generated particles. In spite the limitations associated with the deployed techniques, both applicable SMPS and ATOFMS allow simultaneous online physical and chemical characterisation of artificial and ambient particles. The effects of the artificial ageing of the generated particles under the conditions of the current study shall be argued in chapter 6.

CHAPTER 4 PEROXY RADICALS CHEMICAL AMPLIFIER

4.1 Introduction

This chapter describes the practical use of the PEroxy Radical Chemical Amplifier (PERCA) to quantify the levels of generated radicals in the Aerosol Chemical Ageing (ACA) system. The principle of PERCA approach is explained, followed by the experimental set up, calibration and radical measurements in the ACA system. A theoretical investigation using reaction kinetics of gas phase components in the ACA system is also presented. The purpose of this theoretical simiulation is to predict the concentration of radicals in the ACA system operating at high mixing ratio of ozone and to explain PERCA features under the conditions of this study. This was acheived by mimicking the reaction kinetics of the ACA system. The initial formation, concentration, exposure, step decay of OH radical and the steady growth of corresponding species is explored theoretically by modelling the chemical reactions of species exist in the ACA system using reaction kinetics. This is followed by a comparison between observed and modelled HO_x levels in the ACA system at different ozone levels. The interference of gaseous ozone with PERCA signals at high ozone levels is described and justified. Finally, the limitation of PERCA is discussed.

4.2 Peroxy Radical Chemical Amplifier (PERCA)

PERCA was pioneered by Cantrell and Stedman in 1982 with later developments by others (Cantrell et al., 1984; Hastie et al., 1991; Anastasi et al., 1993; Ashbourn et al., 1998; Mihele and Hastie, 2000; Sadanaga et al., 2004; Fleming et al., 2006; Qi et al., 2008; Li et al., 2009). It provides a measurement of the total concentration of peroxy radicals, i.e. $[HO_2] + \sum[RO_2]$, with a

reported low limit of detection of 1 pptv in ambient air, and of 0.1 pptv in a laboratory system (Cantrell et al., 1984).

4.2.1 PERCA principle

The reaction mechanism in PERCA converts trace level of HO_2 radicals into higher levels of NO_2, reaction R 4.1. The OH produced in reaction R 4.1 is recycled back to HO_2 by reactions R 4.2 and 4.3 with CO and O_2, respectively, to further increase the level of NO_2:

$$NO + HO_2 \longrightarrow HO + NO_2 \qquad \text{R4. 1}$$

$$CO + OH \longrightarrow H + CO_2 \qquad \text{R4. 2}$$

$$H + O_2 + M \longrightarrow HO_2 + M \qquad \text{R4. 3}$$

The produced NO_2 can be measured easily via the luminol technique described below. The sensitivity of the technique is limited by radical loss processes such as reaction on the reactor walls, reaction with NO or NO_2, and radical-radical reactions which terminate the chain(Cantrell and Stedman, 1982):

$$HO_2 + \text{Walls} \longrightarrow \text{Non-radical products} \qquad \text{R4. 4}$$

$$OH + NO + M \longrightarrow HONO + M \qquad \text{R4. 5}$$

$$HO_2 + NO_2 + M \rightleftharpoons HO_2NO_2 + M \qquad \text{R4. 6}$$

$$HO_2 + HO_2 + M \longrightarrow H_2O_2 + O_2 + M \qquad \text{R4. 7}$$

The NO_2 yield produced by other sources is inferred by a modulated technique in which a periodic switching of the addition of the CO between the inlet of the reactor (radical mode) and the outlet of the reactor (baseline mode) produces modulated NO_2 signals. The number of HO_x-catalysed cycles before radical removal by termination reaction is defined as the chain length (CL). Some RO_2 radicals can undergo few reaction steps to form HO_2 (Cantrell et al., 1984) which can also be detected if they are readily converted to HO_2 in the PERCA (Qi et al., 2008).

4.2.2 PERCA apparatus and instrumentation

The following sections describe the main components, set-up and the chemical actinometry of a PERCA system. The PERCA experimental set-up used in this work was initially developed to study the the interactions of tropospheric aerosol and HO_x radicals (Faloon, 2011) and was slightly modified to better fit in the ACA system. The PERCA system composed of: a calibration tube, a peroxy radical generator, a chemical amplification reaction tube and an NO_2 detector.

4.2.2.1 The calibration tube

A fused silica tube (60 cm length, 2.5 cm in diameter) mounted vertically on an aluminium metal block was used to calibrate the PERCA system. The total flow in the tube was kept constant at 10 slm while the ratio of dry and wet air introduced to the calibration tube was changed to vary the relative humidity (RH) which was measured just before the air enters the calibration tube. The Reynold number, Re (used to characterize and quantify laminar and turbulent flows, section 2.2.5.1) and the entrance length, Le (the distance required a flow in a tube to travel a before the laminar flow conditions are established, section 2.2.5.1), of the tube were calculated to be 560 and 48.8 cm, respectively.

4.2.2.2 Peroxy radical generator

As the air travels in the calibration tube it passes at a distance of 50 cm from the tube entrance a low pressure UV mercury lamp (Ultra-Violet Products Ltd., 184.9 nm) held vertically in the aluminium metal block, H_2O and O_2 in the air are photolysed by the UV lamp. This photolysis produces a known amount of OH, HO_2, and O_3. The chemical actinometer technique of peroxy radical generation used here has been used in related studies (Creasey et al., 2000; Kanaya et al., 2001; Bloss et al., 2004; Liu et al., 2009; Miyazaki et al., 2010; Faloon, 2011) and can be summarized by the following equations:

$$H_2O + hv \longrightarrow OH + H$$

R4. 8

$$H + O_2 + M \longrightarrow HO_2 + M$$

R4. 9

$$O_2 + hv \longrightarrow 2O$$

R4. 10

$$O + O_2 + M \longrightarrow O_3 + M$$

R4. 11

The air loaded with generated radicals are sampled by PERCA reaction tube at a constant flow rate of 2.0 slm while O_3 is measured by ozone monitor (2B Technologies, Model 205) sampled at a flow rate of 1.5 slm. To cool the UV lamp and to avoid the formation of O_3 in ambient air, a flow of 1 slm of nitrogen free oxygen was sent into the metal block cavity which houses the lamp. Figure 4.1 shows the setting of the calibration tube and the peroxy radical generator.

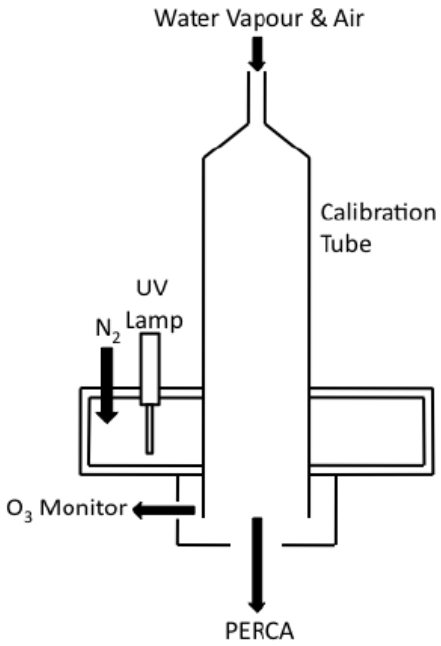

Figure 4. 1 The calibration tube and the peroxy radical generator setting (Faloon, 2011).

4.2.2.3 PERCA reaction tube

A cylindrical Pyrex glass tube (2 cm in diameter and 25 cm in length) was used as PERCA reaction tube. Air sampled through the reaction tube at a constant flow of 2.0 slm (Re of 139 and Le of 9.3 cm) is mixed immediately with CO (0.1 slm) at 0.05 ppm and NO (0.01 slm) at 3 ppm flows which are injected to the top of the tube via a glass sleeve fitted with Perfluoroalkoxy alkanes (PFA) Union Tee. Consequently, the chain reaction is initiated and proceeds to form NO_2. The NO_2 formed from any other sources other than the chain reaction is measured periodically as a background signal by switching off the addition of CO downstream so that the chain reaction is terminated yielding the NO_2 background signals. As NO is added at the top of the tube and N_2 and CO are introduced alternatively between the top and the bottom of the tube, the total flow through the system was kept constant while changing from background to

measurement mode. The CO shifting flow is accomplished automatically every one minute via solenoid valves controlled by a computer.

In PERCA measurement mode CO is introduced at the top of the tube resulting in amplification reaction and the recorded signal reaches its maximum. However, in PERCA background mode CO is introduced at the bottom of the tube resulting in reaction termination and the recorded signal reaches its minimum. The difference in the PERCA signals between the measurement and the background modes produces obvious modulated signals which can be used to determine the concentration of HO_x. Figure 4.2 shows typical modulation signals from the NO_2 monitor used to calculate the concentration of NO_2 produced from the difference between the average of 30 s of measurement mode data and 30 s of background mode.

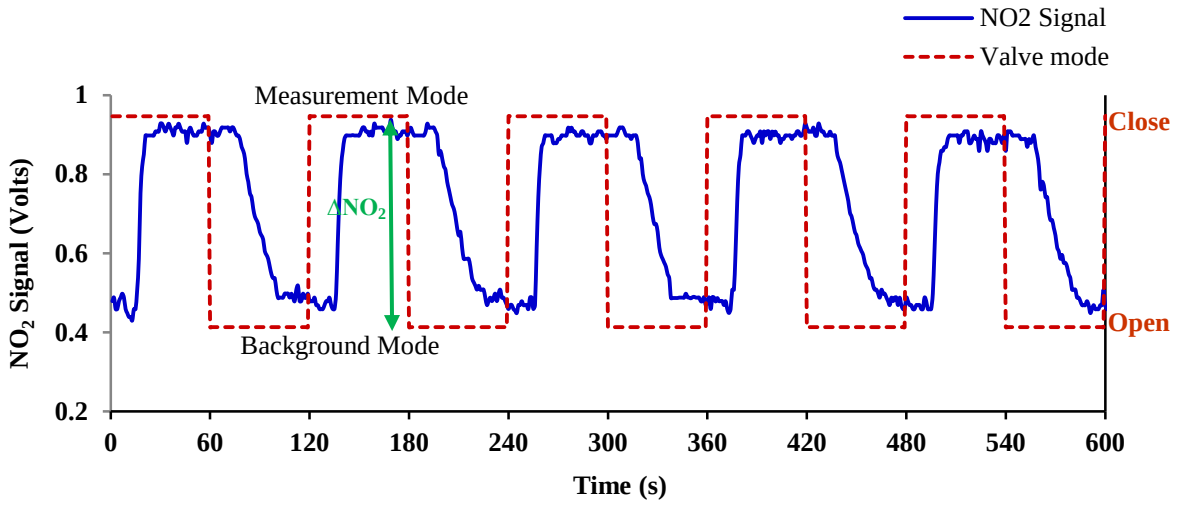

Figure 4. 2 Typical PERCA signals at RH=65.0±0.2%. The solid blue line shows PERCA signals and the dashed red lines shows the valves mode controlling the PERCA. When the valve is closed, PERCA signal is high indicating measurement mode. When the valve is opened, PERCA signal is low indicating background mode.

In this chemical actinometer technique, reaction R 4.8 and R 4.9 are used to obtain the production rate of HO_2:

$$\frac{d[HO_2]}{dt} = j_{H_2O,184.9nm}[H_2O] = I_{184.9nm}\sigma_{H_2O,184.9nm}\phi_{HO_2,184.9nm}[H_2O]$$

Eq 4. 1

And reaction R 4.10 and R 4.11 are used to derive the production rate of O_3:

$$\frac{d[O_3]}{dt} = j_{O_2,184.9nm}[O_2] = I_{184.9nm}\sigma_{O_2,184.9nm}\phi_{O3,184.9nm}[O_2]$$

Eq 4. 2

Where j denotes the photolysis coefficient of a reactant, x, with absorption cross section σ, and a quantum yield ϕ, at a particular wavelength λ, and a light flux I, and it is given by equation:

$$j_{x,\lambda} = I_{\lambda}\sigma_{x,\lambda}\phi_{x,\lambda}$$

Eq 4. 3

Integrating equation Eq 4.1 and Eq 4.2 and recalling that O_2 and H_2O are exposed to the same light flux, $I_{184.9\ nm}$, for the same period of time, the concentration of HO_x can be quantified by the following resulting equation:

$$[HO_2] = \frac{\sigma_{H_2O,184.9nm}\phi_{HO_2,184.9nm}[H_2O][O_3]}{\sigma_{O_2,184.9nm}\phi_{O_3,184.9nm}[O_2]P}$$

Eq 4. 4

where σ_{H2O}, σ_{O2} are the absorption cross section for H_2O and O_2 were determined experimentally for this particular system and calibration technique by Faloon (2011) and were found to be $9.35x10^{-20}$ molecule^{-1} cm^2, $1.51x10^{-21}$ molecule^{-1} cm^2, respectively. P is the profile factor of the laminar flow (section 2.2.5.1) and was also measured experimentally by Faloon (2011) and found to be 1.92. ϕ_{HO2} and ϕ_{O2} are 1 (Atkinson et al., 2004) and 2 (Washida et al., 1971), respectively. O_3 was recorded during the calibration experiment and $[O_2]$ was calculated as 0.21[M]) where [M] is the molecular concentration of air, calculated using the ideal gas law under the experimental conditions of this study, 2.45×10^{19} molecules cm^{-3}:

$$\frac{N}{V} = \frac{P}{kT}$$

Eq 4. 5

where P is the ambient pressure calculated in Pascals, *V* is the volume measured in cubic centimeters, *N* is calculated in moles, and T is the averaged measured temperature in kelvins, k is the Boltzmann constant and has the value of 1.38×10^{-23} J K^{-1}.

Finally, the water concentration, [H_2O], was calculated from the averaged observed relative humidity, RH%, over the 10 minutes typical duration of a calibration experiment using the following relationships:

$$RH\% = \frac{\text{Partial pressure of } H_2O \text{ (e)}}{\text{Saturated pressure of } H_2O \text{ } (e_s)} \times 100$$

Eq 4. 6

The saturated vapour pressure of water, e_s, was calculated using Antoine equation:

$$\log(p) = A - \frac{B}{T + C}$$

Eq 4. 7

where A, B and C are constants equal to 5.40221, 1838.675 K and -31.737 K, respectively at T=273– 303 K (NIST, 2011). The obtained partial pressure is applied in the ideal gas law to get the water concentration in molecules cm^{-3}. Appendix B, Figure B-6, shows O_3 mixing ratio, relative humidity, and temperature trends during PERCA 10 minutes sampling periods at which data were averaged and obtained values were used to work out CL levels. Once the CL has been measured and the change in NO_2 between the background and measurement modes has been determined then the concentration of HO_2 can be measured using the following equation:

$$CL = \frac{\Delta[NO_2]}{[HO_x]}$$

Eq 4. 8

PERCA system can also detect OH and RO_2 radicals as they can start the reaction chain. OH and HO_2 radicals are present in the AFT in the absence of the organic aerosol while all radicals including RO_2 are expected to be present during the oxidation process of organic particles takes place.

4.2.3 Calibration procedure

Two calibrations are required for the PERCA prior measurements; the regular calibration of the response of NO_2 detector, the so called NO_2 calibration, and the calibration to determine the conversion factor CL of radicals into NO_2, the so called HO_2 calibration. These calibrations were performed prior HO_x measurements from the ACA system and on the same day of the experiment.

4.2.3.1 Calibration of NO_2 analyser

NO_2 is quantified using LMA-3 Luminox instrument (Scintrex Ltd.) via a chemiluminescence detection system. LMA-3 is a highly sensitive, lightweight and portable instrument for continuous monitoring of NO_2 in air. Unlike other chemiluminescent instruments it measures NO_2 directly and does not require prior conversion of NO_2 to NO. The response time of the instrument is less than 1 s with sensitivity better than 5 pptv (Fehsenfeld et al., 1990) .

Principle of the method

LMA-3-Luminox analyser operates by detecting the chemiluminescence produced when NO_2 encounters a surface wetted with a specially formulated, alkaline, luminol solution. The method

of analysis, first described by Maeda et al. (1980), is based on a chemiluminescence reaction with a reagent solution, luminol (5-amino-2, 3-dihydro-l, 4 phthalazinedione):

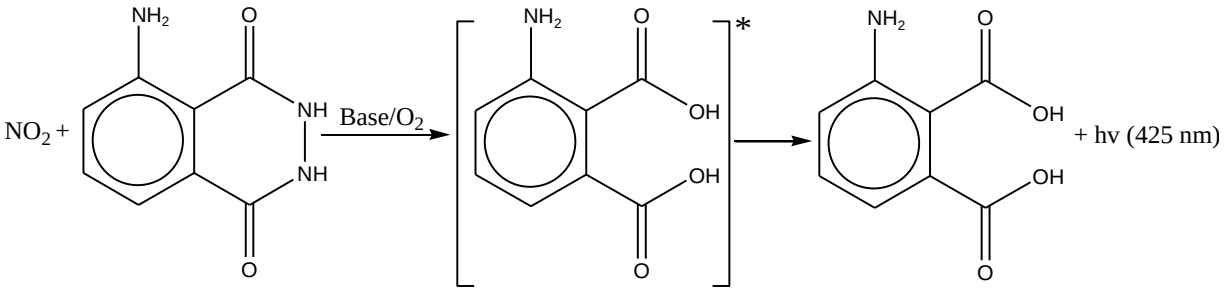

R4. 12

Sampled air is drawn through a reaction chamber by an internal air pump. A special wick in the reaction chamber is permanently replenished with luminal solution by an internal liquid pump at a flow rate of about 0.05 cm^3 s^{-1}. Fresh luminal solution is drawn by the liquid pump to the reaction chamber from a 250 cm^3 bottle located in the instrument and the liquid coming out the reaction chamber is pumped into a second 250 cm^3 waste bottle. On the wick surface, NO_2 from the sampled air is chemically transformed by reaction with luminol and emits a luminous light with a wave length of 425 nm. The intensity of this luminescence, which is proportional to the NO_2 concentration, is viewed and amplified by a photomultiplier and transformed into an electrical signal. The analogue signal is also transferred via BNC connector to a data acquisition PC.

Calibration procedure

In PERCA technique, the NO_2 detector should be accurately calibrated in order to determine the concentration of NO_2 resulted from the chemical amplification of HO_x i.e. measured NO_2 in a sampled air indicates the absolute concentration of HO_x in that sample.

The NO_2 calibration was accomplished by mixing known flows of pure air and NO_2 (0.89 ppm) using the calibration tube shown in Figure 4.1. The NO_2 and the pure air flows proportionality was varied in the calibration tube every 7 minutes. The signal values were averaged over the last 5 minutes for each sample. Appendix B, Figure B-7 displays the response of the NO_2 analyser to changes in the flows proportionality of pure air and gaseous NO_2, while appendix C, Table C-1, shows typical air to NO_2 flows for NO_2 analyser calibration experiment. The obtained calibration curve, shown in Figure 4.3, was then used to infer the NO_2 mixing ratio in PERCA calibration and measurements experiments.

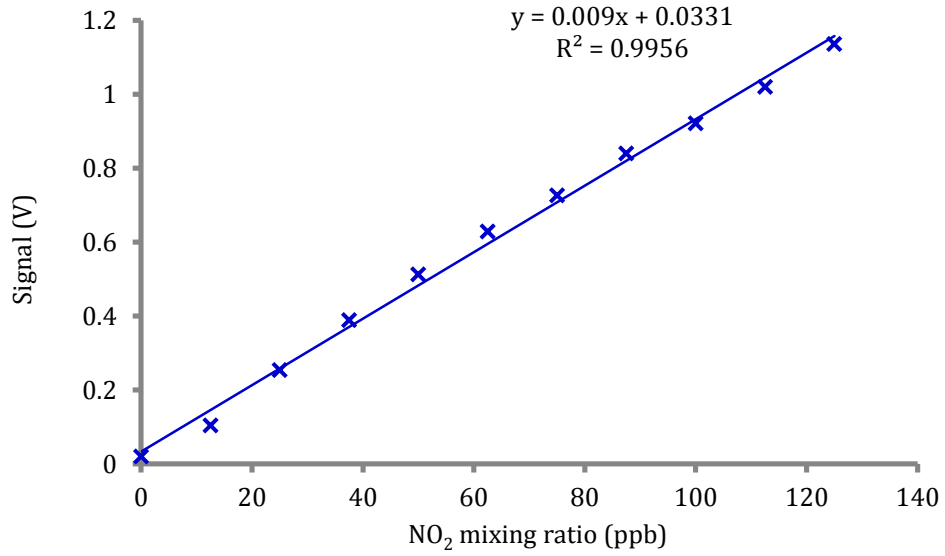

Figure 4. 3 Typical NO_2 calibration curve used to infer PERCA signal. The magnitude of the errors at each measurement point was determined, found to be minor and thus omitted from the presentation.

4.2.3.2 Calibration of HO_x

The experimental set up for calibrating the PERCA is shown in Figure 4.4. The PERCA was calibrated over the relative humidity range of 0.5-95% to obtain the CL at each RH% using the equation Eq 4.8.

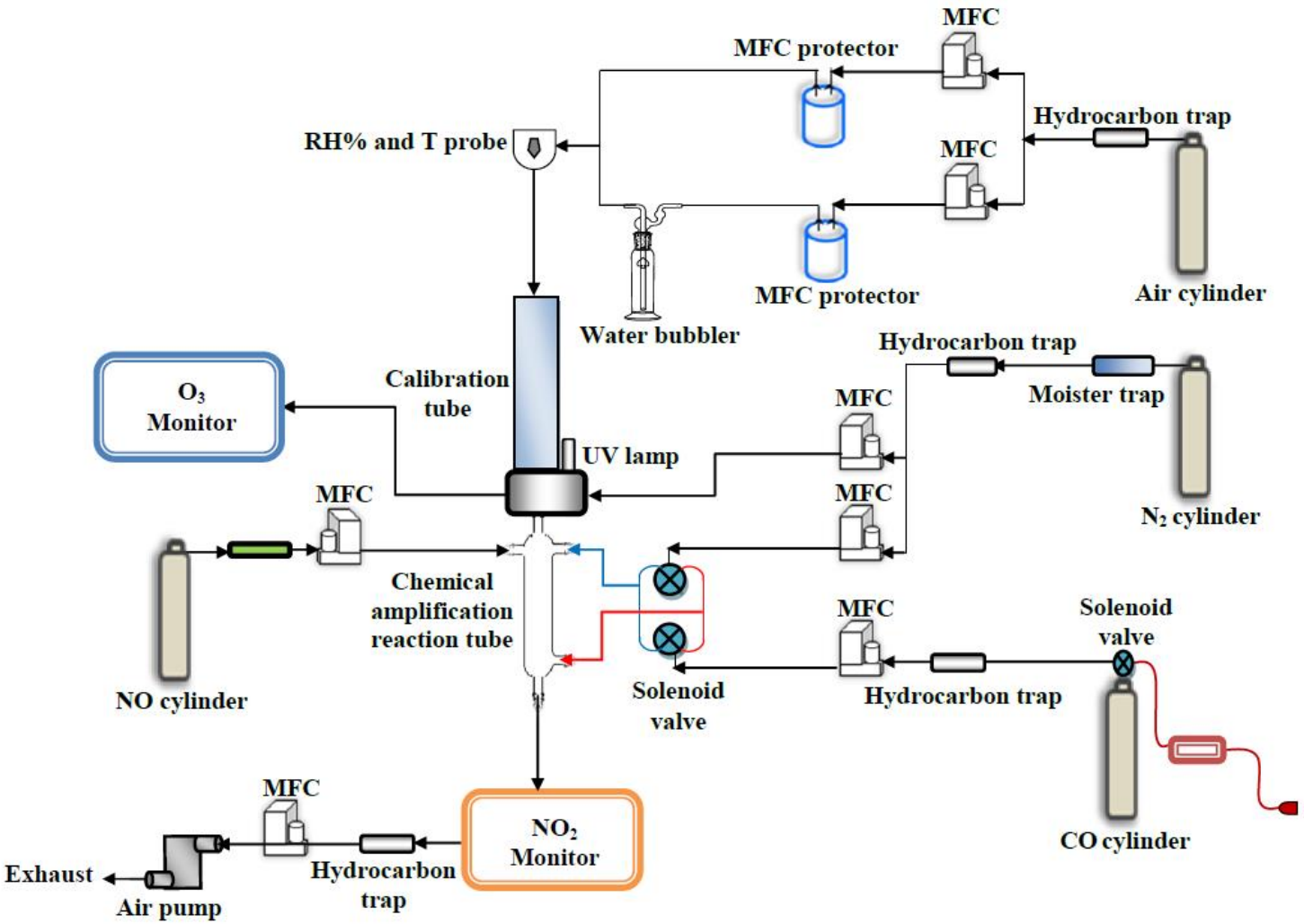

Figure 4. 4 Schematic diagram of the apparatus used for the calibration of PERCA showing principal interconnections between components.

A flow recipe was set for the calibration system and was controlled by IGI systems (LAB Interface 130410, v1.0) software. Typical flow recipe (Appendix C, Table C-2) is performed at 12 minutes sampling duration (the first 2 minutes is given for system stabilization and are excluded from the analysis), flow of PERCA exhaust was 2 slm, N_2 light cavity was 1 slm, NO was 0.01 slm, CO and N_2 were each 0.1 slm, and wet to dry flows were varied to produce a range of RH of 0.5-95% at a total flow rate of 10 slm. The results of this calibration experiment yielded 11 independent HO_x concentrations which varied from 8.3×10^7 to 1.8×10^{10} molecules cm^{-3} giving a corresponding average CL range of 2594-42, respectively. Table 4.1 summarizes the results of PERCA calibration while Figure 4.5 displays PERCA calibration curve.

Table 4. 1 Typical wet to dry flows for PERCA calibration experiments and corresponding RH% and chain length (CL).

Wet flow (slm)	Dry flow (slm)	RH (%)	Chain Length (CL)	Relative standard deviation (%)
0.0	10.0	0.5	2594	20
1.0	9.0	8.2	246	15
2.0	8.0	17.0	156	15
3.0	7.0	26.6	129	13
4.0	6.0	35.4	114	11
5.0	5.0	44.8	74	13
6.0	4.0	54.1	66	12
7.0	3.0	63.5	59	11
8.0	2.0	73.1	52	15
9.0	1.0	85.9	49	12
10.0	0.0	95.0	42	11

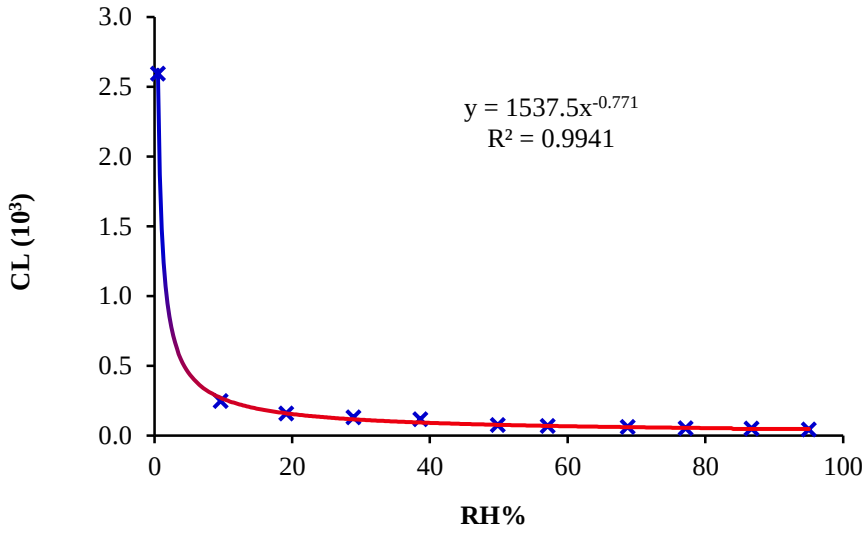

Figure 4. 5 PERCA calibration curve used to calculate HO_x in the ACA system.

As it can be seen from the Figure above, the CL is relative humidity dependent. The CL decreases exponentially as the relative humidity increases which was observed in related studies (Mihele et al., 1999; Reichert et al., 2003; Fleming et al., 2006; Li et al., 2009). This qualitative result of HO_x dependency on water might indicates the involvement of water in HO_x losses. Reported experimental analysis and simulation results proposed wall losses in addition to three depletion reactions enhanced at high relative humidity (Reichert et al., 2003):

$$OH + CO \xrightarrow{nH_2O} \text{nonradical products} \qquad \text{R4. 13}$$

$$CO + HO_2 \xrightarrow{nH_2O} CO_2 + OH \qquad \text{R4. 14}$$

$$NO + HO_2 \xrightarrow{nH_2O} \text{nonradical products (e.g } HNO_3) \qquad \text{R4. 15}$$

Appendix B, Figure B-8 and B-9 display the PERCA response and the corresponding concentration of HO_x as a function of RH%, respectively. The obtained CL calibration curve can be adopted for HO_x quantification in the ACA system.

4.2.4 PERCA implementation into the ACA system

After PERCA calibration, the PERCA reaction cell was allowed to stabilize for 30 minutes while sampling directly from the AFT at a flow rate of 2 slm prior the measurements. Reagent gases (CO, NO and N_2) were added to the sampled flow allowing the amplification chemistry to take place in the PERCA reaction cell. The experimental procedure and the conditions of the reaction cell during the measurement were identical to the calibration procedure and condition, the flows of the gases are listed in appendix C, Table C-2. The response of the NO_2 detector measuring NO_2 modulation for the sampled air was analysed to give the absolute concentration of HO_x in the ACA system. Typically measured HO_x concentration in the ACA system was in the range $(8.0\pm0.4)\times10^9$ to $(1.2\pm0.6)\times10^{10}$ molecules cm^{-3} corresponds to an exposure range of 1.2×10^{12} to 1.8×10^{12} molecules cm^{-3} s.

HO_x radicals in the ACA system were generated in-situ at RH 65.0 ±0.2% (chapter 2, section 2.2.6.3) while ozone mixing ratio was maintained at ~100 ppb. This particular ozone level was chosen following the observed suppression in PERCA modulation signals at high ozone mixing ratio. This PERCA complication which might be due to the fact that PERCA technique measures modulated NO_2 signals at ppb levels making active species (such as ozone) in the ACA system significantly interfere with PERCA chemistry by generating elevated NO_2 in the background measurement. To account for PERCA behaviour when coupled with the ACA system, a numerical simulation described here is proposed to explain PERCA signal trends when sampling from the ACA system. What follows is a detailed description of a chemical simulation to describe the oxidation environment of the artificial atmosphere of the ACA system.

4.3 Simulation study of the oxidation environment in the ACA system

This simulation is an attempt to derive an expression to calculate HO_x levels in the ACA system which operates at conditions that significantly affect the PERCA performance. The high ozone levels in the ACA system interferes with PERCA signals making HOx measurements a challenging task. The first step in this simulation is to model the initial concentration, exposure and production rate of OH based on the principle of the generation approach and the experimental conditions under the study. The next step is to initiate the interconversion process of the gas phase components using reaction kinetics in order to establish the oxidants levels in the ACA atmosphere.

4.3.1 Concentration and exposure of OH radicals

OH exposure, the concentration of OH in molecules cm^{-3} integrated over the reaction time in the AFT, determines how fast aerosol and their oxidation products are oxidized. The ACA photochemistry produces OH via photolysis of ozone by ultraviolet light in the presence of water vapour which is the main source of hydroxyl radicals in this artificial system. As described in chapter 2, section 2.4.1.2, ozone production in the ACA system is accomplished externally using UV lamp emits a narrow band of 184.9 nm utilizing synthetic air as the feed gas:

$$O_2 + h\nu\,(184.9\text{ nm}) \longrightarrow 2O\,(^3P) \qquad \text{R4. 16}$$

$$O\,(^3P) + O_2 + M \longrightarrow O_3 + M \qquad \text{R4. 17}$$

Ozone is then introduced to the AFT reactor for in-situ production of excited singlet atomic oxygen O (^1D) via the photolysis of O_3 at 254 nm:

$$O_3 + hv\ (245\ nm) \longrightarrow O(^1D) + O_2$$

R4. 18

A fraction of O (^{1}D) atoms reacts with the water vapour in the AFT reactor and produces OH:

$$O(^1D) + H_2O \longrightarrow 2OH$$

R4. 19

This fraction of O (^{1}D) atoms that produces OH largely depends on the concentration of H_2O. However, the bulk of O (^{1}D) atoms collides with N_2 or O_2 and quenched to ground state oxygen atoms:

$$O(^1D) + N_2 \longrightarrow O(^3P) + N_2$$

R4. 20

$$O(^1D) + O_2 \longrightarrow O(^3P) + O_2$$

R4. 21

The kinetic rate equation for R 4.16 is:

$$\frac{d[O_2]}{dt} = -j[O_2]$$

Eq 4. 9

Photolytic rate coefficients, j, may be calculated by integrating the absorption cross section, σ, the quantum yield, Φ, and the spherical irradiance, F, at the wavelength of the irradiance, 184.9 nm, at a known temperature:

$$j = \sigma_{O,1849nm} \times \Phi_{O1849nm} \times F_{1849nm}$$

Eq 4. 10

From R 4.16 and R 4.17:

$$\frac{d[O_3]}{dt} = -2\frac{d[O_2]}{dt}$$

Eq 4. 11

By substituting equation Eq 4.10 into Eq 4.9 and integrating the resultant equation over the reaction time in the ACA system, t,:

$$[O_3] = [O_2] \times \sigma_{O,184.9nm} \times \phi_{O,184.9nm} \times F_{184.9nm} \times t$$

Eq 4. 12

Rearranging equation Eq 4.12 yields:

$$F_{184.9nm} = \frac{[O_3]}{[O_2] \times \sigma_{O_2,184.9nm} \times \phi_{O,184.9nm} \times t}$$

Eq 4. 13

where $[O_3]$ is the concentration of ozone produced in the ACA system (5×10^{14} molecules cm^{-3}), $[O_2]$ is calculated as 21% of the molar concentration of the air, 0.2[M] ([M] estimated as 2.45×10^{19} molecules cm^{-3}), $\sigma_{O2,184.9nm}$ for O_2 is 1.23×10^{-20} cm^2 molecules^{-1} (Bloss et al., 2004), ϕ_O is 2, and t is the residence time of O_3.

Similarly from reaction R 4.18 and R 4.19:

$$\frac{d[OH]}{dt} = 2 j_{O_3}[O_3] F_{OH}$$

Eq 4. 14

And

$$j_{O_3} = F_{254}\sigma_{O_3,254}\phi_{O^1D}$$

Eq 4. 15

The F_{OH} in equation Eq 4.14 is a factor introduced to account for the O (^{1}D) losses via reaction R 4.20 and R 4.21 to correct for calculated OH level in the system and can be calculated as:

$$F_{OH} = \frac{k_1[H_2O]}{k_1[H_2O] + k_2[N_2] + k_3[O_2]}$$

Eq 4. 16

where k_1, k_2 and k_3 are 2.1 x 10^{-10}, 4.1 x 10^{-11} and 3.3 x 10^{-11} cm^3 $molecules^{-1}$, respectively (Haynes, 2012). $[O_2]$ calculated as described above and $[H_2O]$ as explained in section 4.2.2.3 while $[N_2]$ is calculated as 0.78[M], where [M] is the molar concentration of air and it is calculated as described earlier and found to be 2.45×10^{19} molecules cm^{-3}

The light flux, F_{254nm}, is estimated from:

$$F_{254nm} = 15F_{184.9} \text{ (Haynes, 2012)}$$

Eq 4. 17

However, the light intensity of the two UV lamps irradiate at 184.9 nm used to generate ozone and at 254 nm used to photolyse ozone in the AFT was found to be not identical and thus a correction factor (x) was required to account for the difference in the light intensity between the two lamps:

$$F_{254nm} = 15F_{184.9}.x$$

Eq 4. 18

The value of *x* was determined experimentally and was found to be 0.66 as will be described in the section below.

Substituting equation Eq 4.15 into equation Eq 4.14 leads to equation Eq 4.19:

$$\frac{d[OH]}{dt} = 2[O_3] \times \sigma_{O_3,254nm} \times \phi_{O^1D} \times F_{254nm} \times F_{OH}$$

Eq 4. 19

Integrating equation Eq 4.19 over the reaction time in the ACA system, t, results in the equation used to infer OH radical in the ACA system:

$$[OH] = 2[O_3] \times \sigma_{O_3,254nm} \times \phi_{O^1D} \times F_{254nm} \times F_{OH} \times t$$

Eq 4. 20

The calculated [OH] using this approach was 5.0×10^{13} molecules cm^{-3} while OH exposure and production rate at the established residence time of the ACA system was found to be 6.4×10^{15} molecules cm^{-3} s and 3.5×10^{11} molecules cm^{-3} s^{-1}, respectively.

Determination of lamp relative intensity factor (x)

The purpose of this experiment is to measure the relative intensity factor between two different UV pen-ray lamps (Ultra-Violet Products Ltd., λ = 184.9 nm, model 90-0003-01 and 90-0004-07). This factor is to be used in the calculation of the flux conversion between two wavelengths, 184.9 nm and 254 nm, needed in the HO_x calculation.

The experiment was conducted in the dark. The UV lamp to measure its intensity was mounted vertically. A 184.9 nm filter (Acton) resides between the UV lamp and a photodiode detector. After careful setting, checking for connection and beam alignment, the background signal was recorded initially with the UV lamp turned off, this background signals was repeatedly measured for each lamp. After, turning on the UV lamp the output signal (volts) of the photodiode is recorded over 10 minutes period and the corresponding signals were averaged and subtracted from the background signal. The ratio of the light intensity of the UV lamp radiates at 254 nm to that at 184.9 nm is found to be 0.66.

4.3.2 Step concentration of species in the ACA system

Species levels in the ACA system can be described by considering production and losses processes competing with OH production mechanism under the conditions employed. Table 4.2 depicts self and cross reactions which contribute to the loss and production processes of species

Table 4. 2 Production and loss rate constants of HO_x in the ACA system (Sander et al., 2011)

Reaction	Equation	Constants (molecules cm^3 s^{-1})
1	$OH + HO_2 \rightarrow H_2O + O_2$	$k_1=1.10\times10^{-10}$
2	$HO_2 + O_3 \rightarrow OH + 2O_2$	$k_2=1.90\times10^{-15}$
3	$HO_2 + HO_2 \rightarrow H_2O_2 + O_2$	$k_3=5.26\times10^{-12}$
4	$OH+O_3 \rightarrow HO_2+O_2$	$k_4=7.30\times10^{-12}$
5	$OH + OH \rightarrow H_2O + O$	$k_5=1.80\times10^{-12}$
6	$OH + OH \rightarrow H_2O_2$	$k_6=4.69\times10^{-12}$
7	$OH + H_2O_2 \rightarrow H_2O + HO_2$	$k_7=1.80\times10^{-12}$

present in the system under the oxidation condition of this study and in the absence of aerosol. The secondary production and loss of HO_x via the interaction of gaseous species including O_3 with the condensed phase of aerosol is assumed to be negligible based on experimentally observed HO_x levels in aerosol and aerosol free atmosphere (8.0%). From such consideration, it is worth considering secondary production and loss routes of HO_x radicals in the ACA system. This simulation is based on real operating conditions of oxidation such as constant relative humidity of 65.0%, 100 ppb O_3 and elevated levels of HO_x. The purpose of such simulation is to estimate the HO_x budget of the artificial atmosphere within the residence time of the system and to interpret observed PERCA signal which corresponds to HO_x levels. This can be simply illustrated by considering species interconversion within the system, in particular, OH, HO_2, O_3 and H_2O_2. For OH, reaction 1, 4, 5, 6, 7 are sink steps while reaction 2, is a formation step. The reaction constant, k´, for the OH production via the O^1D chemistry is derived from Eq 4.19 as:

$$\frac{d[OH]}{dt} = 2[O_3]\times \underbrace{\sigma_{O_3,254nm}\times\phi_{O^1D}\times F_{254nm}\times F_{OH}}_{k'}$$

Therefore the derived production rate of OH form O^1D chemistry, which represents the main source of OH and the initiator of cross and self-reaction in the ACA system, can be expressed as:

$$\frac{d[OH]}{dt} = 2k'[O_3]$$

Eq 4. 21

The following differential rate expressions can be used to describe the change in the concentration of OH:

$$\frac{d[OH]}{dt} = 2k'[O_3] - k_1[OH][HO_2] + k_2[HO_2][O_3] - k_4[OH][O_3] - 2k_5[OH]^2 - 2k_6[OH]^2 - k_7[OH][H_2O_2]$$

Eq 4. 22

Similarly for HO_2, reaction 1, 2, and 3 are sink steps while reaction 4 and 7, are formation steps. The following differential rate expressions are therefore used to describe the change in the concentration of HO_2:

$$\frac{d[HO_2]}{dt} = -k_1[OH][HO_2] - k_2[HO_2][O_3] - 2k_3[OH_2]^2 + k_4[OH][O_3] + k_7[OH][H_2O_2]$$

Eq 4. 23

The dominant removal steps for O_3 are reaction 2 and 4, this can be written as:

$$\frac{d[O_3]}{dt} = k'[O_3] - k_2[HO_2][O_3] - k_4[OH][O_3]$$

Eq 4. 24

Finally, for H_2O_2, reaction 3 and 6 are formation steps while reaction 7 is a removal step, these processes lead to the following reaction rate expression:

$$\frac{d[H_2O_2]}{dt} = 2K_3[HO_2]^2 + 2K_6[OH]^2 - K_7[OH][H_2O_2]$$

Eq 4. 25

Using this simplified set of ACA reactions and by integrating the above differential rate expressions at a reaction time step of 0.01s, the system shows to evolve a steady state condition at about 15 s from the start of the reaction where UV light is continually absorbed by the system but chemical species concentrations remain constant with time. Figure 4.6 demonstrates the output of this simulation for the analysed concentrations of species of interest in the ACA as a function of time.

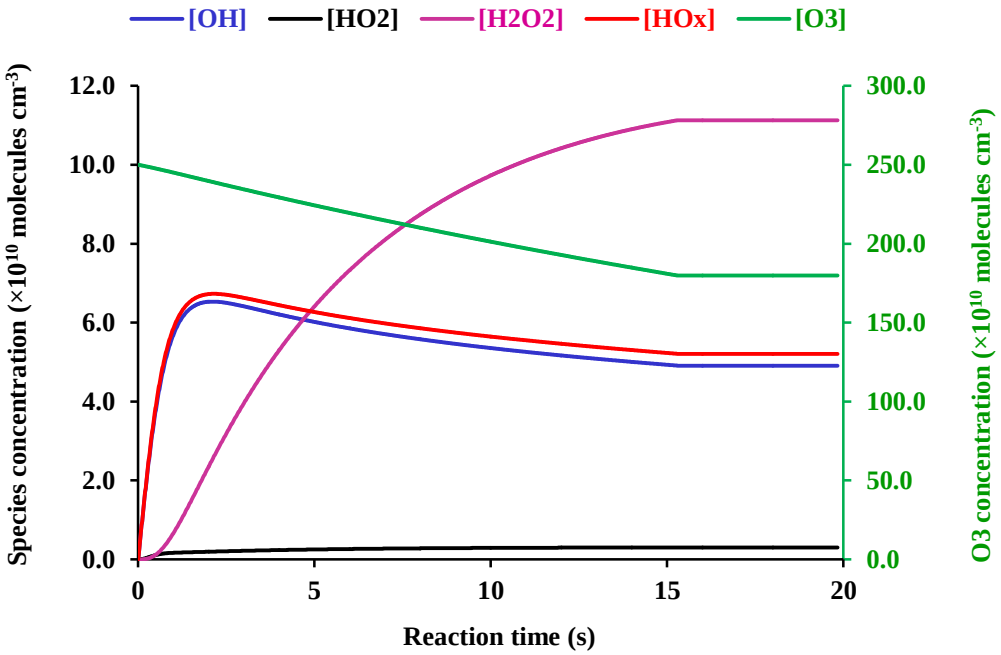

Figure 4. 6 Simulation output of species concentration as a function of simulated reaction time following reactant mixing, for the ACA system operating at RH of 65%, O_3 mixing ratio 100 ppb, and ambient temperature and pressure.

4.3.3 Effect of ozone concentration on HO_x levels

The PERCA has been deployed successfully in a number of field campaigns to quantify the atmospheric peroxy radicals (Zanis et al., 2003; Qi et al., 2006). However, the concentration of the reactants in this study is incomparably higher than that in the ambient atmosphere, therefore, the PERCA may be subjected to more significant interferences under the oxidation conditions of

this system. The most active species in the current study known to interfere with the PERCA signal is O_3 (Cantrell et al., 1993; Green et al., 2003). In the presence of ozone, the chain length is reduced dramatically due to the formation of the NO_2 which raises the baseline signal and suppresses the modulation between the background and the measurements signals. The following equation summaries the involvement of ozone in intensifying PERCA response via oxidizing NO to NO_2:

$$NO + O_3 \longrightarrow NO_2 + O_2$$

R4. 22

Indeed it was noted that PERCA modulation signals is disturbed at O_3 mixing ratio above 800 ppb. Additionally, the baseline and measurement mode signals become indistinct as O_3 mixing ratio increases. For this reason, the results of the above simulation were extended to study species interconversion as a function of O_3 mixing ratio. The O_3 mixing ratio was simulated over the entire range of 0.02-20 ppm while keeping all other input parameters constant. Figure 4.8 illustrates the resultant simulated OH, HO_2 and HO_x concentrations as a function of O_3 mixing ratio modelled at real established oxidation conditions of the ACA system.

Figure 4.7 and the zoom in plot of the figure show that at ambient O_3 levels from 20 to 100 ppb, HO_x levels doubled in concentration from 3×10^{10} to ~ 6×10^{10} molecules cm^{-3}, respectively, and that the dominant radical is OH. This is expected as nothing but O_3 is the formation source for OH and loss processes of OH at this O_3 levels are less significant. HO_x concentration peak at 100 ppb marks maximum OH levels at near ambient O_3 mixing ratio. The concentration then shows a steady downward trend and reaches its bottom point of 4×10^{10} molecules cm^{-3} corresponding to an O_3 mixing ratio of 1 ppm. This might reflect the importance of HO_x sink

routes at this level of O_3. HO_x levels starts to increase again and approches a plateau at 6.5×10^{10} molecules cm^{-3} corresponds to O_3 mixing

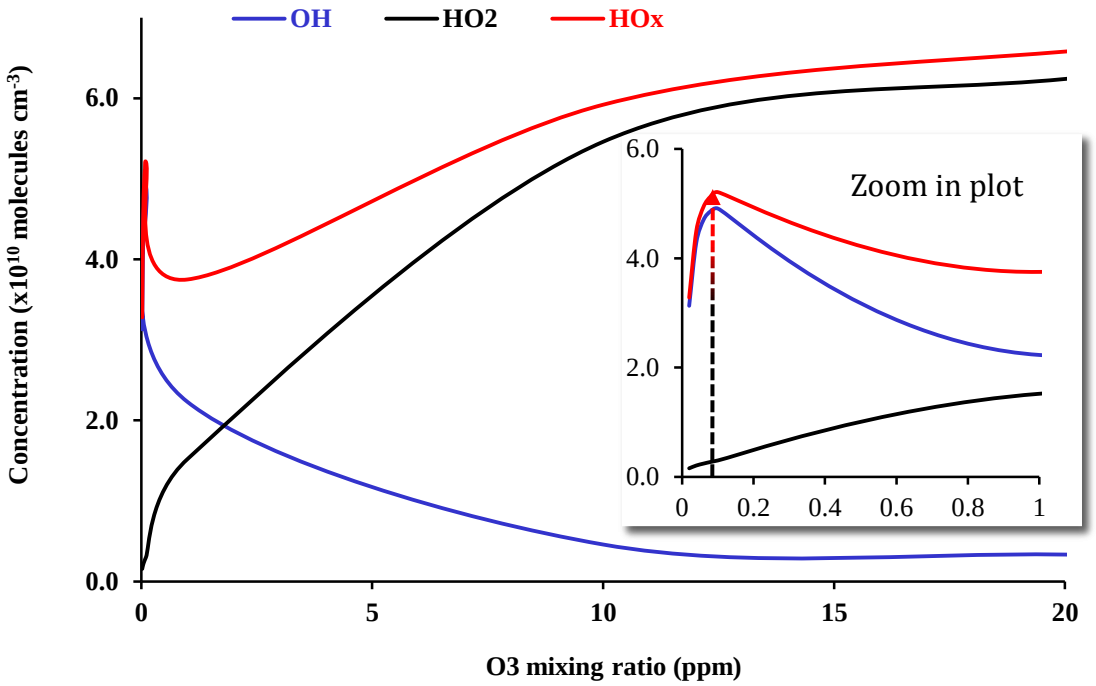

Figure 4. 7 Simulation output of OH, HO_2 and HO_x concentration as a function of ozone mixing ratio in the artificial atmosphere of the ACA system.

ratio of 20 ppm and above. It is obvious that OH levels fall and HO_2 levels rise in response to the increase of O_3 mixing ratio making HO_2 the dominant oxidant at high O_3 mixing ratios (1.5-20 ppm). The result of this simulation indicates that OH radical is preferentially produced at low ozone levels. For this reason the production of radical in this study was adaptly maintained at 100 ppb. Such circumestances has important implications in regards to maximising the oxidation capacity by enhancing the concentration of the most effective oxidants in the system, the OH radical, hence the impact of OH oxidant on organic aerosol can be selectivily revealed. Yet low ozone levels closely mimics the atmospherically relavent conditions and thus PERCA signal is perfectlty modulated. Unlike other approaches in generating HO_x radicals at elevated ozone

mixing ratio (George et al., 2007; Kessler et al., 2012), the OH production under the condition of this study ensure direct oxidation of organic aerosol by OH radical making the oxidation by other means negligible.

4.4 Observed versus simulated HO_x levels

HO_x levels in the ACA system were studied as a function of O_3 mixing ratio between 20 and 800 ppb, at which range the PERCA showed measurable response. The flows in the system were kept constant through all the measurements while ozone mixing ratio was varied by partially covering the UV lamp of the ozone generator with aluminium foil to differing degree. PERCA was set to sample directly from the AFT at each ozone mixing ratio. The corresponding observed O_3 mixing ratios were then used to simulate HO_x levels in the system using the above described model. Figure 4.8 shows the results of the measured and calculated HO_x in the ACA system.

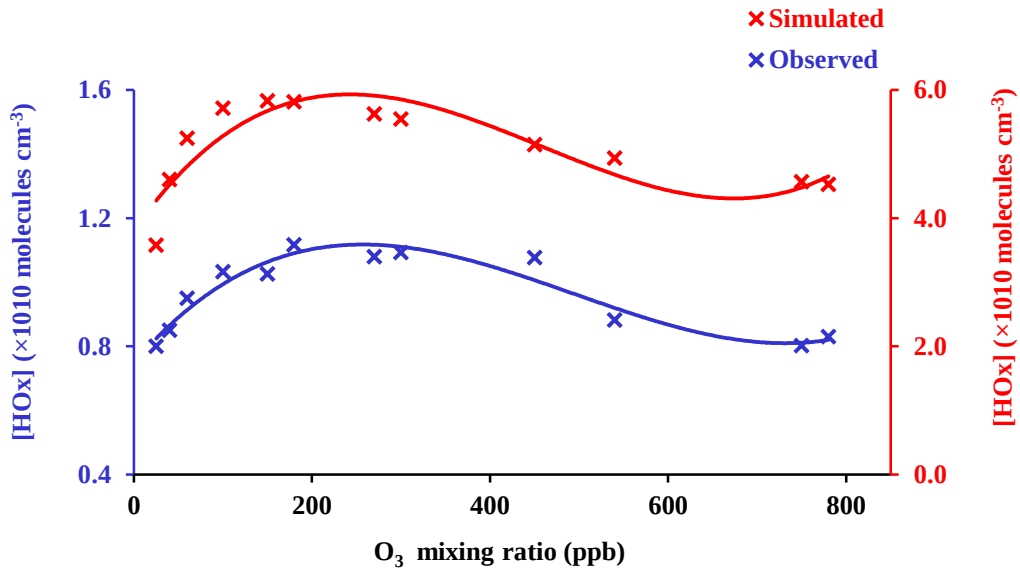

Figure 4. 8 Simulated and observed changes in HO_x levels versus O_3 mixing ratio. The examined range of ozone mixing ratio is determined based on the PERCA detection range (i.e. 20-800 ppb).

Observed HO_x well reproduced the profile of the predicted concentrations but was beneath them by a factor of ~5 as Figure 4.8 exhibits. The overestimation of the simulation in HO_x for the entire range under investigation suggests systematic HO_x losses routes either in the ACA (as simulated by the chemical model) or in the PERCA systems as a result of species interferences or experimental conditions as described above in section 4.2.3.2. For high levels of O_3, PERCA methodology is not applicable as modulation shows to be very poor; however the model simulations confirmed the trend observed at lower ozone levels, namely that the OH level in the ASA system was maximised at lower ozone levels, identifying this regime is that best suited for further experiments. Additionally, oxidation of organic aerosol by OH under moderate O_3 levels is more likely to minimze the effect of other oxidants including O_3, HO_2 and H_2O_2 in processing the organic particles and thus maximizing the role of OH exclusively.

4.5 Effect of organic aerosol on HO_x levels in the ACA system

This experiment was conducted to examine the effect of aerosol on the chemistry of HO_x level in the PERCA system. The experimental procedure followed here is similar to that described in chapter 2, section 2.3. For clean artificial atmosphere measurement, the PERCA was kept sampling from the AFT with aerosol flow substituted by clean dry air. However, for investigating PERCA behaviour when sampling from highly polluted atmosphere with organic particles (5×10^6 particles cm^{-3}) the flow of aerosol was set as usual. Figure 4.9 shows PERCA response in measuring HO_x levels in particle free atmosphere and in the presence of high concentration of organic aerosol, 5×10^6 particles cm^{-3}. While signals were observed to be fairly stable in both

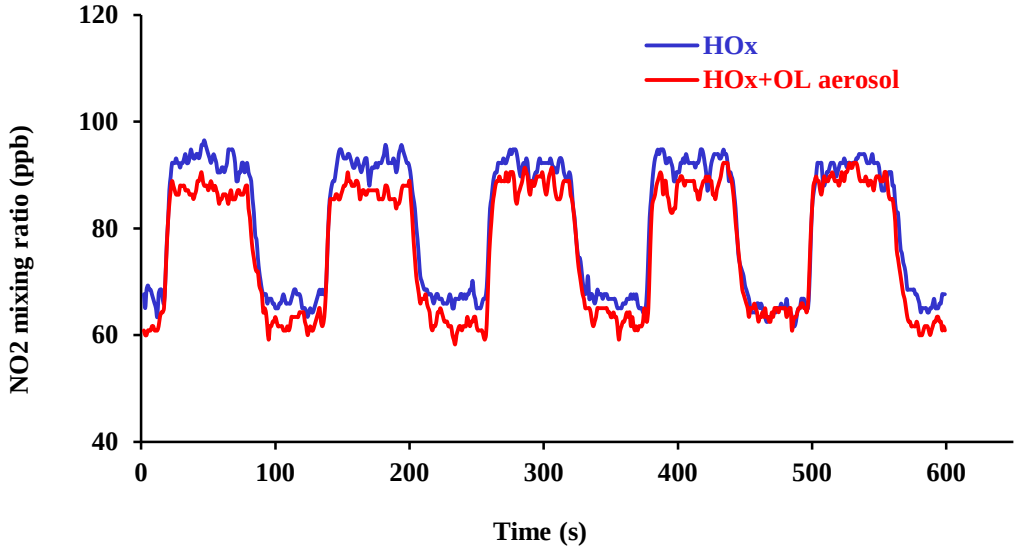

Figure 4. 9 Effect of aerosol on HO_x levels in the ACA system.

cases, a slight drop of 8±0.2% in HO_x concentration was noticed in the presence of organic aerosol. It is clear from the Figure above that high concentation of organic particles has no considerable effect on PERCA signals. The nearly constant obvious modulation in the presence of aerosol during the course of the oxidation reaction can be taken as an indication for PERCA suitability in measuring radicals levels in a system characterised with high levels of organic aerosol. The slight drop in the measured HO_x levels, however, can be attributed to the radical losses to the particle phase.

4.6 PERCA limitation

The complexity of the chain reactions in the PERCA system causes potential background and significant interferences from other species present in the measured atmosphere (Liu et al., 2009). In this study, the PERCA was used to measure HO_x levels in the ACA system operated under elevated O_3 and particles levels and relatively wet condition (65.0±0.2%) which set the background signal of PERCA. Although the presence of high particle concentration showed no

significant effect on PERCA signals, ozone was found to be a troublesome to PERCA chemistry by converting excess NO mixing ratio to NO_2 which significantly amplifies the background signals as explained in section 4.3.3. The wet experimental condition in this study might also affect the absolute measurement of radicals in the system through background interferences from water molecules as the result of the PERCA calibration shows in Figure 4.5.

4.7 Summary

The PERCA was deployed in this study to quantify the levels of generated radicals in the ACA. Typically measured HO_x concentration was in the range $(8.0\pm0.4)\times10^9$ to $(1.2\pm0.6)\times10^{10}$ molecules cm^{-3}, corresponding to an exposure range of 1.2×10^{12} to 1.8×10^{12} molecules cm^{-3} s. The use of high ozone mixing ratio was found to suppress PERCA modulation signals while the relative humidity has the effect of reducing the chain length in the system. The numerical simulation adapted to predict HO_x concentration and to account for PERCA behaviour when coupled with the ACA system suggested a steady state of oxidants concentration within the first 15 s from the start of the reaction. The simulation also indicated that HO_x concentration is dominated by OH radicals at 100 ppb O_3 and that as O_3 mixing ratio increases OH level falls and HO_2 level rises making HO_2 the dominant oxidant at high O_3 mixing ratios (1.5-20 ppm). The simulation and observed PERCA trends with varying ozone mixing ration both suggest better performance of PERCA system as well as good oxidation capability of the ACA system at ~100 ppb of ozone. It is concluded also that high concentation of organic particles in ACA system has no considerable effect on the gas chemistry of PERCA system.

CHAPTER 5 CHARACTERISATION OF AEROSOL CHEMICAL AGEING (ACA) SYSTEM

5.1 Introduction

This chapter deals with the characteristic features of the developed ACA system and is organised as follows. First a comparison between the two methods used in this study to generate aerosols in terms of quality (e.g. monodispersity and size), and quantity of generated aerosols is presented. Then optimization of factors affecting aerosol formation via the homogeneous nucleation of liquid organics is described. These factors include bubbler and reheater temperatures, the flow rate of the carrier gas, and the depth of the liquid in the organic bubbler. Next various aerosol losses routes in the ACA system including losses through the AFT, over time, at humid conditions and losses due to the UV radiation inside the AFT are illustrated. This is followed by a theoretical study to estimate the SOA burden formed by reaction of oxidants with the vapour around pure liquid droplets and thus to account for the possible subsequent gas particle partitioning of the oxidation products from the vapour phase. Oleic acid aerosol is chosen as a model in this theoretical study. The generation of the relative humidity in the ACA system is described. Finally, ozone generation by photolysis of synthetic air and pure oxygen is characterized.

5.2 Characterization of aerosol generation

In this research project, vaporization-condensation and atomization methodologies were applied to generate organic polydisperse aerosols (section 2.2.6.1) which were detected by the SMPS or ATOFMS as explained in sections 2.2.7.1 and section 2.2.7.2, respectively. This section describes the quality and the quantity of the particles and the factors affecting their production under the generation conditions of this study.

5.2.1 Atomization versus homogeneous nucleation

Figure 5.1 shows a comparison in the size distribution of BES particles produced by atomization and vapour condensation techniques. The particles were generated as described in section 2.2.6.1.

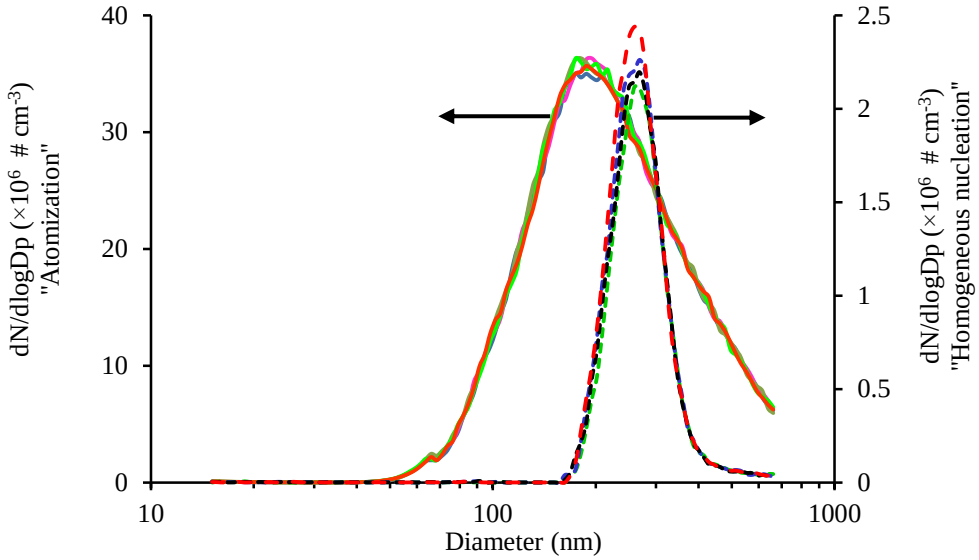

Figure 5. 1 Size distribution of BES polydisperse particles produced by atomization (solid lines) and homogeneous nucleation (dashed lines). Four replicate measurements were performed for each technique.

As it can be seen from the Figure above, atomization of aerosol produced high number concentrations of organic particles, but the geometric standard deviation (σ_g) is in the range of 1.4-1.8. In contrast, the approach of aerosol generation by homogeneous nucleation produced less number concentration of particles with quite uniform particle dispersivity, i.e. σ_g was in the range of 1.1-1.3.

The generation technique of the aerosol for this study was selected for its suitability to the characterisation technique or considering the physical property of the particles. The size of the aerosol particles is important to the detection in the ATOFMS system, which is central to the chemical characterisation experiments. Particles produced via condensation approach are not properly detected by ATOFMS because of their smaller size and their optical property. Therefore,

atomisation technique was used in this study as it offers better solution to generate larger size particle as well as easier choice to modify their optical property. The aerosol atomisation technique was deployed for producing solid or aqueous MA particles from MA solution in water. The same approach was also used to generate OL and BES dry particles from solution in methanol (mixed with traces of a laser dye) prior the chemical characterisation study of the aged particles.

5.2.2 Condition optimization of the homogenous nucleation

Generation of organic droplets via vaporization-condensation is affected by the bubbler and reheater temperatures, the flow rate of the carrier gas, and the depth of the liquid in the organic bubbler. What follows is the study of these parameters and their effects in the ACA system.

5.2.2.1 Temperature of the organic bubbler

The quality of aerosols produced over a temperature range of (50-150°C) of the organic bubbler was examined at a reheater temperature of 200°C and a constant flow rate of 1 slm through the organic bubbler which contained 5 cm^3 of OL or BES. This particular reheater temperature, flow rate, and liquid volume were chosen based on earlier optimisation tests. In this study, two identical sets of organic trap vessels, tubings and fittings were used to generate and load OL or BES aerosols so that areas of evaporation, condensation and carriage were the same. Measurements of the size distribution were made after achieving stable condition at each examined temperature. The organic aerosols were sampled from through the AFT by SMPS. Figure 5.2 shows the results.

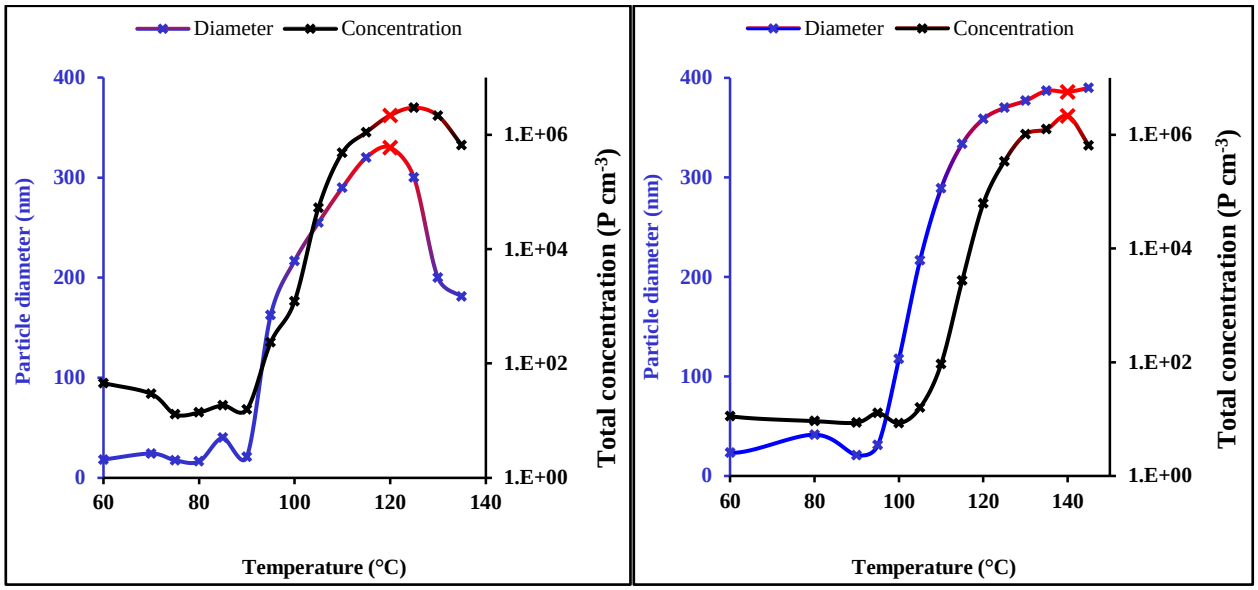

(a) (b)

Figure 5. 2 Effect of the temperature of the organic bubbler on the diameter and the number concentration of: (a) OL and (b) BES particles.

Larger droplets with high number concentration were observed at higher temperature for both OL and BES aerosols. The high temperature made more organic vapour available for homogeneous condensation on a greater number concentration of particles. The 120 °C marked optimum heating temperature for generating OL particles above which particle diameter and number concentration dropped dramatically. Whereas, best quality and quantity of BES particles were found to occur at bubbler temperature of 140°C. In a related study, Chen and Chein studied OL particle generation at a furnace temperature range of 200-280 °C and found suitable heating temperature for generating OL aerosol at 200°C (Chen and Chein, 2006). While Lambe et al generated BES aerosol by the homogeneous nucleation of BES vapour at 145 °C (Lambe et al., 2010). Based on these experimental observation and literature findings, OL and BES aerosol were generated at bubbler temperatures of 120 and 140°C, respectively.

5.2.2.2 Temperature of the reheater tube

The reheating process of the gas mixture leaving the organic bubbler is meant to homogenize aerosol formation (Richard, 2006). The effect of the reheater temperature was explored by sampling BES aerosols through the AFT at a discrete increment in temperatures from ambient to a maximum of 300°C. The total flow rate through the bubbler was kept constant at 1 slm, the bubbler temperature was 140°C and the liquid volume in the bubbler was 5 cm^3. The diameter distributions of the BES droplets under reheater temperature of room temperature, 100°C, 200°C, 250°C and 300°C are shown in Figure 5.3.

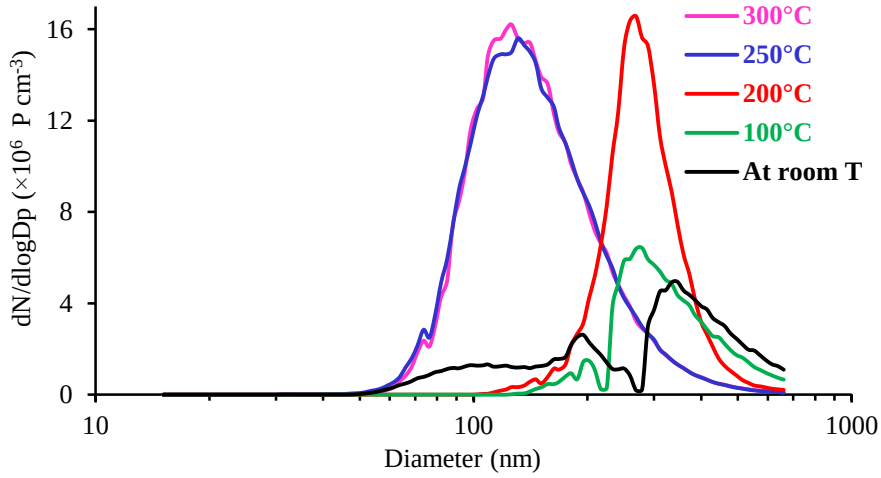

Figure 5. 3 Effect of the reheater temperature on the size distribution of BES droplets.

Better monodispersivity with highest number concentration and desired diameters of particles (mode diameter 280 nm) were generated at 200°C. Particles collected at temperatures below 200 °C were with a wide range of droplet sizes, i.e. highly polydisperse, while particles collected at reheater temperature above 200 °C were the most monodisperse but with smaller size diameter (mode diameter 130 nm). This behaviour can be explained as a result of high vaporization of the liquid BES in the bubbler and thus high availability of BES vapour caused

premature condensation when the reheater temperature was below 200°C. Consequently, high reheating temperature is required to complete the re-evaporation and re-condensation process.

5.2.2.3 Flow rate proportion of the carrier gas through the organic bubbler

The total number of generated particles was investigated at various flow rate ratio between the flow to the organic bubbler and to that of the dilution varying the proportionality of the two flows from 0.08 to 1 slm at a constant total flow rate of 1 slm, bubbler temperature of 120°C, reheater temperature of 200°C and a volume of 5 cm^3 of BES. Figure 5.4 depicts the effect of the flow rate proportionality through the organic bubbler on the total number of BES particles.

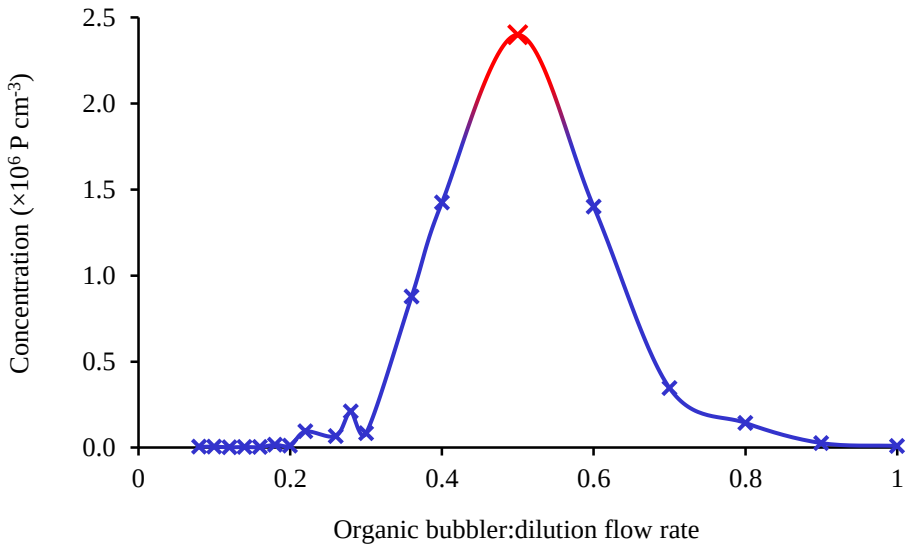

Figure 5. 4 Effect of the organic bubbler to dilution flow ratio on the total number concentration of BES droplets.

The highest number concentration of particles occurred under 0.5 ratio of the two flows. Thus, the suitable flow proportionality for the generation of organic particles chosen was 0.5. The lower number concentration of particles below and above the optimized ratio is an indicative of low efficiency of vapour entrainment in both cases.

5.2.2.4 Liquid depth in the organic bubbler

The effect of the bubbler depth on the size distribution of particles was tested by varying the BES liquid volume in the bubbler (5, 10, 50, and 100 cm^3) while keeping all other parameters constant as described above. The number size distributions of particles measured for different liquid loadings are shown in Figure 5.5.

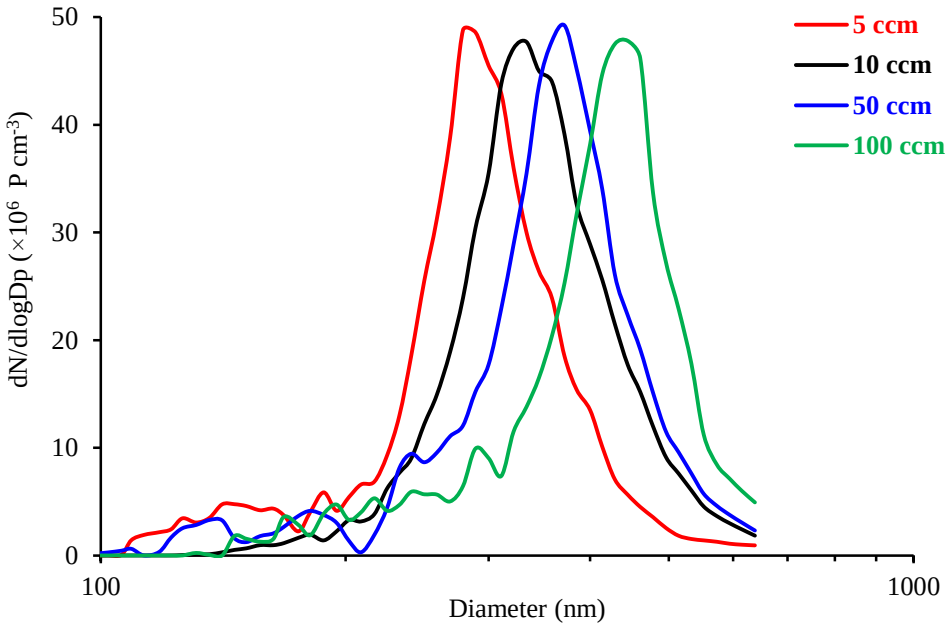

Figure 5. 5 Effect of the liquid BES depth on the size distribution of the generated droplets.

The noticeable features of these size distributions is the formation of larger size particles with less monodispersivity as the liquid depth in the bubbler vessel increases while the number concentration of particles remain relatively comparable. The direct relationship between the liquid depth and particle size indicates more liquid vapour was entrained in the gas stream as the liquid depth increased. For lower σ_g and due to the expense of using organic liquid at larger volume, a volume of 5 cm^3 was selected for bubbler liquid depth.

5.2.2.5 Effect of heating liquid organic

Heating a liquid organic at elevated temperatures in the absence of oxygen for a long period of time can cause a simultaneous change in the chemical and physical properties of the organic compound, an irreversible process known as pyrolysis. The generation of organic aerosol via homogeneous nucleation involves heating the liquid organic such that physical changes including colour and state of the liquid organic were significantly observed. Therefore, it was important to monitor such changes over time in order to study the heterogeneous reaction of oxidants with organic particles. Liquid BES was found to be more stable on heating; additionally it was commercially more available and thus fresh sample was always used in the study. In contrast, OL showed less resistance to heating and changes in colour and state at certain heating periods were noticeable.

To trace the physical changes of OL induced by pyrolysis process, the liquid sample of heated OL was carefully compared with equivalent volume of pure fresh OL in physical appearance and by measuring the size distribution of the two samples under identical conditions.

Pure OL compound is a pale yellowish oily liquid at room temperature with a reported melting point of 12 °C (Hung and Tang, 2010). However, OL solidified at fridge temperature (~4.0°C) as small crystals and appeared white in colour. Following ~20 hours of irregular heating at 120°C, OL colour darkened and when stored at ~4.0°C heated OL had a yellow liquid crystal appearance. These physical changes coincided with a significant change in the shape of the size distribution of OL aerosol (Figure 5.6) and together they demonstrated the thermal decomposition of OL. Fresh OL was thus used in collecting experimental data and its physical appearance was carefully monitored and checked prior and during the experiment and was replaced whenever

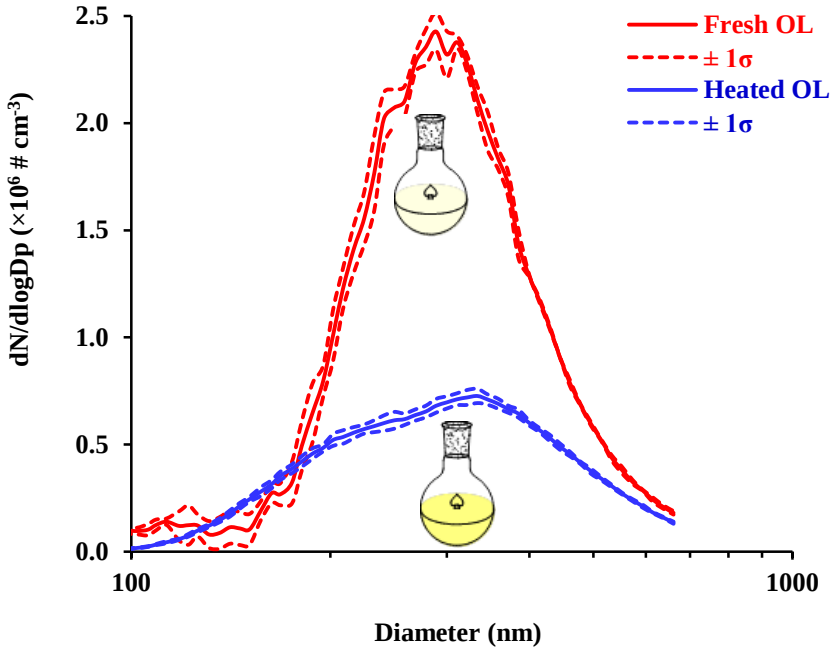

Figure 5. 6 Size distribution of fresh and heated OL showing change in the shape of the size distribution curve and colour on pyrolysis. The uncetainty in the measurements are expressed as ± 1σ.

a sign of thermal decomposition was spotted.

5.3 Characterisation of aerosol loss within the ACA system

5.3.1 Aerosol loss through the AFT

Particle walls losses through the finite volume of the AFTs made of insulating material such as glass or Teflon (Ortega et al., 2013) are expected. To estimating particle walls losses through the AFT in the absence of aging, independent measurements of the aerosol size distribution were made for pure BES particles directly exiting the aerosol generator and particles flown through the AFT. Two different sizes of AFTs were used in the experiment; AFT 1 (1.6 l) and AFT 3 (7.9 l), results are shown in Figure 5.7.

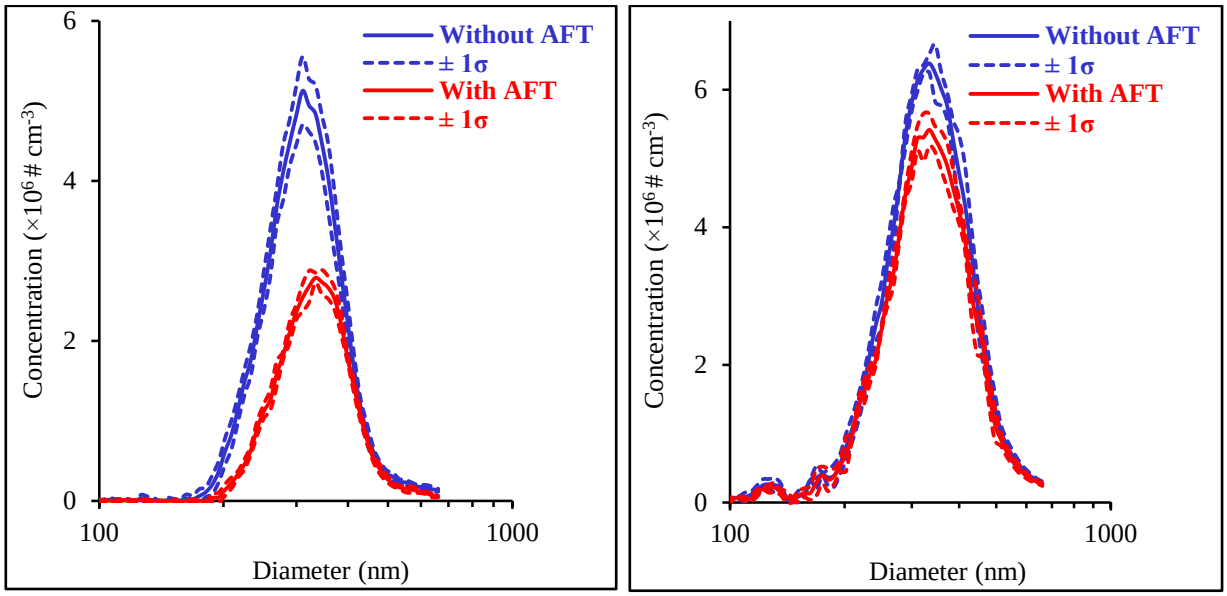

Figure 5. 7 Aerosol walls losses in AFT of a volume of: (a) 1.6 l and (b) 7.9 l.

The observed difference on particle losses between different AFT sizes can be attributed to the difference of the ratio of surface area to volume of the AFTs with more losses observed for higher ratio. It is also clear that larger difference in the number concentration is observed for smaller particles in smaller AFT, however, the losses of aerosol within a particular AFT and particles sizes was reasonably constant i.e. at approximately 45.0% and 15.0 % for AFT volume of 1.6 and 7.9 l, respectively.

5.3.2 Aerosol loss with time

To experimentally investigate the potential particle losses to the AFT walls and tubing in the ACA over the time, BES aerosol was generated by a conventional homogeneous nucleation method under the experimental conditions described above and was let to flow through the AFT for 2 hours. The size distribution of the particles was measured by the SMPS and the total particle number concentration was plotted as a function of time (Figure 5.8).

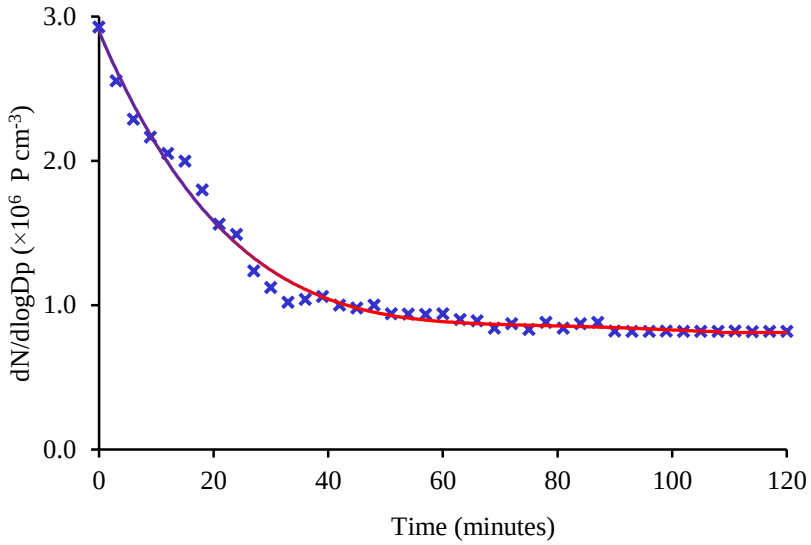

Figure 5. 8 Time dependence of BES aerosol concentration in the ACA system.

The Figure above suggests that the ACA system requires 90 minutes for particles concentration to settle in the ACA system. As a result data collected during the first 90 minutes were not considered in the analysis but were used to monitor particles stability in the system prior the start of the experiment.

5.3.3 Aerosol loss at humid condition

During periods of humid aerosol measurements, there is a uniform and constant reduction in the particles number concentration. Figure 5.9 exemplifies BES size distribution recorded at dry (RH 0.5±0.02%) and wet (RH 65.0±0.2%) conditions while keeping all other experimental conditions identical. The drop in the number concentration of particles at humid conditions can be linked to the effect of the enhanced wall losses at wetter condition (Han et al., 2011) or to the effect of water vapour in the CPC system (Hogrefe and Lala, 2001). Humid air can increase the tendency of particle deposition onto the AFT walls due to an increase in the viscosity of the moist air. Viscous moist boundary layer around particles leads

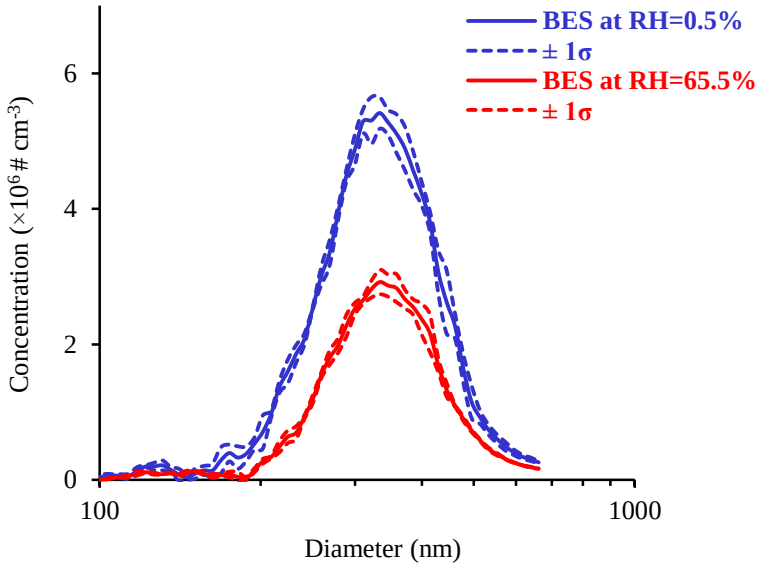

Figure 5. 9 Size distribution of BES aerosol at dry condition (RH=0.5±0.02%) and wet condition (RH=65.0±0.2%). The uncetainty in the measurements are expressed as ± 1σ.

to particles moving towards low velocity zones, i.e. AFT walls thereby increasing the deposition rate. On the other hand, considerable amount of water vapor may be absorbed by liquid butanol in the CPC reservoir and cause a decrease in the vapour pressure of the liquid butanol. This leads to lower supersaturation of the liquid vapour in the CPC saturator and hence particles will be undercounted. It is recommended as a standard operation procedure for the SMPS operated at extended periods of high humidity to drain the liquid butanol reservoir and refill it with fresh butanol as needed. Nevertheless the maximum controllable RH% was 65.0±0.2% in the ACA system, a constant reduction of 48±3% in the total number concentration of the particles was observed. To eliminate the contribution effect of the humidity to the heterogeneous reaction effect of the particles, wet oxidation measurements were carried out for processed and unprocessed particles under the exact humid conditions.

5.3.4 Aerosol loss due to UV light at 254 nm

The effect of the UV radiation at 254 nm inside the AFT on the organic aerosol was evaluated by exposing OL and BES aerosols to the UV radiation at dry condition. The UV lamp was turned 'off' and 'on', respectively, for measurements of unexposed and exposed aerosol UV radiation of 254 nm while all other parameters were kept unchanged. Figure 5.10 shows the results of the experiment.

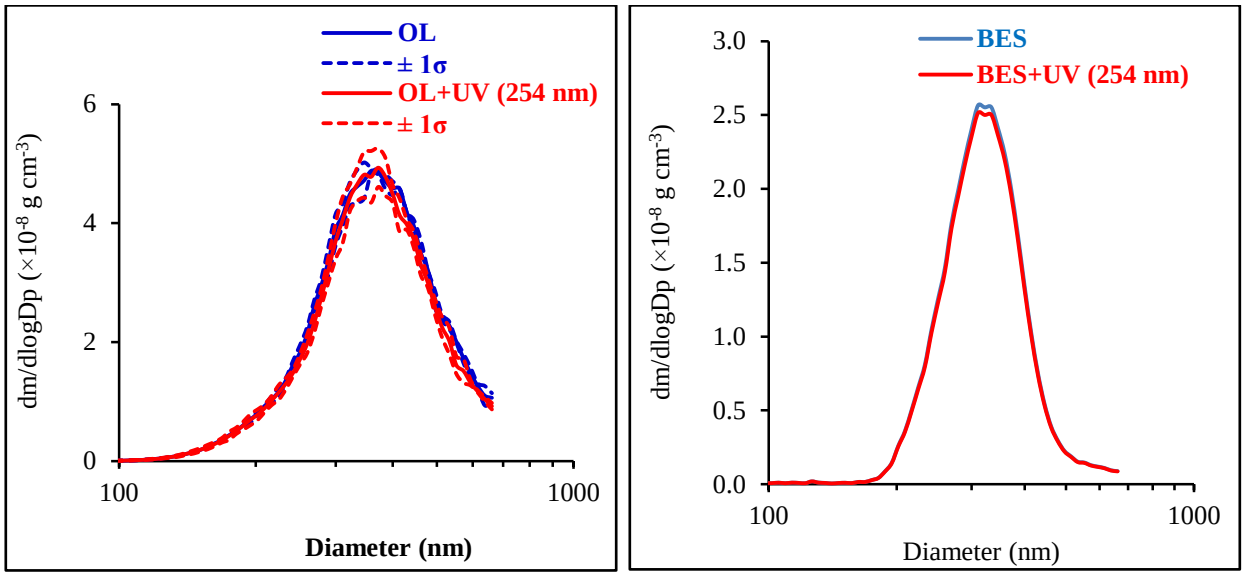

(a) (b)

Figure 5. 10 Effect of the UV radiation at 254 nm on dry: (a) OL and (b) BES aerosol. The uncetainty in the measurements are expressed as ± 1σ.

The effect of the UV radiation at 254 nm in the AFT is negligible for BES aerosol and relatively small (<5% mass loss) for OL as compared to the loss induced by the heterogeneous reaction (physical characterisation of aged particle is presented in chapter 6). Under the experimental conditions of this study (light flux at 254 nm is 2.9×10^{14} photons cm^{-2} s^{-1} (estimated as described in section 4.3.1), τ is 135 s and HO_x concentration range of $(8.0\pm0.4)\times10^{9}$ to $(1.2\pm0.6)\times10^{10}$ molecules cm^{-3}), it is unlikely for the UV radiation at 254 nm to photolyse the

components of pure organic aerosols (carboxylic acids and ester) or aged organic aerosols (carboxylic acids, aldehydes and esters) to a significant extent. In analogous study with similar oxidation condition to the current study, Ortega et al (2013) arrived to a similar conclusion. Additionally, the heterogeneous reaction by elevated OH concentrations are faster than the photolysis reaction of the compounds under the study so the dominant oxidation pathway is expected to be reaction with OH (Ortega et al., 2013).

5.4 Condensed versus gas phase reaction

The vapour pressure of an organic compound is a key parameter controlling its gas-particle partitioning equilibrium between the gas and condensed phases. This partitioning is an important source of the evolution of the SOA. To distinguish between SOA burden formed by reaction with the vapour around pure liquid droplets from reaction in the droplets and to account for the subsequent gas particle partitioning of the oxidation products from the vapour phase and thus possible particle growth, the fraction of the mass in the vapour phase that might contribute to the heterogeneous oxidation of the particles has to be estimated. What follows is the methodology used to estimate the input burden from the ozonolysis of OL vapour to that of the OL condensed phase in the studied ACA system.

5.4.1 Mass ratio of OL in the gas and condensed phases

For pure polydisperse liquid aerosol particles, the vapour pressure (P) around particles of different sizes is described on the basis of Kelvin equation to account for the curvature of the liquid droplets:

$$P = P^0 e^{\frac{2\gamma Vm}{R_p RT}}$$

Eq 5. 1

where P^0 is the actual vapour pressure on a flat surface of the liquid in Pascal and for pure OL liquid at 293.15 K, it is estimated using the segment contribution model developed by Bokis (Bokis et al., 1999) and found to be 4.41 x 10^{-5} Pa, γ is the surface tension of liquid OL, 0.000328 N cm^{-1}, (Chumpitaz et al., 1999), Vm is the molar volume (MW/density) of OL, 282.45 g mol^{-1}/0.891 g cm^{-3}=316.7 cm^3 mol^{-1}, R_p is the radius of OL particles in the polydisperse aerosol obtained from real SMPS data and R (8.314x 10^{+2} N cm K^{-1} $mole^{-1}$) is the universal gas constant. The mass fraction of OL present in the vapour phase of the polydispers aerosol was assumed to be equal to the mass in the vapour phase of the mode diameter particle and was calculated using the ideal gas law:

$$\frac{n}{v} = \frac{p}{RT}$$

Eq 5. 2

However, OL mass in the condensed phase was calculated using the radius of the particles, R_p, in each bin, the density of OL, and the number concentration of particles per cm^3 as the follows:

$$m_{OL} = \frac{4}{3}\pi {R_p}^3 \rho N$$

Eq 5. 3

where m_{OL} is the mass of OL in particles per bin size, ρ is the density of OL (0.891 g ml^{-1}), and N is the total number of OL particles per size bin obtained from the SMPS data. The total mass of pure OL aerosol per cm^3 in equilibrium with its vapour can be calculated by summing up all

masses in each size bin. Subsequently, the ratio of OL mass present in the gas phase to that in the condensed phase OL polydisperse aerosol can be inferred and was found under the experimental condition of this study to be 1×10^{-5}.

5.4.2 Reacted OL mass from the gas phase

The reacted mass of OL in the gas phase is calculated using the reaction rate law:

$$\frac{d[OL]}{dt} = -k[O_3][OL] = -k'[OL]$$

Eq 5. 4

where k is the rate constant, $1x10^{-16}$ cm^3 $molecule^{-1}$ s^{-1}, of an internal alkene (cis-5-decene) is used for the OL gas reaction with O_3 as the gas phase rate constant for OL and O_3 reaction has not been measured (Thornberry and Abbatt, 2004), [OL] is the initial concentration at t=0 s, $[O_3]$ in the vapor phase is calculated from above (Eq 5.2), and t is the reaction time in the AFT i.e. 147 s, measured experimentally from section 2.2.5.2

Integrating and rearranging equation Eq. 5.4 to solve for [OL]:

$$\ln[OL] = \ln[OL]_0 - k't$$

Eq 5. 5

$$[OL] = [OL]_0 e^{-(k't)}$$

Eq 5. 6

$$[OL]_{reacted} = [OL]_0 - [OL]$$

Eq 5. 7

Reacted OL mass in the vapour phase can be calculated from equation Eq. 5.7.

5.4.3 Upper limit of reacted OL mass in the gas phase

Assuming oxidation of gaseous OL shifts the equilibrium towards more evaporation; i.e. the rate of evaporation exceeds the rate of oxidation resulting to net evaporation:

$$OL_{(g)} + O_{3(g)} \longrightarrow \text{Products}$$

R 5. 1

$$OL_{(l)} \rightleftharpoons OL_{(g)}$$

R 5. 2

then integrating the left side of equation Eq 5.4 over the reaction time in the AFT (τ=147 s) gives the upper limit of reacted OL in the gas phase:

$$\Delta[OL] = -k[O_3][OL]\tau$$

Eq 5. 8

5.4.4 Reacted mass of OL in the condensed phase

Reacted OL mass in the condensed phase was calculated based on an assumption of surface reaction of ozone and OL particles which has been detailed in the theoretical study of the heterogeneous reaction between ozone and OL particles (Chapter 6, section 6.2.4). Figure 5.11 summarises the mass of OL present in condensed and gas phases of pure polydisperse OL aerosol and the estimated reacted masses of both phases after being exposed to ozone under the experimental condition of the ACA system. The result of this theoretical study shows that smaller OL droplets ($R_p \leq 10$ nm) have higher vapour pressure than the actual vapour pressure ($P > P^0$, equation Eq 5.1) and thus rapidly evaporate producing greater mass of OL in the vapour phase. However, the fraction of the particles that evaporate completely or with immense vapour pressure generally exist at the lower end of the size distribution and the fraction of such particles is modest. On the other hand, because particle phase reaction is much faster than gas phase reaction

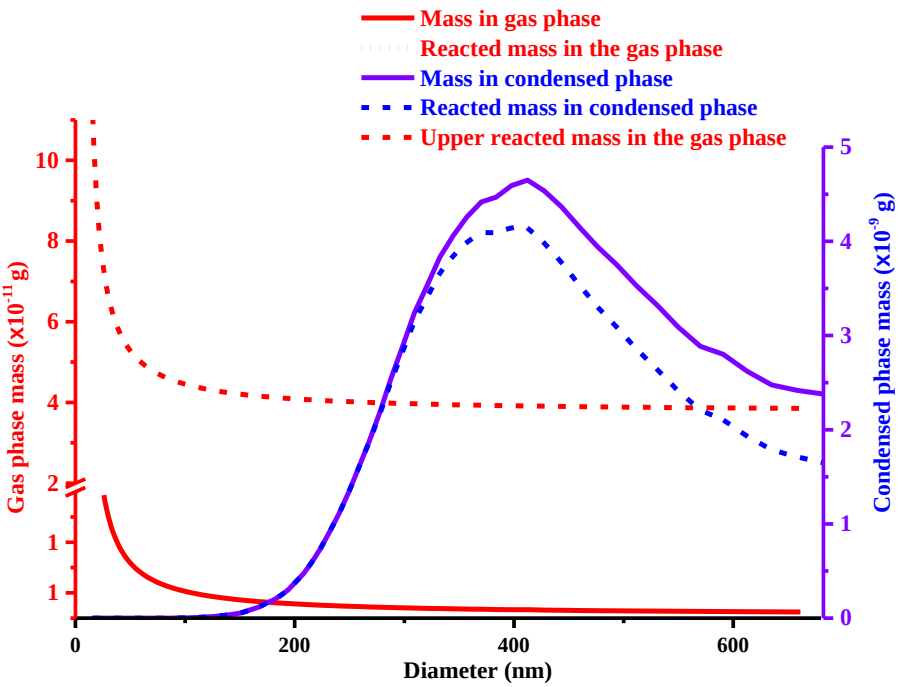

Figure 5. 11 Calculated OL mass present in the gas and condensed phases of pure polydisperse OL aerosol and estimated reacted masses of both phases after being exposed to ozone under the experimental condition of the ACA system.

the mass of reacted OL in the particle phase is more significant than that in the gas phase.

Based on the above estimations and for a pure polydisperse OL aerosol, OL mass is of ~5 orders of magnitude higher in the particle phase than in the gas phase. The mass contribution reacted from OL gas phase is less than that from condensed phase by ~5 orders of magnitude. However, the upper limit of reacted gas phase mass is less than that of the condensed phase by 4 orders of magnitude. It is concluded thus that reaction in the ACA system is taking place in the condensed phase and partitioning of the oxidation products from the vapour phase to the condensed phase is negligible.

5.5 Controlling relative humidity

The relative humidity RH (measured in %) is the ratio between the actual amount of water vapor present in air to the amount of water vapour present in air at saturation (Eq. 2.9). In the ACA system, two flows of dry air controlled by two MFCs were used to generate specific RH% values. The first of which was sent through two water bubblers to create a wet air flow and the second combined downstream the bubblers with the first flow before entering the AFT. The ratio of the two flows (wet:dry), the bubblers size and the temperature determine the output RH% of the atmosphere inside the AFT. Figure 5.12 illustrates the relationship between the resultant RH% and the wet to dry flows at measured ambient temperature. However, the final RH% depends on the overall flow of the AFT.

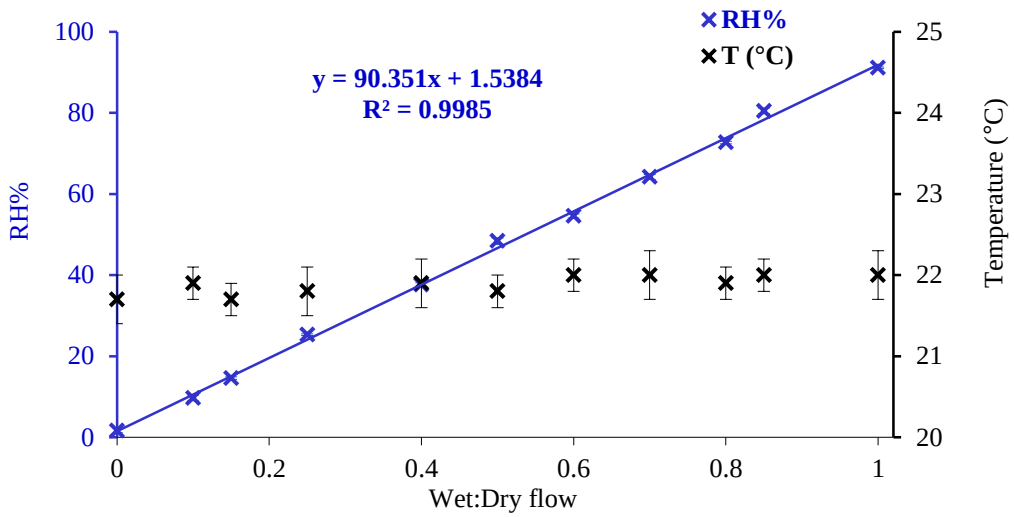

Figure 5. 12 Measured RH% as a function of wet:dry flow at ambient temperature.

This RH% generating methodology was capable to produce a range of RH from 0.5-92.0 (~±0.5)%.

5.6 Characterization of ozone production

As mentioned in section 2.2.6.2, oxidant ozone in the ACA is produced by photolysis reactions involving O_2, thus produced ozone concentration is mainly dependent on the oxygen concentration in the gas stream. For moderate levels of ozone (i.e. less than 25 ppm) meant to oxidize OL, a stream of synthetic air (21 % oxygen) was utilized as a feed gas in the ozone generator vessel. However, for effective ozone production (i.e. more than 100 ppm) meant to oxidize MA, a pure oxygen stream (%) was used as a feed gas instead. The flow to the ozone generator vessel was varied from 50 to 1000 sccm while keeping the total flow in the AFT constant at 3500 sccm. After irradiating the gas stream, loaded ozone was introduced to the AFT where it was further diluted and mixed with other flows (aerosol and dry or wet flow during the oxidation measurements). Whenever oxygen was used as a feed gas, nitrogen gas was added to the dilution flow in a portion such that the final air mixture in the AFT mimics the ambient atmosphere. Figure 5.13 compares ozone production from synthetic air and pure oxygen in the ACA system before being diluted in the AFT. The Figure indicates that under the same experimental condition in the ACA system, pure oxygen was ~4 times more effective in ozone production than synthetic air. It is apparent from the minor error bars within the resultant ozone mixing ratio in the two curves that high outputs of ozone levels in the ACA system was quite stable.

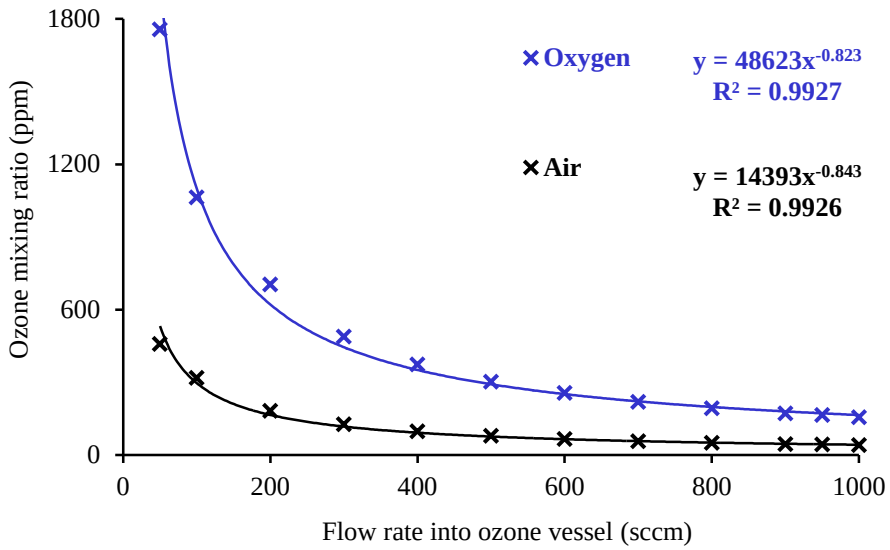

Figure 5. 13 A comparison between ozone production from photolysis of pure oxygen and synthetic air.

5.7 Summary

Optimum operating conditions of ACA system were established based on the characterization study of various parameters affecting the system. It was concluded that aerosol production via atomization gives high number concentrations of particles, but with lower monodispersivity, while aerosol generation by the vaporization-condensation method produces a lower number concentration of particles with quite uniform particle dispersivity. Optimum heating temperatures of the organic bubbler for generating OL and BES via vaporization-condensation method were 120 and 140 °C, respectively. Also better monodispersivity with highest number concentration and desired diameters of particles were generated at 200°C of the reheater temperature. The suitable flow proportionality through the organic bubbler was chosen as 0.5 while a volume of 5 cm^3 of the liquid organic was selected. It was found that heating organic liquid at elevated temperature can result in thermal decomposition of the organic compounds thus it was important

to carefully monitor the physical appearance of the compounds prior the experiment and to replace them with fresh liquid whenever a sign of physical changes was spotted.

The problem of the aerosol losses was identified experimentally, its effects in the ACA study were determined and the experimental procedure in the ACA system was adapted accordingly. Losses within the AFT was found to be reasonably constant, the ageing process system required 90 minutes for particles levels to settle in the ACA system and the effect of the humidity can be eliminated by taking measurements under the exact humid conditions. However, radiating OL or BES aerosol at 254 nm showed insignificant changes to the mass distribution of the particles.

Based on the theoretical study of the gas and condensed phases of OL particles under the study condition, reaction in the ACA system is taking place predominantly in the condensed phase and partitioning of the oxidation products from the vapour phase to the condensed phase was found to be negligible.

The ACA system was capable to produce a range of RH% from 0.5-92.0 (~±0.5) %. Ozone production from photolysis of pure oxygen was ~4 times more effective than synthetic air.

CHAPTER 6 CHEMICAL AND PHYSICAL CHARACTERIZATION OF AGED LABORATORY GENERATED ORGANIC AEROSOLS

6.1 Introduction

This chapter presents the laboratory characterisation of oxidised organic aerosols. Oxidation of organic aerosol has a strong effect on their physical and chemical properties which have significant implications in human health, atmospheric chemistry and climate (Hallquist, 2009; Ervens et al., 2011; Künzi et al., 2013). In light of this, the current study focuses on the heterogeneous reaction (HR) between oxidants (O_3 or OH), and three different single organic compound aerosol proxies: oleic acid (OL), maleic acid (MA) and bis(2-ethylhexyl) sebacate (BES). The results of four different systems are discussed: the oleic acid ozone HR system (OL-O_3 HR), oleic acid hydroxyl radical HR system (OL-OH HR), maleic acid ozone HR system (MA-O_3 HR) and bis(2-ethylhexyl) sebacate hydroxyl radical HR system (BES-OH HR). A large body of relevant theoretical and empirical literature on OL-O_3 HR system is available; the new results in this chapter are presented in the context of the existing literature.

During normal experimental operation, organic aerosol flow was mixed in the AFT, under dry or humidified conditions with and without oxidants. The flows are allowed to mix prior the direct sampling of aerosol from the AFT. If organic aerosol was mixed with ozone at elevated levels (≥20 ppm), oxidized particles with O_3 are measured, however, if organic aerosol mixed with ozone at ~ 100 ppb and irradiated with UV lamp at 254 nm, OH radicals are produced and oxidized particles with OH are measured, otherwise unreacted particles are measured at free oxidants conditions. In all cases, aerosol was sent to the SMPS and the ATOFMS for online measurement of unreacted and reacted particles.

For dry oxidation of solid MA particles, aqueous solution of MA was aerolised and the aerosol was dried before being oxidised and characterised by the SMPS and the ATOFMS. However, for wet oxidation experiment aqueous droplets of MA was directly oxidised and measured by the SMPS and the ATOFMS.

To physically study OL and BES aerosol, pure liquid single component of OL and BES droplets were generated by vaporisation-condensation approach, processed in the AFT and measured by the SMPS. The uncertainties in all measurement data are presented as dashed lined denoted as ± Error and correspond to 1 sigma (σ) uncertainty from the mean size distribution collected and averaged for 10 sampling scans of both reacted and unreacted particles.

For the chemical study, however, liquid OL and BES droplets were generated by nebulising their solution which was prepared in methanol contaminated with trace level of the laser dye nile blue sulphate (NBS), dried prior the oxidation in the AFT and measure by the ATOFMS (chapter 2, section 2.2.6.1, and chapter 3, section 3.6.3).

An additional oxidation experiment using methyl oleate (MOL) aerosol and ozone as an oxidant (MOL-O_3 HR) was performed to emphasis the cyclisation mechanism in the OL oxidation reaction products. Table 6.1 summarises the set of major experiments discussed in this chapter while a full description of the experimental set-up has been detailed in chapter 2.

Table 6. 1 The set of major experiments performed to study the chemical ageing of organic aerosol.

No.	Experiment	Experimental relative humidity	NBS addition (ATOFMS study)
1.	OL-O_3 HR	0.5 ± 0.02%	Yes
2.	OL-O_3 HR	65.0 ± 0.2%	Yes
3.	MOL-O_3 HR	0.5 ± 0.02%	Yes
4.	OL-OH HR	65.0 ± 0.2%	Yes
5.	MA-O_3 HR	10 ±1.0%	No
6.	MA-O_3 HR	92.5 ± 1.5 %	No
7.	BES-OH HR	65.0 ± 0.2%	Yes

6.2 OL-O_3 HR system

6.2.1 Physical characterisation of aged OL aerosol by O_3

The size distribution of both dry (RH=0.5 ± 0.02%) and wet (RH 65.0 ± 0.2%) gas-phase O_3 oxidation of OL particles are shown in Figure 6.1. The ozone concentration measured downstream the AFT was approximately 20±0.15 ppm and the measured reaction time was 147 s. The thick blue line marks the polydisperse particle size classified for unprocessed OL particles while results on the ozonolysis is shown in thick red line. Errors are shown in dashed lines in all cases.

In contrast to the observed particle growth on ozonolysis of OL particles in other studies (King et al., 2004), OL particles are clearly shrinking on oxidation resulting in a mode mobility diameter decrease from 400 to 346 nm and from 372 to 322 nm correspond to a total mass loss of 31.0 ±3.3%, and 26.3 ±2.5% at dry and wet conditions, respectively. This loss in particles mass on oxidation is reasonably consistent with the previously reported observations on the oxidation of OL particles (Morris et al., 2002; Katrib et al., 2004; Katrib et al., 2005b; Lee et al., 2012).

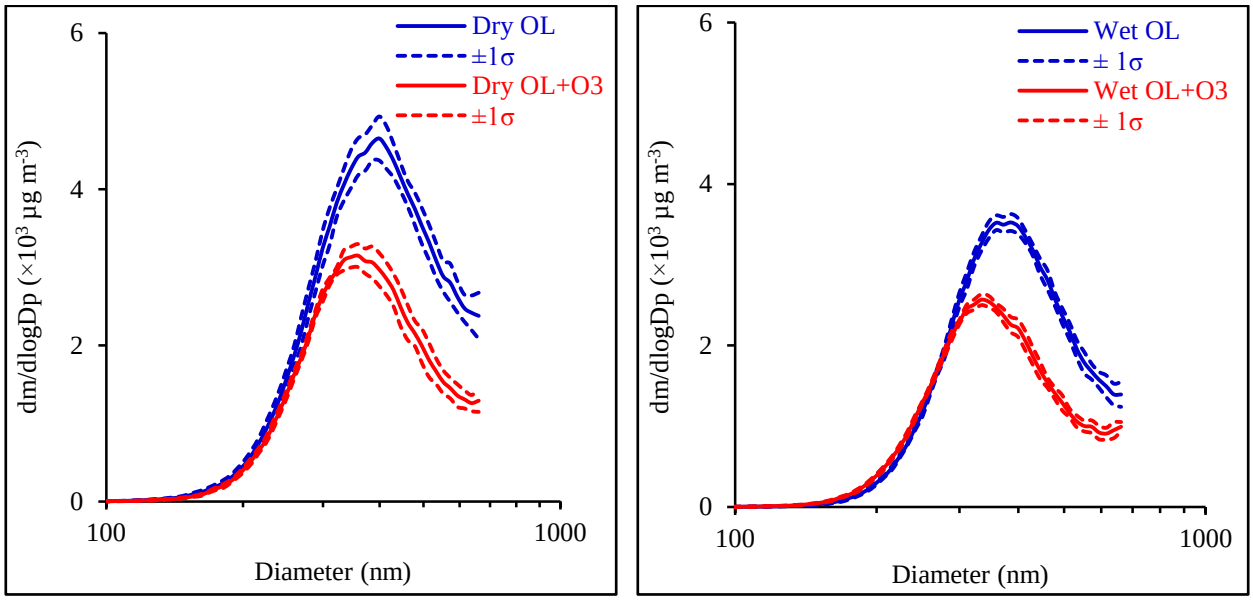

Figure 6. 1 Particle size distribution of 10 averaged samples for: (a) pure and oxidised OL aerosol at dry condition (RH 0.5 ± 0.02%) and (b) pure and oxidised OL aerosol at wet condition (RH 65.0 ± 0.2%). The apparent drop in aerosol number and size with humidity (left vs. right panels) and oxidation (with vs without O_3) is discussed further in section 5.3.3.

There are two likely reasons for the overall net decrease in the particles mobility diameter of aged particles. First, the formation of gas phase volatile products after undergoing oxidation such as the high vapour pressure nonanal, NN, (0.827 g cm^{-3}) (Rudich et al., 2007; Pfrang et al., 2011) and the semi volatile nonanoic acid, NA, (0.905 g cm^{-3}) (Ziemann, 2005; Zahardis and Petrucci, 2007; Vesna et al., 2009). Second, the formation of the condensed phase highly oxygenated products such as azeleic acid, AA, (1.225 g cm^{-3}) and 9-oxononoic acid, ON, (1.019 g cm^{-3}) which have low vapour pressure than that of the parent OL (0.891 g cm^{-3}) and are thus expected to remain in particle phase (Morris et al., 2002; Hearn and Smith, 2004; Katrib et al., 2004; Ziemann, 2005; Hung and Ariya, 2007). This will cause an average increase in the particle density.

Given that less mass loss was observed at humid condition than at dry condition by 6.2%, it is clear that wet oxidation has an effect on the oxidation mechanism. Such conclusion has been

reported in literature for similar oxidation conditions (Gallimore et al., 2011b). OL is essentially insoluble in water and even though some oxidation products are smaller and contain carboxylic acid groups they are also insoluble in water and cannot be hygroscopic at RH 65% as other investigators indicated the mild hygroscopicity of OL in their studies (Andrews and Larson, 1993; Pradeep Kumar et al., 2003; Vesna et al., 2008). Thus the observation of less mass loss at wetter oxidation might indicates that OL reactivity has been depressed in the presence of water. Studies of OL-O_3 HR have reported the involvement of water molecules in the reaction with CIs resulting in the formation of less volatile products and thus less mass losses from the particle (Hearn and Smith, 2004; Katrib et al., 2004; Hearn et al., 2005; Ziemann, 2005; Gallimore et al., 2011b).

6.2.2 Chemical characterisation of aged OL aerosol

Both positive and negative mass spectra were recorded for all detected particles with the positive ion mass spectra providing less chemical information of measured particles. Based on the predicted reaction pathways and experimentally observed mass spectra peaks, most observed oxidation products in aged particles contain carboxylic acid and/or aldehyde moieties which are principally detected in the negative ion mass spectrum as deprotonated molecular ions $[M-H]^-$ presumably formed via proton abstraction. Hence the great abundance of products peaks in the negative ion mass spectra.

6.2.2.1 Spectral analysis of the laser dye, NBS

Although reactions of the laser dye, NBS, with the reactants and products of the oxidation reaction is possible, at such low concentration ratio of [NBS]:[OL] equivalent to 1:500 it is unlikely that NBS alters the formation of the expected oxidation products to a significant extent. Therefore the effect of NBS reaction is assumed to be negligible. Indeed, no significant signals

were detected when NBS particles alone were exposed to ozone (Figure 6.2). Additionally, when OL was added to NBS solution in the absence of O_3, only the deprotonated OL mass signals were observed until ozone was added.

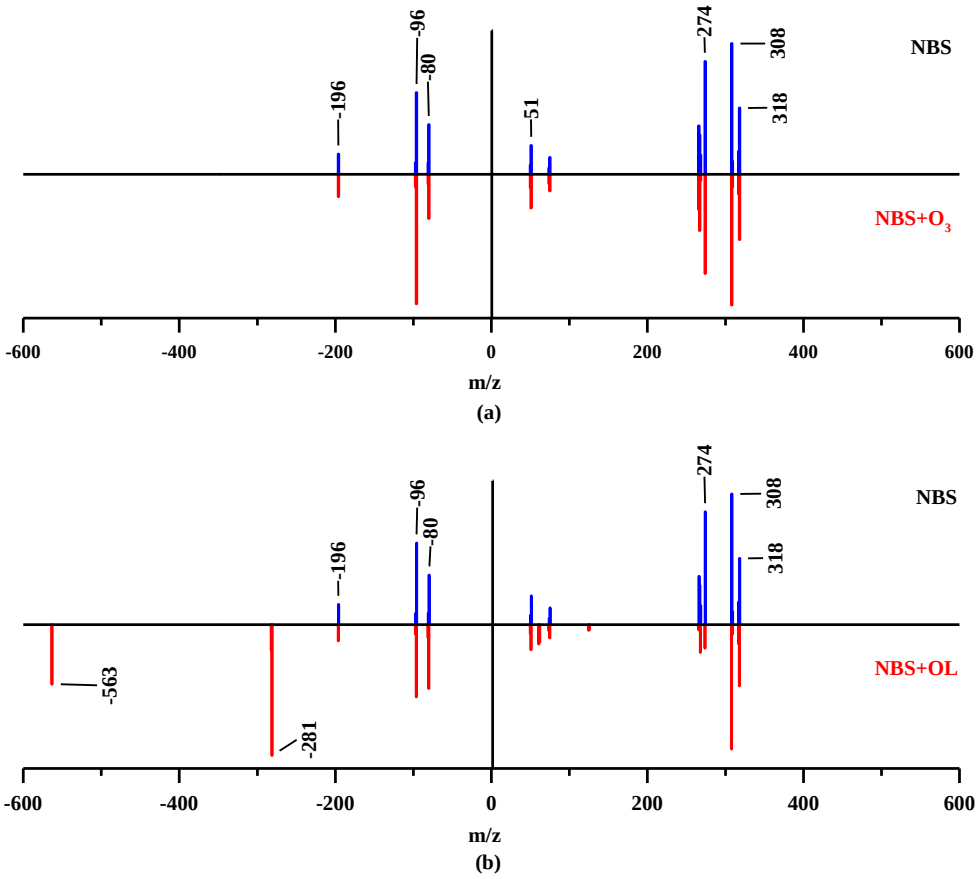

Figure 6. 2 Average of 100 positive and negative mass spectra of: (a) NBS and NBS exposed to O_3 and (b) NBS and OL in NBS solution.

NBS displays three strong signals in the positive spectrum at m/z +274 and +308 assigned for the dye cation fragments and +318 assigned for the unfragmanted cation of the dye. The two strong signals in the negative spectra at m/z -96 and -80 correspond, respectively, to sulphate (SO_4^{2-}) and sulphite (SO_3^{2-}) ions of the dye. It should be noted that NBS peaks were observed in all mass spectra and were not found to interfere with the reaction products peaks. However, for

the ease of the analysis, all NBS peaks are omitted from the analysed mass spectra. Appendix B, Figure B-2, illustrates the structure and the characteristic absorption spectrum of laser day NBS.

6.2.2.2 Spectral analysis of the standards

Peak identification of mass spectra required careful interpretation of observed peaks, the use of mass spectral libraries and results from previous studies. Peak from OL and its major reaction products, AA, NN and NA, were identified through comparison with mass spectra of aerosol generated from single component mixed with traces of NBS. Unfortunately, 9-oxononanoic acid (ON) was not commercially available and a similar structured compound, 4-oxononanoic acid (4-ON), was used to provide information on characteristic and expected ion peaks obtained from ATOFMS. Figure 6.3 depicts typical individual averaged positive and negative mass spectra of individual standards. Unreacted OL aerosol (M 282 Da) was seen as a deprotonated OL molecular ion at m/z = -281 and as a singly deprotonated dimer at m/z -563. The deprotonated molecular ions of AA (M 188 Da), NA (M 158 Da), NN (M 142 Da) and 4-ON (M 172 Da) major peaks were observed at m/z -187, -157, -141 and -171 respectively, while the singly deprotonated dimers of AA and NA were measured at m/z -375 and -315, respectively. In the positive ion mass spectra of AA a signal at m/z +155 was attributed to the fraction of the molecule after the loss of HO_2 fragment $[M\text{-}HO_2]^+$. However a molecular ion peak measured at m/z +113 in the NA positive ion mass spectra was assigned to the molecular fragment of NA after the loss of CO_2H, $[M\text{-}CO_2H]^+$.

It is important to note that the ATOFMS sensitivity depends on the molecular composition of different compounds in the particle (chapter 3, section 3.6.2). To investigate ATOFMS sensitivity, a solution containing a mixture of equimolar concentration of OL, AA, NA, NN and

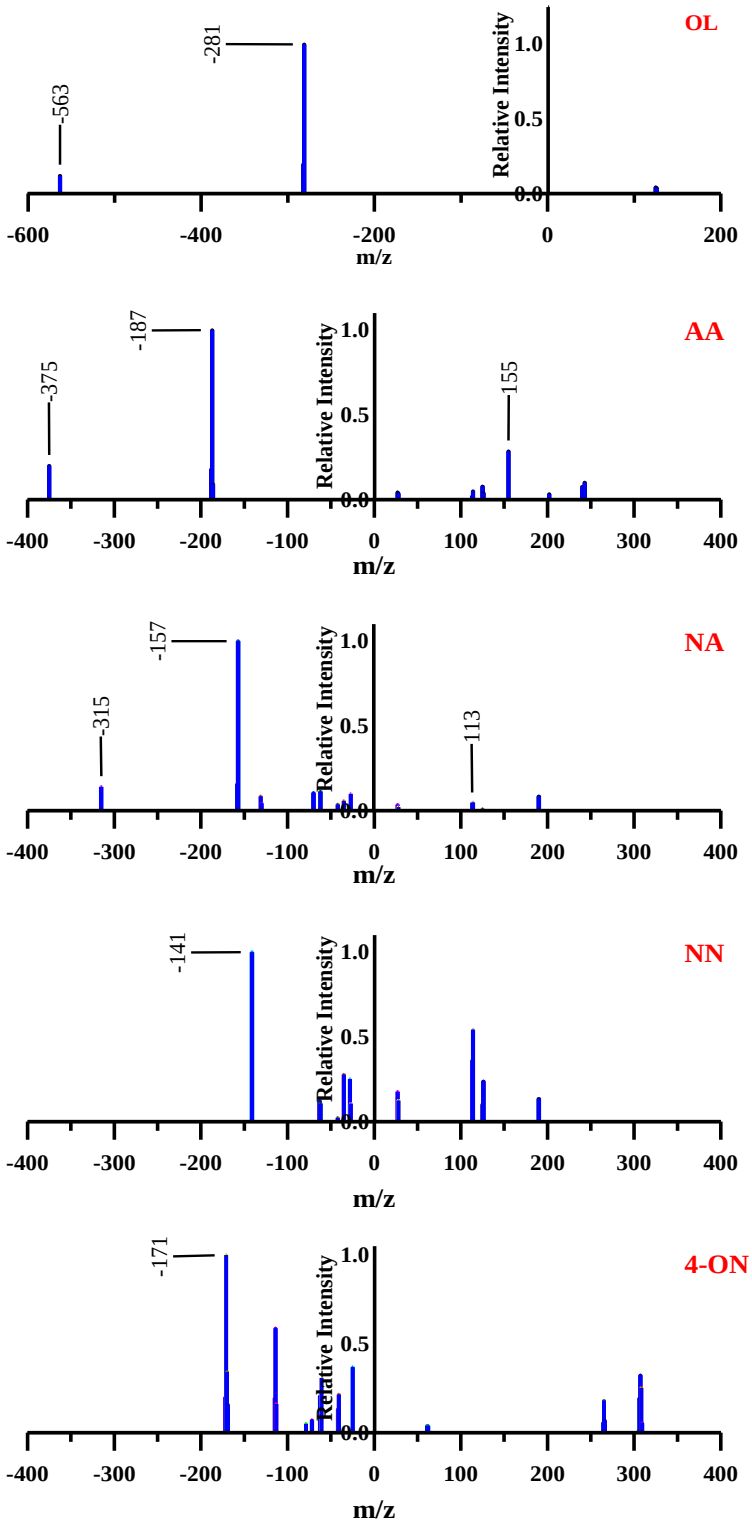

Figure 6. 3 Average of 100 positive and negative ion mass spectra of single particle component of OL, AA, NA, NN and 4-ON.

4-ON was examined under the same experimental conditions (section 2.2.7.2). It is assumed that the ATOFMS will have the same sensitivity to 4-ON as to ON. Figure 6.4 shows the results of the ATOFMS sensitivity for the compounds under investigation.

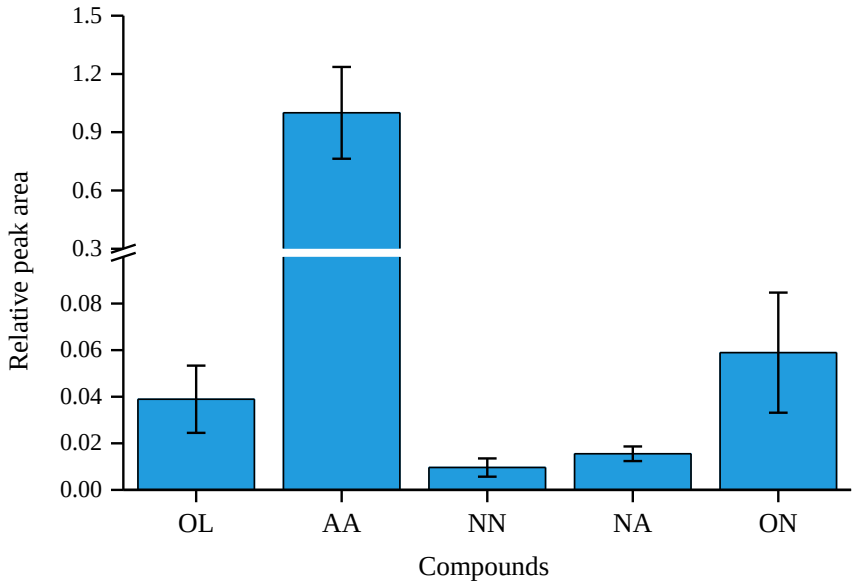

Figure 6. 4 Average of 200 negative ion mass spectra of aerosol containing a mixture component of OL, AA, NA, NN and 4-ON compounds.

Analysis of 200 mass spectra of the mixture reveals different efficiencies of ATOFMS sensitivity from which a sensitivity correction factor (SCF) can be obtained to compensate for this inconsistency. The result indicates that AA peak area (m/z -187) is about 95% as great as OL peak (m/z -281) or 4-ON (m/z -171) while both NN and NA produced relatively poor peak at m/z -141 and -157, respectively. Their peak area were only 1.0% and 1.5% that of AA. This observation indicates a combination of two factors, the volatility of both NN and NA as well as the limited sensitivity of the ATOFMS. Previous studies on NN detection using soft ionisation and ultra-high resolution mass spectrometry also showed weak NN peaks in the mass spectra.

The authors attributed their observation to the poor signal produced from aldehydes by the deployed techniques (Grimm et al., 2006; Hosny et al., 2013).

It should be noted that standard for the high molecular weight oxidation products are not available commercially and difficult to synthesise. Hence a calibration for signal:concentration for the mass spectra of aged OL particle was not possible.

6.2.2.3 Spectral analysis of aged OL particles

In this study, the chemically characterized aged particles by ATOFMS fall in the size range of ~0.2-2.1 µm. This is because ATOFMS has low detection efficiency of smaller size particles (chapter 3, section 3.6.2). On the other hand, the maximum greatest particle size produced by nebulisation approach was 2.1 µm. Nevertheless, spectroscopic analysis of ATOFMS data within this size range highlights two particle size bins with distinctly different chemical composition: small size particles (D_p<0.3 µm) characterised by the presence of lower molecular weight compounds than the parent OL molecules (m/z<282) and larger particles (D_p>0.3 µm) marking the enhanced formation of higher molecular weight (HMW) compounds (m/z>282). Given that the measured peaks combination was consistently observed at particle size larger than 0.3 µm, throughout this discussion particle size smaller than 0.3 µm are referred as small and particles above this size as large particles. What follows is peak identification of the oxidation products formed as a result of the OL-O_3 HR classified into large and small size bins.

Mechanisms and mass spectrometric analysis of small size particles

Chapter 1, section 1.8, detailed the mechanism of the OL-O_3 HR and (scheme 6.1) summarises the initial reaction steps in the OL-O_3 HR system.

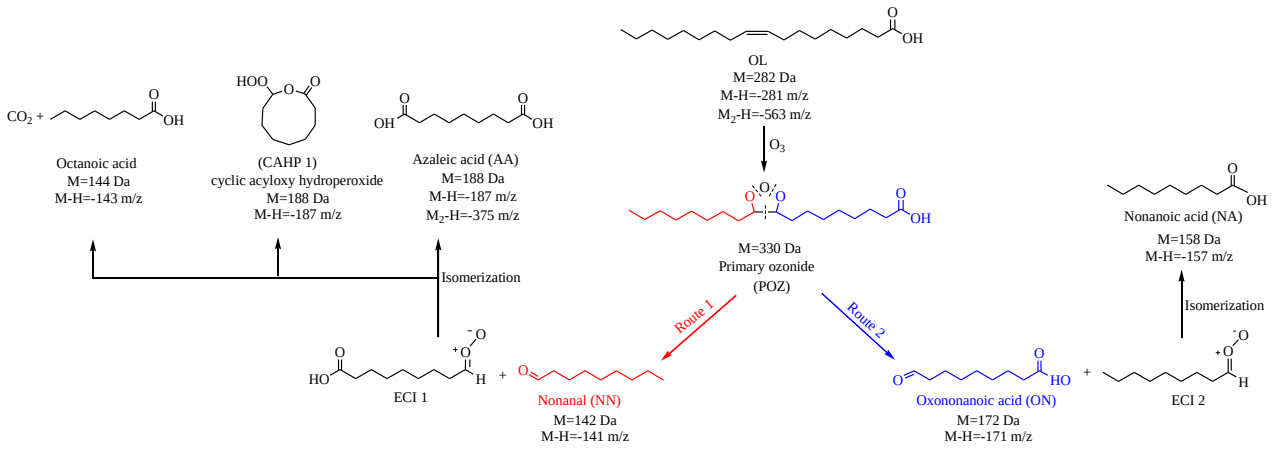

Scheme 6. 1 Initial steps and primary products of OL oxidation by O_3.

The analysis of mass spectra collected for 300 small reacted OL particles (Figure 6.5) was ideal for identifying 3 primary products of oxidised OL particles (AA, ON, and NA). Peaks at m/z=-143, -169, -219, -329, -439 were suggested for other primary and secondary ozonolysis products of OL. Signals measured at m/z -17 and m/z -45 can be indicate CO_2H^- and OH^- losses from oxidised products, respectively, Positive ion mass spectra provided little information in this size bin.

The detected signal at m/z -143 is proposed for octanoic acid (OcA) (M 144 Da) while the observed peak at m/z -169 is likely to be oxecane-2,10-dione (OD) (M 170 Da) which has not been reported previously in OL-O_3 HR. The proposed formation route of OD is the subsequent dehydration of CAHP 1 isomerised from ECI1:

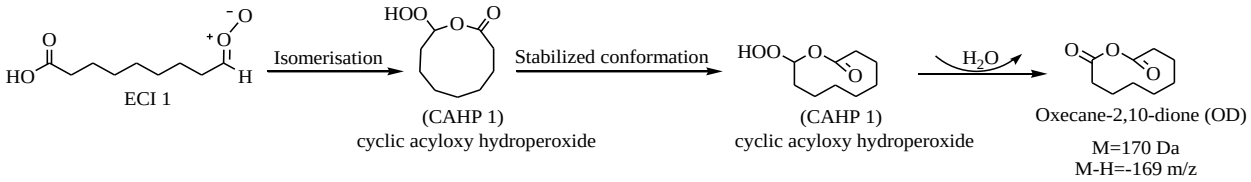

R 6. 1

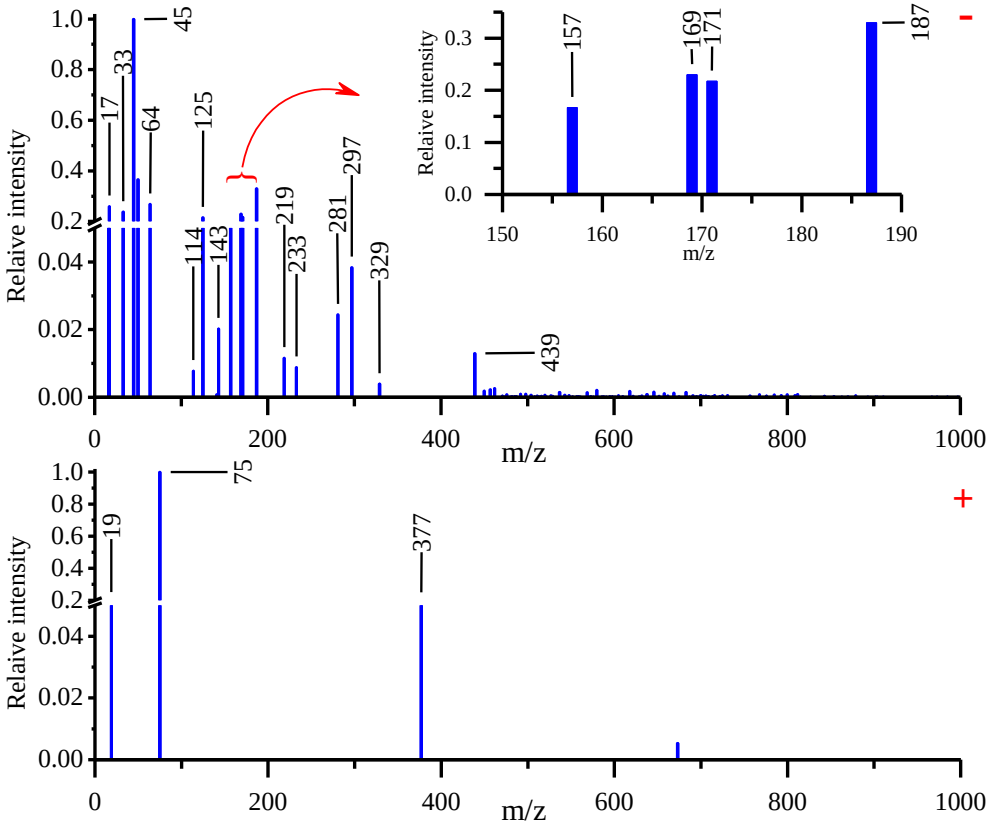

Figure 6. 5 Averaged ATOFMS negative and positive ion mass spectra of small processed OL particles (Dp<0.3 μm).

Unfortunately, the compound OD was not commercially available and no surrogate compound was found from suppliers and very little information are available for this compound. To emphasis the formation of OD via the suggested approach described above, methyl oleate (MOL) aerosol was subjected to the ozonolysis process under exactly the same oxidation conditions of reactants concentration, residence time, temperature and relative humidity established for OL oxidation. MOL is the analogue ester to OL which lacks an acidic hydrogen and therefore the initially formed CI is not expected to easily rearrange to a cyclic product as in the case of its counterpart in OL oxidation. The ATOFMS spectrometric analysis of MOL showed that MOL follows parallel primary and secondary reaction paths to that of OL ozonolysis

as it has been reported in literature (Hearn et al., 2005). Scheme 6.2 shows the initial reaction ozonolysis steps of MOL while the averaged mass spectra of aged MOL are presented in Appendix B, Figure B-10.

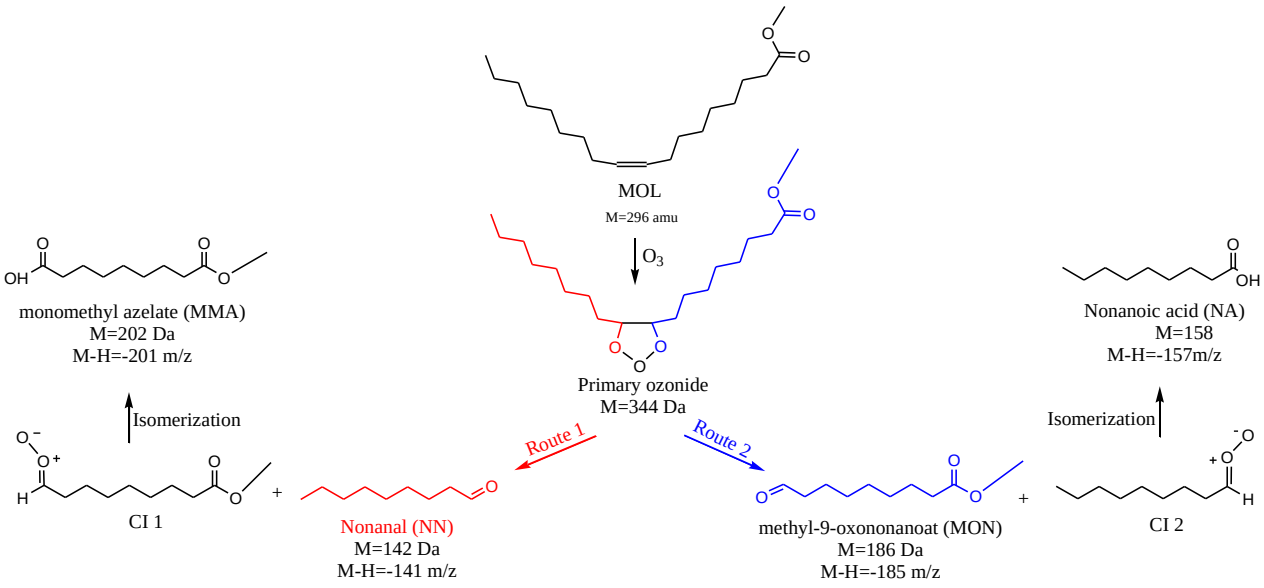

Scheme 6. 2 Initial steps and primary products of MOL oxidation by O_3.

While AA was observed exclusively from OL oxidation, monomethyl azelate (MMA) was found to be the main oxidation product of MOL in addition to NN, NA and methyl-9-oxononanoat (MON).

As expected, no peak was observed at m/z=-169 in the processed MOL spectra. It is apparent that the presence of carboxylic acid moiety in CI1 formed in the case of OL-O_3 HR is responsible for the cyclisation process and appears to be difficult in the case of CI1 product formed from MOL ozonolysis. This implies also more stabilization pathways for CI1 in the case of OL oxidation and thus wider range of primary and secondary products which can enhances particle mass losses. The study of the reactive uptake coefficients (γ) of OL and MOL by Hearn

et al (2005) suggested that the carboxylic acid moiety in oleic acid accounted for 36% of OL losses. Indeed HMW compounds observed in aged MOL oxidation was far less than those detected in aged OL particles.

The other observed peaks of processed OL particles at m/z= -329, and -439, can be suggested, respectively, to be the POZ (scheme 6.1) and secondary reaction product of CI2 with OL (reaction R 6.2).

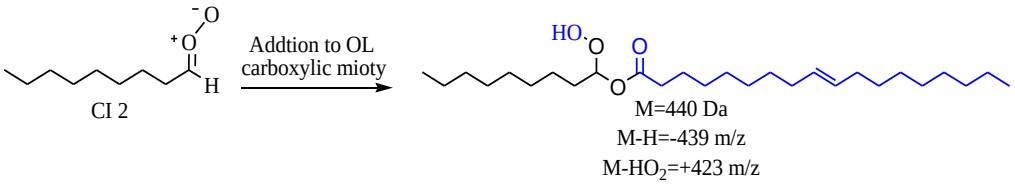

R 6. 2

Mechanisms and mass spectrometric analysis of large size particles

The three frames, a, b, and c, in Figure 6.6 show averaged negative and positive ion mass spectra of 700 bulky aged OL particles. The averaged negative ion mass spectrum observed for aged OL particles at an aerodynamic diameter above 0.3 µm is more complex but compatible with the hypothesis of secondary chemistry and the formation of HMW products. Generally, the spectrum demonstrates a strong peak of unreacted parent OL at m/z -281 and the appearance of the major oxidation products upon ozone exposure. All four primary products are found to be in the particle phase including volatile NN which was not detected in smaller size particles. In contrary, the signal of OcA and OD which are formed through the molecular rearrangement of CI1, were not detected in greater particles which might reveal that isomerization is predominant in smaller particles and that it is the only formation source for these products. Both negative and positive averaged mass spectra are characterized by the presence of HMW products presumably formed

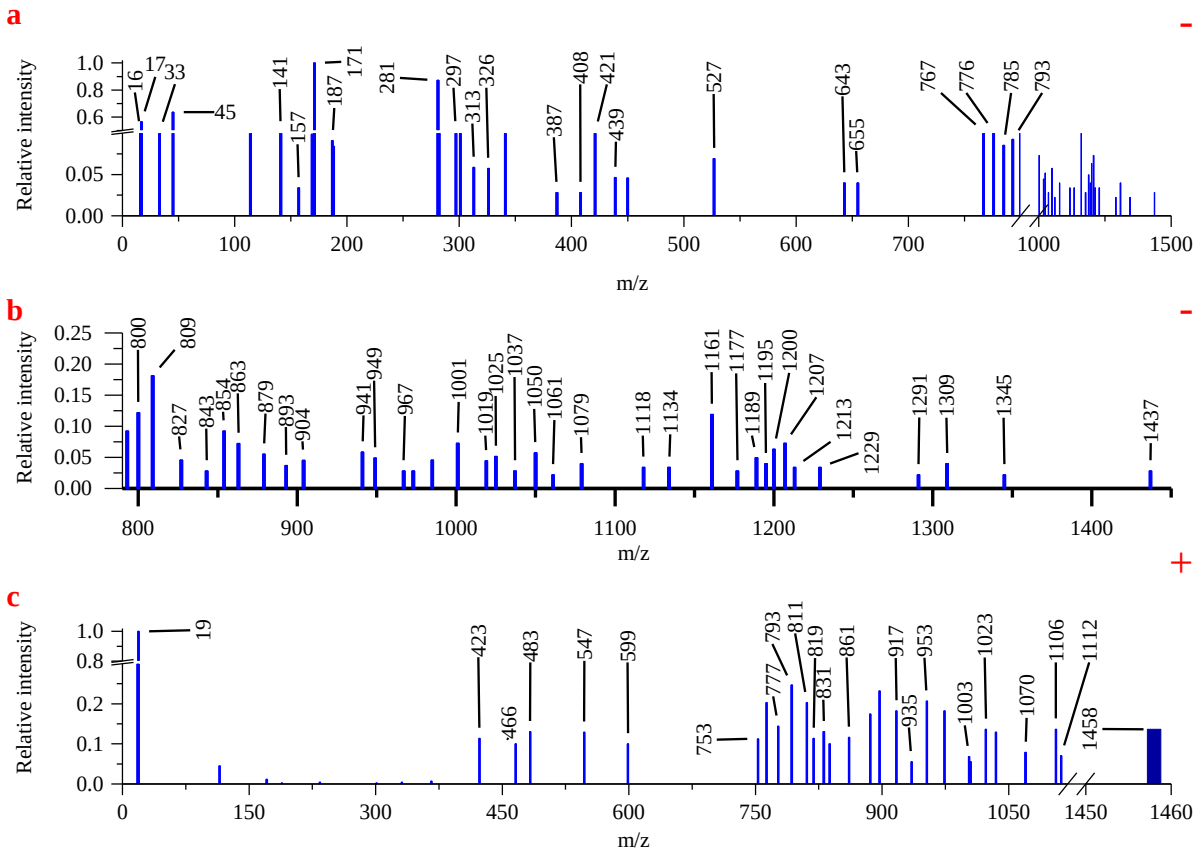

Figure 6. 6 Averaged mass spectra of dry aged OL particles (Dp>0.3 µm): (a) negative ion MS (b) zoom in plot of Figure (a) and (c) positive ion MS.

by polymerization propagators via secondary reactions. Studies have evidenced reportedly the secondary chemistry of OL-O_3 HR (Katrib et al., 2004; Hearn et al., 2005; Ziemann, 2005; Reynolds et al., 2006; Zahardis et al., 2006; Zahardis and Petrucci, 2007; Lee et al., 2012; Hosny et al., 2013). Secondary chemistry arises primarily from the reactivity of CIs which leads to numerous association reactions of CIs including self-reactions, reaction with CIs respective carbonyl compounds, reaction with solvents, carboxylic moiety and alkene functionality. The presence of CIs in the liquid condensed phase minimizes their molecular rearrangement (Katrib et al., 2004) via solvent cage effect (Park et al., 2006) and maximizes their lifetimes. Therefore,

reaction probability of CIs with their corresponding carbonyl compounds to form secondary ozonide (SOZ) or with the alkene functionality become more significant (Neeb et al., 1998; Moise and Rudich, 2002; Zahardis et al., 2005). Hung et al (2005) identified ON and CI1 as polymerization propagators, CI2 as a polymerization terminator and NN as a released product which has never been associated in the formation of HMW products.

In this study, the observed polymerization propagators are the CIs, the primary product AA, NA, ON, the secondary products 9-oxooctadecanoic acid (Ox1) and 10-oxooctadecanoic acid (Ox2) and 9-oxooctadecanedioic acid (Ox3), which will be discussed below.

The molecular structures of the observed HMW signals were assigned based on polymerization mechanisms proposed in literature for related OL-O_3 HR studies (Smith et al., 2002b; Hearn and Smith, 2004; Katrib et al., 2004; Hung et al., 2005; Zahardis et al., 2005; Reynolds et al., 2006; Zahardis et al., 2006; Hung and Ariya, 2007; Zahardis and Petrucci, 2007). For instance, peak at m/z -297 can be assigned for two isomer forms of oxooctadecanoic acid depending on the type of the CI and the side the CI added across the double bond of OL to form a C_{27} peroxides which can cleave to yield the primary products ON or NN. Similarly, the detected signal at m/z -327 is determined as a reaction product between OL double bond and the CI1, exclusively, as CI2 does not contain a carboxylic moiety. Scheme 6.3 illustrates proposed mechanism and products structures formed as a result of the reaction between CI1 and the alkene functionality of OL.

The presence of peaks correspond to Ox1 or 2 in the OL-O_3 HR has been reported previously (Hearn and Smith, 2004; Zahardis et al., 2006; Hung and Ariya, 2007) while the reaction mechanism and products structures were first hypothesized by Katrib and co-workers

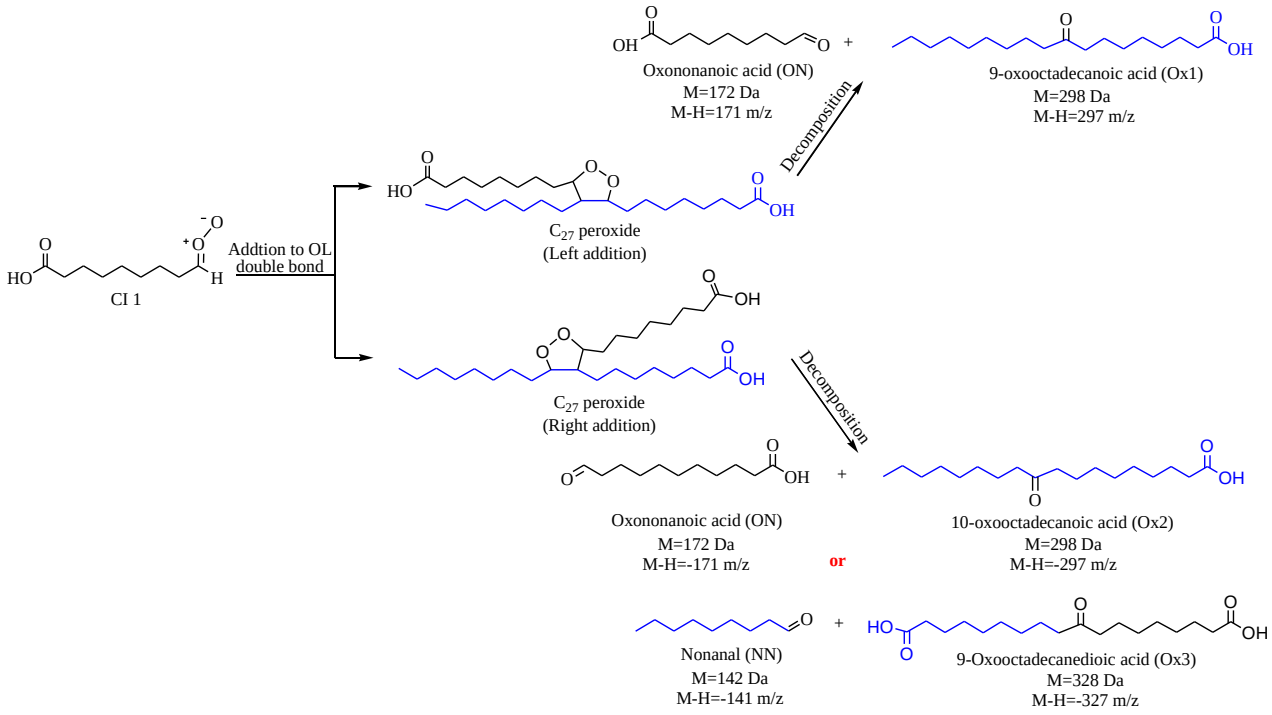

Scheme 6. 3 A proposed scheme illustrates mechanism and products structures formed as a result of the reaction between CI1 and the alkene functionality of OL.

(2004). The spectroscopic analysis of this study shows considerable correlation with products Ox1, 2, and 3 in a number of suggested HMW products. This is explained by the existence of the carboxylic acid functionality which offers coupling sites with other CIs. The measured negative ion peaks at m/z -1019, -1189, and -1207 provide more evidence of the incorporation of OX1 or 2 as linear polymerization propagators. However, the ion peak measured at m/z -644 is consistent with the formation of the ozonolysis product resulted from the reaction of two ions of CI1 and the two carboxylic moiety of one molecule of Ox3, scheme 6.4 proposes a possible arrangement.

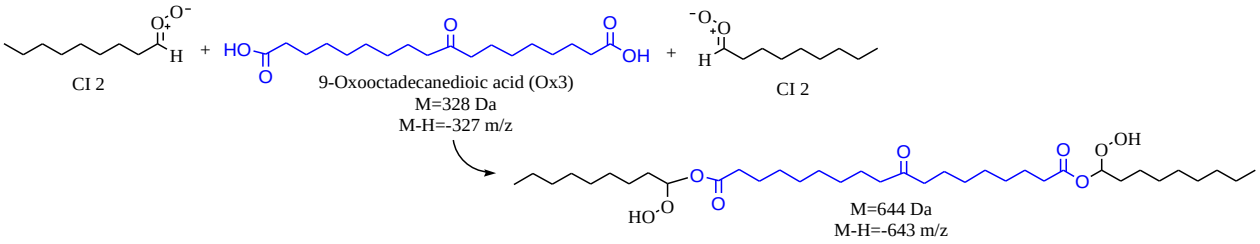

Scheme 6. 4 Proposed arrangement for the observed peak at m/z -643.

The addition of CI2 terminates the polymerization reaction as the $-CH_3$ group cannot react further (Hung et al., 2005). The major HMW products ions at m/z -1025, -1079, -1214, -1292, -1310, -1346, -1438, and -1524 may also correspond to polymerization products of Ox3 joined with other propagators. Table D-1, appendix D, proposes possible combinations of these reaction propagators for most observed peaks.

The ion peak appear at m/z -313 is possibly due to the formation of AAHP produced by the reaction of CI1 and OcA which is the only observed secondary product associated with OcA:

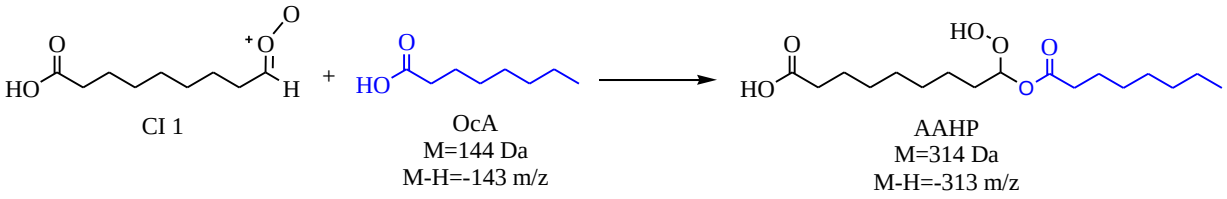

R 6. 3

Products relate to the secondary reaction of ON are also observed in a number of peaks. The negative ion at m/z -341 is most likely due to the combination of ON and CI1 to form AAHP with a loss of one molecule of water. Although the same combination can lead to the formation of SOZ, in such arrangement a water molecule cannot be removed. The in situ dehydration of AAHP in the OL-O_3 HR was first observed and described by Zahardis and coworkers (2006). The resultant proposed structure suggests possible additional moieties linking from molecules

ends, the aldehyde and carboxylic acid groups, thereby growing into a HMW linear polymer, scheme 6.5 explains.

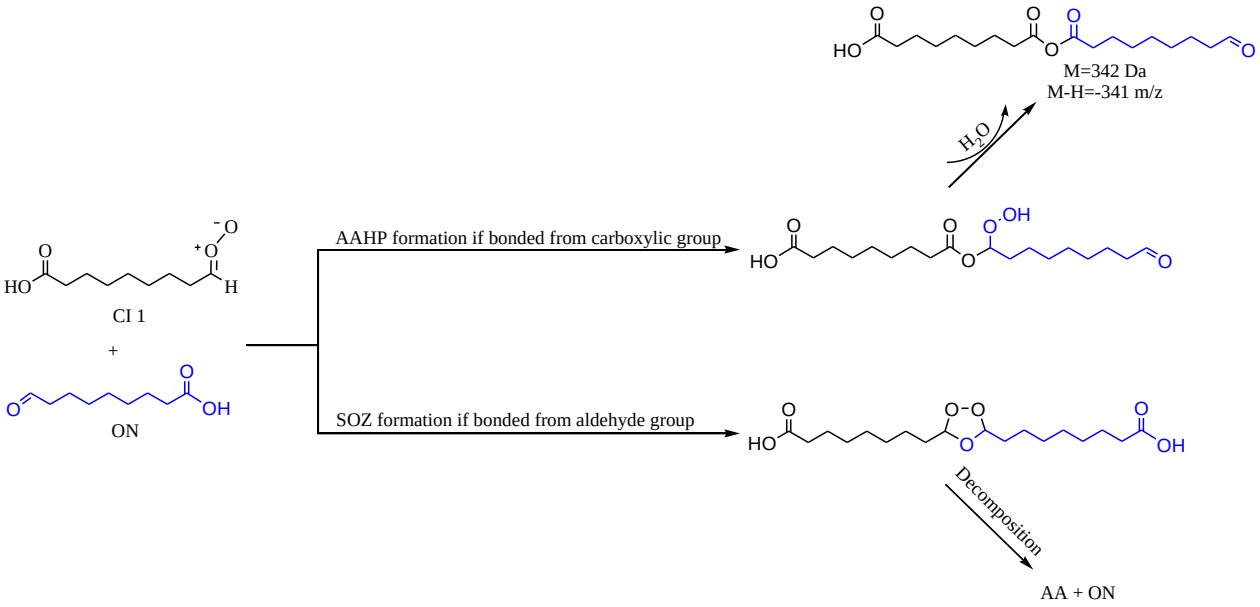

Scheme 6. 5 Suggested reaction pathways and products of the secondary reaction between CI1 and ON.

The reaction product between CI2 and the carboxylic moiety of OL was also detected at m/z -439 and at m/z +423 due to a proton OH group losses, respectively. This product is also determined as AAHP (R 6.4) but with alkene functionality. Dehydration or/and cycloaddition of O_3 or CIs to the double bond are further expected reaction pathways for this product.

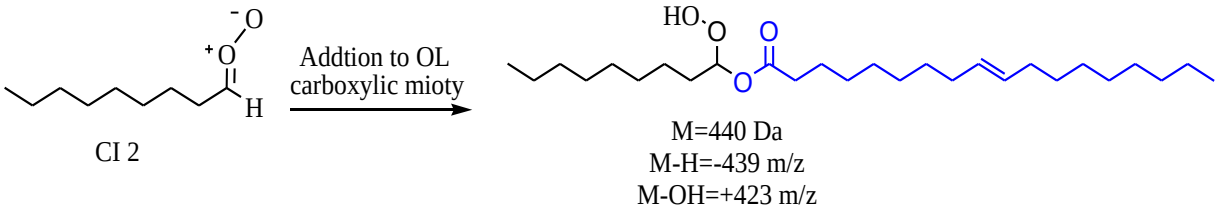

R 6. 4

The product ion observed at m/z -527 is expected to be formed from the reaction between AA molecule and two molecules of CI1 to form AAHP intermediate with a subsequent loss of two water molecules to form polyanhydride. Positive ion peaks at m/z +483 and +466 correspond

to $[M\text{-}CO_2H]^+$ and $[M\text{-}(CO_2H)\text{-}(OH)]^+$ further support the proposed structure. Prominent signals measured at m/z -17 and m/z -45 can be taken also as an indication of the CO_2H^- and OH^- losses from oxidised products, respectively, which also reflects the efficient oxidation environment of OL aged particles. The presence of two terminal carboxylic acid groups in the proposed product can lead to a possible chain growth by linking additional CIs. Scheme 6.6 shows the suggested pathway.

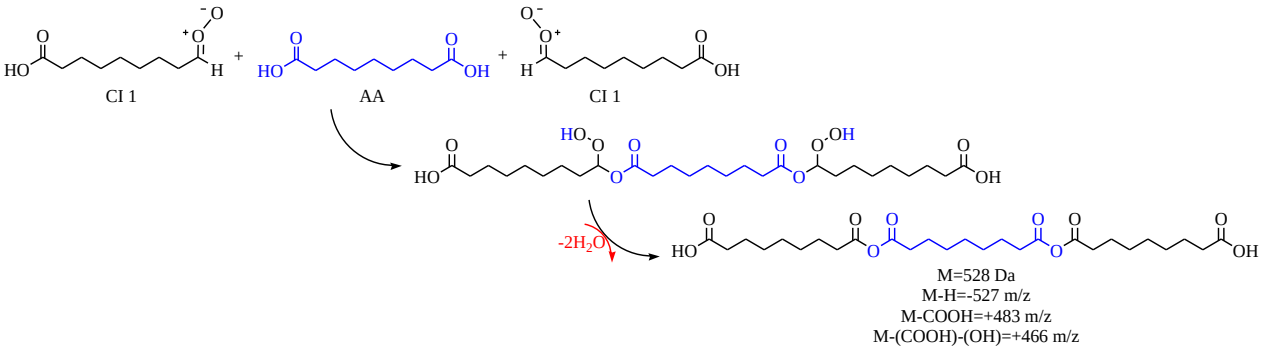

Scheme 6. 6 Proposed reactants combination, reaction mechanism and products for the observed peaks at m/z -527, +466 and +483.

Appendix D, Table D-1, provides a summary of possible components and propagators combinations of observed negative and positive peaks, while scheme 6.7 proposes possible primary and secondary pathways and products of OL-O_3 HR categorised by particle size with detailed secondary chemistry of CI1 as it was found to be the predominant primary product in small particles and the main component unit in HMW compounds observed consistently in bulkier particles.

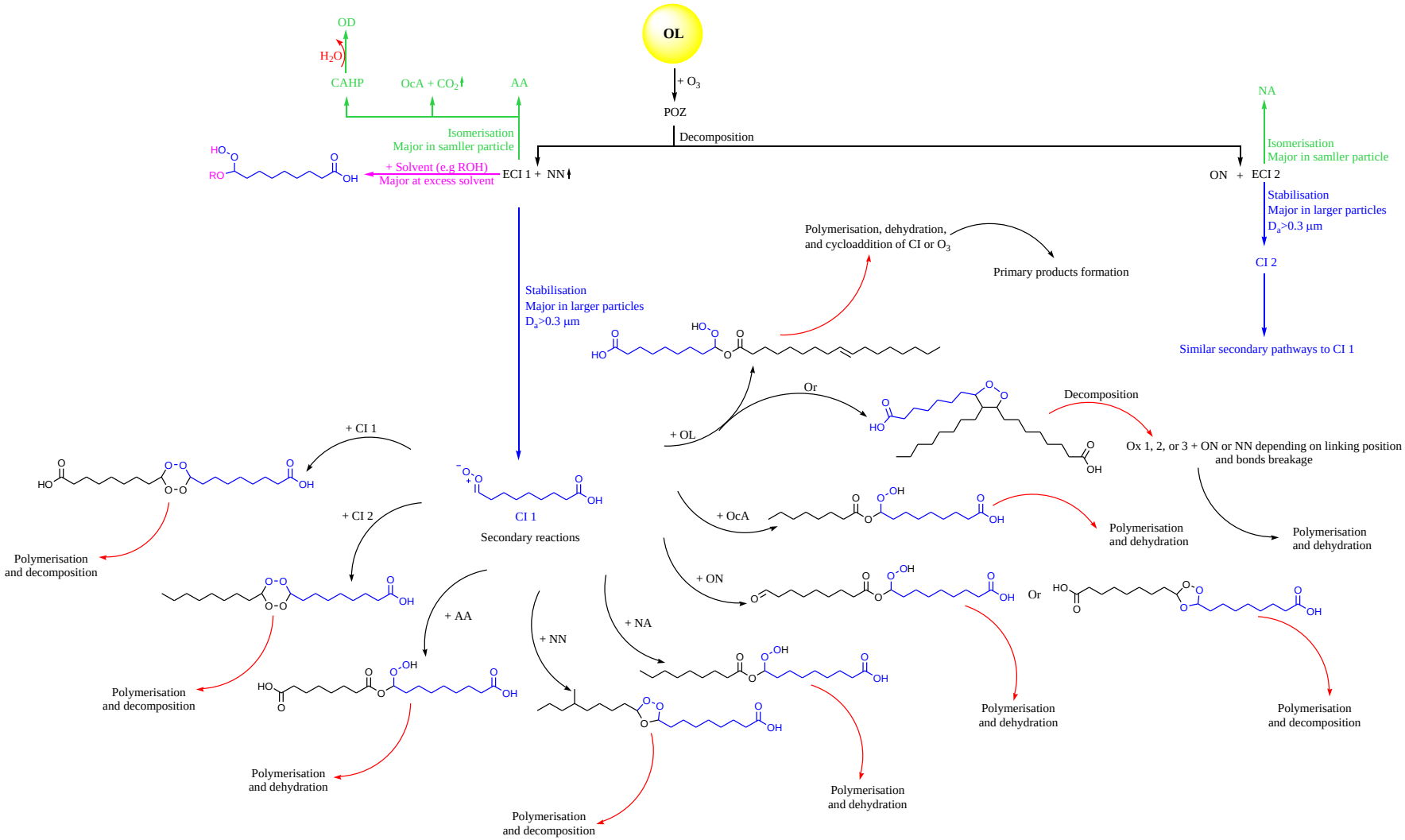

Scheme 6. 7 A summary proposed for primary and secondary pathways and products of OL-O_3 HR categorised by particle size with detailed secondary chemistry of CI1 as AA was found to be the predominant primary product in small particles and the main component unit in the HMW compounds observed consistently in bulkier particles.

6.2.3 Particle composition as a function of particle size

The feasibility of the ATOFMS as a semi-quantifiable approach to study the particle components distribution over the size range of particles has been discussed in chapter 3, section 3.6.3. The selected compounds for this analysis; OL, NN, AA, ON, NA and HMW compounds, were classified using the MS-Analyse and Microsoft Access.

6.2.3.1 Particle composition of aged OL particle at dry condition

Figure 6.7 shows the chemical composition of 1000 aged OL particles processed at dry condition, RH 0.5 ± 0.02%, classified into narrower size bins (a). The overall composition of the aged OL polydisperse aerosol (b) and the corresponding size distribution (c) is also shown in the same

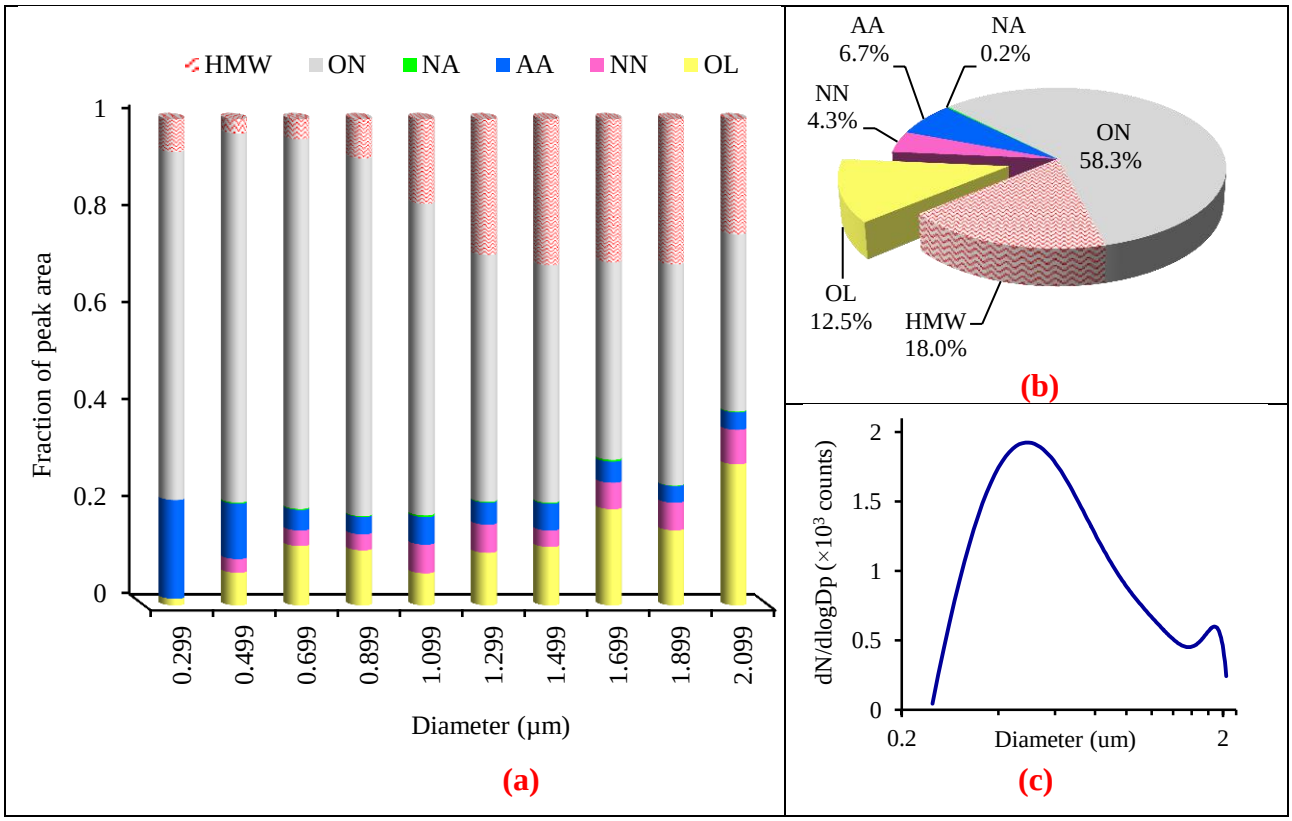

Figure 6. 7 ATOFMS data analysis of: (a) peak area signals for the components of dry (RH 0.5±0.02%) as a function of particle size, (b) total components fraction, and (c) corresponding size distribution, in the aged OL polydisperse aerosol.

figure. This figure neglects uncertainties in both the measured peak area, and the conversion from ATOFMS signal to mass concentration, for clarity of presentation. In reality, there will be an uncertainty (precision) associated with the analysis of the ATOFMS data to obtain the peak area values (Panel 6.7a), and in application of the calibration factors to derive fractional composition (as presented in Panel 6.7b). As outlined in Section 6.2.2.2 the latter were found to be modest (values in Table 6.2), with the possible exception of 9-oxononanoic, for which no commercial standard was available and 4-oxononanoic acid was used as a surrogate. Uncertainties in these calibrations could affect the extent of the trends in aerosol composition discussed below, but not their overall presence or absence. Due to the variability of the ATOFMS sensitivity as indicated in chapter 3 (section 3.6.2 and section 3.6.3) and evident in this chapter (section 6.2.2.2), the measured SCF of the compounds (from section 6.2.2.2) were adapted to compensate for the ATOFMS differing sensitivities. Since accurate SCF for the HMW was difficult to measure, an upper limit value was estimated based on the molar ratio of the reacted OL and the produced primary oxidation products. That is, the ratio between the signal of OL and the total signals of the four primary oxidation products (AA, NN, NA and ON) was used to estimate the molar ratio between unreacted OL and the products (1 mole of OL produces 2 moles of the primary products (see scheme 6.1 and table 6.2) and hence the SCF for the HMW products was estimated. The result of applying the SCF to the measured data in Figure 6.7 is shown in Figure 6.8. The magnitude of the uncertainty ($\pm 1\sigma$) was estimated from the measured uncertainty values of the SCF (Figure 6.4) and is presented in Table 6.2.

Figure 6.8 indicates a definitive difference in the chemical composition of particles according to their size. The finest particle size found to contain less unreacted OL than larger particles. The appreciable OL signal in larger size bins reveals incomplete oxidation of OL. OL

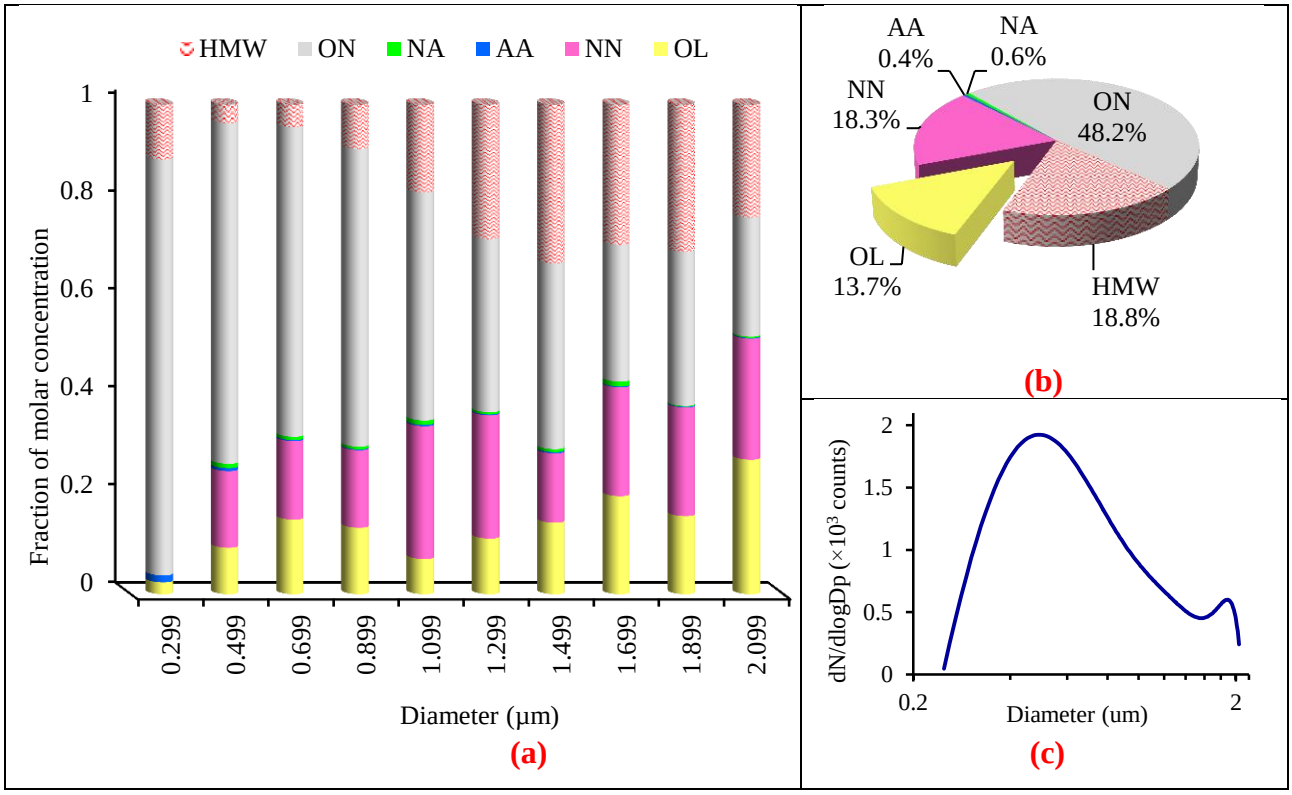

Figure 6. 8 ATOFMS data analysis of: (a) corrected peak area signals for the components of dry (RH 0.5±0.02%) as a function of particle size, (b) corrected total components fraction, and (c) corresponding size distribution, in the aged OL polydisperse aerosol.

molecules in smaller particles (at a diameter size of 200 nm and less) are homogeneous in concentration and thus particles at this size and below are well mixed making organic phase diffusion less important as a limiting process (Smith et al., 2002b; Smith et al., 2003; Pfrang et al., 2010; Shiraiwa et al., 2010). It is expected that excess concentration of O_3 ($5x10^{14}$ molecules cm^{-3}) reacted away larger fraction of small particle while reaction with larger particle resulted in significant alteration in the physical and chemical properties of particles surfaces leaving appreciable amount of unreacted OL in the bulk of the particles.

NN was not detected substantially in smaller particles but was repeatedly observed in larger particles with obvious peak. It is likely that NN has low particle phase yield in small particles due to its volatility and the fact that it is produced via gas-phase reaction. NN signals, however, was frequently enhanced in large particle spectra since its concentration in these particles was evolved from the secondary reaction within the particles and that products in these particles might reduce

Table 6. 2 Corrected measured data and associated uncertainty of the composition of aged OL aerosol under dry condition (RH 0.5±0.02%).

Size bin (μm)	OL		NN		AA		NA		ON	
	Molar fraction	±1σ	Molar fraction	±1σ	Molar fraction	±1σ	Molar fraction	±1σ	Molar fraction	±1σ
0.00-0.299	0.024	0.009	0.000	0.000	0.0142	0.0034	0.0000	0.0000	0.85	0.37
0.300-0.499	0.095	0.035	0.157	0.064	0.0060	0.0014	0.0090	0.0018	0.70	0.30
0.500-0.699	0.152	0.056	0.160	0.066	0.0021	0.0005	0.0068	0.0014	0.63	0.28
0.700-0.899	0.136	0.050	0.159	0.065	0.0017	0.0004	0.0055	0.0011	0.61	0.27
0.900-1.099	0.072	0.027	0.272	0.111	0.0024	0.0006	0.0092	0.0019	0.47	0.20
1.000-1.299	0.114	0.042	0.252	0.103	0.0019	0.0004	0.0045	0.0009	0.35	0.15
1.300-1.499	0.146	0.054	0.142	0.058	0.0026	0.0006	0.0059	0.0012	0.38	0.17
1.500-1.699	0.200	0.074	0.222	0.091	0.0017	0.0004	0.0101	0.0020	0.28	0.12
1.700-1.899	0.159	0.059	0.222	0.091	0.0013	0.0003	0.0017	0.0003	0.32	0.14
1.900-2.099	0.275	0.102	0.247	0.101	0.0015	0.0004	0.0025	0.0005	0.24	0.11

the effective vapour pressure of NN thus remains in the particle phase and not fully volatilize. Most researchers identified NN as a major volatile products (Moise and Rudich, 2002; Katrib et al., 2004; Thornberry and Abbatt, 2004; Lee *f.*, 2012; Hosny et al., 2013), while few investigators detected NN in the particle phase (King et al., 2004; Hung and Ariya, 2007).

By contrast, the signal of AA which arises from the rearrangement of CI1 was detected in smaller particles, but it diminished from most reacted larger particles suggesting the involvement of AA in the secondary chemistry associated more with larger particles. This is a consequence of the reaction of AA (in larger particles) with excess OL (and other products) to form high molecular weight species (section 6.2.3.2).

NA which arises from CI2 did not show similar trend to its counterpart, AA, and was detected in small and in comparable fractions of most size bins. This might reflects the volatility nature of NA and possibly the lower detection sensitivity of ATOFMS for NA.

Relatively high sensitivity of ATOFMS towards ON as compared to NN and NA was observed. The steady decrease in ON fraction as particle size increases can be taken as an indication for the involvement of ON in the secondary reaction associated with larger particles (see scheme 6.5 and table D-1, Appendix D). This explains also the disappearance of AA signals from large particles which are scavenged by these alternate pathways to form ON as proposed in scheme 6.3 and 6.5.

Figure 6.8 also suggests that the HR in larger particles enhances significantly the formation of HMW products (>282 m/z). Larger particles are expected to contain more of ECIs near the surface resulting from higher O_3 levels and more excess of OL in the bulk leading to more formation of HMW compounds. Hence the concurrent detection of HMW compounds signals with OL signal in large particles.

The chemical composition of large particles which shows excess OL, more NN and HMW products with less AA suggests that the formation mechanism of the oxidation products is affected by the amount of OL in the particles which is appreciable in greater size of the particles, leading to more ECIs self-reactions, reaction with unreacted OL, and oiligomers and polymers formation in large particles. The low fraction of OL in small particles, however, minimizes these secondary pathways and maximizes the formation of the SOZ which virtually dissociates to form the four primary oxidation products. The quantification analysis of processed OL particles with core-shell by Katrib and co-worker (2004) showed no trend for AA with increasing OL layer thickness and high ON yield as compared to AA and NA yields was observed. They attributed their finding to the reactivity of the AA and NA precursors, CIs, being scavenged through the secondary chemistry.

The overall composition of the aged OL polydisperse aerosol is shown in Figure 6.8 (b) and contains 13.7% unreacted OL, 18.3% NN, 0.4% AA, 0.6% NA, 48.2% ON and 18.8% HMW compounds. The corresponding size distribution is shown in Figure 6.8 (c).

6.2.3.2 Particle composition of aged OL particle at wet condition

The plots in Figure 6.9 below shows the corrected observed product distribution in the binned sizes of 1000 aged OL particles processed at relatively wetter condition, RH 65.0 ± 0.2%. The magnitude of the uncertainty (± 1σ) was estimated from the measured uncertainty values of the SCF (Figure 6.4) and is presented in Table 6.3.

The figure shows a significant shift in the components distribution of the binned sizes as compared to dry oxidation. Generally, no obvious trends are observed for most particles components. The most noticeable difference between dry and wet oxidation is the drop in the proportion of HMW products from 18.8% at dry oxidation to 4.1% at wet oxidation while

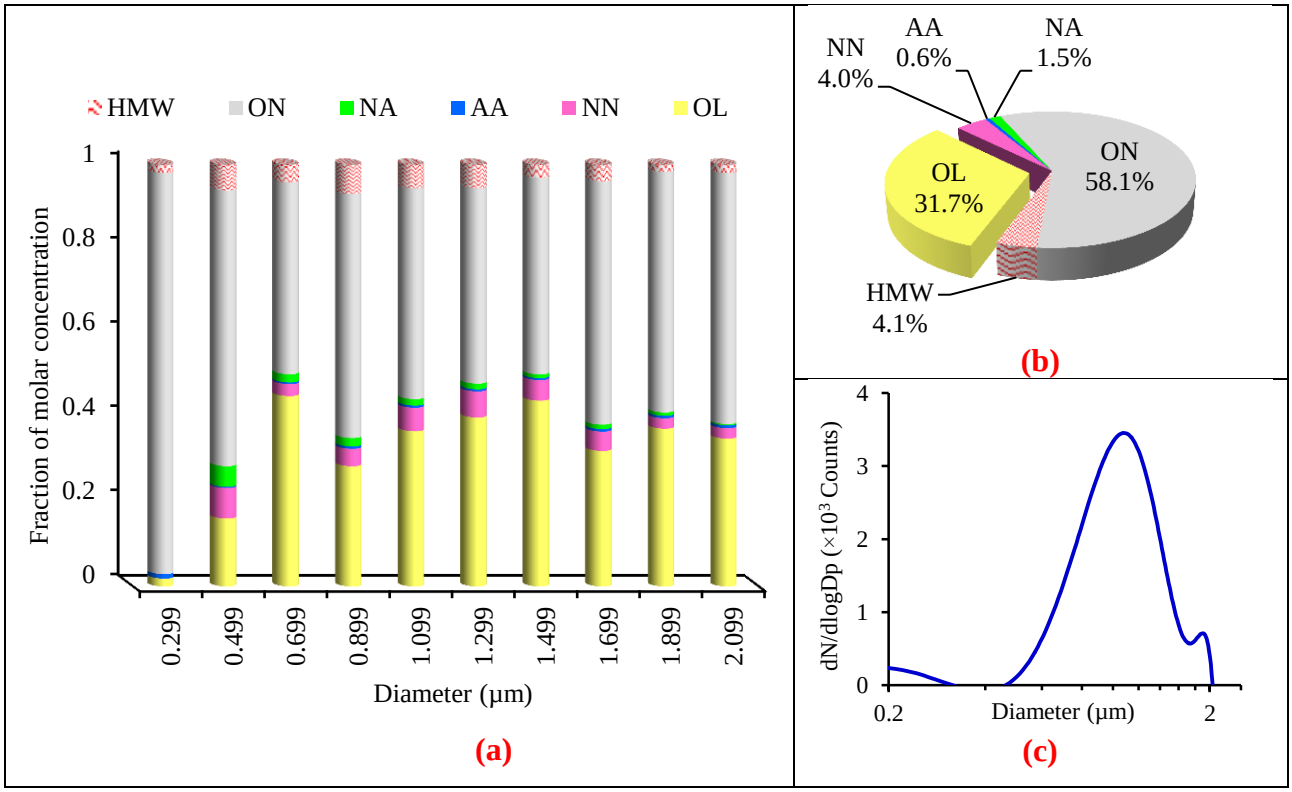

Figure 6. 9 ATOFMS data analysis of: (a) corrected peak area signals for the components of wet (RH 65.0±0.2%) as a function of particle size, (b) corrected total components fraction, and (c) corresponding size distribution, in the aged OL polydisperse aerosol.

unreacted OL increases from 13.7% to 31.7% in dry to wet conditions, respectively, for the polydisperse aerosol (Figure 6.9 (b)) of which the corresponding size distribution is shown in Figure 6.9 (c). It implies that CIs show a preference for reaction with water molecules over the reaction with OL at humid condition. This chemistry results in less destruction of additional OL molecules via the secondary pathways and hence the higher portion of unreacted OL and the limited amount of HMW products are observed concomitantly at wetter condition. This also justifies the observed decline in the NN signal from 4.3% in dry oxidation to 0.7% in wet oxidation. The secondary chemistry associated with the formation of NN in the bulk of the droplet (scheme 6.3) is suppressed by the involvement of CIs with the reaction with water. The

Table 6. 3 Corrected data and associated uncertainty of the composition of aged OL aerosol under wet condition (RH 65.0±0.2%).

Size bin (μm)	OL		NN		AA		NA		ON	
	Molar fraction	±1σ	Molar fraction	±1σ	Molar fraction	±1σ	Molar fraction	±1σ	Molar fraction	±1σ
0.00-0.299	0.02	0.01	0.00	0.00	0.011	0.002	0.000	0.000	0.95	0.42
0.300-0.499	0.16	0.06	0.07	0.03	0.003	0.001	0.049	0.010	0.65	0.29
0.500-0.699	0.45	0.17	0.03	0.01	0.004	0.001	0.019	0.004	0.45	0.20
0.700-0.899	0.29	0.11	0.04	0.02	0.006	0.001	0.020	0.004	0.58	0.25
0.900-1.099	0.37	0.14	0.06	0.02	0.005	0.001	0.015	0.003	0.50	0.22
1.000-1.299	0.40	0.15	0.06	0.03	0.005	0.001	0.013	0.003	0.46	0.20
1.300-1.499	0.44	0.16	0.05	0.02	0.005	0.001	0.009	0.002	0.47	0.20
1.500-1.699	0.32	0.12	0.05	0.02	0.006	0.001	0.010	0.002	0.58	0.25
1.700-1.899	0.37	0.14	0.02	0.01	0.006	0.001	0.008	0.002	0.57	0.25
1.900-2.099	0.35	0.13	0.02	0.01	0.007	0.002	0.003	0.001	0.60	0.26

result of the physical study of the OL-O_3 HR (section 6.2.1) with lesser observed mass losses during the wet oxidation supports this argument. Additionally, the analysis of the mass spectra of aged OL particles at wetter conditions (Appendix B, Figure B-11) reveals the presence of the secondary oxidation product resulted from the reaction between CI1 and water molecules at m/z -205 (R6.5).

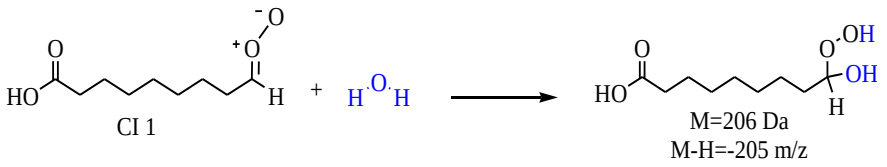

R 6. 5

It can be seen also in Figure B-11 that less HMW peaks were measured at wetter condition as compared to those found in the mass spectra of aged dry OL particles. Maximum m/z for aged wet particles was measured at m/z -1037 as compared to that of dry oxidation detected at m/z + 1458 for (Figure 6.6). Although Lee et al (2012) found no RH% dependence for the OL-O_3 HR system, Vesna and co-workers (2009) indicated an increase in the oxidation products in response to the increase in RH%. They also observed an increase in the reactivity of OL with ozone and more secondary product yields were measured at humid condition. However, this study indicates less reactivity of OL and less formation of HMW products at humid conditions. The reported decrease in NN yield agrees well with this study. The relatively low ozone concentration (200 ppb up to 1800 ppb), longer reaction time (2 hour), smaller size particles (75 nm in diameter), oxidation and measurement techniques used in their study might be responsible for the differences in the results between the two studies.

6.2.4 Theoretical study of the OL-O_3 HR

The section describes a theoretical study of the OL-O_3 HR. The experimentally measured observations to be modelled here: (1) component distribution of aged OL particles as a function of size, (2) component percent yields of aged polydisperse OL particles, and (3) change in mass distribution of a pure polydisperse OL aerosol on dry oxidation.

6.2.4.1 Overview of model structure

The model uses molar stoichiometric analysis of ozonolysis primary and secondary pathways to predict components distribution of aged OL particles as a function of size, component percent yields of aged polydisperse OL particles, and the change in the mass distribution of a pure polydisperse OL aerosol on dry oxidation. It provides a quantitative tool for interpretation of reactants and products yields in the particle phase following surface and bulk reactions. The volatility of the products is also considered as a major route for particle mass losses observed in the physical characterization of aged particles. The assumptions made here are primarily based on independent measurements of physical and chemical changes of aged polydisperse OL aerosol and literature-based estimated fittings.

OL molecules in particles at a size of 200 nm in diameter are homogeneous in concentration making particles of this size and below well mixed i.e. organic phase diffusion less important as a limiting process (Smith et al., 2002b; Smith et al., 2003; Ammann and Pöschl, 2007; Pfrang et al., 2010; Shiraiwa et al., 2010). On this basis, it is assumed that ozone initially reacts out a surface layer of 100 nm depth from pure OL particles producing a surface barrier dominated by the initial generation of volatile and non-volatile products. This surface reaction (SR) is assumed to be irreversible; that is:

$$OL_{(l)} + O_{3(g)} \longrightarrow \text{Products}$$

R 6. 6

The ‘diffuso-reactive length, l , regarded as the characteristic distance from the particle surface up to which a gas molecule diffuses and proceeds effectively to chemical reaction (Pfrang et al., 2010), namely:

$$l = \sqrt{\frac{D_l(O_3)}{k_2[OL]}}$$

Eq 6. 1

where, D_l is the diffusion coefficient for O_3 in the gas phase to the organic liquid, 1.0×10^{-9} m^2s^{-1}, (estimated based on the diffusion of oxygen gas in organic solvents) (King et al., 2009), $k_2= 10^6$ $M^{-1}s^{-1}$ and [OL]=3.16 M, yielding a value of 18 nm. This surface depth reflects the distance O_3 molecules will diffuse per a reactive characteristic time ($1/k_2[OL]$) which is calculated for this study to be 0.3 µs. The diffusion of O_3 through the reacting layer takes ($l_p/k_2[OL]l$) second per a reactive characteristic time. For example a reaction depth of 100 nm takes 1.6 µs to react completely with O_3. Accordingly, reaction in particles with $D_p\leq200$ nm thus proceeds to completion within the first 1.6 µs forming primarily the first generation products via SR as a major pathway. Secondary reactions are not significant in the SR and therefore the rate of reactants or the products losses through this route at this particle size range is negligible. This is because most products are primary, and the smaller particles reacted rapidly and completely to form secondary material, leaving no unreacted primary material.

However, particles with $D_p>200$ nm react via SR for the first 1.6 µs at a depth of 100 nm forming a surface barrier of primary ozonolysis products. This particular depth was chosen

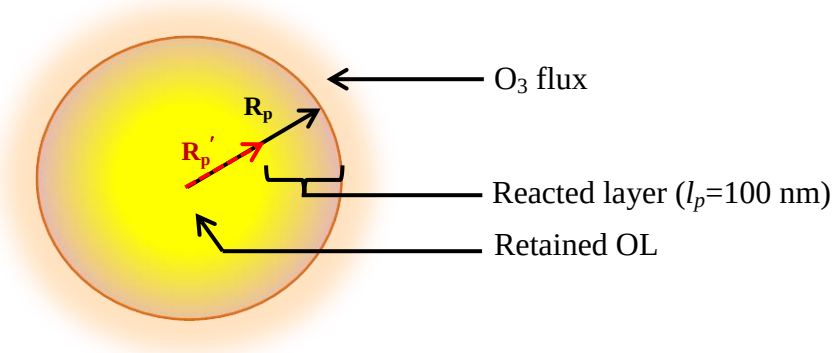

Figure 6. 10 OL droplet showing O_3 flux toward the droplet, reacted shielding surface layer, and unreacted retained OL.

because it fits the observed mass loss of the aged particles. The reacted layer is expected to induce physical and chemical changes of particles surface (Katrib et al., 2005a; Knopf et al., 2005; Ammann and Pöschl, 2007; Huff Hartz et al., 2007; Shiraiwa et al., 2010; Pfrang et al., 2011; Shiraiwa et al., 2012a). Thus O_3 diffusivity to the bulk of the particles decreases and OL-O_3 SR slows as oxidation products are formed and saturate the surface of the particles making organic phase diffusion the limiting process. Therefore SR become less significant and shifts toward secondary bulk reaction (BR) as concentrated primary oxygenated products diffuse into the bulk of the particles or unreacted organic phase diffuse to the oxidized layer. Bulk chemistry therefore follows mainly secondary pathways where CIs react with primary products, retained OL, or undergo self-reaction to form secondary HMW products.

6.2.4.2 Surface reaction (SR)

As is hypothesised earlier, OL in a layer depth of 100 nm from the particle surface presumably reacts completely with gaseous O_3 via surface reaction and form the primary products. The mass of unreacted OL in larger particles can be calculated by assuming sphericity of pure and processed OL particles. The reacted mass of OL within the 100 nm of pure droplet can be calculated using the sphere volume and OL density as follows:

$$m_{OL} = \frac{4}{3}\pi(R^{3}{}_{p} - R'^{3}{}_{p}) \times \rho_{OL}$$

Eq 6. 2

where m_{OL} is the reacted mass of OL and R_p-R_p'=l_p. This reacted mass is expected to form products both in particle and gas phases. The flow chart in Figure 6.11 and Table 6.4 describe the analytical approach taken in estimating the yields of retained OL and the oxidation products in aged OL particles following the initial SR of the particles i.e. particle composition after 1.6 µs oxidation time. For analytical simplicity, a concentration of one mole of OL is assumed to be processed completely following the two possible oxidation reaction pathways shown in scheme 6.1 with equal probability. The sum of the moles of the four primary oxidation products (AA, NN, NA and ON) per mole of OL is 2 (Zahardis and Petrucci, 2007).

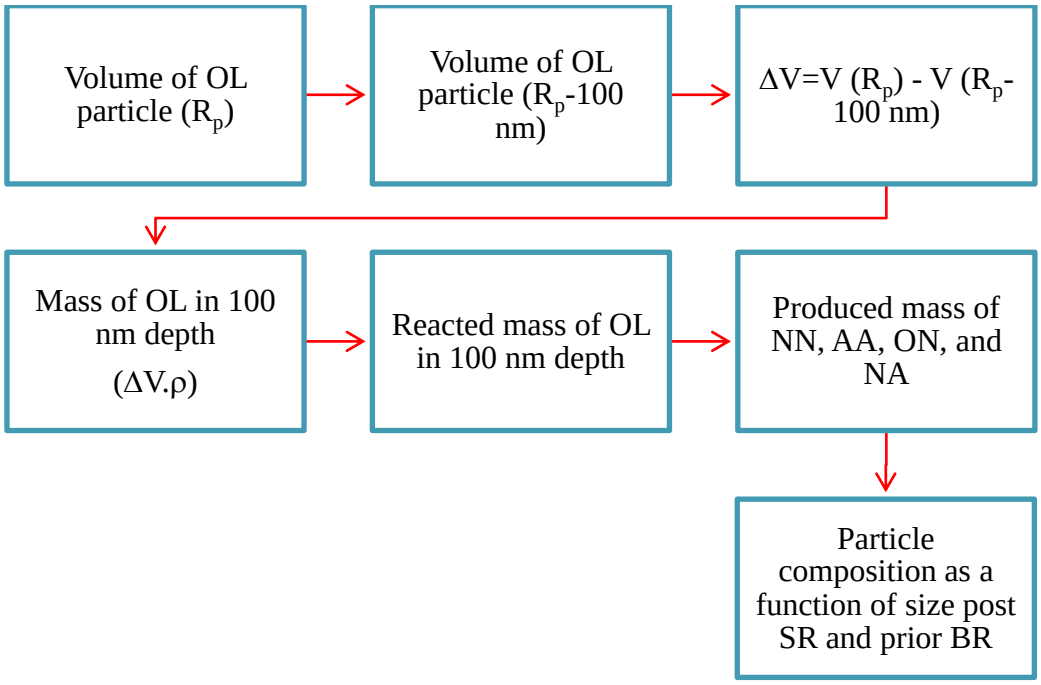

Figure 6. 11 A flow chart showing analysis steps in estimating the reacted mass of OL in the OL-O_3 HR and the corressponding mass of the oxidation products.

Table 6. 4 Analytical approach to estimat the yields of retained OL and the oxidation products in aged OL particles following the initial SR of the particles within the 100 nm surface depth.

	OL	O_3	NN	EC1	EC2	ON
Moles before SR	1	excess	0	0	0	0
Moles after SR	0	excess	0.5	0.5	0.5	05
MW (g mol^{-1})	282.5	48	142.2	188.2	158.2	172.2
Mass (g)			71.1	94.1	79.1	86.1
Density (g cm^{-3})	0.891		0.827	1.225	0.905	1.019
Volume (cm^3)			86.0	76.8	87.4	84.5
Volume fraction of products in the aerosol phase			0.26	0.23	0.26	0.25

Figure 6.12 shows the calculated mass of initially formed primary oxidised products NN, ON, ECI1, ECI 2, and retained OL following the SR within 100 nm depth as a function of size. The figure indicates that smaller particles up to 200 nm in diameter composed of 100% oxidation

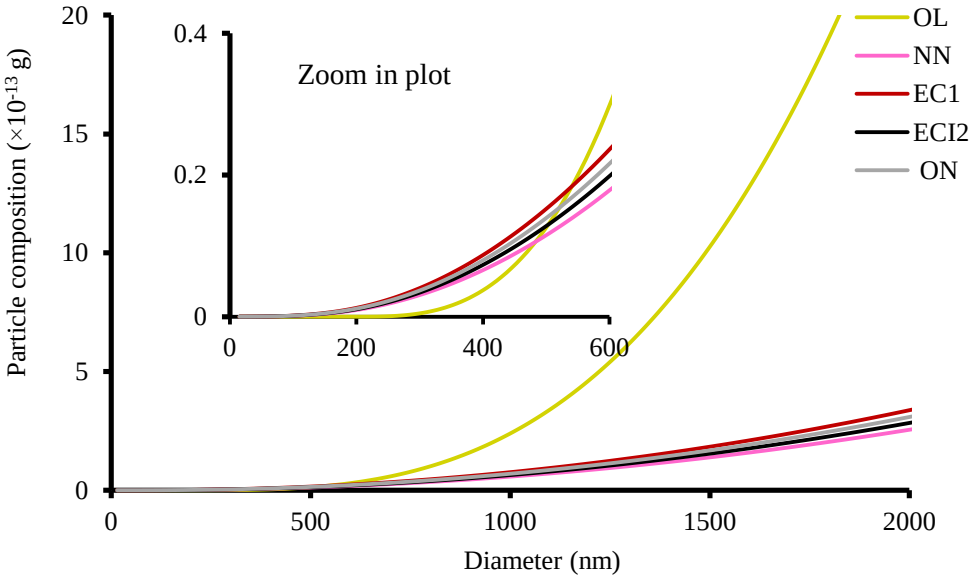

Figure 6. 12 Estimated mass of primary oxidised products NN, ON, ECI1, ECI2, and retained OL following the SR within a 100 nm depth as a function of size.

products with no retained OL; however, as particle size increases the mass fraction of retained OL in the bulk of the particles become dominant. This unreacted amount of OL is shielded from SR with a protective layer of oxygenated products.

The flow chart in Figure 6.13 illustrates OL ozonolysis process showing the initial production steps of the major oxidation products and main CIs depletion pathways involved in the secondary chemistry and the formation of HMW products.

6.2.4.3 Evaporation and isomerization

NN is a highly volatile compound especially in AFT based experiments, making its detection very challenging (Asad et al., 2005; Zahardis and Petrucci, 2007). Indeed NN signal was only detected appreciably in large size particles. It is therefore reasonable to conclude the major yield of NN produced from SR to be in the gas phase and limited yield is formed in the condensed phase. The

molar concentration of NN formed from SR and remains in the condensed phase can be calculated as follows:

$$NN_m = (1 - x)\, NN_{mi} \qquad \text{Eq 6. 3}$$

where NN_m is the molar concentration of NN in the particle phase, x is the fraction of NN formed in the gas phase and NN_{mi} is the initial molar concentration of NN formed following the SR. The best fitting literature-reported value for x is 0.95 (Vesna et al., 2009).

From Figure 6.13, the possible fate of ECIs, produced via initial SR, is divided into several depletion pathways with each pathway describing a particular CI elimination. The first pathway describes the fate of CIs through isomerization to the corresponding carboxylic acids AA and

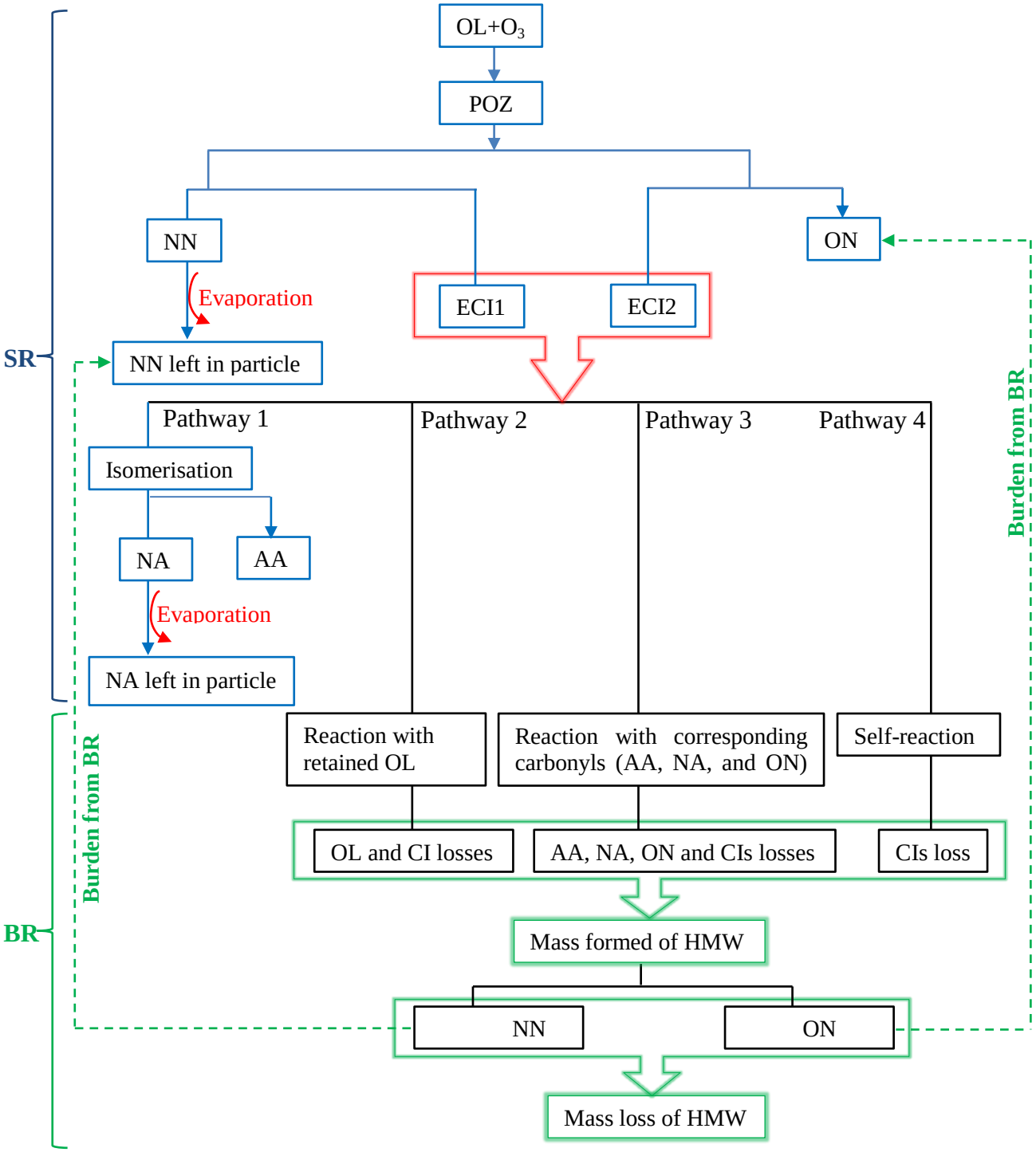

Figure 6. 13 Reaction scheme of OL ozonolysis process showing the initial production steps of the major products and main CIs depletion channels involved in the secondary chemistry leading to the formation of HMW products

NA. The model proposes a steady decrease in the isomerization process as a result of changing particles composition with changing particles sizes. To allow for this behavior, the molar load of CI, m_{CI}, was modeled as a function of the ratio between the reacted and the initial OL masses present in each size bin i.e. OL_{mass}/OL_{mass0}. This proposal maximizes CIs availability and minimizes the corresponding isomers masses as particles diameter increases making CIs long living species in bulkier particles. Larger particles contain greater amount of unreacted OL therefore stabilizing CIs. The amount of AA and NA, respectively, formed from this pathway can be estimated as:

$$AA_m = CI1_{mi} (OL_{mass}/OL_{mass0})$$

Eq 6. 4

$$NA_m = CI2_{mi} (OL_{mass}/OL_{mass0})$$

Eq 6. 5

where AA_m, $CI1_{mi}$, NA_m, and $CI2_{mi}$ are molar concentration of AA, the initial molar concentration of CI1, the molar concentration of NA and the initial molar concentration of CI2, respectively.

The residual molar concentration of CI1 and CI2 left in particles following isomerization in each size bin can be inferred as follows:

$$CI1_m = CI1_{mi} - AA_m$$

Eq 6. 6

$$CI2_m = CI2_{mi} - NA_m$$

Eq 6. 7

However, ATOFMS analysis of small size particles show small signals for NA when compared to bigger particles indicating a loss channel of the formed mass occurred at the surface

of the particles. Ziemann (2005) did not detect NA in the particle phase which he attributed to its volatility (Ziemann, 2005). It is conceivable therefore to allow partial formation of NA in the gas phase. The NA formed from this pathway and remains in the particle phase following vaporization can be calculated as follow:

$$NA_{mp} = (1 - x)\ NA_{m}$$

Eq 6. 8

where NA_{mp} is the molar concentration of NA remains in the particle phase and x is the fraction of NA formed in the gas phase. The proposed fitting value for x is 0.7. Figure 6.14 illustrates components trends with size of aged polydisperse OL particles following partial isomerization and evaporation of corresponding products.

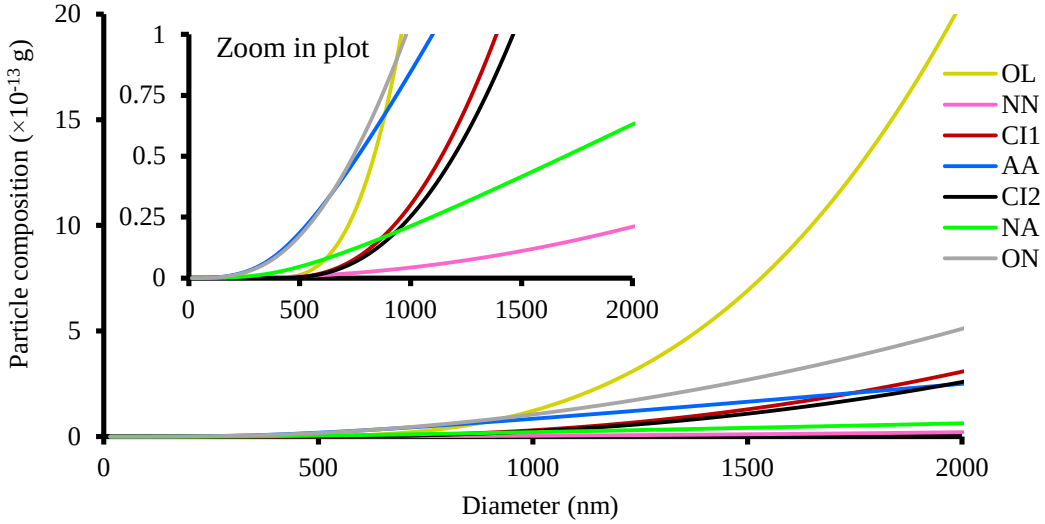

Figure 6. 14 Illustration of components trends with size of aged polydisperse OL particles following partial isomerization and evaporation of volatile products.

6.2.4.4 Bulk reaction (BR)

The yields of the initial species resulted from the SR analysis is used to simulate the particle compositions as a result of BR. The simulation of the BR is based on the reactivity of CIs within

the particle interior which provides further depletion routes for CIs. The second pathway of CIs depletion (Figure 6.13) accounts for the consumption of CIs in the reaction with unreacted mass of OL. The model reserved the maximum fraction of CIs exclusively in bulky particles for the reaction with OL as it presents in excess.The foundation of this reservation can be explained by the reactivity of the carboxylic acid and alkene moieties of OL with the CIs. The spectrometric analysis of this study shows that the double bond in OL is efficient in reacting with CIs (section 6.2.2.3). However modelling CIs reactivity at equal affinities to the alkene and carboxylic acid moieties of OL resulted in a close simulation of the experimentally observed mass distribution obtained from the SMPS data. The molar loss of CI via pathway 2 can be estimated as follows:

$$CI1_{my} = y\, CI1_{m}$$

Eq 6. 9

$$CI2_{my} = y\, CI2_{mp}$$

Eq 6. 10

Where $CI1_{my}$ and $CI2_{my}$ are the molar concentration of CI1 and CI2 subjected to reaction with OL, y is the fraction of CI moles involved in the reaction with OL, $CI1_{m\ and}\, CI2_{mp}$ are the molar concentration of CI1 and CI2 left from pathway 1. The very close fitting value to our experimental observation for y would be 0.5, this leads to the molar concentration of OL consumed in pathway 2:

$$OL_{m} = CI1_{my} + CI2_{my}$$

Eq 6. 11

The third pathway of CIs elimination describes the reaction of CIs with the first generation products, AA, NA, and ON and, respectively. Implementing literature-reported measurements and experimental observations of this study, NN is not involved in this consumption route. In this pathway, it is expected that CIs react primarily in little particles with the first-generation products

AA, NA, ON as they present in highest concentrations than OL. However, as particles increase in diameter, reaction with excess OL is favoured over that with AA, NA, or ON which present at low portions in larger particles. For modelling purpose of this system, the available residue of CIs is further divided at an equiratio manner in the reaction with available AA, NA, ON as well as CIs self-reaction in the fourth pathway which depicts the self-reactions of the remaining CIs to form HMW products. The losses of CIs moles from pathway 3 and 4 are calculated as follows:

$$CI1,2 = (1 - y) \times CI_{my}$$

Eq 6. 12

whereas losses of primary products from pathway 3 is calculated as follows:

$$AA_m, NA_m, ON_m = ((1 - y)/4) \times (CI_{my})$$

Eq 6. 13

It is apparent from above that pathways 2, 3, and 4 (Figure 6.13) are responsible for the formation of HMW products. The mass of the combined known reactants (CIs, OL, and primary products) makes the total contributions for the formation of HMW mass that is:

$$HMW_{mass} = CI_{mass} + OL_{mass} + AA_{mass} + NA_{mass} + ON_{mass}$$

Eq 6. 14

This mass of HMW products is subsequently reduced through the formation of the primary products, NN and ON. AA and NA are not formed in this route rather their precursors are consumed in the secondary chemistry that results in the formation of NN and ON. To arrive at a satisfactory estimate for the diminished amount of HMW and thus the amount formed of NN and ON, the formation of these products is coupled to the reaction mechanism between OL double bond and CI1 or 2 to form OX1, 2, or 3 (scheme 6.3). According to the proposed mechanism and in the case of the reaction between CI1 and the double bond of OL, the three possible

decomposition pathways of the C_{27} peroxide lead to the formation of about 60% ON and 30% NN. However, in the case of CI2, NN is the only primary product formed following the three decomposition pathways of the C_{27} peroxide regardless of the attacking position of the CI2 to the double bond or the bond of C_{27} peroxide to break but CI2 exists in less proportion due to evaporation. Nevertheless, reaction of CI1 and 2 with the double bond of OL, collectively, yields more ON than NN. The decay in the HMW mass can be estimated thus as follows:

$$\Delta HMW_{mass} = HMW_{mass} - NN_{mass} - ON_{mass}$$

Eq 6. 15

where ΔHMW_{mass} is the mass loss of HMW compounds following the formation of NN and ON. The frequently observed NN signals in big particles size can be thus explained as a result of secondary reaction taking place in the bulk of the particle where evaporation of volatile compounds is minor. The abundant of OX1, 2, and 3 as a unit component in identified HMW compounds further support the efficiency of the alkene functionality in OL to react with CIs and thus the formation of the primary products NN and ON. Additionally, the observed modest decrease in ON with particle size reveals a significant source which the model suggest to be the reaction between CIs and the double bond of OL.

Hearn and Smith (2004) observed NN and ON yields in OL polydisperse aerosol at a particle size of 800 nm to be larger than the yields of the other products which they attributed to the existence of secondary reactions involving CIs. Their observation fits the simulated composition of aged larger particles. Further support for this yields simulation at large size particles is from Katrib et al (2004) who found that AA as a minor component in the oxidized condensed phase while ON as a major product. Their explanation for the appearance of these

unidentified products is the secondary reaction of CIs with the OL C=C double bond. The observed low yield of AA (4%) and appreciable ON yield (28%) in the HR between O_3 with pure OL particles (0.02-0.5 µm) by Ziemann also evident the efficiency of the secondary chemistry in the excessive reduction of AA and its precursor (Ziemann, 2005).

6.2.4.5 Model output

Aged particle compositions

Figure 6.15 shows the model output of aged particles components yields as a function of size modelled at a size range of 0.015-1.999 µm.

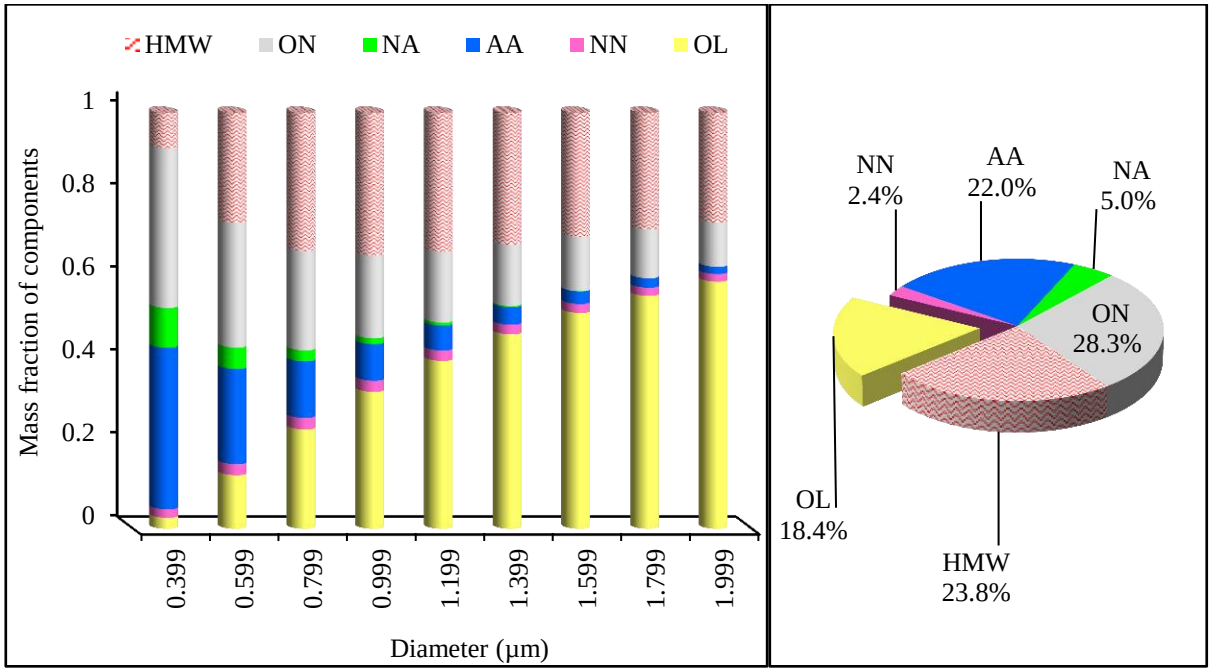

Figure 6. 15 (a) Modelled particles composition of aged OL particles as a function of size and (b) net composition of aged polydisperse OL aerosol.

The model output shows some consistent features between simulated and observed trends in the components distribution as a function of size. There is a significant amount of OL remained unreacted; this amount is more appreciable in aged bulkier particles. It is plausible in

this study to reason out ATOFMS measurements of unreacted OL as a function of size (section 6.2.3.1) and the modelling simulation of excess OL present in aged particles to indicate that the oxidation of the organic phase at some stage is deviated from surface HR between gaseous O_3 and liquid OL to bulk reaction within the particle interior. This stage remarks the formation of a surface layer rich with the first generation oxidation products insulating the particle interior and inhibiting species exchange between the interior and the exterior thereby minimizing O_3 accessibility to the bulk and preventing volatile products formed via secondary reaction from escaping the particles. This explains also the observed concomitance availability of volatile NN with the HMW compounds which is trapped in the particle bulk by oxygenated products. Katrib et al (2005) postulated their observations of the presence of unreacted OL in processed mixed oleic acid (OL)/stearic acid (SA) oxidized particles to the change in the chemical environment surrounding the organic liquid highlighting the importance of particle phase and chemical morphology of particle under oxidation process. They attributed the observed drop in O_3 reactive uptake from $\gamma = 1.25 \times 10^{-3}$ to $\gamma = 0.15 \times 10^{-3}$ for particle composition 100/0 to 50/50 of OL/SA to the decrease in the diffusivity of both gaseous O_3 and liquid organic OL (Katrib et al., 2005a).

However, the imperfect fitting of the modelled composition of aged polydisperse aerosol (Figure 6.15) to the observed components (Figure 6.8, (a) and (b)) is most likely to be the cause of the unavoidable ATOFMS limitations. The trend in AA, HMW and OL components with size show similar behaviour but deviates in the products yields. Calculated NN yield is far less than the observed value which might indicate less evaporation of NN from the particles. The variation in ATOFMS sensitivity towards compounds, the particle size dependent of the LDI efficiency with the smaller particles being fully sampled and larger particles being partially sampled and the

simplicity of the model are the likely cause for the conflict between estimated and measured chemical composition of the aged OL particles.

6.2.4.6 Change in the mass distribution of OL poly disperse aerosol

The ability of the model to estimate the change in total mass distribution of aged OL polydisperse aerosol was examined by considering the number concentration of particles in each size bin. The modelled components mass of each size bin was multiplied with the measured number of particles in that size bin without any additional change in the model input parameters. The model simulation was applied to the size range of 0.015-0.571 µm which is the overlapping size range between the model, ATOFMS and the SMPS measurements. The effect of components densities was also simulated and it was found that the change in products density on oxidation has no significant effect on the total mass loss of aged OL polydisperse on oxidation.

The mass of each component was calculated based on the molar formation of the compounds following surface and bulk reactions as described in details above (section 6.2.4). The diameter of the aged particles was modelled at constant density by assuming the density of the pure and aged particles remains unchanged i.e. the density of the particles before and after oxidation is equal to the density of OL. The change in the particles diameter was calculated using the following formula:

$$R_p = \sqrt[3]{\left(\frac{3m_{Total}}{4\pi\rho_{OL}}\right)}$$

Eq 6. 16

where m_{Total} is the sum of the mass of all components in processed particles and ρ_{OL} is the density of OL (0.891 g cm^{-3}). However, particles diameter considering individual components was calculated using the following formula:

$$R_p = \sqrt[3]{\frac{3V_{Total}}{4\pi}}$$

Eq 6. 17

where V_{Total} is the total volume of all components fractions (see Table 6.2) composing the aged particles in the examined size range, that is:

$$V_{Total} = V_{OL} + V_{NN} + V_{AA} + V_{ON} + V_{NA} + V_{HMW}$$

Eq 6. 18

The volume of each component is calculated from the component mass present in the particle and the density of that component ($V=m/\rho$). The density of the HMW is estimated to be 1.12 g cm^{-3} based on the experimental study of particles density changes on oxidation by Katrib and coworkers (2005 b). The simulated mass loss in particles is plotted against the obtained particles diameters at both constant and changing density. Figure 6.16 compares the measured and the simulated mass distribution of OL polydisperse aerosol.

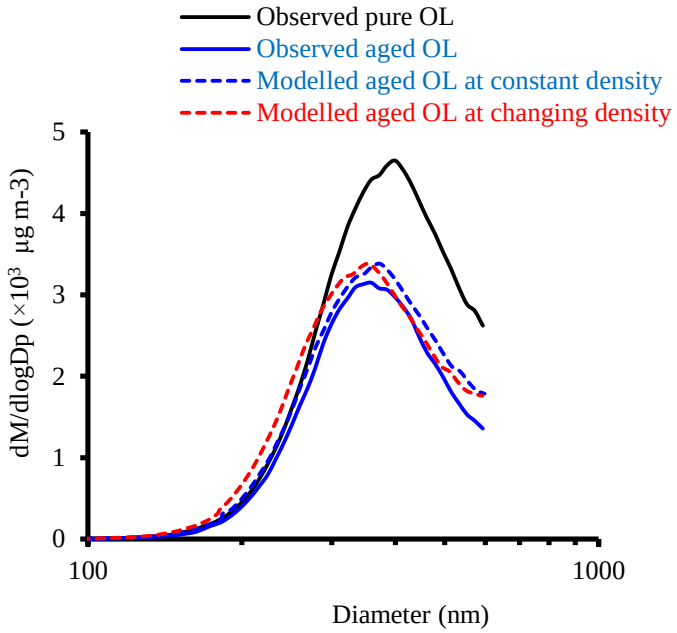

Figure 6. 16 Measured and modelled mass loss of OL polydisperse aerosol on oxidation by O_3.

The observed mass loss was 31.0 ±3.3% measured at constant density, while the theoretical study shows that 26.7% of the polydisperse aerosol mass is lost on initial oxidation of 100 nm of OL layer. However, to accurately simulated the observed decay in the mass distribution of aged OL particles, the reacted layer can by adjusted to 150 nm. In this case the modelled more mass loss is calculated due to the formation of the volatile products (NN and NA) thus the two curves well agree in the mass distribution of the aged OL particles.

6.2.4.7 Sensitivity study of the model

To determine the parameters most influential on model results, the sensitivity of the analysis is examined here by varying each input variable by ±20% relative standard deviation one-at-a-time while other parameters held constant. The input values are reaction depth (*lp*), masses of NN and NA formed in the gas phase. Table 6.5 below shows the numerical results of these calculations.

Table 6. 5 Sensitivity study of the parameter influencing the theoretical study of the OL-O_3 HR.

Parameter	Low System value-20% RSD	System value	High System value+20% RSD	Particle mass loss (%)		
				Low	System	High
lp (nm)	80	100	120	24.1	**26.7**	28.1
NN evaporation %	76	95	100	22.5	**26.7**	27.7
NA evaporation %	56	70	84	25.1	**26.7**	28.3
HMW ρ (g cm^{-3})	0.896	1.12	1.344	26.7	**26.7**	26.7

From the table, the most sensitive parameters in the study of the OL-O_3 HR are the reaction depth, l_p, and products volatility. The change in the particle mass loss as a result to changing ±20% in the l_p, NN and NA evaporation cause a significant change in the mass losses

corresponds to 24.1-28.1%, 22.5-27.7% and 25.1-28.3%, respectively. However, the change in the density of the HMW products showed no effect of the mass loss of the particles.

6.3 OL-OH HR system

6.3.1 Physical characterisation of aged OL aerosol by OH radical

Gas-phase reaction of organics with ·OH constitutes a potential mass loss process of particles (Atkinson, 1997). Being unsaturated organics, OL is expected to react with OH faster than saturated alkyl carboxylic acids, making OL a relatively short-lived species in the atmosphere (da Silva, 2010). Alkenes react with both ·OH and O_3, however, reaction of alkene with ·OH often dominating over the reaction with O_3 reaction (Atkinson, 1997; Aschmann et al., 2000). Indeed the physical study showed that exposing OL aerosol to 100 ppb in the absence of ·OH did not show significant changes under the condition of this study (Appendix B, Figure B-12). However, on exposure to ·OH $(1.2\pm0.6)\times10^{10}$ molecules cm^{-3} a decrease in the mode mobility diameter from 300 to 289 nm was observed. In addition, a total of 18.0% loss in the organic mass was observed. Figure 6.17 displays the results of the physical study of the OL-OH HR.

The mass loss in the OL-OH HR system is attributed to the formation of the gaseous species such as NN (Tedetti et al., 2007; Rathouský et al., 2011) and CO_2 (Rathouský et al., 2011). Other reported principal products in the reaction between OH and OL include ON, AA, heptanal, octanal, and decanal (Rathouský et al., 2011).

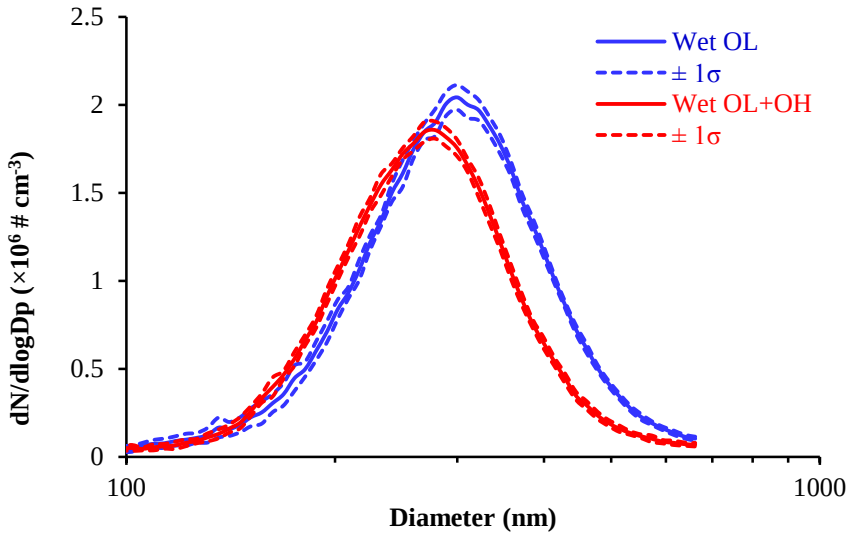

Figure 6. 17 Particle size distribution of 10 averaged samples of pure OL aerosol and OL aerosol exposed to OH at RH 65.0 ± 0.2%.

6.3.2 Chemical characterisation of aged OL aerosol by ·OH

The mechanism of the HR between OL and ·OH has not been sufficiently elucidated (Feltham et al., 2000). No adequate experimental studies are available for OL-OH HR to allow data interpretation. Experimentally, it is more challenging to study the reaction between alkene, in particular long chain, and OH as there are more than one possible site of attack (Feltham et al., 2000). Organics vulnerable to oxidation by ozone will be more susceptible to oxidation by OH. The sheer number of saturated carbons on OL grants more H-abstraction than OH addition to the double bond of OL (Robinson et al., 2006). On the basis of the little amount of knowledge available, the spectrometric analysis of the OL-OH HR study is speculated on conventional oxidation reaction of OH radical with alkene.

Under tropospheric conditions, the alkene OH radical reactions proceed mainly by the rapid addition reaction to the double bond in preference to H-abstraction reaction forming a hydroxyalkyl radical (R·). For asymmetrical molecule about the double bond (such as OL

molecule), the addition of OH radical to the molecule is expected to lead to isomeric hydroxyalkyl radicals (Lightfoot et al., 1992; Aschmann et al., 2000; Rathouský et al., 2011). R· reacts with O_2 to form the corresponding alkyl peroxy (RO_2) (Lightfoot et al., 1992; Atkinson et al., 1999; Atkinson and Arey, 2003). The subsequent oxidation reactions of the key intermediate RO_2 proceeds by a chain mechanism reaction, involving NO, NO_2, NO_3, HO_2 or other RO_2 radicals (Lightfoot et al., 1992). However, in the case of OL-OH HR of this study RO_2 is expected to react with available species in the system such as OH, HO_2, RO_2 radicals or CIs. The negative average ion mass spectra of OL aerosol exposed ·OH is shown in Figure 6.18.

Analysis of the average mass spectra of OL particles oxidised by OH radical shows that NN and ON are identified as major products appearing at m/z values of -141 and -171, respectively.

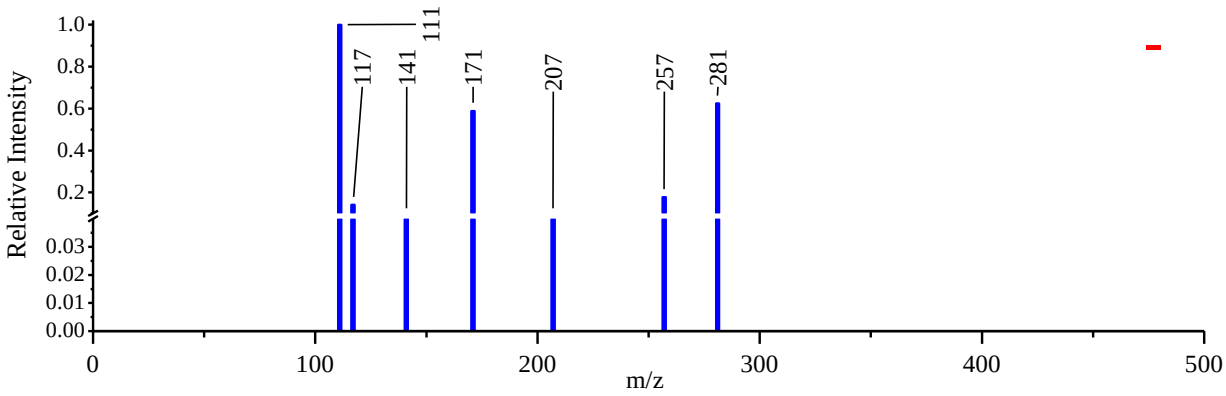

Figure 6. 18 Average negative ion mass spectra of processed OL with OH

Peaks attributed for AA and NA were not measured. This observation partially agrees with the reported measurements of Rathousky and coworkers who detected considerable signals for NN and ON and minor signals for AA and NA on photocatalyst experiment conducted to study the decomposition of thin layers of OL (Rathouský et al., 2011). The formation of the primary products NN and ON reveals that OL-OH HR is dominated by the addition reaction of OH to OL

double bond. However, the presence of lower molecular weight (LMW) than the primary products (NN and ON) suggests also hydrogen abstraction reaction. LMW compounds maybe identified as products with hydroperoxides, carboxylic acids, aldeyhydes, ketones and alcohol functionalities. Scheme 6.7 suggests OH radical to trigger a chain reaction involving ON as a possible nominee for the observed peak at m/z -117 (M 118) in addition to other suggested undetected small oxygenated compounds (M 120, 118, 102 and 100 Da). Similarly the peak at m/z -207 might represent the formation of a secondary oxygenated compound formed as a result of the chain reaction of ON initiated by OH. However, the major peak observed at m/z -257 can be assigned to two possible chemical formulas routed from the addition reaction of OH to the double bond followed by a sequence of chain reactions as scheme 6.8 demonstrates.

The final oxygenated product corresponds to the multiple additions of oxygen atoms resulting in a combination of aldehyde, ketone, hydroxyl groups in place of hydrogen atoms in the OL molecule. The reasonable conclusion to be built here is that the OL molecules have reacted with a number of OH radicals to form multiple oxygenated functional groups. Unreacted OL acid is also detected at m/z -281 with no significant changes in signal magnitude observed among particles with different sizes. Peaks at m/z higher than that detected for the parent OL were not observed in the case of OL-OH HR.

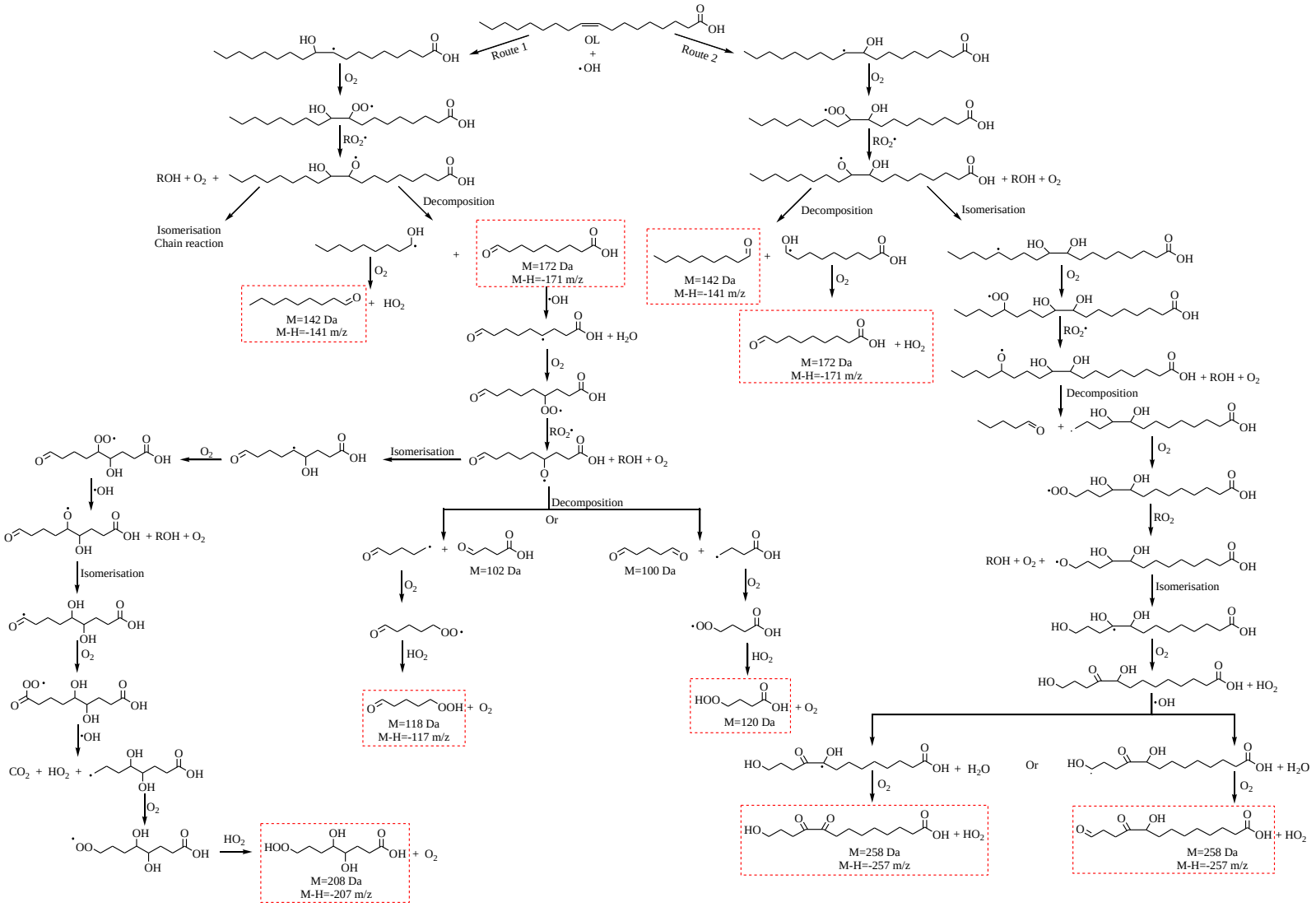

Scheme 6. 8 Proposed steps, reaction mechanism and possible assignment for observed peaks of oxigenated primary and secondary products (in red dashed squares) of OL oxidation by OH.

6.4 MA-O_3 HR system

6.4.1 Physical characterization of aged MA aerosol

Under the established conditions of the chemical ageing of OL particles (RH 0.5-65.5%, τ 147 s and O_3 mixing ratio 20 ppm), no physical or chemical changes were observed for the HR of MA aerosol and ozone (MA-O_3 HR) and very little physical change was observed at RH 10 ±1.0% with no detected change in the chemical composition of particles even when particles were exposed to higher O_3 mixing ratio up to 50 ppm. On the one hand, MA has two carboxylic acid groups bound to adjacent -HC=CH- of its molecular backbones resulting in molecular space hindrance and strong electron-withdrawing effects caused by the two carboxyl groups (Chen et al., 2005). On the other hand, MA particles are solid at room temperature and RH 10 ±1.0%. The reported deliquescence relative humidity of MA at room temperature is 87.5% (Najera et al., 2010) below which MA aerosols are assumed to remain solid. Therefore, MA particles were extremely difficult to oxidise under similar oxidation conditions to that of OL particles. Due to the slow reaction between MA and ozone, a relatively high ozone concentration of 100±0.6 ppm and wetter condition of RH 92.5 ± 1.5 % were used to achieve an appreciable ageing degree of MA particles. The particle size distributions of pure and aged MA particles under these conditions are presented in Figure 6.19.

From Figure 6.19 it can be clearly observed that aqueous MA particles decrease in the size as a result of ozone exposure. The decrease in the mode mobility diameter is from 188 to 146 nm. The corresponding inferred total mass loss of the polydisperse aerosol is 39.5 ±5.1%. Analogous experimental studies showed that the formation of CO_2 and formic acid HCO_2H are the major

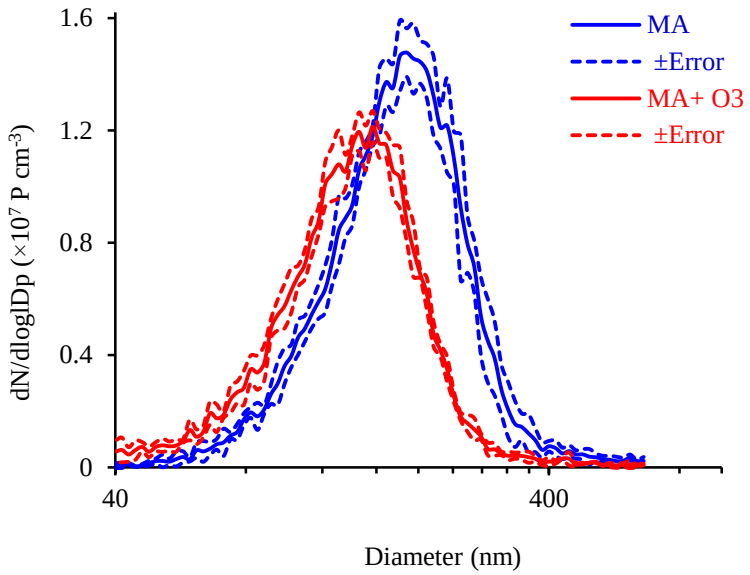

Figure 6. 19 Particle size distribution of 10 averaged samples of pure MA aerosol and MA aerosol exposed to O_3 at RH 92.5 ± 1.5%. The apparent drop in aerosol number with oxidation (with vs without O_3) is discussed further below.

gas-phase products responsible for the particles mass loss (Oliviero et al., 2001; Najera et al., 2010).The chemistry of the formation of these gas-phase products is consistent with the CIs mechanism (Najera et al., 2010). Laboratory experiments of MA-O_3 HR showed that major oxidation products and intermediates include small molecular weight products such as formic acid, glyoxylic acid, glyoxal, oxalic acid and CO_2 (Shende and Levec, 1999; Oliviero et al., 2001; Najera et al., 2010; Gallimore et al., 2011a). It is reported also that the rate of the evolution of some products was higher for aqueous particles than dry particles (Najera et al., 2010; Gallimore et al., 2011a; Chan and Chan, 2012).

6.4.2 Chemical characterization of aged MA aerosol

By analogy to the OL-O_3, on the basis of the intermediates observed, and according to literature (Najera et al., 2010; Gallimore et al., 2011a; Chan and Chan, 2012), MA obeys similar reaction pathways to that of OL with a dominant difference in the abilities of the decarboxylation and polymerisation processes between the two acids. MA and corresponding oxidation products undergoe decarboxylation easily (Shende and Levec, 1999; Oliviero et al., 2001). In a corresponding study, analysis of the gas phase of MA-O_3 HR has shown the formation of CO_2 which was attributed to the consecutive decarboxylation reactions from the products to CO_2 (Oliviero et al., 2001). Conversely, decarboxylation for OL without the use of a catalysis at elevated temperature is difficult (Na et al., 2010). On the other hand, the current study shows that polymerization products involving the parent MA molecule were indiscernible in the MA-O_3 HR possibly due to the molecular space hindrance of MA structure.

As it common in the ozonolysis of unsaturated organic species, an unstable POZ is produced which either isomerizes or decomposes to form an ECI and glyoxylic acid (GA). The ECI stabilises to CI which also isomerizes to form products in the condensed phase such as oxalic acid (OxA), or in the gas phase such as formic acid (FA) and CO_2. In a similar fashion to OL-O_3 HR, a series of secondary reactions involving the CI and the earliest products formed is expected.

By means of ATOFMS analysis of pure dry and aqueous MA particles and aged aqueous particles, only few peaks were observed in the mass spectra of aqueous MA particles following reaction with O_3. The limited observed changes in the mass spectra of aged MA is attributed to the low sensitivity of the ATOFMS to oxidation products within the aerosol phase which are expected to be formed at low concentrations under the experimental conditions of this study. It is likely also that the products are converted through the series of the secondary chemical reactions

to form lower molecular mass intermediates which eventually decompose to carbon dioxide following the evolution of the primary products (Oliviero et al., 2001).

The proposed mechanisms and products of aqueous MA-O_3 HR are shown in scheme 6.9. Averaged representative mass spectra obtained for dry MA, aqueous MA and aged aqueous MA aerosols are shown in Figure 6.20. Each data set corresponds to 500 averaged mass spectra of particles.

For both dry and aqueous aerosols spectra the characteristic particle-phase features at m/z -115 and -231 appear to indicate the singly deprotonated (M 116) and the singly deprotonated dimer of MA (M 232), respectively. In wet unprocessed MA aerosols, the additional feature observed at m/z -133 and m/z +19 can be taken to be indicative of MA solvation and are assigned, respectively, to $[M\text{-}H+H_2O]^-$ and $H3O^+$. On ageing aqueous MA aerosol, the corresponding peaks of unprocessed aerosol are still visible but show an apparent decrease in the relative intensity suggesting significant consumption of MA by ozone.

Scheme 6.20 shows subtle appearance of few new peaks on oxidation. The peak at *m/z* -73 is proposed to the deprotonated M-H of GA (M 74). However, the measured peak at *m/z* -89 indicates the formation of OxA (M 90) from the direct isomerization of the CI or via the secondary reaction route of CI with water. OxA might also be routed from the dehydration process of the oxidation product hydroxyacetyl hydroperoxide (HAHP) formed via the addition reaction of water to the CI. Under elevated humid conditions i.e. aqueous MA particles, water molecules are added to the CI forming HAHP (Shende and Levec, 1999; Najera et al., 2010; Chan and Chan, 2012). It should be pointed out that HAHP was not detected in this study possibly due to its low concentration or low ATOFMS sensitivity towards it. However, HAHP

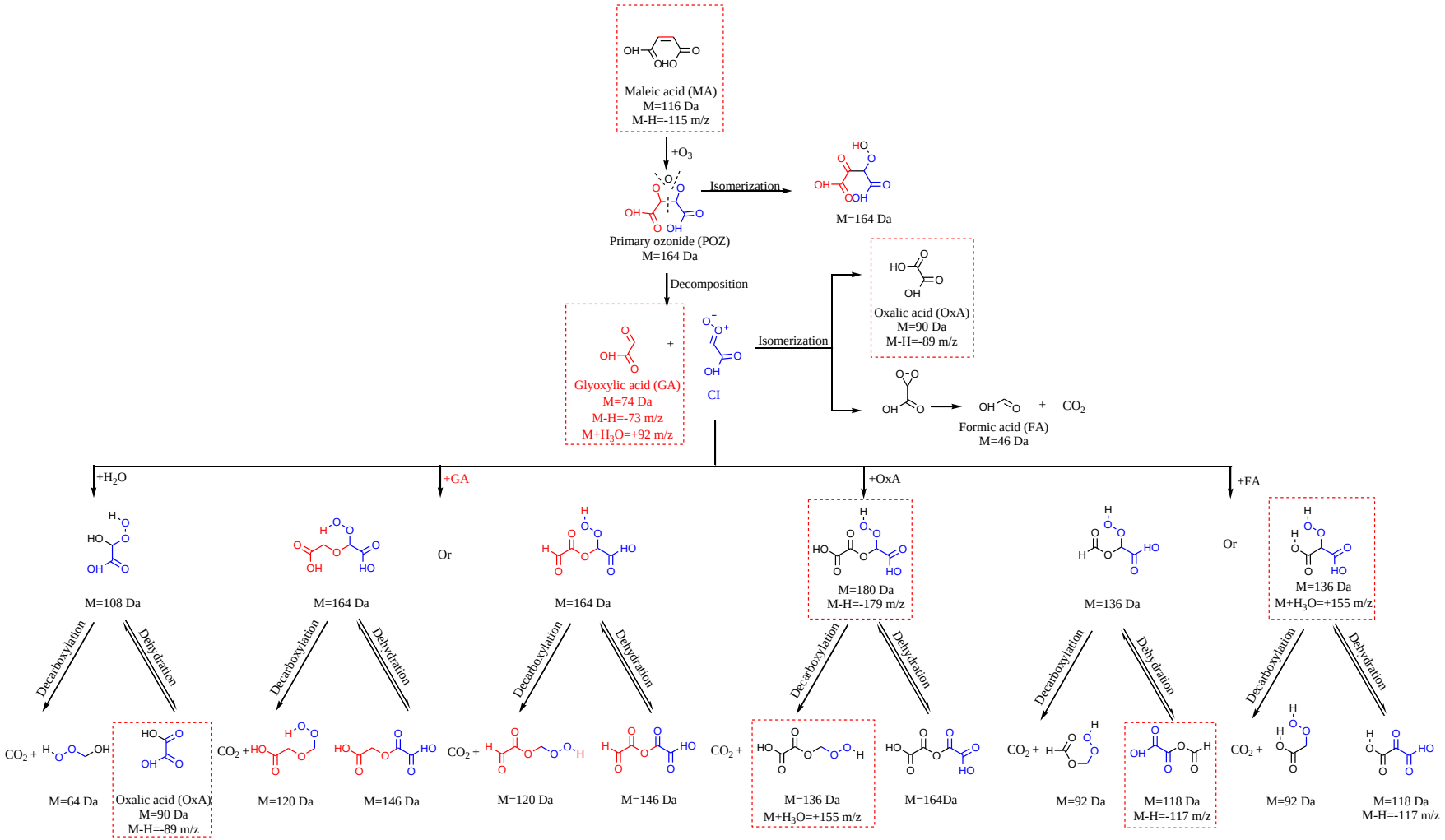

Scheme 6. 9 Proposed reaction pathways and oxidation products for MA-O_3 HR. Observed products are indicated in dashed square

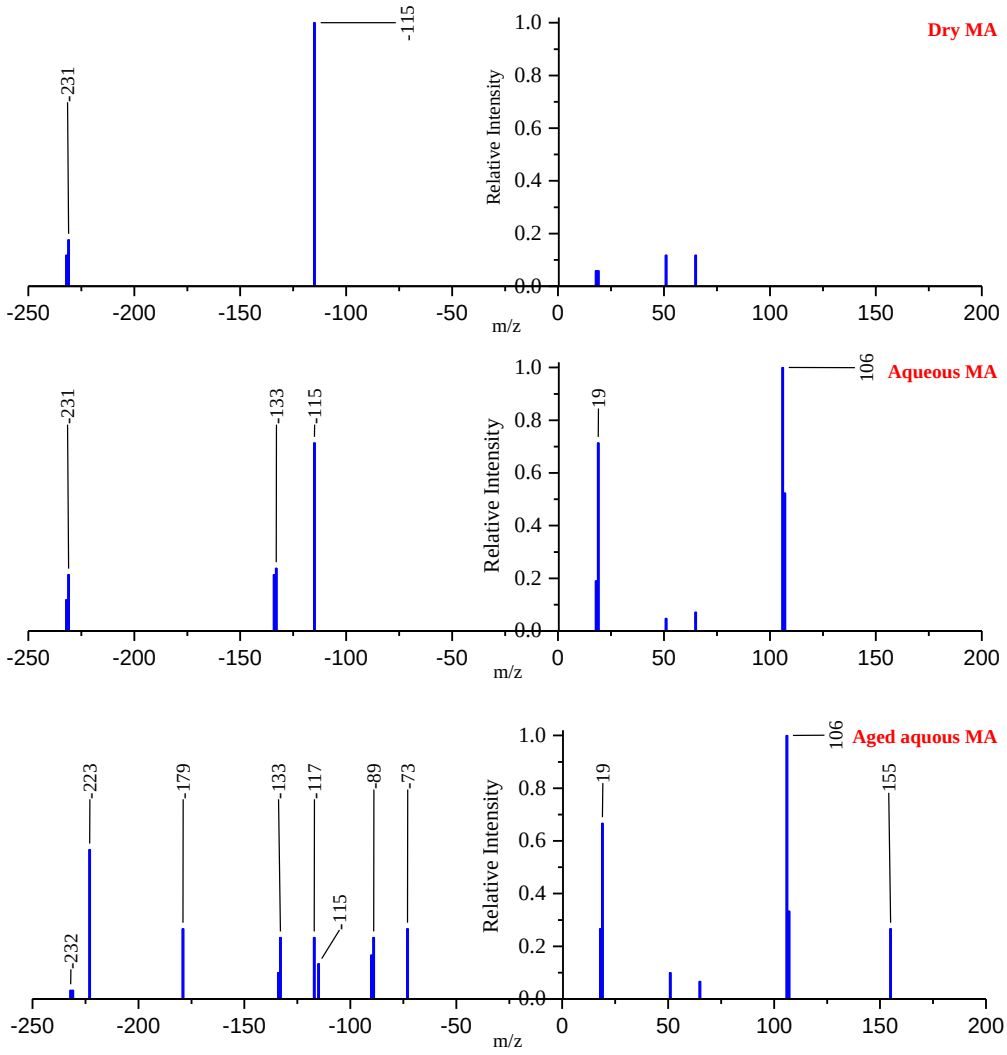

Figure 6. 20 Averaged mass spectra of: (a) pure dry MA (RH 10 ±1.0%), (b) pure wet MA (RH 92.5 ± 1.5 %), and (c) aged wet MA (RH 92.5 ± 1.5 %) aerosols.

was frequently reported and proposed as an oxidation product for MA-O_3 HR (Najera et al., 2010; Chan and Chan, 2012). The peak, m/z -179, could potentially result from the direct reaction between the CI and the OxA, the decarboxylation product of which appears in the positive ionization spectra at m/z +155 attributed to M+[H_3O^+]. Some observed m/z peaks in a related study maybe speculated to different compounds and hence different reaction routes were proposed (Gallimore et al., 2011a). However, it is worth noting that the proposed oxidation

products and reaction pathways in this study are explained primarily on the base of the reactivity of the initially formed CIs and observed m/z peaks.

6.5 BES-OH HR system

6.5.1 Physical characterization of aged BES aerosol

Figure 6.21 illustrates measurements of the physical study of the BES-OH HR system.

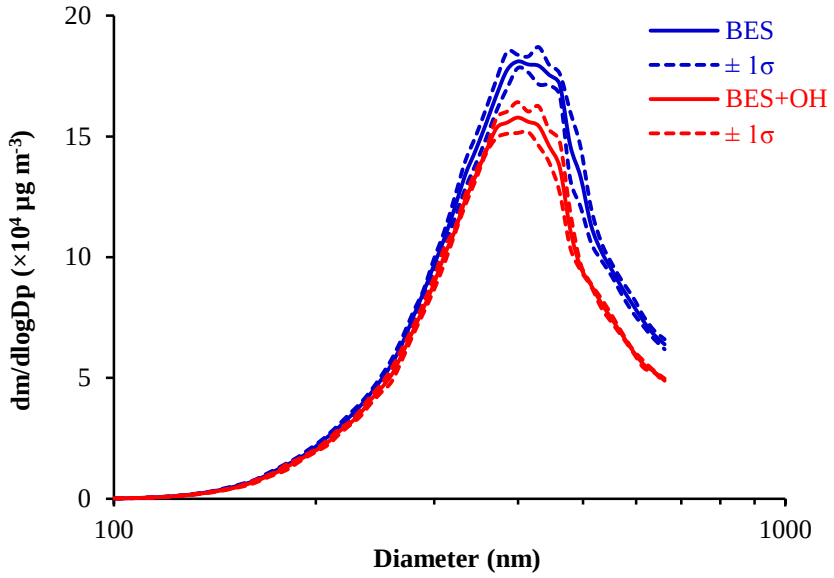

Figure 6. 21 Particle size distribution of 10 averaged samples for pure and oxidised BES aerosol oxidised at RH 65.0 ± 0.4%.

A decrease in the total organic mass of about (15.6 ±2.0)% was measured on exposure to ·OH. As observed for the OL-O_3/OH HR and MA-O_3 HR, the results of BES-O_3 HR indicate appreciable loss of particles mass on oxidation. George et al (2007) reported a decrease in particles volume of about 17% at a comparable OH exposure to the current study. The authors attributed the observed changes to the release of oxygenated volatile organics from the particles and the formation of oxidized products mainly containing carboxylic groups (George et al., 2007).

6.5.2 Chemical characterization of aged BES aerosol

Unfortunately, the spectra of pure and processed BES particles showed only the presence of the NBS signals. The reason for ATOFMS poor detection of BES aerosol is currently unclear but it is possible that NBS did not work well in the case of dry BES aerosol where the organic solvent, methanol, is necessary to solubilise the dye NBS in BES. This can be explained as the NBS/BES mixed particles aerosol passes through the silica dryers decreasing the miscibility of NBS and pure BES and resulting in two immiscible dry pure particles, solid NBS particles which are detectable by ATOFMS and liquid BES particles which are undetectable by ATOFMS. Although the solubility of the laser dye NBS in individual pure liquids of BES and OL is not known, a simple solubility test of NBS in OL and BES pure liquids showed that NBS is more soluble in OL. This might indicates better optical properties of dry OL particles making them absorb enough energy in the ionisation region and thus measurable in the ATOFMS. However, in the case of BES and in the circumstance of solvent absenteeism the NBS/BES components are less miscible and therefore dry BES are optically not strong enough to absorb energy resulting in poor detection of the particles.

6.6 Summary

The system of OL-O_3 HR, OL-OH HR, MA-O_3 HR, and BES-OH HR were chosen to investigate the heterogeneous particle-phase reaction as simplified cases simulating atmospheric conditions. Individual system was characterised physically using SMPS and chemically using ATOFMS. Generally, results demonstrate physical and chemical changes of particles on oxidation. The observed decrease in particles size and the corresponding mass loss of particles mass is attributed to the formation of oxygenated volatile products on oxidation. The fates of the oxidation products

from individual system are either volatilization to the gas phase or particle partitioning of highly oxygenated products.

In the case of OL-O_3 HR, OL reactivity showed RH and size dependent with more OL destruction and further formation of HMW compounds observed in the absence of the water at larger size particles. Although the thin layer OL coating experiment by Katrib et al (2004) and the millimeter size OL droplet study by Hung and coworkers (2005) have suggested the influence of the particle size on the reaction pathways, the current work reports explicitly a particle size dependence in the OL-O_3 HR studies as a major finding. Oligomers formation of high molecular weight up to 1524 Da was proposed based on measured ATOFMS signals (see table D-1, appendix D). This is much higher than molecular weight for unidentified HMW products, which was 1023 Da (Hung and Ariya, 2007).

The results of OL-OH HR showed that OL molecules react with a number of OH radicals as a result of a chain reaction initiated by OH addition reaction to the double bond of OL. H-abstraction reaction is also found to be responsible for the formation of products characterised by multiple oxygenated functional groups. In comparison to the OL-O_3 HR, no HMW were measured when OL was reacted with OH radicals.

Unreacted dry and wet MA aerosols showed different mass spectral features suggesting MA solvation at wetter condition. No change on the mass spectra was observed when dry solid MA aerosol was exposed O_3. However, ozonolysis at high RH showed the appearance of few peaks attributed to the formation of highly oxygenated products.

It is clear from these results that the HR of organic particles has the potential to alter the physical properties and the composition of the phase products which has a number of potentially

important consequences in the role of atmospheric implication. Details of these implications are to follow in chapter 9, section 9.5.

CHAPTER 7 KINETIC STUDY OF THE HETEROGENEOUS REACTION BETWEEN OZONE AND OLEIC ACID

7.1 Introduction

This chapter focuses on the kinetics of the oleic acid ozone heterogeneous reaction (OL-O_3 HR). Firstly, the behaviour of OL particles moving through the fluid in the ACA system is described. Secondly, the adaption of the resistor model to estimate the reactive uptake coefficient of ozone on OL particles is investigated, followed by a theoretical calculation of the rate limiting process in the OL-O_3 HR system. The goal of the adaption of the resistor model is to better understand the oxidative processing of OL by ozone and the parameters that contribute to the overall uptake process. Thirdly, the observed reactive uptake coefficient of ozone on OL aerosols is compared with the modelled reactive uptake coefficient. Finally, the predicted life time of atmospheric OL particles is discussed.

7.2 Theoretical kinetics of OL-O_3 HR

7.2.1 Particles regime in the ACA system

The process of diffusion of a gas to the interface of the particle depends on the relative size of a particle suspended in a gas and the mean free path of the gas molecules around it. This is characterized by the Knudsen number, a dimensionless parameter, Kn (Jacobson, 2005):

$$Kn = \frac{\lambda}{R_p}$$

Eq 7. 1

The Knudsen number, Kn, is defined as the ratio of the mean free path, λ, of the gas to the particle radius, R_p. The mean free path, λ, is the average distance travelled by a gas molecule before it collides with another molecule and it is on the order of ~ 60 nm at standard temperature and pressure (STP, 0°C, 1 atm) for air molecules as well as atmospheric species existing at low concentration with respect to air molecules (Ammann and Pöschl 2007). The following equation is used to calculate the λ (John, 1986):

$$\lambda = \frac{1}{\sqrt{2}\pi\sigma^2 N_g}$$

Eq 7. 2

where σ is the diameter of the gas molecule, for O_3 diameter 0.4 nm (Vieceli et al., 2004), N_g is the number concentration of gas molecules in molecules cm^{-3}, for air N_g is 2.45×10^{19} molecules cm^{-3} estimated using the ideal gas law as described in chapter 4, section 4.2.2.3. The mean free path for O_3 molecules using equation Eq 7.2 is 57.4 nm, calculated for the experimental conditions of this study.

In the case where particle diameter (D_p) is much larger than λ of the surrounding gas molecules, the gas behaves as a continuous fluid, continuum regime ($D_p >> \lambda$, $Kn << 1$), and the flow of the gas is limiting. However, for particle size smaller than λ of the surrounding gas molecules, gas molecule move discretely around the particles which resembles another gas molecule, kinetic regime ($D_p << \lambda$, $K >> 1$) and the interfacial mass transport is limiting. In the transition regime, where particle size equals the mean free path of the gas molecules, ($D_p \approx \lambda$, $Kn \approx 1$), both gas phase diffusion and interfacial mass transport can be limiting (Seinfeld and Pandis, 2006).

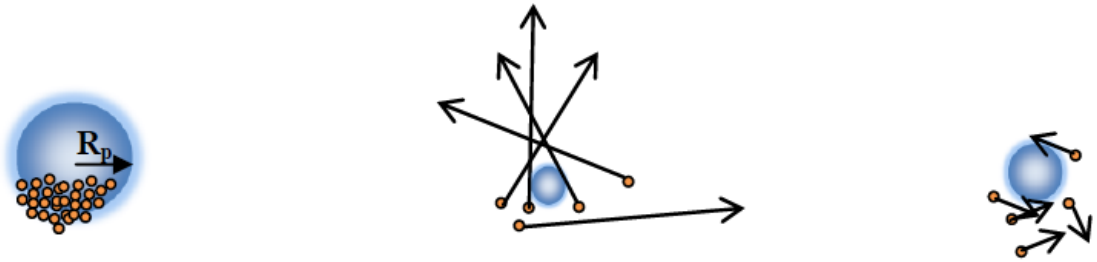

Figure 7. 1 Schematic of the three regimes of suspending fluid-particle interactions: (a) continuum regime (Dp>>λXi), (b) kinetic regime (Dp<<λXi), and (c) transition regime (Dp≈λXi).

The calculated range of Kn for the polydisperse OL aerosol is 7.6-0.2 corresponds to particles diameter range of 15.1-661 nm, this means that the particles size falls in the transition regime, where the mean free path of diffusing O_3 molecules is of the same order as the OL particle diameter, ($D_p \approx \lambda$, $Kn \approx 1$), the gas is thus behaves as a transition fluid.

7.2.2 The resistor model

The resistor model is a common model that has been widely applied in laboratory studies of heterogeneous reactions (King et al., 2008). The resistor model focuses on condensed phase species depletion and provides description of chemical reactions and mass transport based on kinetic theory of gases, condensed phases and interfaces for both simple and complex systems. It treats individual processes in a heterogeneous reaction analogously to an electrical circuit represented by a conductance, Γ. The resistor model takes into account the contribution of each process to the overall rate of the uptake of the gas-phase species by particles, including gas-phase diffusion (Γ_g), thermal accommodation (α) and reaction at the surface, and the solvation (Γ_{sol}) and reaction (Γ_{rxn}) in the bulk. The inverse of each conductance, 1/ Γ, is a resistance to the

uptake (conductance = (resistance)$^{-1}$) that represents one of the processes shown in Figure 7.1. Aerosol chemical kinetic of each process is, therefore, identified, quantified, added in a similar way to resistors in an electric circuit, and related to the overall particle phase species uptake coefficient, γ:

$$\frac{1}{\gamma} = \frac{1}{\Gamma_g} + \frac{1}{\alpha} + \frac{1}{\Gamma_{rxn} + \Gamma_{sol}}$$

Eq 7. 3

where γ, is the net probability of the reaction uptake, $1/\Gamma_g$ is the resistance of the gas-phase diffusion, $1/\alpha$ is the resistance to mass accommodation coefficient, $1/\Gamma_{rxn}$ is the resistance of the reaction in the bulk liquid phase, and $1/\Gamma_{sol}$ is the resistance of the solubility and diffusion in the bulk liquid phase. Except for $1/\alpha$, which is by definition already normalized (as it will be defined shortly), each of the terms in the equation above has been normalized and made unitless by dividing by the number of collisions per unit area per second of gas with surface:

$$\frac{N_g \bar{c}}{4} = \frac{N_g}{4}\sqrt{\frac{8RT}{\pi M}} = N_g\sqrt{\frac{RT}{2\pi M}}$$

Eq 7. 4

Where, N_g is the gas concentration (moleculescm^{-3}), $\bar{c}$ is the average molecular speed of the gas molecules, R is the gas constant (8.314 J K^{-1} mol^{-1}), T is the temperature (K), and M is the molecular weight of the gas.

7.2.3 Reactive uptake of O_3 by OL particles using the resistor model

To account for the contribution of the processes involved in the overall uptake of the ozone by OL particles, the inverse of each consecutive resistance processes, $1/\Gamma$, is calculated as described below.

Resistance to the gas-phase diffusion, $1/\Gamma_g$

The first step in the heterogeneous reaction is the diffusion of the O_3 gas into the interface. The diffusion process is determined by the gas-phase diffusion coefficient (D_g) and the frequency of the gas-surface collision. The number of collisions of a gas molecule per unit area of a particle per second is given as:

$$\text{Number of collisions of a gas molecule per unit area of a particle per second} = \frac{N_g \bar{c}}{4} \quad \text{Eq 7. 5}$$

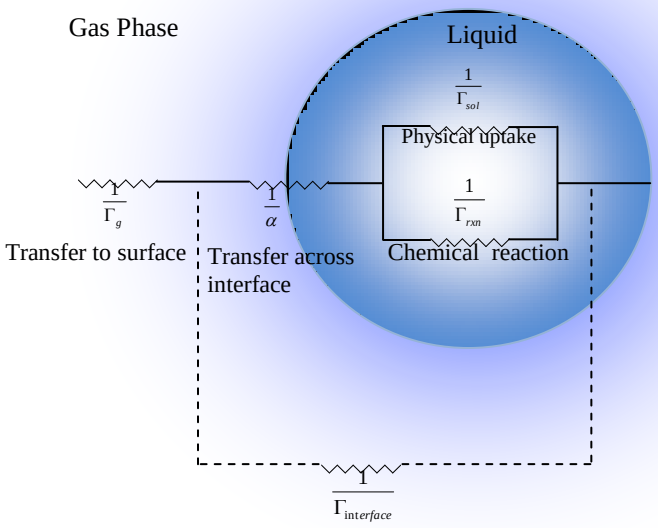

Figure 7. 2 Schematic of resistance model of gas-droplet interaction showing: $1/\Gamma_g$: the resistance of the gas-phase diffusion, $1/\alpha$: the resistance to mass accommodation coefficient, $1/\Gamma_{rxn}$: the resistance of the reaction in the bulk liquid phase, 1/sol: the resistance of the solubility and diffusion in the bulk liquid phase and $1/\Gamma_{interface}$: the reaction of the gas at the interface (Finlayson-Pitts and Pitts Jr, 2000b).

The number of O_3 molecules diffusing to the particle surface is given as:

$$4\pi D_g R_p N_g /(1+\lambda K_n)$$

Eq 7. 6

The formulation $(1+\lambda K_n)$ is suggested to account for gas molecules diffusivity in the transition regime and approximation values of λ are provided in literature (Finlayson-Pitts and Pitts Jr, 2000b):

$$\lambda \approx \frac{1.33+0.71/K_n}{1+1/K_n}$$

Eq 7. 7

Assuming OL particles are perfect spheres, the rate of diffusion to the surface per cm^2 per second can be inferred from the following equation:

$$(4\pi D_g R_p N_g /(1+\lambda K_n))/4\pi R_p{}^2 = D_g N_g /((1+\lambda K_n)R_p)$$

Eq 7. 8

where D_g is the gas-phase diffusion coefficient, for most atmospheric oxidants such as O_3, OH, and NO_x, $D_g = 1.8\times10^{-5}$ m^2 s^{-1} (King et al., 2009; Shiraiwa et al., 2011). N_g for O_3 N_g is 5×10^{14} molecules.cm^{-3}, and R_p is the particle radius ($2R_p=D_p$) of OL particles. The overall normalized resistance to the rate of collisions of the gas-phase diffusion for the transition regime, $1/\Gamma_g$, can be found as:

$$\frac{1}{\Gamma_g} = (1+\lambda K_n)\frac{\bar{c}D_p}{8D_g}$$

Eq 7. 9

where $\bar{c}$ is O_3 average molecular speed (360.2 ms^{-1}) calculated from the following equation:

$$\bar{c} = \sqrt{\frac{8RT}{\pi M}}$$

Eq 7. 10

where R is 8.314 J K^{-1} mol^{-1}, T is 294 K, and M is the molecular weight of O_3 (0.048 kg mol^{-1}).

Resistance to mass accommodation, 1/α

Following gas diffusion to the interface, gas molecules are taken up at the surface. They enter the interface region and then the bulk of the liquid. The mass accommodation coefficient (α), is used to describe the efficiency of the gas molecules at the interface. It is defined as the ratio of the number of gas molecules taken up by the interface to the number of collisions of gas molecules and the particles surface:

$$\alpha = \frac{\text{Number of gas molecules taken up by the surface}}{\text{Number of gas-surface collisions}}$$

Eq 7. 11

No value has been reported for the mass accommodation coefficient for ozone on an organic droplet and the value reported for aqueous droplets, $\alpha = 10^{-2}$, is used instead. (King et al., 2008).

Resistance to reaction in the liquid phase (Γ_{rxn})

Assuming irreversible reaction between O_3 and OL molecules in the bulk liquid, the normalised resistance to the reaction in the liquid phase, $1/\Gamma_{rxn}$:

$$\frac{1}{\Gamma_{rxn}} = \frac{\bar{c}}{4HRT\sqrt{D_l k}}$$

Eq 7. 12

where H is the Henry's law constant (H for O_3 between air and an organic layer is assigned an estimated value 480 mol m^{-3} atm^{-1}) (King et al., 2009), R is the gas constant (8.204×10^{-5} atm m^3 mol^{-1} K^{-1}), T is the temperature in Kelvin (294 K), D_l is the diffusion coefficient in the liquid phase (for O_3 in the gas phase and organic liquid $D_l=1.0\times10^{-9}$ m^2 s^{-1}) (King et al., 2009), k ($=k_2[OL]$) is the first order rate constant (s^{-1}) for the reaction of O_3 with OL assuming uniform concentration of OL (fast OL diffusion) and a steady state $[O_3]$ concentration ($d[O_3]/dt=0$). k_2, the second order rate coefficient for O_3 reacting with oleic acid, 10^6 $M^{-1}s^{-1}$.

Resistance to solubility and diffusion in the liquid phase (Γ_{sol})

Assuming no reaction is taken place in the bulk liquid and dissolved gas molecules to be in Henry's law equilibrium ($H=[X]/P_x$), the rate of transfer of the gas across the interface directly depends on the gas liquid-phase concentrations between the interface and the bulk as well as inversely on the exposure time of liquid droplets to the gas. This is because as the uptake occurs, evaporation back to the gas phase becomes important. Normalised resistance of gas solubility, Γ_{sol}, can be expressed as:

$$\Gamma_{sol} = \frac{4HRT}{\bar{c}}\sqrt{\frac{D_l}{\pi t}}$$

Eq 7. 13

where H, R, T, $\bar{c}$ and D_l are as described above and t in this study case is 147 s.

The overall calculated probability that the collision between O_3 molecule and OL particle leads to a reaction, γ, was calculated using equation Eq 7.3 (Finlayson-Pitts and Pitts Jr, 2000b) for the entire range of the polydispaerse aerosol and found to be in the order of ~ 4.2×10^{-3}.

7.2.4 Rate limiting process in the OL-O_3 HR

The table below compares the relative speeds of different processes in the OL-O_3 HR for this study. The calculated characteristic time of each step involved in the reaction allows identifying the rate determining process for this particular study conditions.

Table 7. 1 Characteristic times associated with the uptake of ozone into liquid OL particle of 300 nm in diameter and reaction in the bulk phase.

Process	Expression for characteristic time (Finlayson-Pitts and Pitts Jr, 2000b)	Characteristic time (s)
Gas-phase diffusion	$\frac{R_p^2}{\pi^2 D_g(O_3)}$	1.3×10^{-10}
Mass accommodation	$D_l(O_3)\left(\frac{4HRT}{\alpha u_{av}}\right)^2$	1.7×10^{-15}
Organic phase diffusion	$\frac{R_p^2}{\pi^2 D_l(O_3)}$	2.3×10^{-6}
Organic phase reaction	$\frac{1}{k_2[OL]}$	3.2×10^{-7}

From the table, gas diffusion and mass accommodation processes of O_3 into OL particles are fast processes and thus not rate limiting processes. However, the O_3 phase diffusion and reaction are slower and therefore likely the rate determining processes.

7.3 Measured kinetics of OL-O_3 HR

Many previous studies measured reaction kinetics of OL-O_3 HR by monitoring the loss of the gas-phase O_3 (Moise and Rudich, 2002; Thornberry and Abbatt, 2004; Knopf et al., 2005) In the present work, the kinetics of the OL-O_3 HR was studied by monitoring the change in the OL

condensed phase signal. Such approach defeats limitations related to overvaluing reaction uptake associated with other gas-phase O_3 losses due to nonreactive uptake such as physical adsorption and reactive uptake by the liquid vapour which are both indistinguishable from the loss linked to reaction in the bulk of the liquid (Smith et al., 2002b).

The kinetics of the OL-O_3 HR was measured by following the total peak area signals of OL at m/z -281 collected from ATOFMS spectral data sets for reacted and unreacted OL particles. The reaction time was varied by using three different AFT volumes (section 2.2.5) while keeping the total flow in the AFTs constant at 3.5 slm which results in reaction time of 20, 50 and 135 s. O_3 concentration was held at a steady level of 20 ±0.15 ppm (5±0.04 x10^{14} molecules cm^{-3}) and in excess of OL total concentration by at least a factor of 2.3 such that O_3 concentration is assumed to be constant at all time and hence in steady pseudo state. The experiment was performed at two relative humidities, RH 0.5 ± 0.02% and RH 65.0 ± 0.2%.

7.3.1 Measured reactive uptake of O_3 by OL particles

The kinetics were evaluated using a model that has been adopted successfully in a number of related studies (Morris et al., 2002; Smith et al., 2002b; Hearn and Smith, 2004; Ziemann, 2005). The mathematical formulation of the model is:

$$\left[\frac{Signal_t}{Signal_{t=0}}\right]^{1/2} = 1 - [H(D_l k_2)^{1/2}][3P/2R_p[OL]_0^{1/2}]t$$

Eq 7. 14

where $[Signal_t/Signal_{t=0}]$ is the ratio of the mass spectral signals of peak area at m/z -281 at time t and 0. As defined earlier, H is the Henry's law solubility constant of O_3 in OL, D_l is the diffusion

coefficient of O_3 in OL, 1.0×10^{-9} m^2 s^{-1}, K_2 is the second-order rate coefficient for OL-O_3 HR (10^6 $M^{-1}s^{-1}$), while P is the partial pressure of O_3 (20 ppm, 2.0×10^{-5} atm), R_p is the particle radius taken as the mode radius of the polydisperse aerosol (1.5×10^{-7} m, and $[OL]_0$ is 3.16 M (OL density 0.891 g cm^{-3} and MW=282.5 g mol^{-1}) (Smith et al., 2002a). A plot of $[Signal_t/Signal_{t=0}]^{½}$ *versus* the reaction time, t, yields a non-linear graph, Figure 7.3, with an initial steep slope that falls with time. From equation Eq 7.14, the linear regression of $[Signal_t/Signal_{t=0}]^{½}$ *versus* the reaction time, t, yields a slope, b, of the line equal to:

$$[H(Dk_2)^{1/2}][3P/2R_p[M_0]^{1/2}]$$

Eq 7. 15

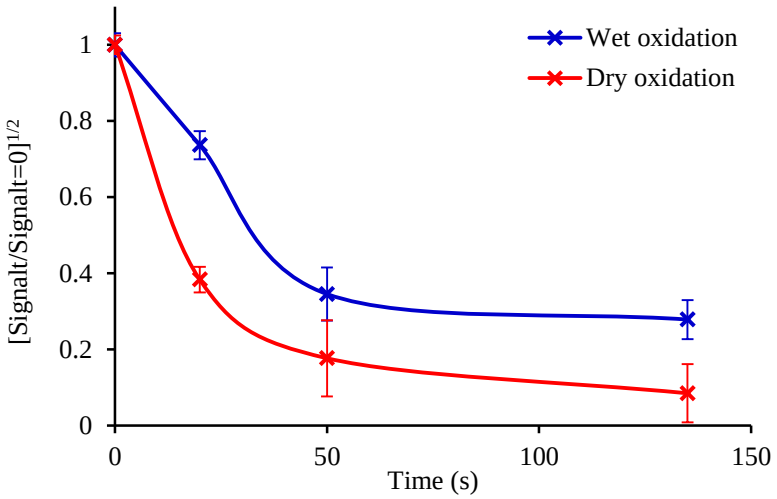

Figure 7. 3 Time-dependent decay of OL from the reaction of O_3 with OL particles at dry condition (RH 0.5 ± 0.02%) in blue and at wet condition (RH 65.0 ± 0.2%) in red.

The reaction probability, γ, can be calculated using the following formula (Ziemann, 2005):

$$\gamma = 4H(Dk_2)^{1/2}[RT(Y_{t=0})^{1/2}/c]$$

Eq 7. 16

From equations Eq 7.15 and Eq 7.16 and the value of the slope in Figure 7.3, γ can be calculated from the following rearranged equation:

$$\gamma = 4\left[\frac{2R_p b}{3P}\right]\left[\frac{RT}{c}\right][OL]_0$$

Eq 7. 17

The resulted γ values are $(2.3\pm0.06)\times10^{-5}$ and $(2.0\pm0.05)\times10^{-5}$ for dry and wet oxidation of OL, respectively. The underestimation of observed reaction probability as compared to calculated value ($4.2x10^{-3}$) reveals a reduced measured O_3 uptake to the particles. The imperfect linear trend of $[Signal_t/Signal_{t=0}]^{½}$ *versus* the reaction time in Figure 7.3 above indicates a change in the reaction rate as oxidation progresses which implies a decrease in reaction probability over time. This trend suggests possible changes in particle composition as products evolved resulting on deceleration of the oxidation process and thus a decrease in the reaction uptake of O_3. This is consistent with the surface reaction of OL particles which was concluded in chapter 6, section 6.2.3.1 and theoretically explained in section 6.2.4. The slightly lower observed γ at wetter condition indicates that the presence of water molecules minimises the secondary reaction of OL thus the smaller observed mass losses during the wet oxidation compared to the dry oxidation. Indeed analysis of the mass spectra of aged OL particles at wetter conditions (chapter 6, section 6.2.3.2) reveals the presence of the secondary oxidation product resulted from the reaction between CI1 and water molecules resulting in less OL destruction at high relative humidity.

To estimate the change in the change in γ over time, the slope was calculated at 10 s interval points from the start of the reaction (Figure 7.3) using OriginPro 9.0. The values of the slopes were used to calculate γ using equation Eq 7.17. Figure 7.4 below represents the estimated decay of γ over time.

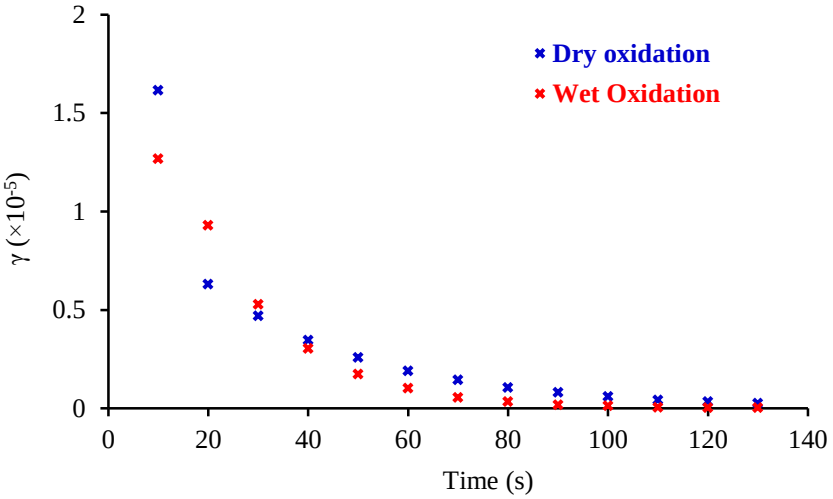

Figure 7. 4 Estimated reaction uptake of O_3 by OL polydisperse particles at 10 s interval points from the start of the dry oxidation reaction (in blue) and wet oxidation reaction (in red).

The clear downward trend of γ from 1.6×10^{-4} to 2.5×10^{-6} and from 1.3×10^{-4} to 2.1×10^{-7} at dry and humid condition, respectively, indicates that the rate of the OL-O_3 HR decreases with time. The observed behaviour of γ with time is most likely to be due to the continued dilution of OL reactant in the particles surface as the oxidation products evolved with time. There is evidence that the phase, matrix and viscosity of aged aerosol have considerable effect on the kinetics of O_3 uptake (Knopf et al., 2005; Pope et al., 2010a**;** Pfrang et al., 2011; Chan and Chan, 2012; Hosny et al., 2013). Generally, literature studies of reaction uptake of O_3 by OL show poor agreement between one study with another. Laboratory set ups, reactor design and operating conditions strongly affect the measurement of the reaction uptake. Table 7.2 shows some reported reactive uptake of O_3 by OL.

Table 7. 2 Reported literature values for reactive uptake of ozone by oleic acid.

Methodology	Particle size	O_3 concentration Molecules cm^{-3}	Detection	Reactive uptake	References
AFT	15-660 nm	5×10^{14}	ATOFMS	Calculated 4.2×10^{-3} Measured (RH 0.8%) 2.3×10^{-5} (RH 65.0%) 2.0×10^{-5}	Current study
AFT	800 nm	$(2\text{-}3)\times10^{15}$	CIMS	$(7.5\pm1.2)\times10^{-4}$	(Hearn and Smith, 2004)
CFT	-	1×10^{14}	CIMS	$(8.3\pm0.2)\times10^{-4}$	(Moise and Rudich, 2002)
AFT	200-600 nm	2×10^{14}	AMS	$(1.6\pm0.2)\times10^{-3}$	(Morris et al., 2002)
AFT	680 nm to 2.45 μm	3.4×10^{15}	SPMS	$(7.3\pm1.5)\times10^{-3}$-$(0.99\pm0.09)\times10^{-3}$	(Smith et al., 2002b)
AFT	300-600 nm	$2.5\text{-}25\times10^{14}$	CIMS	$(1.38\pm0.06)\times10^{-3}$ $(8.8\pm0.5)\times10^{-4}$	(Hearn et al., 2005)
CFT	-	$\sim1.3\times10^{12}$	CIMS	$(8.0\pm1)\times10^{-4}$	(Thornberry and Abbatt, 2004)
EC	200 nm	7×10^{13}	TDPBMS	$(6.1\pm5)\times10^{-4}$	(Ziemann, 2005)
AFT	1-15 μm	2.5×10^{14}	AMS	$(1.25\pm0.2)\times10^{-3}$	(Katrib et al., 2005a)
CFT	-	$2\text{-}4\times10^{12}$	CIMS	$(6.4\pm0.05)\times10^{-5}$	(Knopf et al., 2005)
OL monolayer on pendant drop in a reaction chamber	Droplet surface area 0.1-0.15 cm^2	2×10^{14}	ADSA	$(2.6\pm0.1)\times10^{-6}$	(Gonzalez-Labrada et al., 2007)

ADSA axisymmetric drop shape analysis, AFT: aerosol flow tube, AMS: aerosol mass spectrometer, CFT: coated flow tube, CIMS: chemical ionization mass spectrometer, SPMS: single-particle mass spectrometer, TDPBMS thermal desorption particle beam mass spectrometer.

7.3.2 Atmospheric life time of OL particle

The lifetime for the pure laboratory generated OL particles with respect to ozonolysis can be estimated by the effective rate constant of the pseudo first order reaction (Ziemann, 2005):

$$\ln\left[\frac{Signal_t}{Signal_{t=0}}\right] = -k_{eff}\,t$$

Eq 7. 18

From equation Eq 7.18, the value of k_{eff} for OL particles is the coefficient of t. From the slopes of the lines in Figure 7.5, the value of k_{eff} is 0.0329 and 0.0181for dry and wet particles. However, these values are measured at ozone mixing ratio of 20±0.15 ppm for OL particles in the size range of 15-660 nm. The corresponding values for a polluted atmosphere containing 100 ppb of ozone would be reduced by a factor of 1:20. Therefore, the estimated life time of OL is 1.7 and 3.1 hours, at dry and wet conditions, respectively.

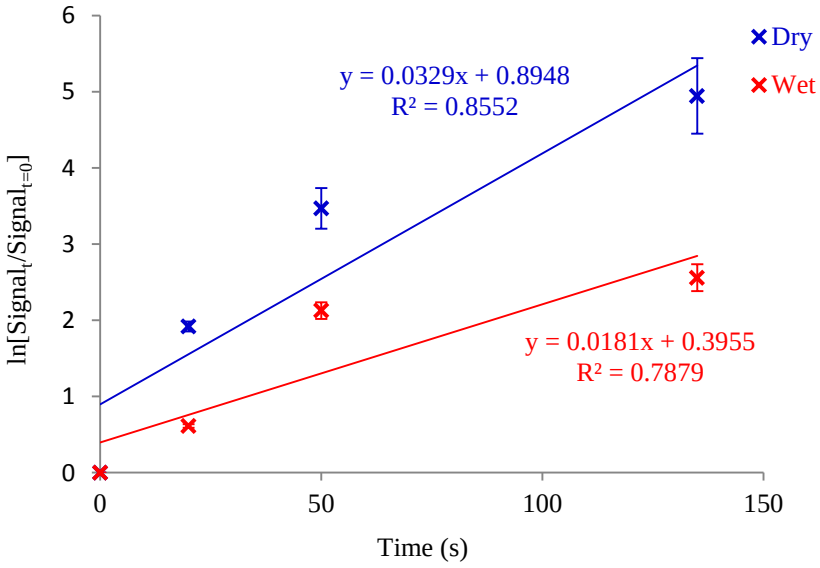

Figure 7. 5 ATOFMS signal measured for aged OL particles with time under dry condition (RH 0.5 ± 0.02%) in blue and at wet condition (RH 65.0 ± 0.2%) in red.

It is noted that reported life time of OL at atmospheric mixing ratio of 100 ppb ozone is in the order of seconds to minutes (Morris et al., 2002; Knopf et al., 2005; Ziemann, 2005; Zahardis and Petrucci, 2007). Ziemann (2005) estimated a lifetime of ~30 minutes for pure OL and ~15 hours

for mixed OL with monocarboxylic acid particles. However, a much shorter life time for pure OL than measured here was reported by Morris and co-worker (2002) who estimated a lifetime of a few minutes.

The anomaly between longer field atmospheric life time reported at an order of days (Zahardis and Petrucci, 2007) and shorter laboratory life time of OL is likely due to the fact that OL in ambient aerosols is found in particles with high viscousity semi-solid mixtures in which the diffusive transport of both ozone or OL to the surface is slowed down (Knopf et al., 2005; Shiraiwa et al., 2012b). The relatively longer laboratory lifetime reported for OL in this study indicates closer results to the reported real atmospheric lifetime. The laboratory experimental conditions applied here gave more reasonable life time for OL.

7.4 Summary

The studied particle size in the OL-O_3 HR system falls in the transition regime, the gas is thus behaves as a transition fluid. Accordingly, the overall calculated γ found to be in the order of ~ 4.2×10^{-3} with the O_3 phase diffusion and reaction processes are the rate determining processes. However, Experimental measurements showed that γ value is $(2.3\pm0.06)\times10^{-5}$ and $(2.0\pm0.05)\times10^{-5}$ for dry and wet oxidation of OL, respectively. The low observed reaction probability as compared to calculated value was taken as an indication of particle surface alteration as products evolved. The estimated life time of OL is 1.7 and 3.1 hours, at dry and wet conditions, respectively.

CHPTER 8 ARTIFICIAL CHEMICAL AGEING OF ATMOSPHERIC PARTICLES

8.1 Introduction

This chapter discusses the applicability of the ACA system on real ambient atmospheric particles. One of the prime objectives in this study is to find evidence of ageing real ambient particles. For all the ambient experiments examined here, the core of the ageing technique is to expose ambient particles to elevated levels of oxidants that equivalent to several days of exposure in the real atmosphere as summarised in chapter 2, section 2.4.

It was hoped that exposing ambient aerosols to high levels of oxidants under the established laboratory ageing conditions will pose measurable changes in the physical and chemical properties of the examined particles. However, most investigated aerosols in the urban environment were found to be dominated by secondary oxygenated species. The urban sites under study and the prevailing meteorological conditions could complicate the ageing process of the particles.

During normal operation, ambient air was introduced continuously to the AFT, mixed with either ozone loaded flow or a blank flow of synthetic air. These flows are allowed enough time to mix in the AFT. If ambient aerosol are mixed with ozone and exposed to UV light at 254 nm, OH radicals are produced and aerosol processed by OH is measured. If, however, ambient aerosol is mixed with air loaded ozone only, aerosol processed by ozone is detected; otherwise unreacted aerosol is characterised. The residence time of the particles in the AFT was maintained at ~135 seconds. Air samples were subjected to oxidation and no oxidation alternatively for 30 minutes each. The methodology behind introducing a sample into the AFT before being measured by the

ATOFMS and the SMPS remained consistent and in line with those outlined in chapter 2, section 2.4.

What follows is a description of experiments sites, examples of measured ATOFMS and SMPS spectra of real ambient particles exposed to oxidants and the predominant meteorological condition during the measurements, and the applicability of the developed ACA system on real ambient particles.

8.2 Experiments sites

The sites selected for the experiment of ageing ambient aerosol were situated at the University of Birmingham campus. Site A at the school of Bioscience building (52°27'1.12" N and 1°56'0.60" W) and site B at the building of Sport and Exercise Sciences (52°26'56.03" N and 1°56'5.72"W) are both typical urban sites located within the University of Birmingham campus about 3.5 km southwest the centre of Birmingham city. The two sites about 500 m apart and are shown in Figure 8.1.

8.3 School of Bioscience building (Site A)

Initially oxidation of ambient particles was conducted from Site A, the School of Biosciences building. The site is situated on the basement floor and has an immediate access to the outside.

Meteorological data during the period of ageing experiments were collected from a local weather station at the University of Birmingham campus. The hourly parameters provided included wind speed, wind direction, temperature and relative humidity. These parameters are presented to support the data interpretation. However, hourly variations in particulate matter with aerodynamic diameter less than 2.5 μm ($PM_{2.5}$) were obtained from the Automatic Urban and Rural Network (AURN) site. The data of this particular size of particles was chosen in accordance to the measured particles by the ATOFMS and the SMPS in the site.

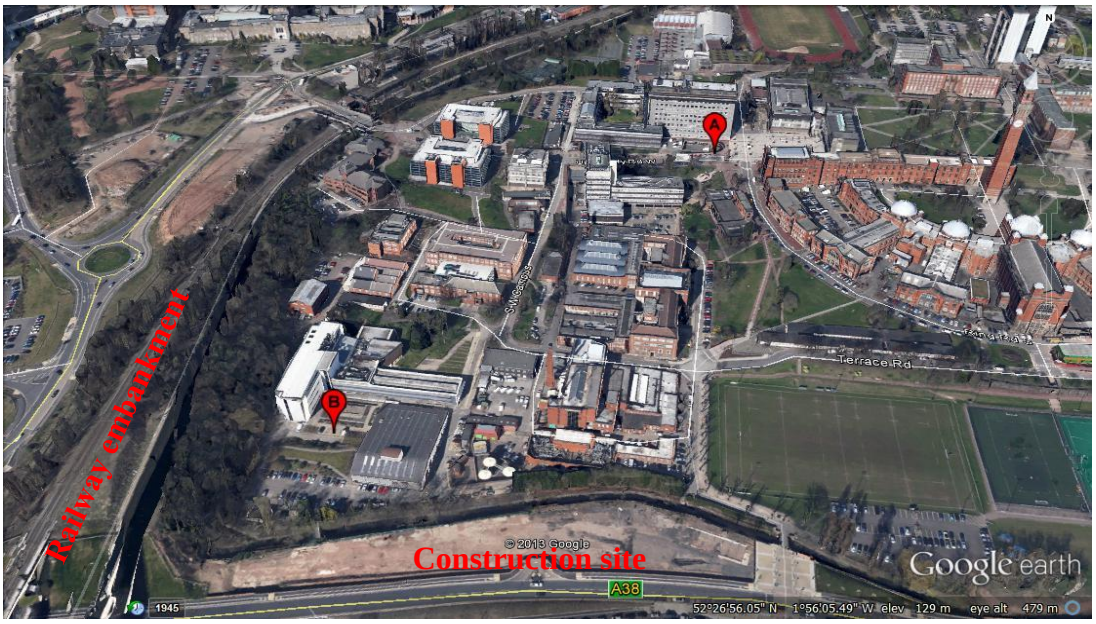

Figure 8. 1 A map showing experiments sites of ageing ambient aerosol, site A: the school of Bioscience building and B: the building of Sport and Exercise Sciences at the University of Birmingham campus.

On the September 14th, 2012, oxidation of ambient particles by ozone was conducted. The time period of the oxidation experiment was characterized by east and east southerly winds with a strength of 1.8-6.3 m s^{-1}. The daytime temperatures and relative humidities ranged from 15.2 to 16.7°C and from 53.4 to 60.8%. On the September 17th, 2012, ambient particles were exposed to high concentration of OH radical. The wind was predominantly north-easterly with strength of 3-6.4 m s^{-1} while temperatures and relative humidities values ranged from 12.7 to16.5°C and from 50.0-78.1%. The atmosphere was characterised by moderately low particulate measurements during the ageing experiments in the investigated days. The UK newly-introduced average exposure for $PM_{2.5}$ is 25 µg m^{-3} (Monks et al., 2012). Wind roses, hourly data of prevailing wind speed, temperature, and relative humidity for the respective experimental periods are shown in Figures 8.2 and 8.3, respectively. The AURN hourly particulate matter data collected for the experiment period is presented in Figure 8.4.

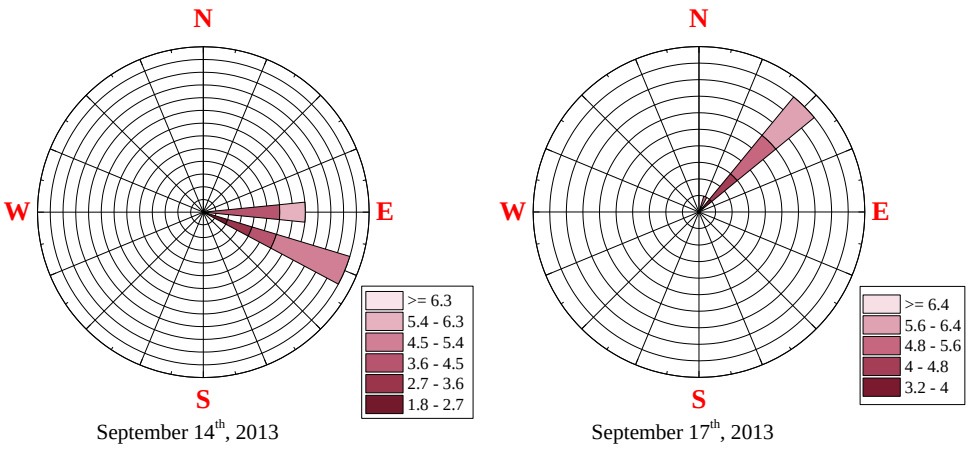

Figure 8. 2 Main wind directions and speeds during the periods of ageing atmospheric particles; 8:00 am to 6:00 pm.

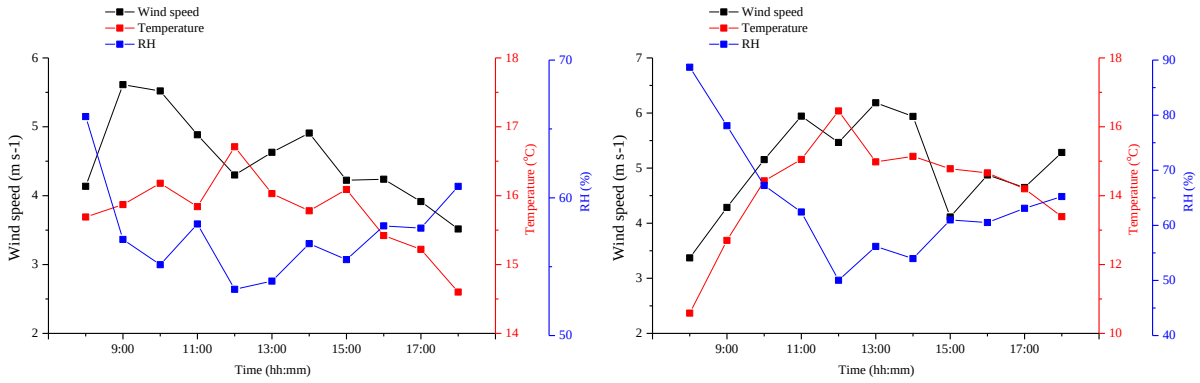

(a) (b)

Figure 8. 3 Variations of wind speed, ambient temperature and relative humidity during the ageing experiment period from 8:00 am to 6:00 pm on the: (a) September 14th 2012 and (b) September 17th 2012.

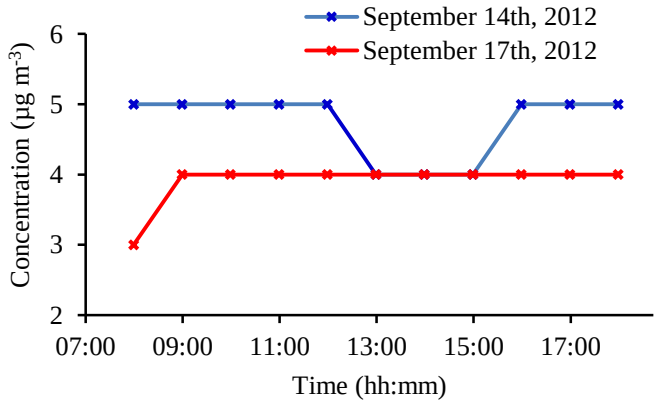

Figure 8. 4 Variations of $PM_{2.5}$ concentrations at site A during the measurement periods.

For ageing experiments, ambient particles were sampled, exposed to ozone or OH radical and characterized using the ATOFMS and the SMPS. In total, six samples were collected for 3 oxidation trials. Figure 8.5 illustrates the averaged mass and size distribution spectra of exposed and unexposed ambient particles to ozone collected on the September the 14th, 2012, whereas Figure 8.6 shows those of exposed and unexposed ambient particles to OH radical collected on the September the 17th, 2012. The results analysed from ATOFMS are based on 200-300 detected particles in each sample. The positive and negative peaks exhibit signal intensities of chemical species that appeared in both exposed and unexposed particles to ozone or OH radical. The tick mark in the y axis represents a relative intensity break from 0.06 to 0.2. Although the two distinct species types, organic and inorganic, were observed in all detected particles, the majority of the observed signals indicate the presence of organic constituents in the examined aerosol indicating the influence of the combustion processes, road dust, and the natural rubber content of vehicles tire wear debris (Dasch and Cadle, 1989; Rogge et al., 1993a; Cheung et al., 2013). The series of carbon clusters with m/z progression of ±n12 or ±n12+1 which are ±36, ±48, ±60, ±72, ±84, ±108, ±120 and ±132 appear in both positive and negative going peaks. It is well established that diesel engines emit soot i.e. carbonaceous particulate matter (Nikzadfar and Shamekhi, 2014). Soot particles are not expected to respond significantly to the oxidative aging (Vlasenko et al., 2008) and known to act as a catalyst for atmospheric oxidation of atmospheric species such as SO_2 to SO_4^{2-} (Dasch and Cadle, 1989).

Peaks detected at m/z +51, +63 and +77 are signatures of aromatic particles from tyre wear compounds and are assigned for $[C_4H_3]^+$, $[C_5H_3]^+$ and $[C_6H_5]^+$, respectively (Dall'Osto and Harrison, 2012; Hamilton et al., 2013).

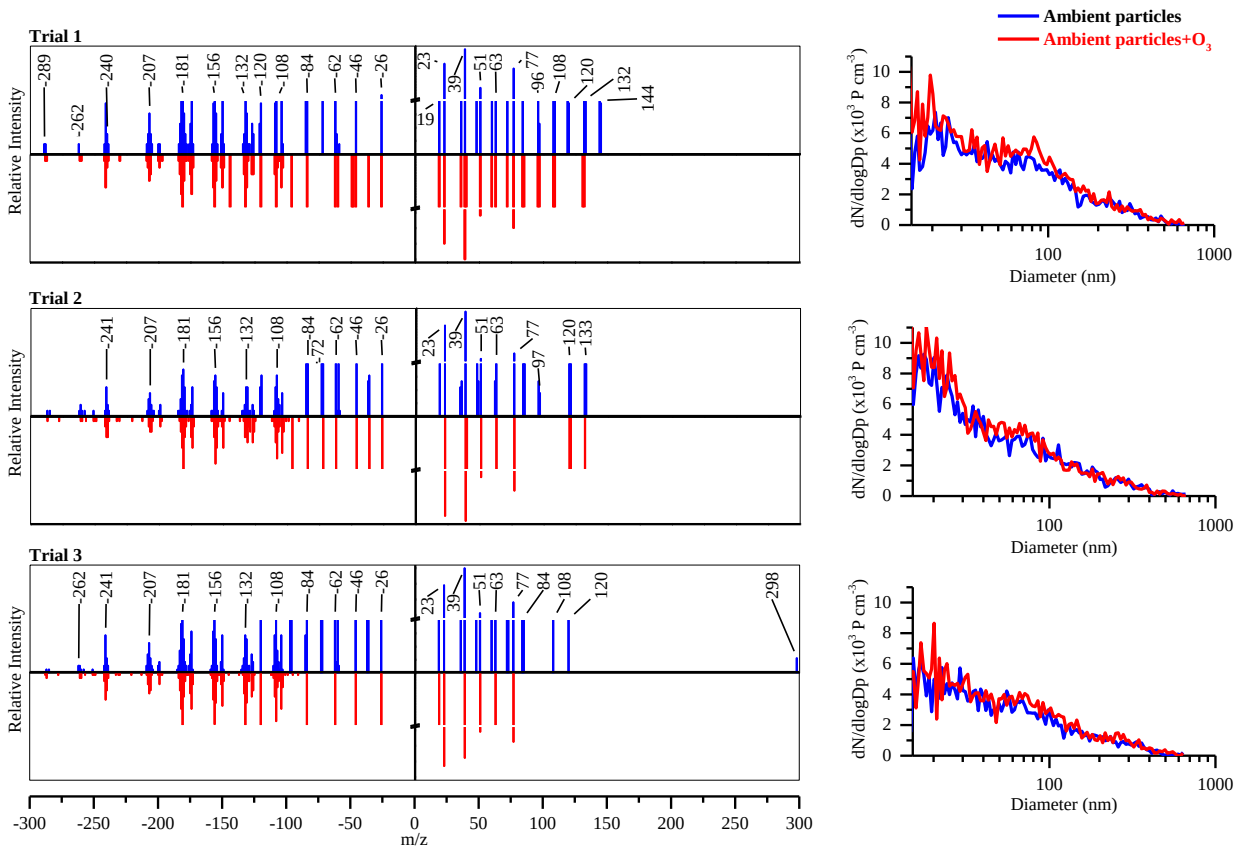

Figure 8. 5 Example of ATOFMS differential averaged mass spectra and SMPS averaged size distribution spectra of unexposed and exposed particles to O_3 taken on September 14th, 2012.

The most frequently observed prominent inorganic signals in the sampled particles appearing at m/z +19, +23, +39 and +40 are assigned for hydronium (H_3O^+), sodium (Na^+), potassium (K^+) and calcium (Ca^+), respectively. The presence of H_3O^+ is taken as an indicative of wet particles (Sierau et al., 2014) which is consistent with the high relative humidity associated with the sampling time. Ca and Na are usually regarded as originating from dust and sea salt, respectively (Bi et al., 2011) while K from smoke of biomass burning (Silva et al., 1999).

Negative peaks at m/z -26, -46, -62 might indicate the presence of cyanide (CN^-), nitrite (NO_2^-) and nitrate (NO_3^-), respectively. The occurrence of nitrite and nitrate (NO_x) signals in all trials is consistent with the road traffic, which is rich in NO_x (Dall'Osto and Harrison, 2012). NO_x

components in aerosol is taken as a strong evidence for secondary processing of particles during transport (Bi et al., 2011). However, the CN^- peak suggests typical soil particles (Hamilton et al., 2013).

The unassigned peaks of higher molecular weight compounds appearing in the negative ion spectrum may be indicative of humic-like substances which have been found in natural waters and soil and seem to account for a significant fraction of organic aerosol mass (Samburova et al., 2005).

Generally, the clear spectra with reproducible peaks and the measured species seen in all oxidation trials in Figure 8.5 indicates well-mixed aged ambient aerosol which is consistent with the prevailing speed of wind during the ageing experiments. Oxidants in winds directly oxidise the primary emissions from the source as well as the background air that is mixed with the emissions (Robinson et al., 2006). This can explain the negligible change observed in the chemical content of particles after being exposed to ozone and therefore the significant impact of meteorological condition during the measurements.

It is clear also from the SMPS spectra of exposed and unexposed particles to ozone that the predominant particle size is <0.1 μm which is below the detection limits of the ATOFMS. Local emission was found to largely composed of ultrafine particles in urban areas (UFPs, d<100 nm) (Cheung et al., 2013). Hence no appreciable change was observed in the size distribution of the measured particles before and after being exposed to ozone within the measured particles size. It is expected that the relatively high average wind speed during the experiments day would influence the size distributions and reduce the concentrations of primary pollutants. Figure 8.6 shows ATOFMS and SMPS spectra for exposed and unexposed ambient air particles to OH recorded on the September 17th, 2012.

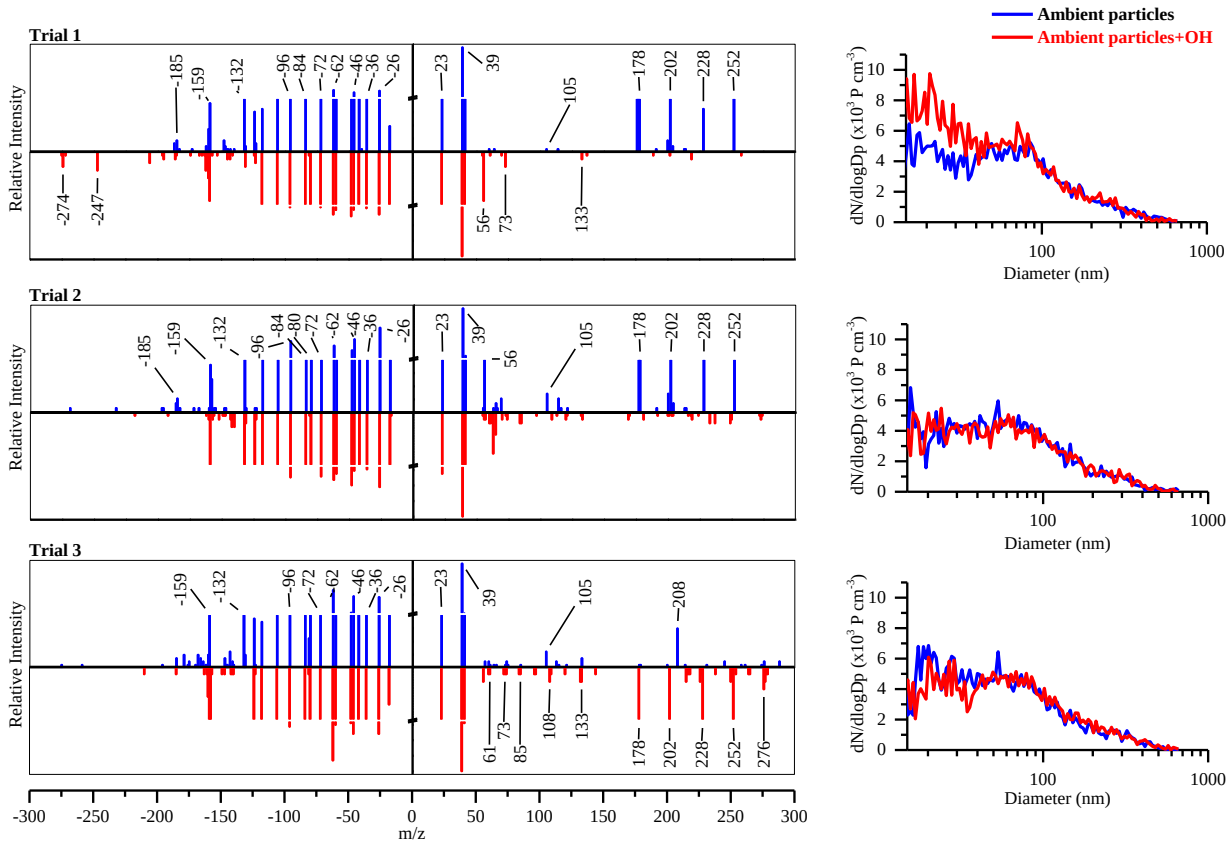

Figure 8. 6 Example of ATOFMS differential averaged mass spectra and SMPS averaged size distribution spectra of unexposed and exposed particles to OH taken on September 17th, 2012.

In addition to the carbon clusters observed with m/z progression of ±n12 or ±n12+1 and Na^+ and K^+ positive ion peaks, the spectra shows signatures usually attributed to polycyclic aromatic hydrocarbons (PAHs) at m/z above +100 (Gross et al., 2000; Gross et al., 2005; Sullivan and Prather, 2005; Kreider et al., 2010; Dall'Osto and Harrison, 2012). The measured PAHs in this study belong to the group of persistent organic pollutants (POPs) which have widespread occurrence formed from the incomplete combustion of organic materials such as those formed from incineration plant and domestic burning wood (Maliszewska-Kordybach, 1999; Sullivan and Prather, 2005). Some of the PAHs (such as anthracene, fluoranthene and

benzo[a]pyrene (Lammel et al., 2009)) are known to resist degradation and thus remain in the atmosphere for long periods of time (Roy and René, 1998; Maliszewska-Kordybach, 1999). Moreover, oxidation of PAHs is much slower in particle phase due to the shielding effect from the gas-phase (Lammel et al., 2009). They are reported to be the most easily detected compounds as their parent ion (M·+) using ATOFMS due to their high molar absorptivity at 266 nm (Silva and Prather, 2000). Table 8.1 displays a number of PAHs and oxygenated aza polycyclics analyzed using ATOFMS (Silva and Prather, 2000).

Table 8. 1 Polycyclic Aromatic Hydrocarbons (PAHs) and Oxygenated Aza Polycyclics analysed using ATOFMS (Silva and Prather, 2000)

Compound	MW
Naphthalene	128
Acenaphthene	154
1,5-Dihydroxynaphthalene	160
Fluorine	166
Phenanthrene	178*
Phenanthridine	179
9-Fluorenone	180
Perinaphthenone	180
Fluoranthene	202*
Pyrene	202*
2-Methylanthraquinone	208*
Phenanthraquinone	222
Chrysene	228
Perylene	252*
Benzo[*ghi*]perylene	276
Coronene	300

** Detected in this study.*

The negative peaks at m/z -26, -46, -62, -80 and -96 representing, respectively, CN^-, NO_2^-, NO_3^-, SO_3^-, and SO_4^-. High particles contents of sulphur oxides are very common in urban atmospheres

(Chen et al., 2006a) and known to arise from fuel-derived particles (Chen et al., 2006a; Sajjad et al., 2014) such as those emitted from fossil fuels combustion operated by electric utilities and industry (Jones et al., 2012; Fallah et al., 2014). As it characterised above, strong signal intensities of nitrite and nitrate species in ambient particles are associated with vehicle exhaust emission and indicate chemical transformation of atmospheric particles. The abundance of such species in ambient particles is taken as a sign of 'aged' particles (Huang et al., 2012).

8.4 School of Sport and Exercise Sciences (Site B)

The location of the second site was chosen because of its close proximity to three major sources of emissions, the Bristol roadside, a medium traffic density, the of electric trains about 200 m to the west of the site, and a construction activity of a building rising from 4 to 9 storeys tall (Victoria Hall Birmingham Student Accommodation Phase 3) was found at approximately 100 m south the site. The campaign of ageing ambient particles at this site was from March 11th to April 8th, 2013 during which the UK experienced severe winter weather and unseasonably low temperatures with significant snowfalls.

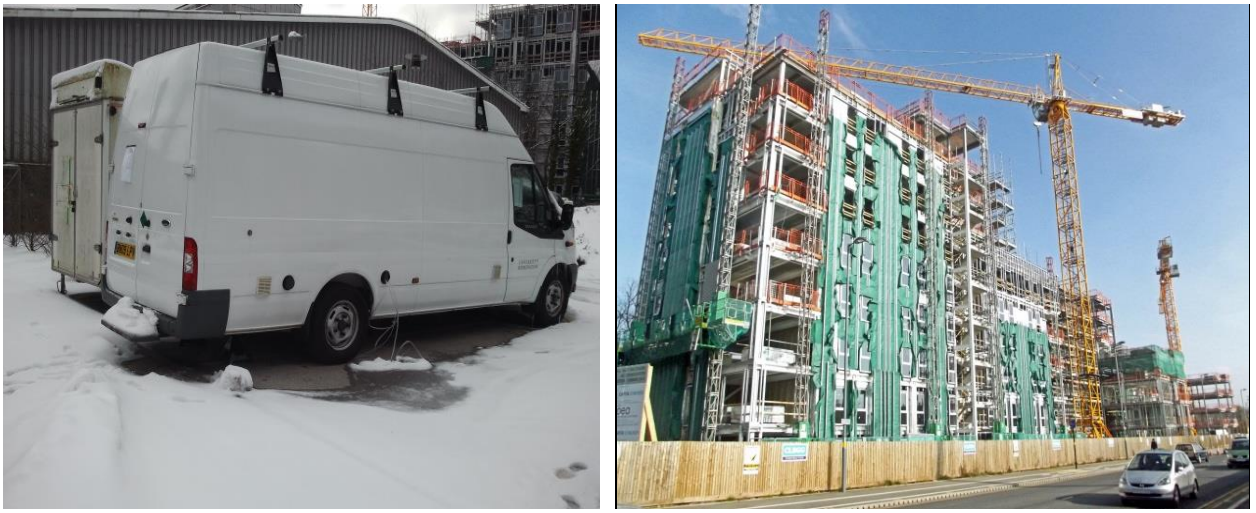

Figure 8. 7 Photography showing the mobile laboratory at site B (left) and the construction site 100 m south (right).

8.4.1 Physical and chemical characterization of ambient particles

After onsite calibration of ATOFMS and prior the ageing experiments, the ATOFMS efficiency, the size and the chemical composition of ambient particles at the site were examined. The ATOFMS was kept sampling for three days including the weekend of March 15th to 17th, 2013. Figure 8.8 and Figure 8.9 show, respectively, ATOFMS size and mass spectra recorded for the collected particles from site B.

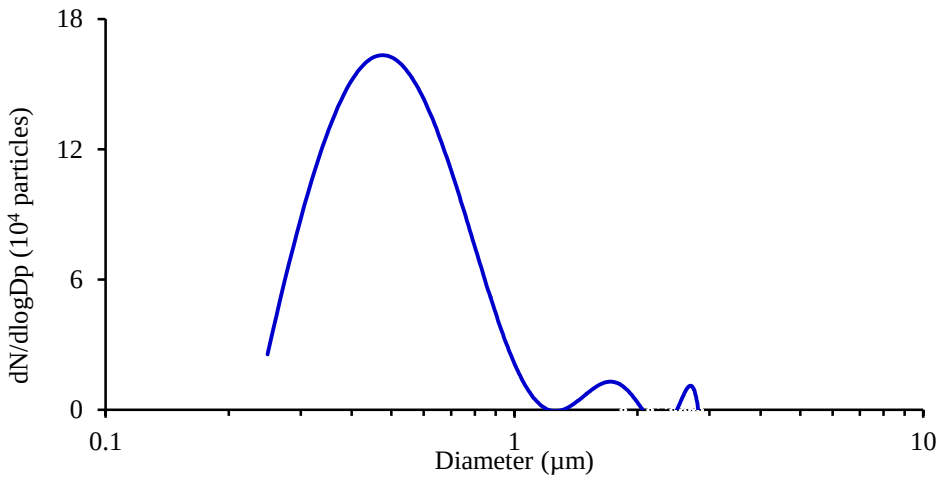

Figure 8. 8 ATOFMS average size distribution spectra recorded for the collected particles from site B between March 15th to 17th, 2013.

During this sampling period the ATOFMS successfully sized and ionised 69,606 particles. The averaged mass spectrum was thought be a statistical representation of what was present in the air prior the period of the ageing experiments. Most observed positive and negative signals are typical peak patterns of carbon clusters. These are ±m/z of 24, 36, 48, 60, 72, 84, 96, 108 and 132. Positive peaks at +23, +38, +39, +40, and +41 can be assigned for Na^+, $C_3H_2^+$, K^+, Ca^+ and K^+ or $C_3H_5^+$, respectively. Negative peaks at m/z -26, -46, -62, -80, -96 and -97 are assigned for CN^-, NO_2^-, NO_3^-, SO_3^-, SO_4^- and HSO_4^-, respectively.

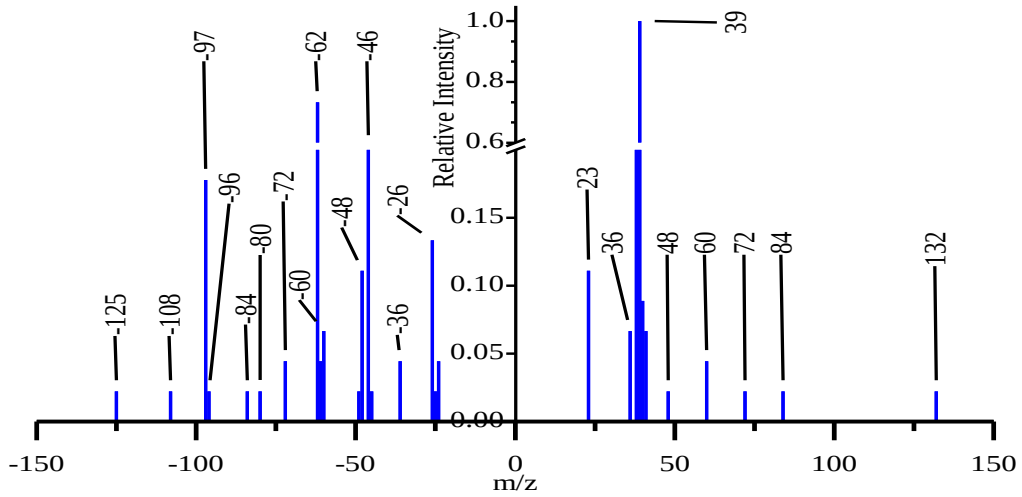

Figure 8. 9 ATOFMS average mass spectra recorded for the collected particles from site B between March 15th to 17th, 2013.

8.4.2 Artificial ageing of ambient particles

The oxidation experiment of ambient particles by ozone and OH radical was performed in site B on the March 18th and 19th, 2013, respectively, these days were characterised by low wind speeds. For the duration of the ageing experiment by ozone, meteorological data showed that the winds at the site mainly blow from the southwest. Temperatures and relative humidities fluctuate in the ranges of 0.2-6.4°C and 60.5-97.0%. Experiment of exposing ambient particles to OH radical was done for the next day, the March 19th, 2013. The vast majority of winds were westerly with a strength range of 0-2.4 m s^{-1}. The ambient temperature and relative humidity during the experiment period varies from 1.2 to 5.0°C and from 75.5 to 96.4%. Wind roses for the perspective periods of ageing experiments are indicated in Figure 8.10. Hourly parameters of wind speed, temperature, relative humidity and ambient variation in particulate matter concentration with time is shown in Figure 8.11 and 8.12, respectively.

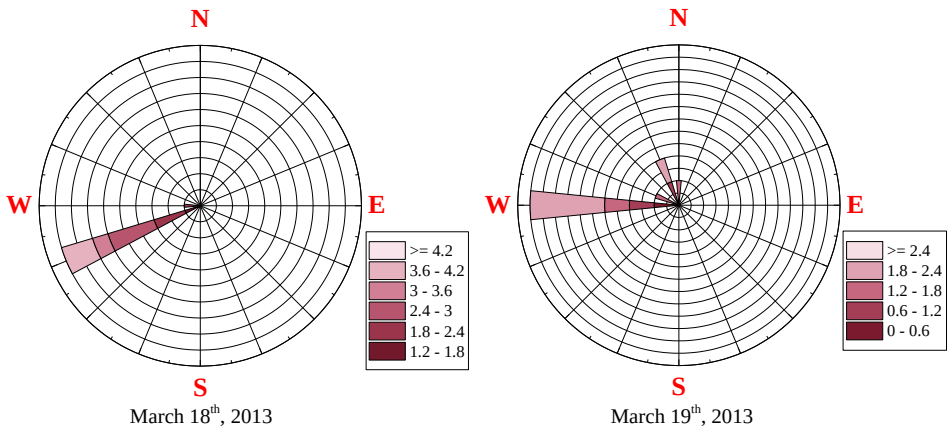

Figure 8. 10 Main wind directions and speeds during the periods of ageing atmospheric particles; 8:00 am to 6:00 pm.

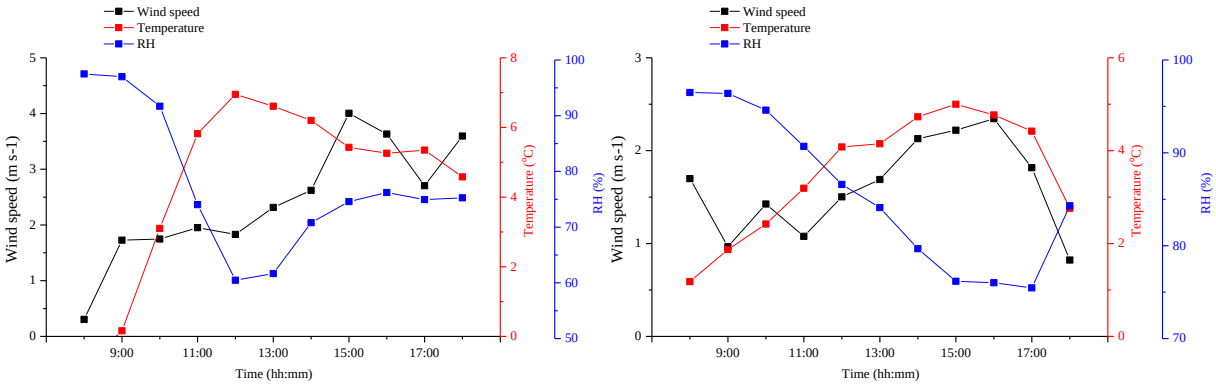

(a) (b)

Figure 8. 11 Variations of wind speed, ambient temperature and relative humidity during the ageing experiment period from 8:00 to 16:00 on the: (a) March 18th 2013 and (b) March 19th 2013.

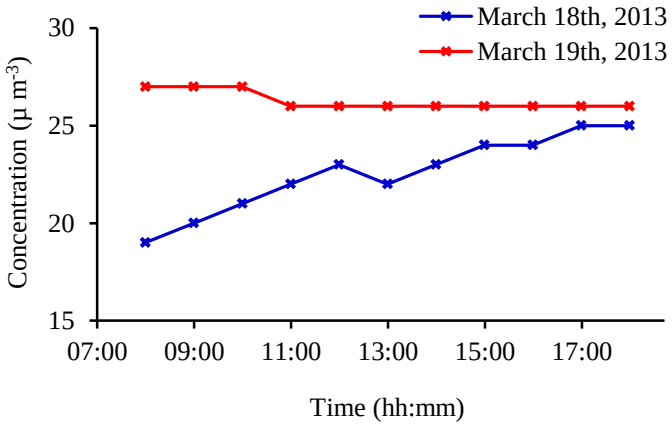

Figure 8. 12 Variations of $PM_{2.5}$ concentrations at site B during the measurement periods.

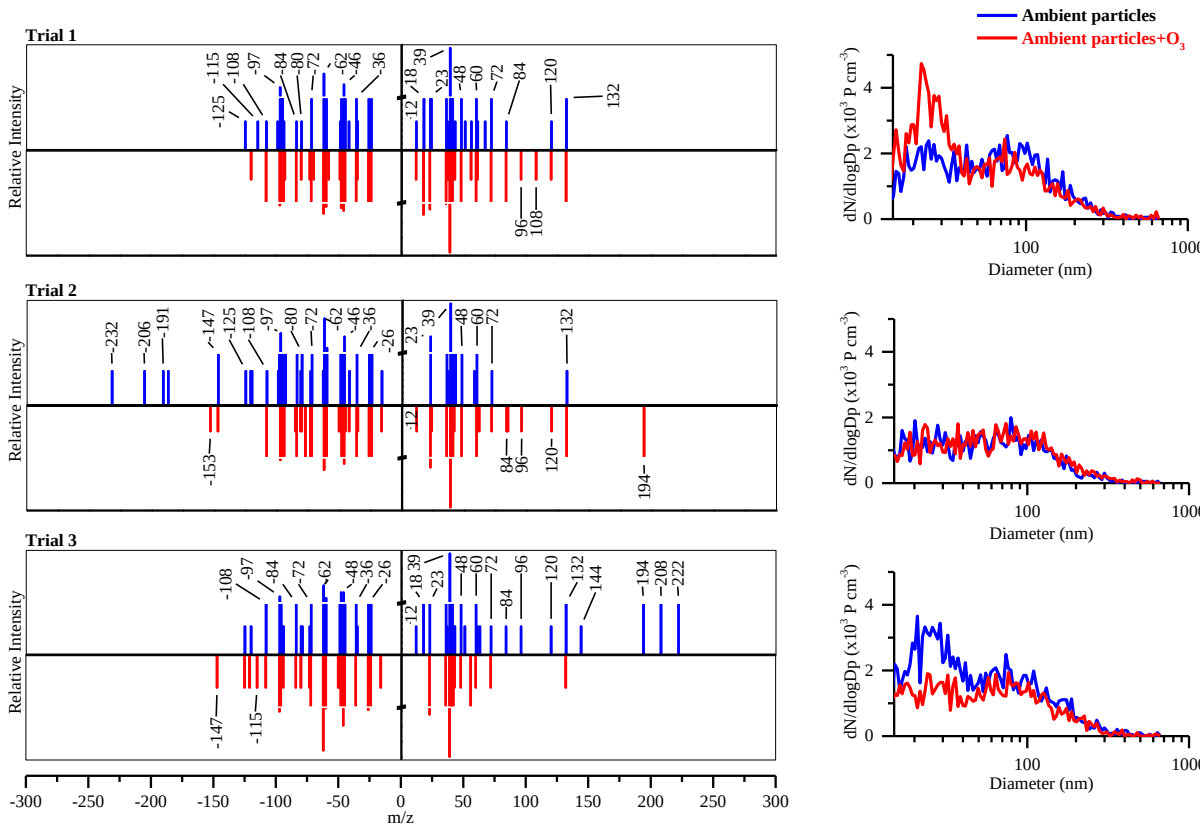

Figure 8. 13 Example of ATOFMS differential averaged mass spectra and SMPS averaged size distribution spectra of unexposed and exposed particles to O_3 taken on March 18th, 2012.

Figure 8.13 illustrates the averaged mass spectrum of exposed and unexposed ambient particles to ozone collected on the March 18th 2013. The observable peaks change in the recorded spectra is not reproducible and peaks tend to occur randomly with differing frequencies within all ageing trials including with and without ozone exposer. Thus this observation cannot reflect a reliable difference in the chemical contents of particles on oxidation. The observation might indicate surges of inhomogeneous particles measured during the experimental periods of ambient particles.

The spectra shows symptomatic of the urban environment signals corresponding to NO_x, SO_x, a series of carbon clusters appear randomly in both positive and negative peaks of both

exposed and unexposed particles in addition to elemental positive signals of Na, Ca, PAH and ammonium (NH_4^+). Major input source of NH_4^+ is from agricultural fertilizer (Paulot and Jacob, 2013).

The spectrometric analysis of the mass spectra suggests certain amount of ageing has occurred to the detected particles, air parcels arriving to the site were not well mixed and the presence of POPs during the ageing periods. Although the size distribution does show a noticeable growth in the lower size bin in some trials, the observation cannot be correlated with the ageing process since it is occurring inconstantly. The variation in the emission sources, durations and frequencies in the site appears to be primarily responsible for the observed changes in the particles mass and size spectra rather than the subjected oxidation event. For example, the diurnal variations in the motor vehicle emissions associated with morning and late evening rush hours combined with infrequent construction emission related to operating heavy machinery equipment and irregular rail emission at the site contribute to the complexity of the ageing experiment. This might be consistent with the cold still weather condition (wind speed remained below 4.2 m s^{-1} at a steady direction) during the experiment day which resulted in poor mixing of ambient aerosols.

Figure 8.14 displays ATOFMS and SMPS spectra for ambient air particles with and without OH radicals recorded on the March 19th, 2013. Beside the component synonymous with urban type particles explained above, characteristic peaks of iron (Fe) is observed at m/z +56 in oxidation trials 1 and 2. The fragment detected in the negative ion mass spectra at m/z -45 indicates oxygenated moiety usually attributed to the presence of the carboxylic group, CO_2H^- (Silva et al., 1999; Moffet et al., 2008; Wang et al., 2013) and features highly processed organic aerosols (Silva et al., 1999; Zhang et al., 2005).

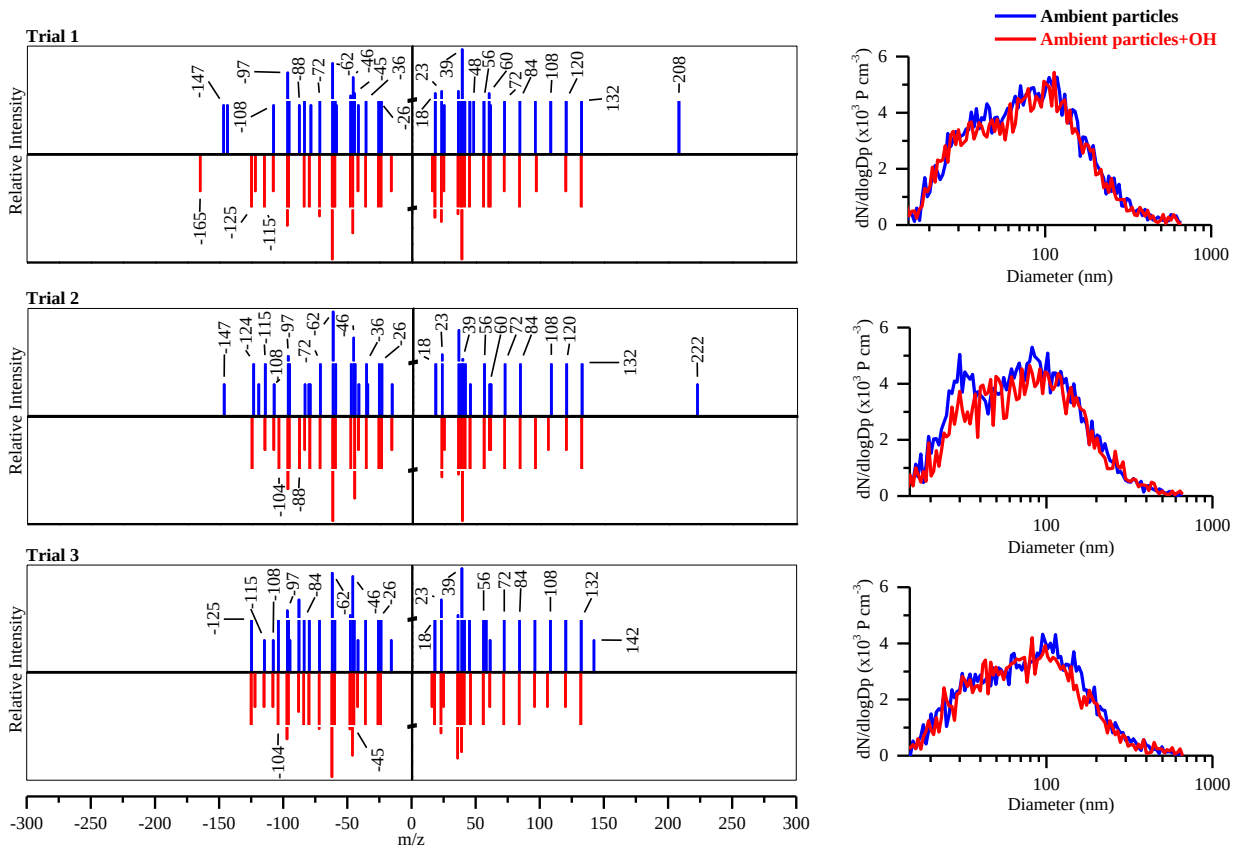

Figure 8. 14 Example of ATOFMS differential averaged mass spectra and SMPS averaged size distribution spectra of unexposed and exposed particles to OH taken on the March 19th, 2012.

Peaks in the negative ion mass spectra at m/z –72, –88 and –104 may have been also due to iron oxides FeO^-, FeO_2^- and FeO_3^- (Smith, 2007), respectively. The strong intensity signals of carbon clusters and Fe combined with the wind direction which was blowing from the railway side suggest the influence of dust from the railway.

Studies have reported high iron and carbon contents in dust from rail way tunnels (Seaton et al., 2005). Iron containing particles in railways result from friction processes such as braking and wheel-track contract (Ripanucci et al., 2006; Midander et al., 2012). It is likely that the high relative humidity during the measurements enhances the solubility and the ambient oxidation

processes of iron. The positive spectra of the detected particles also shows signals due to particles PAH (m/z +208) inconstantly in exposed and unexposed particles.

The random appearance of peaks within the measured spectra indicates significant changes in the background composition during the ageing period. As previously outlined, the variations in the ATOFMS measurements are results of the changeable background compositions experienced during the campaign because of the nature of the experiment site and the corresponding weather conditions.

To exemplify the inconsistency in the experimental observations, signals of two abundant species HSO_4^- (taken as a marker for air mass composition) and CO_2H^- (taken as an oxidation marker as described above) with comparable loads in the measurements recorded on the March 19th 2013 are studied. Figure 8.15 is generated by averaging the first 10 minutes signals of HSO_4^- and CO_2H^- collected for both exposed and unexposed particles to OH radical. Signals were correlated

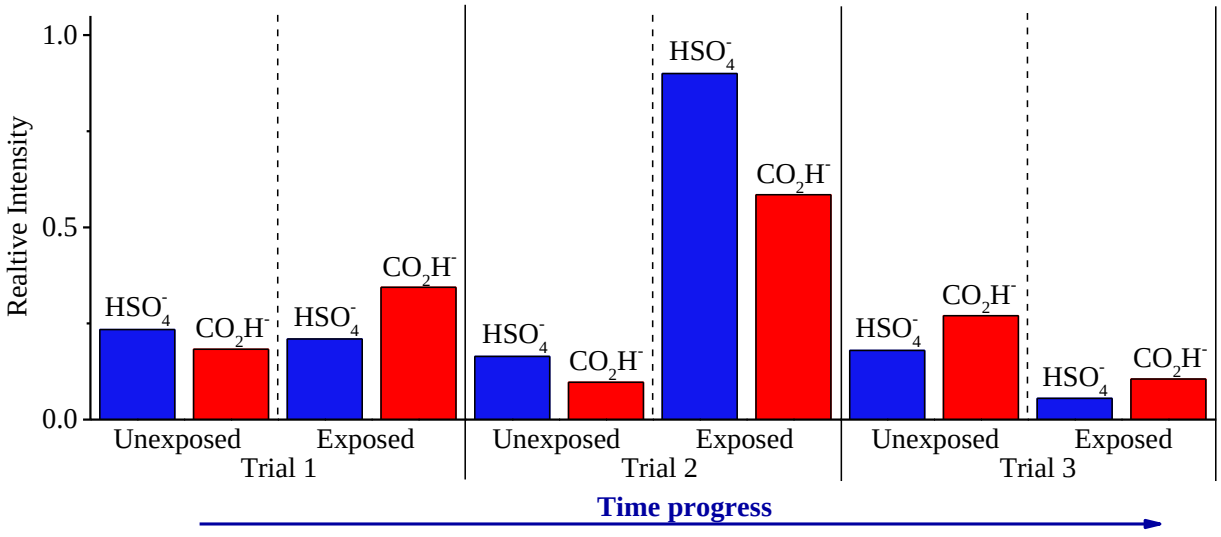

Figure 8. 15 Variations in the HSO_4^- and CO_2H^- averaged signals among experimental trials of exposed and unexposed ambient particles to OH radical. Experiment conducted on the March 19th 2013.

with the oxidation process and the progressing time of the experiment (from 8:00 am to 6:00 pm) as the figure illustrates. HSO_4^- and CO_2H^- do not show clear repeatable responses to the oxidation process. Rather they occur randomly within the duration of the ageing experiment. Additionally, they dramatically differ in their trends from one data set to the other and from one processing trial to another. Generally, the analysis likely indicates sudden surges of particles arriving at different time during the ageing process. For instance, exposed particles to OH in trial 2 marks the maximum portion of CO_2H^- and HSO_4^- species in the averaged 10 minutes period with the HSO_4^- intensities higher than that of CO_2H^-. Conversely, exposed particles in trial 3 indicate minimum levels of oxidised CO_2H^- and HSO_4^- with the CO_2H^- slightly higher. This inconsistency might reflect the significant variation in the experiment background with time making the effect of the artificial ageing negligible. It is likely that the diurnal variation in the emission and the secondary formation of particulate matter together with the changeable meteorological condition are responsible of the indiscernible changes observed in the mass spectra signals. Although it is noticed in Figure 8.15 an increase in the CO_2H^-:HSO_4^- ratio on oxidation (0.8-1.6), the decrease in the ratio does not hold for the entire oxidation period and further investigation is required to explore the factors that determine the trend of in the CO_2H^-:HSO_4^- ratio on oxidation. The available data are not sufficiently precise to conclude that there is a measurable change in composition, a conclusion reinforced by the opposite sign in response (for the CO_2H^-:HSO_4^- ratio) between trial 2 and trials 1 and 3.

8.5 Applicability of the ACA system in ambient environment

The analyses of the ambient experiments show that the ACA system has limited efficiency in processing particles at urban environment. Various attempts were made to maximize the impact

of the artificial ageing events on ambient aerosols and minimise the effect of other uncontrollable variables such as the changes in the ambient background conditions. Ageing experiments were repeated at different sampling duration time, sampling time, reaction residence time and oxidants concentrations. Attempt to reduce background variability in particle composition and enhance particle mixing before entering the AFT was made by introducing ambient particles to the mobile laboratory. However, data analyses repeatedly show no reliable changes on oxidation or poor reproducibility of the observed signals.

It is likely under the circumstances of highly oxidized particles background that the amount of the artificially aged material is limited due to the small probability of the ageing event as compared to the probability of background ambient ageing.

Another important possibility is that ambient urban aerosols might exist as primary particles coated by secondary organic and/or inorganic species shielding the primary material in the particle core and inhibit ageing. Studies have reported constantly the formation of secondary coating on primary particles and the significant effects of this coating on their physicochemical properties (Yamato and Tanaka, 1994; Cruz and Pandis, 1998; Khalizov et al., 2009; Deboudt et al., 2010; Stratmann et al., 2010; Pratt and Prather, 2012; Bond et al., 2013; Girard et al., 2013). Such conclusions have been made experimentally and theoretically in this study (chapter 6, section 6.2). It has been established that the heterogeneous reaction of OL with ozone results in significant alterations of the particle surface properties and potentially decreases the ozone uptake by the particles.

The experimental factors in this study imposed relevant limitations. The largest drawback may be associated with characterisation techniques. Firstly, the ablation ionisation process of the particles within the ATOFMS depends mainly on the laser irradiance and the physicochemical

properties of the particles (chapter 3, section 3.6.2). Secondly, the ATOFMS operates most efficiently for particles with aerodynamic diameter between 0.3 μm and 3 μm with limited efficiency for smaller particles. The measurements made in the current project show that the largest portion of ambient particles constitutes of UFP by number which is in good agreement with literature studies of urban particles (Bzdek et al., 2012) but below the detection limit of the characterisation techniques. This means that the majority of the chemically characterised particles do not reflect the actual population of the ambient particles. Third, ATOFMS detection depends largely on the chemical composition of the particles (Allen et al., 2006). The diverse sensitivity of the ATOFMS combined with multi-element detection on a single ambient particle adds more challenges to the analysis. The assignment becomes more complicated as preferentially detected species like the alkali metals become abundant components of atmospheric aerosols (Silva and Prather, 2000; Dall'Osto et al., 2005; Dall'Osto et al., 2009).

The fluctuation in the relative humidity and temperature during measurements times (8:00-17:00 hours) might contribute significantly to the characterisation methodology. On the one hand, particle components respond differently to relative humidity and temperatures changes (Shiraiwa et al., 2011). For example a change of 2-3°C of ambient temperature can affect the formation rate of certain particle types by an order of magnitude (Easter and Peters, 1994) resulting in particles "bursts" that is temperature dependent. Studies also have shown that water vapour is transported to particles by molecular diffusion on much faster time scale than that of particles transport (Leeuw, 1990). From other hand, the efficiency of the sampling equipment, the ATOFMS and the SMPS, are in a marked degree influenced by the sample matrix as it explained in chapter 3, section 3.6.2, and postulated for the SMPS system in chapter 5, section 5.3.3. Note that the sampling instruments were housed inside a mobile laboratory, shown in Figure 8.7, and a heater

or an air conditioner was used in an attempt to maintain reasonable temperature stability during the measurements.

It is noted that some studies have examined successfully the oxidation of ambient particles (George et al., 2008; Jimenez et al., 2009; George and Abbatt, 2010; Shiraiwa et al., 2011; Wong et al., 2011; Ryder et al., 2014), however, employed methodology, investigated sites, weather conditions, monitoring equipment and characterised properties of the particles varied considerably. For instance, sites such as remote forests were investigated at time periods characterised with fairly stable warm weather conditions, high production levels of fresh biogenic organic aerosol and less impact from other emission sources such as biomass burning. Monitoring equipment varies with accordance to the measured features of the processed particles; those include aerodyne aerosol mass spectrometer, aerodyne time of flight aerosol mass spectrometer, SMPS, and ATOFMS. Studied properties of interest cover chemical composition, degree of oxidation (Oxygen:Carbon ratio) in particles, cloud condensation nuclei activity, and aerosol size distribution.

8.6 Summary

Unfortunately, there is little that can be learned from the artificial ageing of ambient particles under the study occasion and circumstances. To summarize, the short series of ambient experiments showed that aerosols arriving at the proposed measurements sites are likely to have undergone excessive chemical and physical transformations that forbidden further alteration motivated by the artificial ageing process. It is found that application of laboratory ageing system to real atmospheric conditions was very challenging as primary particles would not survive long during emissions and downwind transportation from a source to a receptor site. A proximate

multi-activity urban site in conjunction with variable weather conditions resulted in more diversity background which was highly time and weather condition dependent.

CHAPTER 9 CONCLUSION, ATMOSPHERIC IMPLICATIONS AND FUTURE DIRECTIONS

9.1 Introduction

The aim of this study was to construct a setup for ageing OA and to investigate the change in chemical and physical properties and aged OA. This chapter draws out the experimental conditions of the ACA system used to process and characterise aged organic aerosols. The major findings, contributions, implications, challenges and future directions of this work are also covered in the following sections.

9.2 Aerosol chemical ageing system

In chapter 2, the aerosol chemical ageing (ACA) experimental protocol has been described as a real-time flow reactor aging system of organic aerosol that operates at atmospheric pressure and temperature with elevated levels of particles and oxidants. The plug residence times varies from ~20 to 135 seconds. Ozone production levels ranged from tens of ppb up to 100 ppm. However, typical measured HO_x levels ranged from $(8.0\pm0.4)\times10^{9}$ to $(1.2\pm0.6)\times10^{10}$ molecules cm^{-3}, corresponding to an exposure range of 1.2×10^{12} to 1.8×10^{12} molecules cm^{-3} s. This laboratory exposure is equivalent to 9.3-20.1 days of ambient atmospheric oxidation. The physical and the chemical composition of the aged laboratory generated particles were monitored in real time using SMPS and ATOFMS systems, the fundamental aspects of their operational approaches have been detailed in chapter 3.

Chapter 4 explained the methodology used to measure the absolute HO_x levels in the ACA system using a PERCA. Measured signals of HO_x were subjected to significant disturbance above ozone mixing ratio of 800 ppb making PERCA application at the experimental conditions of this

study challenging. The theoretical simulation of the artificial atmosphere in the ACA system showed that the production processes of OH radical becoming less important and sink routes are more significant as ozone levels increase. The simulation also suggested that OH levels fall and HO_2 levels rise in response to the increase of O_3 mixing ratio making HO_2 the dominant oxidant at extreme O_3 mixing ratios (1.5-20 ppm). Accordingly, it was concluded that the ACA system is at optimum oxidation capability when operating at moderate O_3 mixing ratio which also mimic ambient atmospheric levels. It was also concluded that at this level of O_3 other oxidants including O_3, HO_2 and H_2O_2 will have minimum effect in processing the organic particles and thus the role of OH is maximised. The overestimation of the simulation in HO_x levels in the system suggested systematic HO_x loss routes either in the ACA or in the PERCA system as a result of species interferences or experimental conditions (e.g. RH%). For high levels of O_3, the PERCA methodology is not applicable as modulation shown to be very poor.

The burden of the SOA formed by reaction of O_3 with the vapour of pure OA was assessed theoretically in chapter 5. Based on the theoretical study of the gas and condensed phases of OL particles under the conditions of this study, the mass contribution reacted from OL gas phase is less than that from condensed phase by about 5, orders of magnitude. This was taken as an indication for the reaction in the ACA system to predominantly take place in the condensed phase and that the contribution from the partitioning of the oxidation products from the vapour phase to the condensed phase was thus negligible.

9.3 Artificial chemical ageing of laboratory generated aerosols

The laboratory studies of OL-O_3 HR, OL-OH HR and MA-O_3 HR systems provided evidence for the ageing process of POA to produce SOA with either high volatility oxygenated products that

evaporate to the gas phase or highly oxygenated heavier products that partition to the condensed phase. It was concluded (in chapter 6).

In this thesis, a new approach of addition of the laser dye, NBS, to OL particles led to a remarkable improvement in the LDI efficiency. As a consequence, the chemical contents of aged OL particles were characterized successfully.

It was concluded from the analysis of the mass spectra of aged particles that early generation products in the condensed phase may undergo a series of secondary reactions involving dehydration, polymerization and aldehyde, ketone and acid formations. For the OL-O_3 HR system under dry conditions, the study confirmed the formation of oligomeric material of up to m/z of 1450. The cyclic compound, oxecane-2,10-dione (OD), which has not been reported previously in OL-O_3 HR is proposed as one of the oxygenated products formed in the early stages following the subsequent isomerisation of the ECI.

The ability of ATOFMS in this study to distinguish between both reacted material at the surface and unreacted material from the bulk of aged OL particles is not fully justified. One interpretation could be that the addition of the NBS laser dye to OL particles has effectively modified the optical properties of the particles (chapter 3, section 3.6.3). Consequently, enough energy was absorbed by the particles resulting in explosive vaporization or large etching depths from the measured particles. Alternatively, it could be the effect of unreacted OL diffusing from the bulk to the surface of the particle that takes place during the particles journey through the ATOFMS system. Both possibilities will result in the detection of reacted and unreacted material from the particles.

A significant contribution from this study was the conclusion drawn for the semi-quantitative observation of variation in particle compositions as a function of their size. Product

formation and the reaction mechanism of OL-O_3 HR under dry conditions was found to be size sensitive which has not been explicitly reported previously based on experimental investigations.

The observed size dependence of the reactivity of the OL particles was explained by a theoretical study of the OL-O_3 HR. In this sense, a significant amount of OL remained unreacted; this amount is more noticeable in aged large particles.

The approach used to measure the reactive uptake of ozone by OL, γ, led to a value of $(2.3\pm0.06)\times10^{-5}$ and $(2.0\pm0.05)\times10^{-5}$ for dry and wet oxidation of OL, respectively. The difference in the reactivity of OL at different relative humidities with more OL destruction observed in the absence of the water is justified by the preference of CIs for reaction with water molecules over the reaction with OL under humid conditions. This result accords with other studies where ozone was found to be more effective in oxidising OL particles at dryer than under wetter conditions (Hearn and Smith, 2004; Katrib et al., 2004; Hearn et al., 2005; Ziemann, 2005).

The wide variations among reported laboratory results for measured reaction probability, γ, can be attributed mainly to the differences in the ageing methodologies and operating conditions. However, the overestimation of the calculated γ ($4.2x10^{-3}$) as compared to the observed value indicated a reduced measured O_3 uptake to the particles. The interpretation that was made comes from the time dependency of γ which was taken as an indication of surface reaction dominance that leaves a significant amount of unreacted OL in the bulk of the particles. The changes in the particle surface composition as products formed during oxidation result in deceleration of the reaction uptake of O_3.

The atmospheric lifetime of OL particles with respect to O_3 reaction was estimated to be 1.7 and 3.1 hours, under dry and wet conditions, respectively. Reported values measured by other

authors span between orders of seconds to tens of minutes (Morris et al., 2002; Knopf et al., 2005; Ziemann, 2005; Zahardis and Petrucci, 2007). The anomaly between the longer field atmospheric lifetimes reported at an order of days (Zahardis and Petrucci, 2007) and shorter laboratory lifetimes of OL is likely due to the fact that OL in ambient aerosols is found in particles with high viscosity semi-solid mixtures in which the diffusive transport within the particle phase of both ozone or OL is slowed down. The relatively longer laboratory lifetime reported for OL in this study indicates closer results to the reported real atmospheric lifetime. The laboratory experimental conditions applied here gave more reasonable life time of OL.

The OL-OH HR has been investigated in this project which marks the early beginning in studying the oxidation of OL particles with OH radicals. The results showed that a molecule of OL is subjected to multiple attacks by a number of OH radicals. Both addition reaction of OH to the double bond of OL and H abstraction reaction are concluded. The two reaction mechanisms are responsible for the formation of products characterised by the presence of multiple oxygenated functional groups. In contrast to the OL-O_3 HR, no high molecular weight oligomers were measured when OL was reacted with OH radicals.

Another important finding here is the impact of the oxidant identity on the oxidation products with OH radical showing more of a scavenging phenomenon (formation of lower molecular weight products) and ozone showing enhancement of oligomeric products formation. The depletion of oligomeric compounds formation when OH radical is used as an oxidant was postulated in relevant studies (Iinuma et al., 2005).

A discernible difference in the mass spectra of unreacted MA aerosol measured by ATOFMS at high and low relative humidity was observed. The extra peaks appearing in the mass spectra of wet particles indicated MA solvation. Only, at high relative humidity MA particles

respond to ozone exposure suggesting that particle state likely facilitates diffusion of ozone into the particle.

In both of the investigated aged organic acids, OL and MA, particles have shown that the formed products are highly oxygenated compounds mainly composed of peroxides, carboxylic acids or aldehydes functionalities, but higher oligomers could not be detected in the case of MA, indicating differences in structure and reactivity of the CIs of MA and OL.

9.4 Artificial chemical ageing of ambient aerosol

The applicability of the ACA system was tested on real atmospheric particles. It was found that extrapolation of laboratory procedures to the ambient urban atmosphere may be problematic. Possible interpretations included concerning the mechanism of the ACA of ambient aerosol are influenced by the complexity of the particle matrix, ambient particle phase, presence of highly oxidized particles, oxidation of the volatile organic carbons from the gas phase and variations in meteorological factors (such as wind speeds and direction, temperature and relative humidity).

9.5 Implications of ageing atmospheric organic aerosol

OA reacts efficiently with oxidants producing VOCs among the products that are appreciably partitioned to the gas phase as is evidenced from the observed loss of particle mass and volume. The oxygenated particle phase products induce more alterations in the physiochemical properties of the particle. Both VOCs and oxygenated particle phase products formed during ageing atmospheric particles have significant impacts on human health, atmospheric chemistry and physics and climate which are explained in the following sections.

9.5.1 Human health implication

VOCs such as those produced during the ageing process of OL and MA particles (section 6.3.2 and section 6.4.2) may be detrimental to human health (Jimenez et al., 2009). They enter the human body through respiratory system and skin (Phillips et al., 1999). VOCs can be adsorbed on atmospheric particles, followed by reaction within the particle phase, and generate new possibly toxic volatile or condensed phase organic species.

There are few recent studies investigating the health effects of SOA (Künzi et al., 2013). A very recent study has speculated that 9-oxononanoic acid (ON), which is one of the major oxidation product in this study in aged OL particles, stimulates enzymatic activity that causes pulmonary hypertension, perturbs blood fluidity and affect cardiovascular events (Ren et al., 2013). Also carboxylic acids evolved during particle oxidation, such as formic acid and oxalic acid, are primarily irritant and corrosive and reported to cause kidney damage (Malachowski and Goldberg, 1999).

9.5.2 Atmospheric chemistry and physics implication

SOA may act as sink or source of reactive species such as OH and HO_2 thus affecting the chemistry of the gas phase (Stockwell et al., 2011). For example, the OL-O_3 HR and MA-O_3 HR reactions generate free radicals which are an important source of radicals at night time when photolytic sources of radicals are at its minimal.

As explained in chapter 6, the heterogeneous reaction of organic particles directly alters the size, density and chemical composition of the particles. These are the key parameters controlling the particle's removal and optical properties of the particles. While the size of the particle has considerable impact on the deposition velocity and scattering of light, the identity of the species

in particles is the principal character driving light absorption. Generally, aging organic aerosol results in the formation of light absorbing species. The large numbers of organic functionalities in SOA such as carboxylic acid, hydroxyl, ketone and aldehyde groups may result in an absorbing matrix that can exhibit optical properties dramatically different from those of parent molecules. On the other hand, the presence of absorbing compounds in organic particles can stimulate photosensitization processes which might lead to either reduction and oxidation of intermediates and products (Kolb et al., 2010). As a conclusion aged organic particles are complex mixtures consisting of numerous compounds thus no potential absorption spectrum is possible to be generalised (Ervens et al., 2011) in order to estimate the optical impact of aged organic particles with confidence.

9.5.3 Climate implication

The direct scattering of light by particles affects climate by altering the radiation force of the atmosphere and hence the solar radiation reaching the surface of the Earth. Due to the enhanced polarity, solubility, hygroscopicity and mixing of oxygenated species in SOA, it is likely that SOA better act as cloud condensation nuclei (CCN) (Rudich et al., 2007). Thus ageing OA may enhance the negative forcing associated with indirect aerosol effects that are mostly mediated by CCN (Zahardis and Petrucci, 2007; Kolb et al., 2010). But oligomerization driven by CIs, as it shown for the case of OL-O_3 HR, prevents the CCN activity of the particles (Schwier et al., 2011), therefore depressing the indirect cooling effect. Moreover, aged particles containing light absorbers may also lead to heating of the lower atmosphere resulting in positive global radiative forcing. The impact of SOA on global radiative forcing is thus of the largest uncertainties in atmospheric science.

9.6 Future directions

The early sections of this chapter have shown that several issues remain unresolved and require further investigation.

Closing the gap between simulated and observed HO_x in the ACA system will require additional considerations to explain the higher modelled than the measured concentration of HO_x radicals. Clearly, the model used to estimate HO_x is too simple and to make it more accurate, the theoretical study of HO_x in the ACA system could be extended to include other mechanisms of losses of HO_x. Moreover, PERCA response could be modified to better fit the chemistry of the artificial atmosphere in the ACA system. Implementation of another type of NO_2 detector with no ozone contribution that converts NO to NO_2 is recommended for such analysis. The luminol approach can be substituted by the laser induced fluorescence (LIF) which potentially avoids ozone interference. PERCA signal can be modified further by minimising HO_x losses in the system. The use of the SO_2 reagent rather than CO and subsequent oxidation of SO_2 to H_2SO_4 which is then detected by CIMS provides better solution for radical losses by avoiding termination reaction (chapter 4, R4.4 and R4.5) (Heard, 2006). However, both of these approaches entail significant additional complexity and cost.

The ACA system was useful to study laboratory generated pure unsaturated and saturated organic aerosols. However, studies with more chemically mixed particles are required to better approximate the atmospheric complexity. Future studies should also consider systems of lower levels of oxidants and longer exposure times to simulate real atmospheric conditions and thus better understand the environmental effects of atmospheric aerosol.

There is no doubt that the ATOFMS has contributed to advances in atmospheric chemistry in recent years, but as a stand-alone instrument, it is not adequate to characterise an aerosol. Combined datasets from both ATOFMS and offline filter based approaches for aerosol measurement offer better characterization of aerosol composition and physical properties.

Only condensed phase species were characterised in the current study making comparison between condensed and gas phase species difficult. Therefore further investigation in this regard is necessary to determine the volatile fractions and to identify the gas phase composition in parallel to the condensed phase.

Finally an issue to consider is the applicability of the ACA procedures to ambient conditions. The inconsistency in the observed trend needs to be further explored with ambient aerosol arising from sources not influenced by high variability. A remote forested site with high biogenic organic aerosol emission might offer a better exhaust venue for studying ambient aerosol processes.

APPENDICES

Appendix A

List of abbreviation

Abbreviation	Meaning
4-ON	4-oxononanoic acid
AA	Azelaic Acid
AAHP	α-acyloxyalkyl hydroperoxides
AFT	Aerosol Flow Tube
ATOFM	Aerosol Time-of-Flight Mass Spectrometer
ATR-FT-IR	Attenuated Total Reflectance Fourier Transform Infrared Spectroscopy
RFT-IR	Reflectance Fourier Transform Infrared Spectroscopy
BES	Bis(2-Ethylhexyl)Sebacate
BR	Bulk Reaction
CAHP	Cyclic Acyloxy HydroPeroxide
ccm	cubic centimetres per minute
CCN	Cloud Condensation Nuclei
CFT	Coated Wall Flow Tubes
CI	Crigee Intermediate
CIMS	Chemical Ionisation Mass Spectrometry
CIs	Criegee intermediates
CL	Chain Length
DART-MS	Direct Analysis in Real Time Mass Spectrometry
ECI	Excited Criegee Intermediate
EDB	ElectroDynamic Balance
EGA	Evolve Gas Analysis
FA	Formic Acid
FIDI	Field-Induced Droplet Ionization
FLIM	Fluorescence Lifetime Imaging Microscopy
FT-ICR-MS	Fourier Transform Ion Cyclotron Resonance Mass Spectrometer

List of abbreviation Continued

Abbreviation	Meaning
FTIR	Fourier transform infrared spectroscopy
GA	Glyoxylic Acid
GC–MS	Gas Chromatography Mass Spectrometry
HAHP	HydroxyAcetyl HydroPeroxide
HMW	High Molecular Weight
HNMR	proton nuclear magnetic resonance
HO_x	OH and HO_2 collection
HPLC	High Performance Liquid Chromatography
HR	Heterogeneous Reaction
H-TDMA	Hygroscopicity Tandem Differential Mobility Analyzer
IC	Ion Chromatography
l	Diffuso-reactive length
L m^{-1}	Litre per minute
LDI	laser desorption ionization
LMW	lower molecular weight
l_p	surface depth
MA	Maleic acid (*cis*-butenedioic acid)
MFC	Mass Flow Controller
MMA	Monomethyl Azelate
MON	Methyl-9-xononanoat
MW	Molecular Weight
NA	Nonanoic Acid
NBS	Nile Blue Sulphate (Bis[5-amino-9-(diethylamino)benzo[a]phenoxazin-7-ium]sulfate)
NN	Nonanal
NO_x	Nitrite and nitrate
OA	Organic Aerosol

List of abbreviation continued

Abbreviation	Meaning
OcA	Octanoic Acid
OD	oxecane-2,10-dione
OL	Oleic acid
OL-O_3 HR	Oleic acid-Ozone Heterogeneous Reaction
ON	9-Oxononanoic Acid
Ox1	9- oxooctadecanoic acid
Ox2	10-oxooctadecanoic acid
Ox3	9-oxooctadecanedioic acid
OxA	Oxalic Acid
PERCA	Peroxy Radical Chemical Amplification
PERCI-MS	Photoelectron Resonance Capture Ionization Mass Spectrometry
PFA	Perfluoroalkoxy alkane
$PM_{2.5}$	Particulate Matter with aerodynamic diameter less than 2.5 μm
POA	Primary Organic Aerosol
POZ	Primary OZonide
PSL	PolyStyrene Latex
PTFE	Polytetrafluoroethylene
RH	Relative Humidity
ROS	Reactive Oxygen Species
ROS	Reactive Oxygen Species
SA	Stearic Acid
sccm	standard cubic centimetres per minute
SCF	sensitivity correction factors
slm	standard litres per minute
SMPS	Scanning Mobility Particle Sizer

List of abbreviation continued

Abbreviation	Meaning
SOA	Secondary Organic Aerosol
SO_x	Sulphur Oxides
SOZ	Secondary Ozonide
SR	Surface Reaction
TDPBMS	Thermal Desorption Particle Beam Mass Spectrometry
VOCs	Volatile Organic Compounds

Appendix B

Experimental Methodology and Results

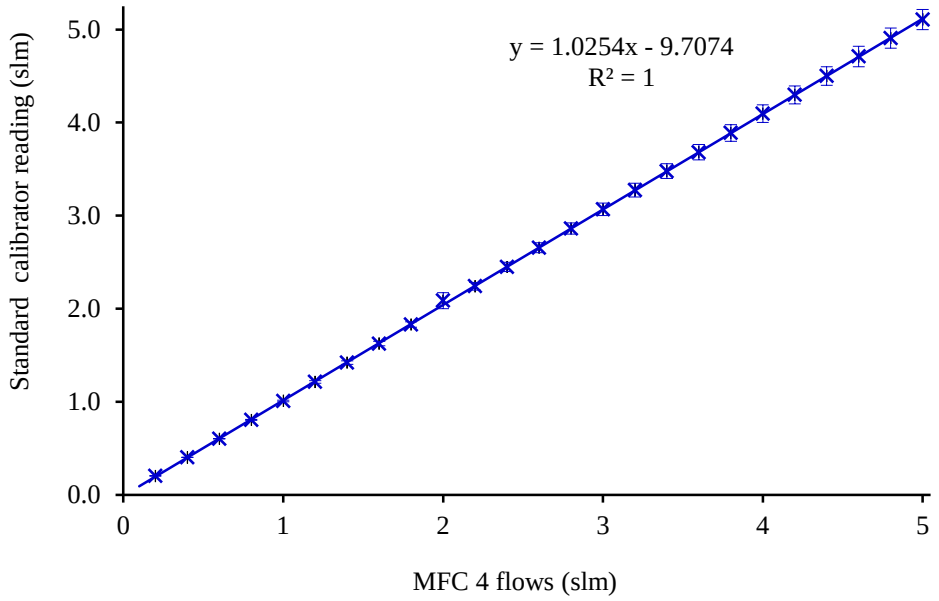

Figure B- 1 A typical calibration curves of a mass flow controller. Calibration was performed as described in section 2.2.2.

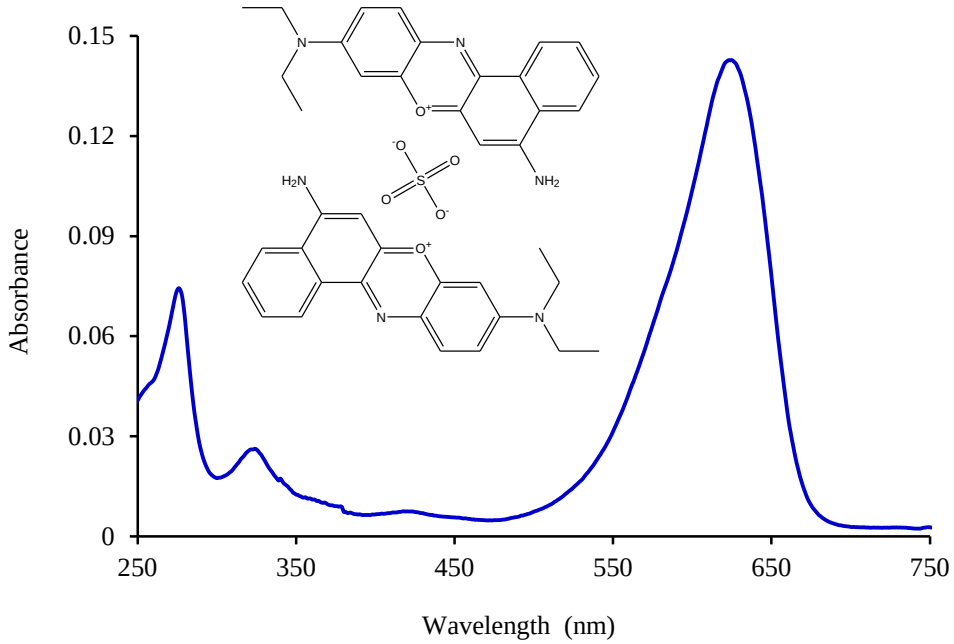

Figure B- 2 Absorption spectrum of NBS in methanol and its molecular structure. NBS ($C_{40}H_{40}N_6O_2.SO_4$), MW 732.87. The spectrum was recorded as described in section 2.2.6.1

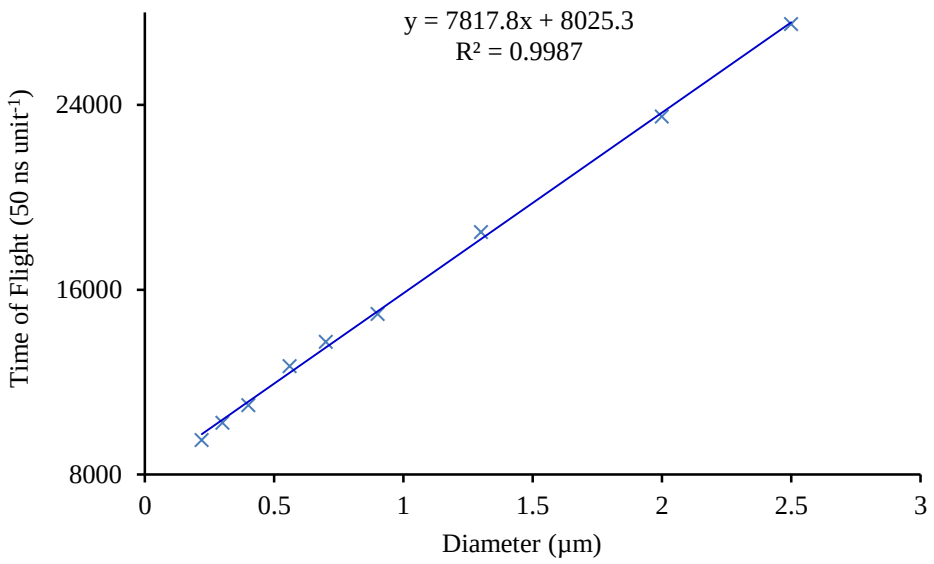

Figure B- 3 ATOFMS size calibration of particle. ATOFMS size calibration was carried out and analysed as described in section 2.2.7.2.

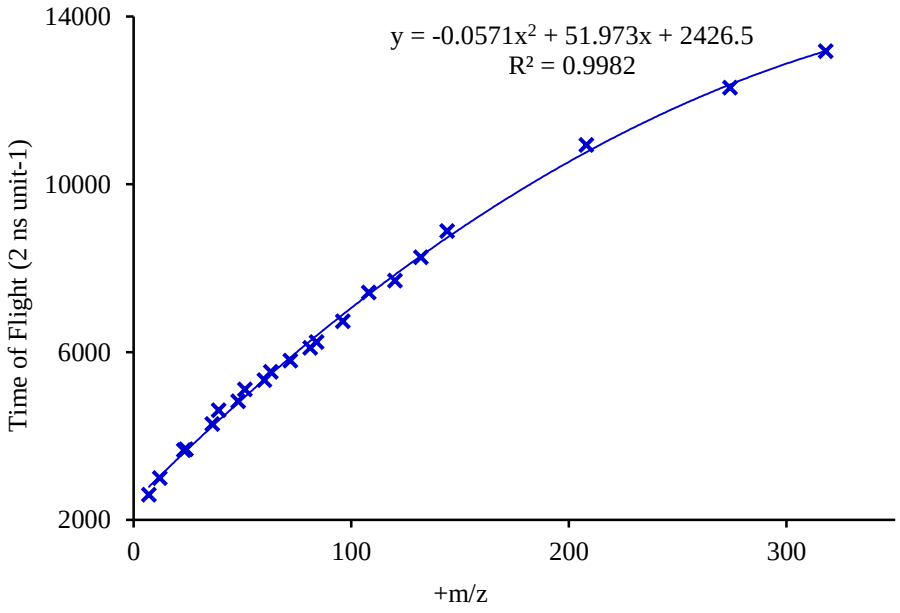

Figure B- 4 ATOFMS positive ion mass calibration. ATOFMS mass calibration was carried out and analysed as described in section 2.2.7.2.

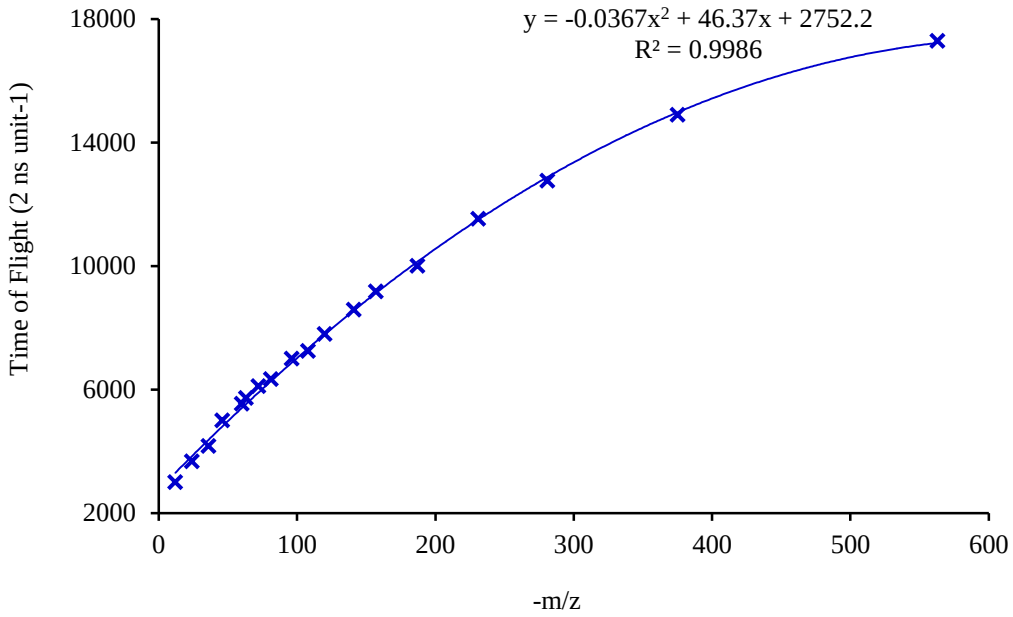

Figure B- 5 ATOFMS negative ion mass calibration. ATOFMS mass calibration was carried out and analysed as described in section 2.2.7.2.

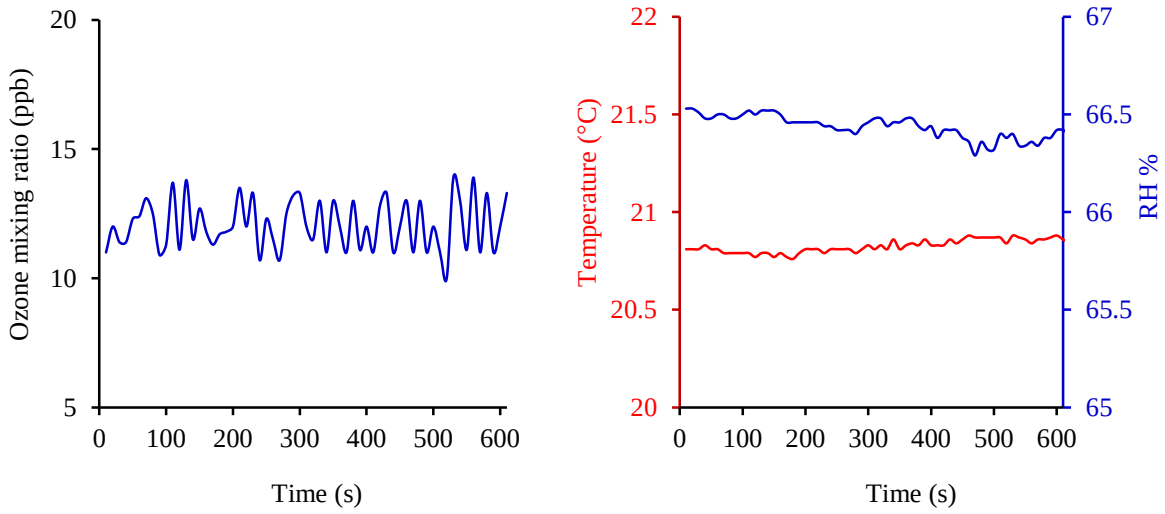

(a) (b)

Figure B- 6 Stability of: (a) ozone levels and (b) RH% and temperature; during PERCA sampling period from the calibration tube. RH%, temperature and ozone mixing ratio were recorded as described in section 4.2.2.3.

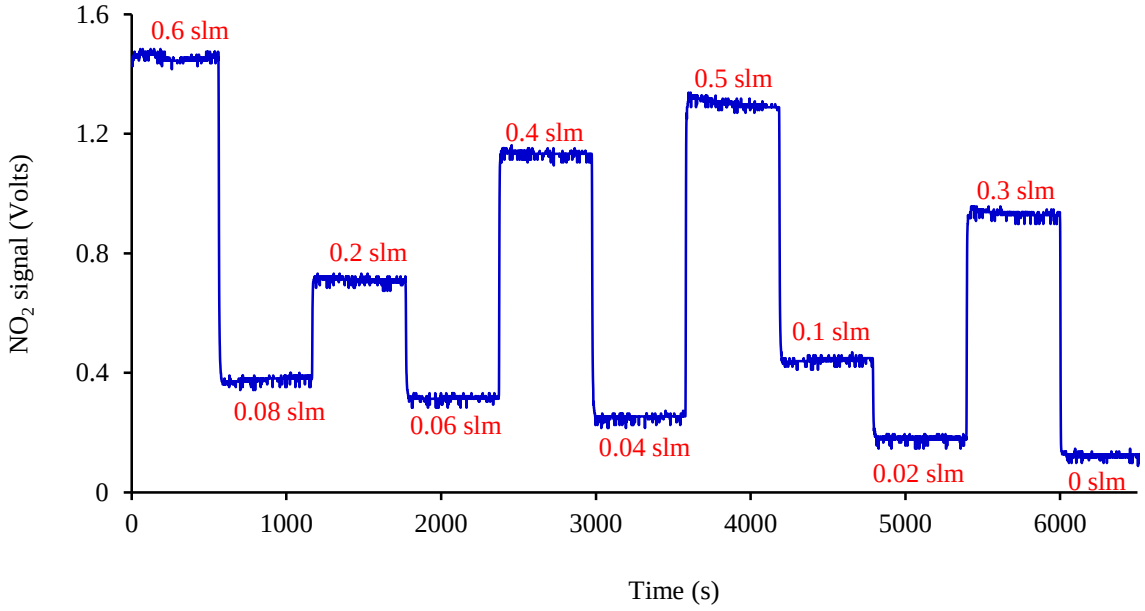

Figure B- 7 NO_2 analyser response to changing flow proportionality of NO_2 and pure air over a period of 10 minutes. Labels in red are the flow of NO_2 gas in slm, total flow was made up to 4 with pure air. A description on the NO_2 calibration methodology and analysis is presented in section 4.2.3.1.

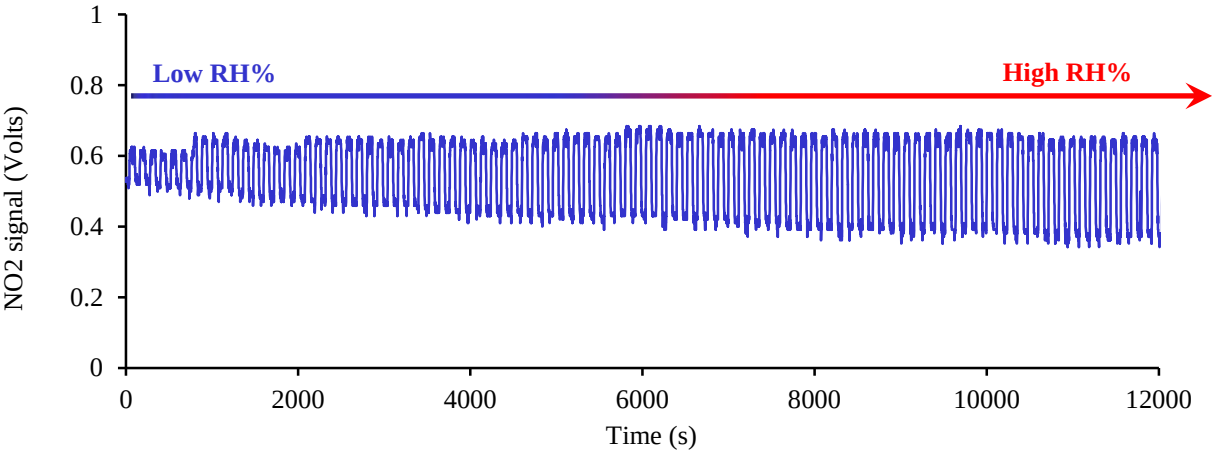

Figure B- 8 PERCA response at the calibrated RH% range (0.5-95%). The calibration methodology and data analysis are described in section 4.2.3.2.

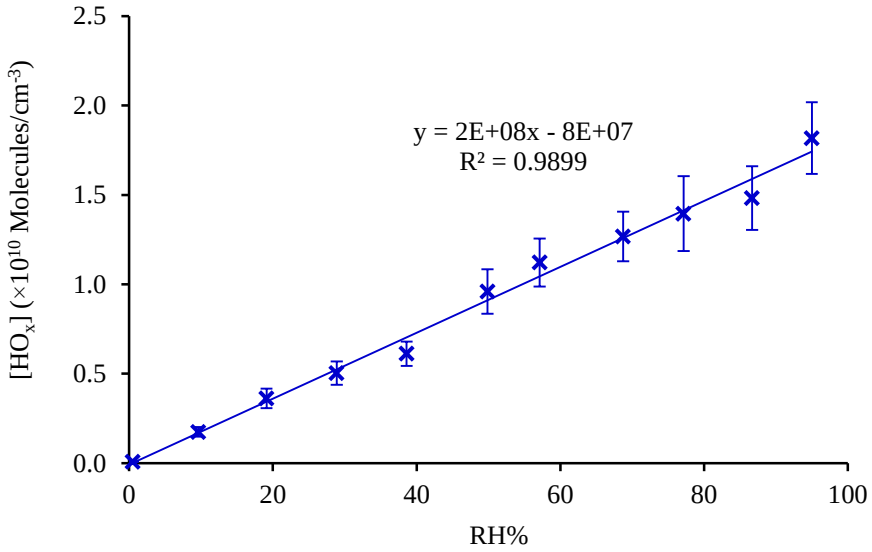

Figure B- 9 HO_x concentration as a function of RH%. The calibration methodology and data analysis are described in section 4.2.3.2.

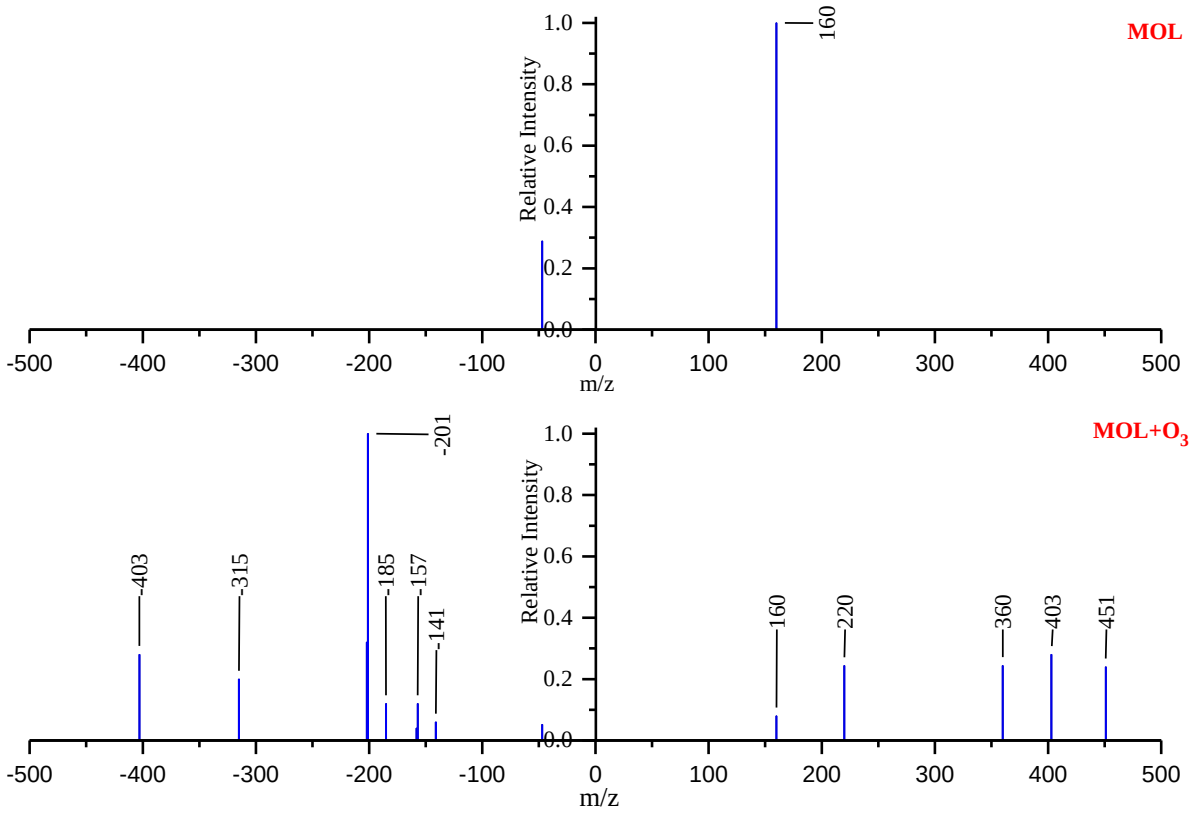

Figure B- 10 Averaged ATOFMS negative and positive ion mass spectra of 200 MOL particles. Section 6.2.2.3 describes the methodology and the purpose of the experiment.

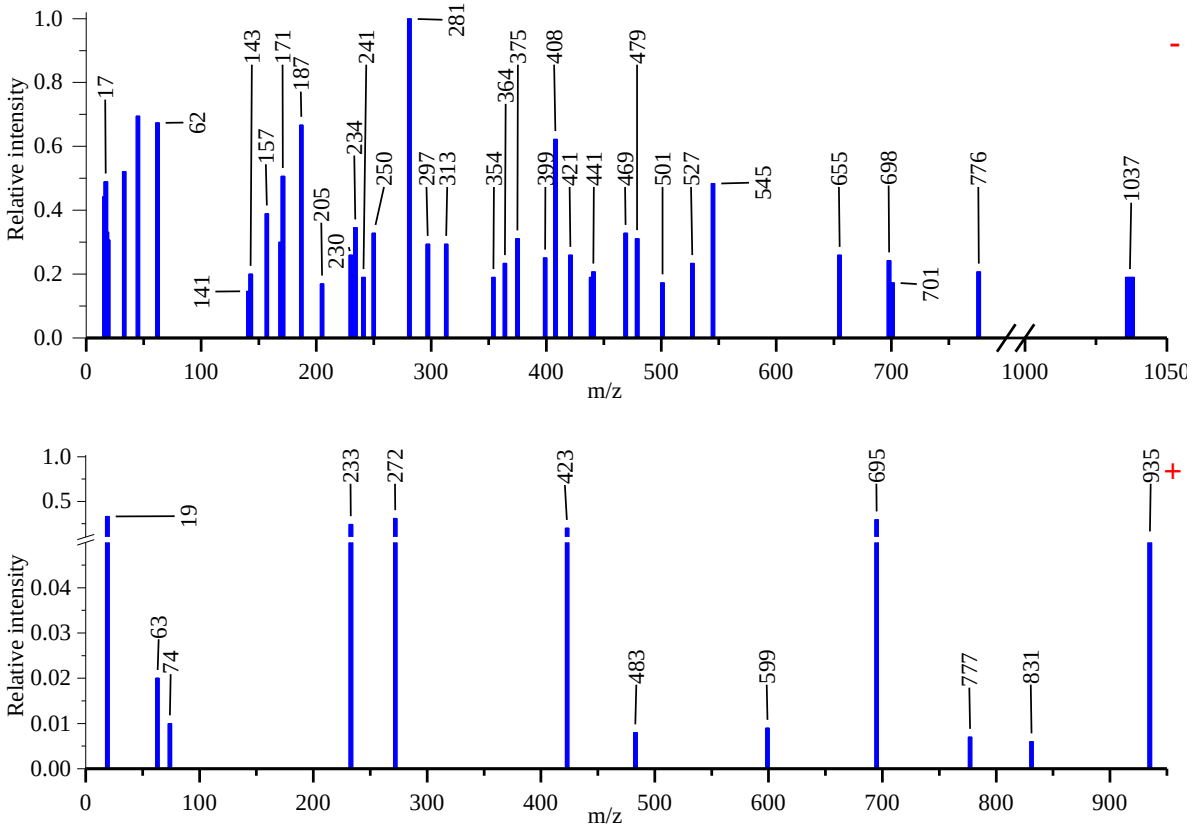

Figure B- 11 Averaged negative and positive ion mass spectra of wet aged OL particles.

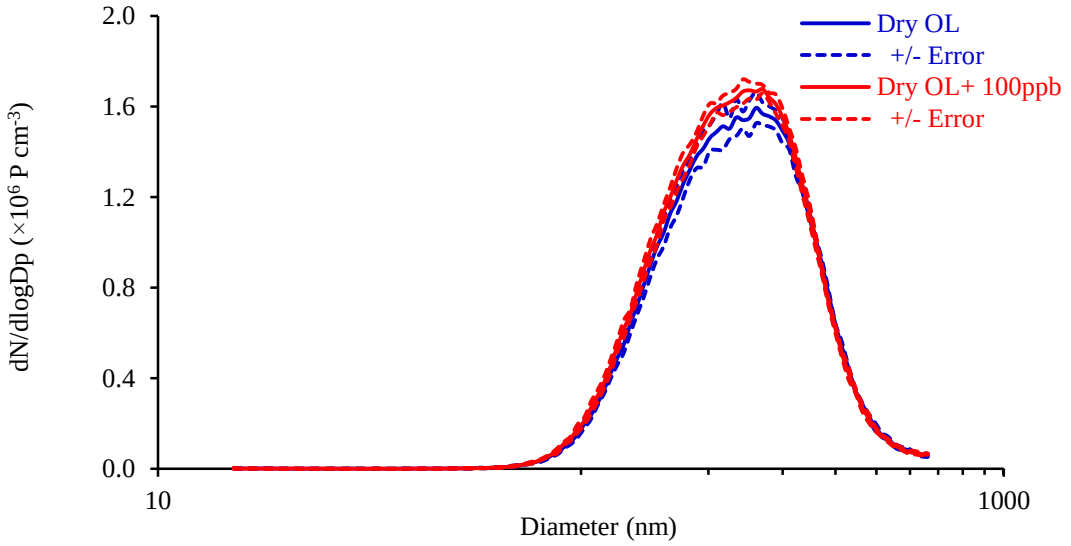

Figure B- 12 Size distribution of pure OL aerosol and exposed OL aerosol to 100 ppb ozone. Section 6.3.1explains the figure.

Appendix C

Tables of calibration recipes.

Table C- 1 Flow recipe for NO_2 calibration experiment. Calibration experiment is described in section 4.2.3.1.

Dwell (minutes)	Flows (slm)			
	PERCA exhaust	NO_2	Air dilution	Total
7	2.0	1.0	3.0	4.0
7	2.0	0.1	3.9	4.0
7	2.0	0.9	3.1	4.0
7	2.0	0.2	3.8	4.0
7	2.0	0.8	3.2	4.0
7	2.0	0.3	3.7	4.0
7	2.0	0.7	3.3	4.0
7	2.0	0.4	3.6	4.0
7	2.0	0.6	3.4	4.0
7	2.0	0.5	3.5	4.0
7	2.0	0.0	4.0	4.0

Table C- 2 Recipe flows for PERCA calibration experiment. Calibration experiment is described in section 4.2.3.2.

RH%	Dwell (minutes)	Flow (slm)						
		Calibration tube		PERCA cell reactor				
		Wet flow	Dry flow	NO	CO	N_2	N_2 cavity	PERCA exhaust
0.5	12	0.0	10.0	0.01	0.1	0.1	1.0	2.0
8.2	12	1.0	9.0	0.01	0.1	0.1	1.0	2.0
17.0	12	2.0	8.0	0.01	0.1	0.1	1.0	2.0
26.6	12	3.0	7.0	0.01	0.1	0.1	1.0	2.0
35.4	12	4.0	6.0	0.01	0.1	0.1	1.0	2.0
44.8	12	5.0	5.0	0.01	0.1	0.1	1.0	2.0
54.1	12	6.0	4.0	0.01	0.1	0.1	1.0	2.0
63.5	12	7.0	3.0	0.01	0.1	0.1	1.0	2.0
73.1	12	8.0	2.0	0.01	0.1	0.1	1.0	2.0
85.9	12	9.0	1.0	0.01	0.1	0.1	1.0	2.0
95.0	12	10.0	0.0	0.01	0.1	0.1	1.0	2.0

Appendix D

Table D-1 A summary of proposed components and possible propagators combinations of observed mass spectra peaks correspond to 44 oxidation products of OL-O_3 HR. Mass spectra analysis is described in section 6.2.2.3.

MW	MS signature		No of composed components								Dehydration (-nH_2O)
	- m/z	+ m/z	NN	OcA	AA or CI1	ON	NA or CI2	Ox1 or Ox2	Ox3	OL	
142	141		1								
144	143			1							
158	157						1				
170	169				1						1
172	171					1					
188	187				1						
298	297							1			
314	313			1	1						
328	327							1			
342	341				1	1					
422	421	377*					1			1	1
440	439	423†					1			1	0
528	527	466*† 483* 547‡			3						3
644	643	599*					2		1		0
656	655				2		2				2
768	767				1		2			1	1
786	785	753≠			1		2			1	0
810	809	793† 777≠			2	1	2				3
844	843	811≠			3		2				2
864	863	819* 831≠			2	1	2				0

The summary of proposed components and possible propagators combinations continued.

MW	MS signature		No of composed components								Dehydration ($-nH_2O$)
	- m/z	+ m/z	NN	OcA	AA or CI1	ON	NA or CI2	Ox1 or Ox2	Ox3	OL	
880	879				3		2				0
894	893	861[≠]			3	1	1				0
950	949	917[≠]			3		1			1	3
968	967	935[≠]			3		1			1	2
974	973				2		2			1	0
986	985	953[≠]			3		1			1	1
1002	1001				3		3				2
1020	1019	1003[†]			3		1	1			0
1026	1025				4				1		3
1038	1037	1005[≠]			3		3				0
1051	1050	1070[‡]			4		2				1
1068	1067	1023[*] 1106[‡]			4		2				0
1080	1079				4				1		0
1162	1161	1112[†≠]			3		2			1	0
1178	1177				3		4				1
1190	1189				4		1	1			1
1196	1195				3		4				0
1208	1207				4		1	1			0
1214	1213				5				1		3
1292	1291				3	1			1	1	3
1310	1309				3	1			1	1	2
1346	1345				3	1			1	1	0
1438	1437				6				1		1
1524		1458[≠]			3		4		1		0

[*]M-CO_2H, [≠]M-HO_2, [†]M-OH and [‡]M+H_3O.

REFERENCES

Agarwal, J. K. and G. J. Sem (1980). Continuous flow, single-particle-counting condensation nucleus counter. *Journal of Aerosol Science*, **11**(4): 343-357.

Aiken, A. C., P. F. DeCarlo, J. H. Kroll, D. R. Worsnop, J. A. Huffman, K. S. Docherty, I. M. Ulbrich, C. Mohr, J. R. Kimmel, D. Sueper, Y. Sun, Q. Zhang, A. Trimborn, M. Northway, P. J. Ziemann, M. R. Canagaratna, T. B. Onasch, M. R. Alfarra, A. S. H. Prevot, J. Dommen, J. Duplissy, A. Metzger, U. Baltensperger and J. L. Jimenez (2008). O/C and OM/OC Ratios of Primary, Secondary, and Ambient Organic Aerosols with High-Resolution Time-of-Flight Aerosol Mass Spectrometry. *Environmental Science & Technology*, **42**(12): 4478-4485.

Alexander Kokhanovsky, A. A. K. (2008). *Aerosol optics: light absorption and scattering by particles in the atmosphere*. Chichester, Praxis Publishing Ltd.

Alfarra, M. R., H. Coe, J. D. Allan, K. N. Bower, H. Boudries, M. R. Canagaratna, J. L. Jimenez, J. T. Jayne, A. A. Garforth, S.-M. Li and D. R. Worsnop (2004). Characterization of urban and rural organic particulate in the Lower Fraser Valley using two Aerodyne Aerosol Mass Spectrometers. *Atmospheric Environment*, **38**(34): 5745-5758.

Allen, J. and R. K. Gould (1981). Mass spectrometric analyzer for individual aerosol particles. *Review of Scientific Instruments*, **52**(6): 804-809.

Allen, J. O. (2004). Quantitative Analysis of Aerosol Time-of-Flight Mass Spectrometry Data using YAADA. Arizona States, Arizona State University: 65.

Allen, J. O. (2005). Software Toolkit to Analyze Single-Particle Mass Spectral Data. 3800. Arizona, Arizona satate University: YAADA

Allen, J. O., P. V. Bhave, J. R. Whiteaker and K. A. Prather (2006). Instrument Busy Time and Mass Measurement using Aerosol Time-of-Flight Mass Spectrometry. *Aerosol Science and Technology*, **40**(8): 615 - 626.

Altieri, K. E., S. P. Seitzinger, A. G. Carlton, B. J. Turpin, G. C. Klein and A. G. Marshall (2008). Oligomers formed through in-cloud methylglyoxal reactions: Chemical composition, properties, and mechanisms investigated by ultra-high resolution FT-ICR mass spectrometry. *Atmospheric Environment*, **42**(7): 1476-1490.

Ammann, M. and U. Pöschl (2007). Kinetic model framework for aerosol and cloud surface chemistry and gas-particle interactions - Part 2: Exemplary practical applications and numerical simulations. *Atmos. Chem. Phys.*, **7**: 6025-6045.

Anastasi, C., R. V. Gladstone and M. G. Sanderson (1993). Chemical amplifiers for detection of peroxy radicals in the atmosphere. *Environmental Science & Technology*, **27**(3): 474-482.

Anderson, D. R., M. J. Booth, P. Collins, D. Ciaparra, J. S. Hodges, P. L. Louer, F. Drewick and M. Dall'Osto (2007). Ultrafine characterisation of emission and impact of ultrafine particulate, European Commission.

Andreae, M. O. (2009). A New Look at Aging Aerosols. *Science*, **326**(5959): 1493-1494.

Andrews, E. and S. M. Larson (1993). Effect of surfactant layers on the size changes of aerosol particles as a function of relative humidity. *Environmental Science & Technology*, **27**(5): 857-865.

Angelino, S., D. T. Suess and K. A. Prather (2001). Formation of Aerosol Particles from Reactions of Secondary and Tertiary Alkylamines: Characterization by Aerosol Time-of-Flight Mass Spectrometry. *Environmental Science & Technology*, **35**(15): 3130-3138.

Asad, A., B. T. Mmereki and D. J. Donaldson (2005). Enhanced uptake of water by oxidatively processed oleic acid. *Atmos. Chem. Phys.*, **4**(8): 2083-2089.

Aschmann, S. M., J. Arey and R. Atkinson (2000). Formation of β-Hydroxycarbonyls from the OH Radical-Initiated Reactions of Selected Alkenes. *Environmental Science & Technology*, **34**(9): 1702-1706.

Ashbourn, S. F. M., M. E. Jenkin and K. C. Clemitshaw (1998). Laboratory Studies of the Response of a Peroxy Radical Chemical Amplifier to HO₂ and a Series of Organic Peroxy Radicals. *Journal of Atmospheric Chemistry*, **29**(3): 233-266.

Atkinson, R. (1997). Gas-Phase Tropospheric Chemistry of Volatile Organic Compounds: 1. Alkanes and Alkenes. *Journal of Physical and Chemical Reference Data*, **26**(2): 215-290.

Atkinson, R. and J. Arey (2003). Atmospheric Degradation of Volatile Organic Compounds. *Chemical Reviews*, **103**(12): 4605-4638.

Atkinson, R., D. L. Baulch, R. A. Cox, J. N. Crowley, R. F. Hampson, R. G. Hynes, M. E. Jenkin, M. J. Rossi and J. Troe (2004). Evaluated kinetic and photochemical data for atmospheric chemistry: Volume I - gas phase reactions of Ox, HOx, NOx and SOx species. *Atmos. Chem. Phys.*, **4**(6): 1461-1738.

Atkinson, R., D. L. Baulch, R. A. Cox, R. F. Hampson, J. A. Kerr, M. J. Rossi and J. Troe (1999). Evaluated Kinetic and Photochemical Data for Atmospheric Chemistry, Organic Species: Supplement VII. *Journal of Physical and Chemical Reference Data*, **28**(2): 191-393.

Atkinson, R. and W. P. L. Carter (1984). Kinetics and mechanisms of the gas-phase reactions of ozone with organic compounds under atmospheric conditions. *Chemical Reviews*, **84**(5): 437-470.

Bailey, P. S. (1958). The Reactions Of Ozone With Organic Compounds. *Chemical Reviews*, **58**(5): 925-1010.

Bailey, P. S. and T. M. Ferrell (1978). Mechanism of ozonolysis. A more flexible stereochemical concept. *Journal of the American Chemical Society*, **100**(3): 899-905.

Barsanti, K. C. and J. F. Pankow (2006). Thermodynamics of the formation of atmospheric organic particulate matter by accretion reactions--Part 3: Carboxylic and dicarboxylic acids. *Atmospheric Environment*, **40**(34): 6676-6686.

Bhave, P. V., J. O. Allen, B. D. Morrical, D. P. Fergenson, G. R. Cass and K. A. Prather (2002). A Field-Based Approach for Determining ATOFMS Instrument Sensitivities to Ammonium and Nitrate. *Environmental Science & Technology*, **36**(22): 4868-4879.

Bi, X., G. Zhang, L. Li, X. Wang, M. Li, G. Sheng, J. Fu and Z. Zhou (2011). Mixing state of biomass burning particles by single particle aerosol mass spectrometer in the urban area of PRD, China. *Atmospheric Environment*, **45**(20): 3447-3453.

Bird, R. B., W. E. Stewart and E. N. Lightfoot (2007). *Transport Phenomena*. New York, John Wiley & Sons, Inc.

Blando, J. D., R. J. Porcja, T.-H. Li, D. Bowman, P. J. Lioy and B. J. Turpin (1998). Secondary Formation and the Smoky Mountain Organic Aerosol: An Examination of Aerosol Polarity and Functional Group Composition During SEAVS. *Environmental Science & Technology*, **32**(5): 604-613.

Bloss, W. J., J. D. Lee, C. Bloss, K. Wirtz, M. Martin-Reviejo, M. Siese, D. E. Heard and M. J. Pilling (2004). Validation of the calibration of a laser-induced fluorescence instrument for the measurement of OH radicals in the atmosphere. *Atmos. Chem. Phys.*, **3**(6): 6029-6061.

Bokis, C. P., C.-C. Chen and H. Orbey (1999). A segment contribution method for the vapor pressure of tall-oil chemicals. *Fluid Phase Equilibria*, **155**(2): 193-203.

Bond, T. C., S. J. Doherty, D. W. Fahey, P. M. Forster, T. Berntsen, B. J. DeAngelo, M. G. Flanner, S. Ghan, B. Kärcher, D. Koch, S. Kinne, Y. Kondo, P. K. Quinn, M. C. Sarofim, M. G. Schultz, M. Schulz, C. Venkataraman, H. Zhang, S. Zhang, N. Bellouin, S. K. Guttikunda, P. K. Hopke, M. Z. Jacobson, J. W. Kaiser, Z. Klimont, U. Lohmann, J. P. Schwarz, D. Shindell, T. Storelvmo, S. G. Warren and C. S. Zender (2013). Bounding the role of black carbon in the climate system: A scientific assessment. *Journal of Geophysical Research: Atmospheres*, **118**(11): 5380-5552.

Brooks, S. D., P. J. DeMott and S. M. Kreidenweis (2004). Water uptake by particles containing humic materials and mixtures of humic materials with ammonium sulfate. *Atmospheric Environment*, **38**(13): 1859-1868.

Brown, M. and C. Arnold (2010). Fundamentals of Laser-Material Interaction and Application to Multiscale Surface Modification. *Laser Precision Microfabrication*. K. Sugioka, M. Meunier and A. Piqué, Springer Berlin Heidelberg. **135:** 91-120.

Bunnelle, W. H. (1991). Preparation, properties, and reactions of carbonyl oxides. *Chemical Reviews*, **91**(3): 335-362.

Bzdek, B. R., M. R. Pennington and M. V. Johnston (2012). Single particle chemical analysis of ambient ultrafine aerosol: A review. *Journal of Aerosol Science*, **52**(0): 109-120.

Calvello, M., F. Esposito, G. Pavese and C. Serio (2010). Physical and optical properties of atmospheric aerosols by in-situ and radiometric measurements. *Atmos. Chem. Phys.*, **10**(5): 2195-2208.

Calvert, J. G., R. Atkinson, J. A. Kerr, S. Madronich, G. K. Moortgat, T. J. Wallington and G. Yarwood (2000). *The mechanisms of atmospheric oxidation of the alkenes*. Oxford, Oxford University Press.

Camredon, M., J. F. Hamilton, M. S. Alam, K. P. Wyche, T. Carr, I. R. White, P. S. Monks, A. R. Rickard and W. J. Bloss (2010). Distribution of gaseous and particulate organic

composition during dark α-pinene ozonolysis. *Atmos. Chem. Phys.*, **10**(6): 2893-2917.

Cantrell, C. A., R. E. Shetter, J. A. Lind, A. H. McDaniel, J. G. Calvert, D. D. Parrish, F. C. Fehsenfeld, M. P. Buhr and M. Trainer (1993). An improved chemical amplifier technique for peroxy radical measurements. *Journal of Geophysical Research: Atmospheres*, **98**(D2): 2897-2909.

Cantrell, C. A. and D. H. Stedman (1982). A possible technique for the measurement of atmospheric peroxy radicals. *Geophys. Res. Lett.*, **9**(8): 846-849.

Cantrell, C. A., D. H. Stedman and G. J. Wendel (1984). Measurement of atmospheric peroxy radicals by chemical amplification. *Analytical Chemistry*, **56**(8): 1496-1502.

Cappa, C. D., E. R. Lovejoy and A. R. Ravishankara (2008). Evaporation Rates and Vapor Pressures of the Even-Numbered C8−C18 Monocarboxylic Acids. *The Journal of Physical Chemistry A*, **112**(17): 3959-3964.

Carlton, A. G., C. Wiedinmyer and J. H. Kroll (2009). A review of Secondary Organic Aerosol (SOA) formation from isoprene. *Atmos. Chem. Phys.*, **9**(14): 4987-5005.

Chan, A. W. H., K. E. Kautzman, P. S. Chhabra, J. D. Surratt, M. N. Chan, J. D. Crounse, A. Kürten, P. O. Wennberg, R. C. Flagan and J. H. Seinfeld (2009). Secondary organic aerosol formation from photooxidation of naphthalene and alkylnaphthalenes: implications for oxidation of intermediate volatility organic compounds (IVOCs). *Atmos. Chem. Phys.*, **9**(9): 3049-3060.

Chan, L. P. and C. K. Chan (2012). Roles of the Phase State and Water Content in Ozonolysis of Internal Mixtures of Maleic Acid and Ammonium Sulfate Particles. *Aerosol Science and Technology*, **46**(7): 781-793.

Chang, R. Y. W., J. G. Slowik, N. C. Shantz, A. Vlasenko, J. Liggio, S. J. Sjostedt, W. R. Leaitch and J. P. D. Abbatt (2010). The hygroscopicity parameter (Îº) of ambient organic aerosol at a field site subject to biogenic and anthropogenic influences: relationship to degree of aerosol oxidation. *Atmos. Chem. Phys.*, **10**(11): 5047-5064.

Charron, A., C. Degrendele, B. Laongsri and R. M. Harrison (2013). Receptor modelling of secondary and carbonaceous particulate matter at a southern UK site. *Atmos. Chem. Phys.*, **13**(4): 1879-1894.

Che, D. L., J. D. Smith, S. R. Leone, M. Ahmed and K. R. Wilson (2009). Quantifying the reactive uptake of OH by organic aerosols in a continuous flow stirred tank reactor. *Physical Chemistry Chemical Physics*, **11**(36): 7885-7895.

Chen, D.-R. and D. Y. H. Pui (1997). Numerical modeling of the performance of differential mobility analyzers for nanometer aerosol measurements. *Journal of Aerosol Science*, **28**(6): 985-1004.

Chen, D., C. Q. Yang and X. Qiu (2005). Aqueous Polymerization of Maleic Acid and Cross-Linking of Cotton Cellulose by Poly(maleic acid). *Industrial & Engineering Chemistry Research*, **44**(21): 7921-7927.

Chen, D. R., D. Y. H. Pui, D. Hummes, H. Fissan, F. R. Quant and G. J. Sem (1998). Design and evaluation of a nanometer aerosol differential mobility analyzer (Nano-DMA). *Journal of Aerosol Science*, **29**(5–6): 497-509.

Chen, T.-M. and H.-M. Chein (2006). Generation and Evaluation of Monodisperse Sodium Chloride and Oleic Acid Nanoparticles. *Aerosol and Air Quality Research*, **6** (3): 305-321.

Chen, Y., N. Shah, F. E. Huggins and G. P. Huffman (2006a). Microanalysis of ambient particles from Lexington, KY, by electron microscopy. *Atmospheric Environment*, **40**(4): 651-663.

Chen, Z., A. Bogaerts and A. Vertes (2006b). Phase explosion in atmospheric pressure infrared laser ablation from water-rich targets. *Applied Physics Letters*, **89**(4): -.

Cheng, H., Z. Zhou and E. Nakamura (2008). Crystal-size distribution and composition of garnets in eclogites from the Dabie orogen, central China. *American Mineralogist*, **93**(1): 124-133.

Cheung, H. C., C. C. K. Chou, W. R. Huang and C. Y. Tsai (2013). Characterization of ultrafine particle number concentration and new particle formation in urban environment of Taipei, Taiwan. *Atmos. Chem. Phys. Discuss.*, **13**(4): 8985-9016.

Chumpitaz, L., L. Coutinho and A. Meirelles (1999). Surface tension of fatty acids and triglycerides. *Journal of the American Oil Chemists' Society*, **76**(3): 379-382.

Creasey, D. J., D. E. Heard and J. D. Lee (2000). Absorption cross-section measurements of water vapour and oxygen at 185 nm. Implications for the calibration of field instruments to measure OH, HO2 and RO2 radicals. *Geophysical Research Letters*, **27**(11): 1651-1654.

Cremer, D., J. Gauss, E. Kraka, J. F. Stanton and R. J. Bartlett (1993). A CCSD (T) investigation of carbonyl oxide and dioxirane. Equilibrium geometries, dipole moments, infrared spectra, heats of formation and isomerization energies. *Chemical Physics Letters*, **209**(5–6): 547-556.

Criegee, R. (1948). Über eine Methyllactolid-Methyläther-Umlagerung. *Justus Liebigs Annalen der Chemie*, **560**(1): 141-148.

Criegee, R. (1953). Über den Verlauf der Ozonspaltung (III. Mitteilung). *Justus Liebigs Annalen der Chemie*, **583**(1): 1-36.

Criegee, R. (1975). Mechanism of Ozonolysis. *Angewandte Chemie International Edition in English*, **14**(11): 745-752.

Cruz, C. N. and S. N. Pandis (1998). The effect of organic coatings on the cloud condensation nuclei activation of inorganic atmospheric aerosol. *Journal of Geophysical Research: Atmospheres*, **103**(D11): 13111-13123.

Cui, Z., X. Hu, S. Liu and Z. Liu (2011). A dual-wavelength overlapping resonance Rayleigh scattering method for the determination of chondroitin sulfate with nile blue sulfate. *Spectrochimica Acta Part A: Molecular and Biomolecular Spectroscopy*, **83**(1): 1-7.

da Silva, G. (2010). Oxidation of Carboxylic Acids Regenerates Hydroxyl Radicals in the Unpolluted and Nighttime Troposphere. *The Journal of Physical Chemistry A*, **114**(25): 6861-6869.

Dall'Osto, M., D. Ceburnis, G. Martucci, J. Bialek, R. Dupuy, S. G. Jennings, H. Berresheim, J. C. Wenger, J. R. Sodeau, R. M. Healy, M. C. Facchini, M. Rinaldi, L. Giulianelli, E. Finessi, D. Worsnop and C. D. O'Dowd (2009). Aerosol properties associated with air masses arriving into the North East Atlantic during the 2008 Mace Head EUCAARI intensive observing period: an overview. *Atmos. Chem. Phys. Discuss.*, **9**(6): 26265-26328.

Dall'Osto, M. and R. M. Harrison (2012). Urban organic aerosols measured by single particle mass spectrometry in the megacity of London. *Atmos. Chem. Phys.*, **12**(9): 4127-4142.

Dall'Osto, M., R. M. Harrison, D. C. Beddows, E. J. Freney, M. R. Heal and R. J. Donovan (2006). Single-particle detection efficiencies of aerosol time-of-flight mass spectrometry during the North Atlantic marine boundary layer experiment. *Environmental Science & Technology*, **40**(16): 5029-5035.

Dall'Osto, M., R. M. Harrison, H. Furutani, K. A. Prather, H. Coe and J. D. Allan (2005). Studies of aerosol at a coastal site using two aerosol mass spectrometry instruments and identification of biogenic particle types. *Atmos. Chem. Phys. Discuss.*, **5**(5): 10799-10838.

Dasch, J. M. and S. H. Cadle (1989). Atmospheric Carbon Particles in the Detroit Urban Area: Wintertime Sources and Sinks. *Aerosol Science and Technology*, **10**(2): 236-248.

Daumont, D., J. Brion, J. Charbonnier and J. Malicet (1992). Ozone UV spectroscopy I: Absorption cross-sections at room temperature. *Journal of Atmospheric Chemistry*, **15**(2): 145-155.

Davis, W. D. (1977). Continuous mass spectrometric analysis of particulates by use of surface ionization. *Environmental Science & Technology*, **11**(6): 587-592.

de Gouw, J. A. and E. R. Lovejoy (1998). Reactive uptake of ozone by liquid organic compounds. *Geophysical Research Letters*, **25**(6): 931-934.

Deboudt, K., P. Flament, M. Choël, A. Gloter, S. Sobanska and C. Colliex (2010). Mixing state of aerosols and direct observation of carbonaceous and marine coatings on African dust by individual particle analysis. *Journal of Geophysical Research: Atmospheres*, **115**(D24): D24207.

Devlin, H. R. and I. J. Harris (1984). Mechanism of the oxidation of aqueous phenol with dissolved oxygen. *Industrial & Engineering Chemistry Fundamentals*, **23**(4): 387-392.

Dommen, J., A. Metzger, J. Duplissy, M. Kalberer, M. R. Alfarra, A. Gascho, E. Weingartner, A. S. H. Prevot, B. Verheggen and U. Baltensperger (2006). Laboratory observation of oligomers in the aerosol from isoprene/NOx photooxidation. *Geophys. Res. Lett.*, **33**(13): L13805.

Donahue, N. M., A. L. Robinson and S. N. Pandis (2009). Atmospheric organic particulate matter: From smoke to secondary organic aerosol. *Atmospheric Environment*, **43**(1): 94-106.

Easter, R. C. and L. K. Peters (1994). Binary Homogeneous Nucleation: Temperature and Relative Humidity Fluctuations, Nonlinearity, and Aspects of New Particle Production in the Atmosphere. *Journal of Applied Meteorology*, **33**(7): 775-784.

Ervens, B., B. Turpin and R. Weber (2011). Secondary organic aerosol formation in cloud droplets and aqueous particles (aqSOA): a review of laboratory, field and model studies. *Atmospheric Chemistry and Physics*, **11**(21): 11069-11102.

Fallah, R. N., S. Azizian, G. Reggers, R. Carleer, S. Schreurs, J. Ahenach, V. Meynen and J. Yperman (2014). Effect of aromatics on the adsorption of thiophenic sulfur compounds from model diesel fuel by activated carbon cloth. *Fuel Processing Technology*, **119**(0): 278-285.

Faloon, K. H. (2011). The Development of a Laboratory System to Investigate The Interactions of Tropospheric Aerososl and HOx Radicals. School of Geography, Earth and Environmental Sciences, College of Life and Environmental Sciences. Birmingham, University of Birmingham. DOCTOR OF PHILOSOPHY: 199.

Fan, J. and R. Zhang (2004). Atmospheric Oxidation Mechanism of Isoprene. *Environmental Chemistry*, **1**(3): 140-149.

Fang, W., L. Gong, X. Shan, F. Liu, Z. Wang and L. Sheng (2011a). Thermal Desorption/Tunable Vacuum–Ultraviolet Time-of-Flight Photoionization Aerosol Mass Spectrometry for Investigating Secondary Organic Aerosols in Chamber Experiments. *Analytical Chemistry*, **83**(23): 9024-9032.

Fang, W., G. Lei, X. Shan, F. Liu, Z. Wang and L. Sheng (2011b). A VUV photoionization organic aerosol mass spectrometric study with synchrotron radiation. *Journal of Electron Spectroscopy and Related Phenomena*, **184**(3–6): 129-133.

Fehsenfeld, F. C., J. W. Drummond, U. K. Roychowdhury, P. J. Galvin, E. J. Williams, M. P. Buhr, D. D. Parrish, G. Hübler, A. O. Langford, J. G. Calvert, B. A. Ridley, F. Grahek, B. G. Heikes, G. L. Kok, J. D. Shetter, J. G. Walega, C. M. Elsworth, R. B. Norton, D. W. Fahey, P. C. Murphy, C. Hovermale, V. A. Mohnen, K. L. Demerjian, G. I. Mackay and H. I. Schiff (1990). Intercomparison of NO2 measurement techniques. *Journal of Geophysical Research: Atmospheres*, **95**(D4): 3579-3597.

Feltham, E. J., M. J. Almond, G. Marston, K. S. Wiltshire and N. Goldberg (2000). Reactions of hydroxyl radicals with alkenes in low-temperature matrices. *Spectrochimica Acta Part A: Molecular and Biomolecular Spectroscopy*, **56**(13): 2589-2603.

Fergenson, D. P., X.-H. Song, Z. Ramadan, J. O. Allen, L. S. Hughes, G. R. Cass, P. K. Hopke and K. A. Prather (2001). Quantification of ATOFMS Data by Multivariate Methods. *Analytical Chemistry*, **73**(15): 3535-3541.

Finlayson-Pitts, B. J. and J. N. Pitts Jr (2000a). Chapter 11 - Analytical Methods and Typical Atmospheric Concentrations for Gases and Particles. *Chemistry of the Upper and Lower Atmosphere*. B. J. Finlayson-Pitts and J. N. Pitts. San Diego, Academic Press**:** 547-656.

Finlayson-Pitts, B. J. and J. N. Pitts Jr (2000b). *Chemistry of the Upper and Lower Atmosphere: Theory, Experiments, and Applications*. California, Academic Press.

Fleming, Z. L., P. S. Monks, A. R. Rickard, D. E. Heard, W. J. Bloss, P. W. Seakins, T. J. Still, R. Sommariva, M. J. Pilling, R. Morgan, T. J. Green, N. Brough, G. P. Mills, S. A. Penkett, A. C. Lewis, J. D. Lee, A. Saiz-Lopez and J. M. C. Plane (2006). Peroxy radical chemistry and the control of ozone photochemistry at Mace Head, Ireland during the summer of 2002. *Atmos. Chem. Phys. Discuss.*, **5**(6): 12313-12371.

Forstner, H. J. L., R. C. Flagan and J. H. Seinfeld (1997). Secondary Organic Aerosol from the Photooxidation of Aromatic Hydrocarbons: Molecular Composition. *Environmental Science & Technology*, **31**(5): 1345-1358.

Fraser, M. P., G. R. Cass and B. R. T. Simoneit (1999). Particulate organic compounds emitted from motor vehicle exhaust and in the urban atmosphere. *Atmospheric Environment*, **33**(17): 2715-2724.

Fuzzi, S., M. O. Andreae, B. J. Huebert, M. Kulmala, T. C. Bond, M. Boy, S. J. Doherty, A. Guenther, M. Kanakidou, K. Kawamura, V. M. Kerminen, U. Lohmann, L. M. Russell and U. Pöschl (2006). Critical assessment of the current state of scientific knowledge, terminology, and research needs concerning the role of organic aerosols in the atmosphere, climate, and global change. *Atmos. Chem. Phys.*, **6**(7): 2017-2038.

Gallimore, P. J., P. Achakulwisut, F. D. Pope, J. Davies, D. R. Spring and M. Kalberer (2011a). Importance of relative humidity in the oxidative ageing of organic aerosols: case study of the ozonolysis of maleic acid aerosol. *Atmos. Chem. Phys.*, **11**(8): 23169-23202.

Gallimore, P. J., P. Achakulwisut, F. D. Pope, J. F. Davies, D. R. Spring and M. Kalberer (2011b). Importance of relative humidity in the oxidative ageing of organic aerosols: case study of the ozonolysis of maleic acid aerosol. *Atmos. Chem. Phys.*, **11**(23): 12181-12195.

Gard, E., J. E. Mayer, B. D. Morrical, T. Dienes, D. P. Fergenson and K. A. Prather (1997). Real-Time Analysis of Individual Atmospheric Aerosol Particles: Design and Performance of a Portable ATOFMS. *Analytical Chemistry*, **69**(20): 4083-4091.

Gard, E. E., M. J. Kleeman, D. S. Gross, L. S. Hughes, J. O. Allen, B. D. Morrical, D. P. Fergenson, T. Dienes, M. E. Gälli, R. J. Johnson, G. R. Cass and K. A. Prather (1998). Direct Observation of Heterogeneous Chemistry in the Atmosphere. *Science*, **279**(5354): 1184-1187.

Gaston, C. J., K. A. Pratt, X. Qin and K. A. Prather (2010). Real-Time Detection and Mixing State of Methanesulfonate in Single Particles at an Inland Urban Location during a Phytoplankton Bloom. *Environmental Science & Technology*, **44**(5): 1566-1572.

George, I. J. and J. P. D. Abbatt (2010). Heterogeneous oxidation of atmospheric aerosol particles by gas-phase radicals. *Nat Chem*, **2**(9): 713-722.

George, I. J., J. Slowik and J. P. D. Abbatt (2008). Chemical aging of ambient organic aerosol from heterogeneous reaction with hydroxyl radicals. *Geophysical Research Letters*, **35**(13): L13811.

George, I. J., A. Vlasenko, J. G. Slowik, K. Broekhuizen and J. P. D. Abbatt (2007). Heterogeneous oxidation of saturated organic aerosols by hydroxyl radicals: uptake kinetics, condensed-phase products, and particle size change. *Atmos. Chem. Phys.*, **7**(16): 4187-4201.

Ghorai, S., B. Wang, A. Tivanski and A. Laskin (2014). Hygroscopic Properties of Internally Mixed Particles Composed of NaCl and Water-Soluble Organic Acids. *Environmental Science & Technology*.

Giggy, C. L., S. K. Friedlander and M. P. Sinha (1989). Measurement of externally mixed sodium containing particles in ambient air by single particle mass spectrometry. *Atmospheric Environment (1967)*, **23**(10): 2223-2229.

Girard, E., G. Dueymes, P. Du and A. K. Bertram (2013). Assessment of the effects of acid-coated ice nuclei on the Arctic cloud microstructure, atmospheric dehydration, radiation and temperature during winter. *International Journal of Climatology*, **33**(3): 599-614.

Goddard, W. A., T. H. Dunning, W. J. Hunt and P. J. Hay (1973). Generalized valence bond description of bonding in low-lying states of molecules. *Accounts of Chemical Research*, **6**(11): 368-376.

Gomez, D., R. Font and A. Soler (1986). Densities and viscosities of aqueous maleic acid solutions between 25 and 90.degree.C. *Journal of Chemical & Engineering Data*, **31**(4): 391-392.

Gonzalez-Labrada, E., R. Schmidt and C. E. DeWolf (2007). Kinetic analysis of the ozone processing of an unsaturated organic monolayer as a model of an aerosol surface. *Physical Chemistry Chemical Physics*, **9**(43): 5814-5821.

Green, T. J., C. E. Reeves, N. Brough, G. D. Edwards, P. S. Monks and S. A. Penkett (2003). Airborne measurements of peroxy radicals using the PERCA technique. *Journal of Environmental Monitoring*, **5**(1): 75-83.

Grimm, R. L., R. Hodyss and J. L. Beauchamp (2006). Probing Interfacial Chemistry of Single Droplets with Field-Induced Droplet Ionization Mass Spectrometry: Physical Adsorption of Polycyclic Aromatic Hydrocarbons and Ozonolysis of Oleic Acid and Related Compounds. *Analytical Chemistry*, **78**(11): 3800-3806.

Gross, D. S., A. R. Barron, E. M. Sukovich, B. S. Warren, J. C. Jarvis, D. T. Suess and K. A. Prather (2005). Stability of single particle tracers for differentiating between heavy- and light-duty vehicle emissions. *Atmospheric Environment*, **39**(16): 2889-2901.

Gross, D. S., M. E. Galli, P. J. Silva, S. H. Wood, D.-Y. Liu and K. A. Prather (2000). Single Particle Characterization of Automobile and Diesel Truck Emissions in the Caldecott Tunnel. *Aerosol Science and Technology*, **32**(2): 152-163.

Guazzotti, S. A., J. R. Whiteaker, D. Suess, K. R. Coffee and K. A. Prather (2001). Real-time measurements of the chemical composition of size-resolved particles during a Santa Ana wind episode, California USA. *Atmospheric Environment*, **35**(19): 3229-3240.

Guenther, A., T. Karl, P. Harley, C. Wiedinmyer, P. I. Palmer and C. Geron (2006). Estimates of global terrestrial isoprene emissions using MEGAN (Model of Emissions of Gases and Aerosols from Nature). *Atmos. Chem. Phys.*, **6**(11): 3181-3210.

Guy, P., Brasseur, J. John, Orlando and S. Geoffrey, Tyndall (1999). *Atmospheric Chemistry and Global change*. New York, Oxford University Press.

Gysel, M., E. Weingartner, S. Nyeki, D. Paulsen, U. Baltensperger, I. Galambos and G. Kiss (2004). Hygroscopic properties of water-soluble matter and humic-like organics in atmospheric fine aerosol. *Atmos. Chem. Phys.*, **4**(1): 35-50.

Haagen-Smit, A. J. (1952). Chemistry and Physiology of Los Angeles Smog. *Industrial & Engineering Chemistry*, **44**(6): 1342-1346.

Hallquist, M., Wenger, J. C., Baltensperger, U., Rudich, Y., Simpson, D., Claeys, M., Dommen, J., Donahue, N. M., George, C., Goldstein, A. H., Hamilton, J. F., Herrmann, H., Hoffmann, T., Iinuma, Y., Jang, M., Jenkin, M. E., Jimenez, J. L., Kiendler-Scharr, A., Maenhaut, W., McFiggans, G., Mentel, Th. F., Monod, A., Prévôt, A. S. H., Seinfeld, J. H., Surratt, J. D., Szmigielski, R., and Wildt, J. (2009). The formation, properties and impact of secondary organic aerosol: current and emerging issues. *Atmos. Chem. Phys.*, **9:** 5155-5235.

Hamilton, J. F., M. T. Baeza-Romero, E. Finessi, A. R. Rickard, R. M. Healy, S. Peppe, T. J. Adams, M. J. S. Daniels, S. M. Ball, I. C. A. Goodall, P. S. Monks, E. Borras and A. Munoz (2013). Online and offline mass spectrometric study of the impact of oxidation and ageing on glyoxal chemistry and uptake onto ammonium sulfate aerosols. *Faraday Discussions*, **165**(0): 447-472.

Han, Y., Y. Hu and F. Qian (2011). Effects of air temperature and humidity on particle deposition. *Chemical Engineering Research and Design*, **89**(10): 2063-2069.

HAO, L.-q., Z.-y. WANG, L. FANG, W.-j. ZHANG, W. WANG, C.-x. LI and L.-s. SHENG (2006). Characterization of products from photooxidation of toluene. *Journal of Environmental Sciences*, **18**(5): 903-909.

Harding, L. B. and W. A. Goddard (1978). Mechanisms of gas-phase and liquid-phase ozonolysis. *Journal of the American Chemical Society*, **100**(23): 7180-7188.

Hastie, D. R., M. Weissenmayer, J. P. Burrows and G. W. Harris (1991). Calibrated chemical amplifier for atmospheric ROx measurements. *Analytical Chemistry*, **63**(18): 2048-2057.

Hastings, W. P., C. A. Koehler, E. L. Bailey and D. O. De Haan (2005). Secondary Organic Aerosol Formation by Glyoxal Hydration and Oligomer Formation: Humidity Effects and Equilibrium Shifts during Analysis. *Environmental Science & Technology*, **39**(22): 8728-8735.

Hatch, L. E., J. M. Creamean, A. P. Ault, J. D. Surratt, M. N. Chan, J. H. Seinfeld, E. S. Edgerton, Y. Su and K. A. Prather (2011a). Measurements of Isoprene-Derived Organosulfates in Ambient Aerosols by Aerosol Time-of-Flight Mass Spectrometry—Part 2: Temporal Variability and Formation Mechanisms. *Environmental Science & Technology*.

Hatch, L. E., J. M. Creamean, A. P. Ault, J. D. Surratt, M. N. Chan, J. H. Seinfeld, E. S. Edgerton, Y. Su and K. A. Prather (2011b). Measurements of Isoprene-Derived Organosulfates in Ambient Aerosols by Aerosol Time-of-Flight Mass Spectrometry - Part 1: Single Particle Atmospheric Observations in Atlanta. *Environmental Science & Technology*, **45**(12): 5105-5111.

Haynes, W. M. (2012). *CRC Handbook of Chemistry and Physics, 93rd Edition*, Taylor & Francis.

Healy, R. M., I. P. O'Connor, S. Hellebust, A. Allanic, J. R. Sodeau and J. C. Wenger (2009). Characterisation of single particles from in-port ship emissions. *Atmospheric Environment*, **43**(40): 6408-6414.

Healy, R. M., J. Sciare, L. Poulain, K. Kamili, M. Merkel, T. Müller, A. Wiedensohler, S. Eckhardt, A. Stohl, R. Sarda-Estève, E. McGillicuddy, I. P. O'Connor, J. R. Sodeau and J. C. Wenger (2012). Sources and mixing state of size-resolved elemental carbon particles in a European megacity: Paris. *Atmos. Chem. Phys.*, **12**(4): 1681-1700.

Healy, R. M., J. C. Wenger, A. Metzger, J. Duplissy, M. Kalberer and J. Dommen (2008). Gas/particle partitioning of carbonyls in the photooxidation of isoprene and 1,3,5-trimethylbenzene. *Atmos. Chem. Phys. Discuss.*, **8**(2): 4727-4764.

Heard, D. (2006). *Analytical Techniques for Atmospheric Measurement*. Oxford, Blackwell Puplishing Ltd.

Hearn, J. D., A. J. Lovett and G. D. Smith (2005). Ozonolysis of oleic acid particles: evidence for a surface reaction and secondary reactions involving Criegee intermediates. *Physical Chemistry Chemical Physics*, **7**(3): 501-511.

Hearn, J. D. and G. D. Smith (2004). Kinetics and Product Studies for Ozonolysis Reactions of Organic Particles Using Aerosol CIMS†. *The Journal of Physical Chemistry A*, **108**(45): 10019-10029.

Heller, J., J. W. Bartha, C. C. Poon and A. C. Tam (1999). Temperature dependence of the reflectivity of silicon with surface oxide at wavelengths of 633 and 1047 nm. *Applied Physics Letters*, **75**(1): 43-45.

Hildebrandt, L., G. J. Engelhart, C. Mohr, E. Kostenidou, V. A. Lanz, A. Bougiatioti, P. F. DeCarlo, A. S. H. Prevot, U. Baltensperger, N. Mihalopoulos, N. M. Donahue and S. N. Pandis (2010). Aged organic aerosol in the Eastern Mediterranean: the Finokalia Aerosol Measurement Experiment â€“ 2008. *Atmos. Chem. Phys.*, **10**(9): 4167-4186.

Hinz, K.-P., R. Kaufmann and B. Spengler (1994). Laser-Induced Mass Analysis of Single Particles in the Airborne State. *Analytical Chemistry*, **66**(13): 2071-2076.

Hinz, K.-P., R. Kaufmann and B. Spengler (1996). Simultaneous Detection of Positive and Negative Ions From Single Airborne Particles by Real-time Laser Mass Spectrometry. *Aerosol Science and Technology*, **24**(4): 233-242.

Hoffmann, T., R.-J. Huang and M. Kalberer (2011). Atmospheric Analytical Chemistry. *Analytical Chemistr*. **83**: 4649 - 4664

Hogrefe, O. and G. Lala (2001). Standard Operating Procedure (SOP) for the Field Operation of the Scanning Mobility Particle Sizer (TSI Model 3936). University at Albany, State University of New York, Atmospheric Science Research Center.

Horie, O. and G. K. Moortgat (1991). Decomposition pathways of the excited Criegee intermediates in the ozonolysis of simple alkenes. *Atmospheric Environment. Part A. General Topics*, **25**(9): 1881-1896.

Hosny, N. A., C. Fitzgerald, C. Tong, M. Kalberer, M. K. Kuimova and F. D. Pope (2013). Fluorescent lifetime imaging of atmospheric aerosols: a direct probe of aerosol viscosity. *Faraday Discussions*, **165**(0): 343-356.

Hsieh, L.-Y., S.-C. Kuo, C.-L. Chen and Y. I. Tsai (2009). Size distributions of nano/micron dicarboxylic acids and inorganic ions in suburban PM episode and non-episodic aerosol. *Atmospheric Environment*, **43**(29): 4396-4406.

Huang, C. Z., Y. F. Li, D. J. Zhang and X. P. Ao (1999). Spectrophotometric study on the supramolecular interactions of nile blue sulphate with nucleic acids. *Talanta*, **49**(3): 495-503.

Huang, Y., H. Chen, L. Wang, X. Yang and J. Chen (2012). Single particle analysis of amines in ambient aerosol in Shanghai. *Environmental Chemistry*, **9**(3): 202-210.

Huff Hartz, K. E., E. A. Weitkamp, A. M. Sage, N. M. Donahue and A. L. Robinson (2007). Laboratory measurements of the oxidation kinetics of organic aerosol mixtures using a relative rate constants approach. *Journal of Geophysical Research: Atmospheres*, **112**(D4): D04204.

Hung, H.-M. and P. Ariya (2007). Oxidation of Oleic Acid and Oleic Acid/Sodium Chloride(aq) Mixture Droplets with Ozone: Changes of Hygroscopicity and Role of Secondary Reactions. *The Journal of Physical Chemistry A*, **111**(4): 620-632.

Hung, H.-M., Y. Katrib and S. T. Martin (2005). Products and Mechanisms of the Reaction of Oleic Acid with Ozone and Nitrate Radical. *The Journal of Physical Chemistry A*, **109**(20): 4517-4530.

Hung, H.-M. and C.-W. Tang (2010). Effects of Temperature and Physical State on Heterogeneous Oxidation of Oleic Acid Droplets with Ozone. *The Journal of Physical Chemistry A*, **114**(50): 13104-13112.

Iinuma, Y., O. Böge, Y. Miao, B. Sierau, T. Gnauk and H. Herrmann (2005). Laboratory studies on secondary organic aerosol formation from terpenes. *Faraday Discussions*, **130**: 279-294.

Jacobson, M. Z. (2005). *Fundamentals of Atmospheric Modeling*. New York, Cambridge University Press.

Jang, M., B. Carroll, B. Chandramouli and R. M. Kamens (2003). Particle Growth by Acid-Catalyzed Heterogeneous Reactions of Organic Carbonyls on Preexisting Aerosols. *Environmental Science & Technology*, **37**(17): 3828-3837.

Jeannet, N., M. Fierz, M. Kalberer, H. Burtscher and M. Geiser (2014). Nano Aerosol Chamber for In-Vitro Toxicity (NACIVT) studies. *Nanotoxicology*(0): 1-9.

Jimenez, J. L., M. R. Canagaratna, N. M. Donahue, A. S. H. Prevot, Q. Zhang, J. H. Kroll, P. F. DeCarlo, J. D. Allan, H. Coe, N. L. Ng, A. C. Aiken, K. S. Docherty, I. M. Ulbrich, A. P. Grieshop, A. L. Robinson, J. Duplissy, J. D. Smith, K. R. Wilson, V. A. Lanz, C. Hueglin, Y. L. Sun, J. Tian, A. Laaksonen, T. Raatikainen, J. Rautiainen, P. Vaattovaara, M. Ehn, M. Kulmala, J. M. Tomlinson, D. R. Collins, M. J. Cubison, E., J. Dunlea, J. A. Huffman, T. B. Onasch, M. R. Alfarra, P. I. Williams, K. Bower, Y. Kondo, J. Schneider, F. Drewnick, S. Borrmann, S. Weimer, K. Demerjian, D. Salcedo, L. Cottrell, R. Griffin, A. Takami, T. Miyoshi, S. Hatakeyama, A. Shimono, J. Y. Sun, Y. M. Zhang, K. Dzepina, J. R. Kimmel, D. Sueper, J. T. Jayne, S. C. Herndon, A. M. Trimborn, L. R. Williams, E. C. Wood, A. M. Middlebrook, C. E. Kolb, U. Baltensperger and D. R. Worsnop (2009). Evolution of Organic Aerosols in the Atmosphere. *Science*, **326**(5959): 1525-1529.

John, H., Seinfeld (1986). *Atmospheric Chemistry and Physics of Air Pollution*. California, John Wiley & Sons, Inc.

.

Johnson, D. and G. Marston (2008). The gas-phase ozonolysis of unsaturated volatile organic compounds in the troposphere. *Chemical Society Reviews*, **37**(4): 699-716.

Jones, A. M., R. M. Harrison, B. Barratt and G. Fuller (2012). A large reduction in airborne particle number concentrations at the time of the introduction of "sulphur free" diesel and the London Low Emission Zone. *Atmospheric Environment*, **50**(0): 129-138.

Kalberer, M., D. Paulsen, M. Sax, M. Steinbacher, J. Dommen, A. S. H. Prevot, R. Fisseha, E. Weingartner, V. Frankevich, R. Zenobi and U. Baltensperger (2004). Identification of Polymers as Major Components of Atmospheric Organic Aerosols. *Science*, **303**(5664): 1659-1662.

Kalberer, M., M. Sax and V. Samburova (2006). Molecular Size Evolution of Oligomers in Organic Aerosols Collected in Urban Atmospheres and Generated in a Smog Chamber. *Environmental Science & Technology*, **40**(19): 5917-5922.

Kalberer, M., J. Yu, D. R. Cocker, R. C. Flagan and J. H. Seinfeld (2000). Aerosol Formation in the Cyclohexene-Ozone System. *Environmental Science & Technology*, **34**(23): 4894-4901.

Kalinowski, J., M. Räsänen, P. Heinonen, I. Kilpeläinen and R. B. Gerber (2014). Isomerization and Decomposition of a Criegee Intermediate in the Ozonolysis of Alkenes: Dynamics Using a Multireference Potential. *Angewandte Chemie International Edition*, **53**(1): 265-268.

Kamens, R. M., H. E. Jeffries, M. W. Gery, R. W. Wiener, K. G. Sexton and G. B. Howe (1981). The impact of [alpha]-pinene on urban smog formation: an outdoor smog chamber study. *Atmospheric Environment (1967)*, **15**(6): 969-981.

Kanakidou, M., J. H. Seinfeld, S. N. Pandis, I. Barnes, F. J. Dentener, M. C. Facchini, R. Van Dingenen, B. Ervens, A. Nenes, C. J. Nielsen, E. Swietlicki, J. P. Putaud, Y. Balkanski, S. Fuzzi, J. Horth, G. K. Moortgat, R. Winterhalter, C. E. L. Myhre, K. Tsigaridis, E. Vignati, E. G. Stephanou and J. Wilson (2005). Organic aerosol and global climate modelling: a review. *Atmos. Chem. Phys.*, **5**(4): 1053-1123.

Kanaya, Y., Y. Sadanaga, J. Hirokawa, Y. Kajii and H. Akimoto (2001). Development of a Ground-Based LIF Instrument for Measuring HOx Radicals: Instrumentation and Calibrations. *Journal of Atmospheric Chemistry*, **38**(1): 73-110.

Kane, D. B., J. Wang, K. Frost and M. V. Johnston (2002). Detection of Negative Ions from Individual Ultrafine Particles. *Analytical Chemistry*, **74**(9): 2092-2096.

Katrib, Y., G. Biskos, P. R. Buseck, P. Davidovits, J. T. Jayne, M. Mochida, M. E. Wise, D. R. Worsnop and S. T. Martin (2005a). Ozonolysis of Mixed Oleic-Acid/Stearic-Acid Particles: Reaction Kinetics and Chemical Morphology. *The Journal of Physical Chemistry A*, **109**(48): 10910-10919.

Katrib, Y., S. T. Martin, H.-M. Hung, Y. Rudich, H. Zhang, J. G. Slowik, P. Davidovits, J. T. Jayne and D. R. Worsnop (2004). Products and Mechanisms of Ozone Reactions with Oleic Acid for Aerosol Particles Having Core−Shell Morphologies. *The Journal of Physical Chemistry A*, **108**(32): 6686-6695.

Katrib, Y., S. T. Martin, Y. Rudich, P. Davidovits, J. T. Jayne and D. R. Worsnop (2005b). Density changes of aerosol particles as a result of chemical reaction. *Atmos. Chem. Phys.*, **5**(1): 275-291.

Kaye, G. W. C. and T. H. Laby (1995). *Tables of Physical and Chemical Constants*, Longman Group Limited.

Kessler, S. H., T. Nah, K. E. Daumit, J. D. Smith, S. R. Leone, C. E. Kolb, D. R. Worsnop, K. R. Wilson and J. H. Kroll (2012). OH-Initiated Heterogeneous Aging of Highly Oxidized Organic Aerosol. *The Journal of Physical Chemistry A*, **116**(24): 6358-6365.

Khalizov, A. F., R. Zhang, D. Zhang, H. Xue, J. Pagels and P. H. McMurry (2009). Formation of highly hygroscopic soot aerosols upon internal mixing with sulfuric acid vapor. *Journal of Geophysical Research: Atmospheres*, **114**(D5): D05208.

Kievit, O., J. C. M. Marijnissen, P. J. T. Verheiljen and B. Scarlett (1992). On-line measurement of particle size and composition. *Journal of Aerosol Science*, **23, Supplement 1**(0): 301-304.

King, M. D., A. R. Rennie, K. C. Thompson, F. N. Fisher, C. C. Dong, R. K. Thomas, C. Pfrang and A. V. Hughes (2009). Oxidation of oleic acid at the air-water interface and its potential effects on cloud critical supersaturations. *Physical Chemistry Chemical Physics*, **11**(35): 7699-7707.

King, M. D., K. C. Thompson and A. D. Ward (2004). Laser Tweezers Raman Study of Optically Trapped Aerosol Droplets of Seawater and Oleic Acid Reacting with Ozone: Implications for Cloud-Droplet Properties. *Journal of the American Chemical Society*, **126**(51): 16710-16711.

King, M. D., K. C. Thompson, A. D. Ward, C. Pfrang and B. R. Hughes (2008). Oxidation of biogenic and water-soluble compounds in aqueous and organic aerosol droplets by ozone: a kinetic and product analysis approach using laser Raman tweezers. *Faraday Discussions*, **137**: 173-192.

Knopf, D. A., L. M. Anthony and A. K. Bertram (2005). Reactive Uptake of O3 by Multicomponent and Multiphase Mixtures Containing Oleic Acid. *The Journal of Physical Chemistry A*, **109**(25): 5579-5589.

Knutson, E. O. and K. T. Whitby (1975). Aerosol classification by electric mobility: apparatus, theory, and applications. *Journal of Aerosol Science*, **6**(6): 443-451.

Koester, C. J. and A. Moulik (2005). Trends in Environmental Analysis. *Analytical Chemistry*, **77**(12): 3737-3754.

Kolb, C., R. Cox, J. Abbatt, M. Ammann, E. Davis, D. Donaldson, B. C. Garrett, C. George, P. Griffiths and D. Hanson (2010). An overview of current issues in the uptake of atmospheric trace gases by aerosols and clouds. *Atmospheric Chemistry and Physics*, **10**(21): 10561-10605.

Kreider, M. L., J. M. Panko, B. L. McAtee, L. I. Sweet and B. L. Finley (2010). Physical and chemical characterization of tire-related particles: Comparison of particles generated using different methodologies. *Science of The Total Environment*, **408**(3): 652-659.

Kroll, J. H. and J. H. Seinfeld (2008). Chemistry of secondary organic aerosol: Formation and evolution of low-volatility organics in the atmosphere. *Atmospheric Environment*, **42**(16): 3593-3624.

Künzi, L., P. Mertes, S. Schneider, N. Jeannet, C. Menzi, J. Dommen, U. Baltensperger, A. S. H. Prévôt, M. Salathe, M. Kalberer and M. Geiser (2013). Responses of lung cells to realistic exposure of primary and aged carbonaceous aerosols. *Atmospheric Environment*, **68**(0): 143-150.

Laj, P., J. Klausen, M. Bilde, C. Plaß-Duelmer, G. Pappalardo, C. Clerbaux, U. Baltensperger, J. Hjorth, D. Simpson, S. Reimann, P. F. Coheur, A. Richter, M. De Mazière, Y. Rudich, G. McFiggans, K. Torseth, A. Wiedensohler, S. Morin, M. Schulz, J. D. Allan, J. L. Attié, I. Barnes, W. Birmili, J. P. Cammas, J. Dommen, H. P. Dorn, D. Fowler, S. Fuzzi, M. Glasius, C. Granier, M. Hermann, I. S. A. Isaksen, S. Kinne, I. Koren, F. Madonna, M. Maione, A. Massling, O. Moehler, L. Mona, P. S. Monks, D. Müller, T. Müller, J. Orphal, V. H. Peuch, F. Stratmann, D. Tanré, G. Tyndall, A.

Abo Riziq, M. Van Roozendael, P. Villani, B. Wehner, H. Wex and A. A. Zardini (2009). Measuring atmospheric composition change. *Atmospheric Environment*, **43**(33): 5351-5414.

Lambe, A. T., A. T. Ahern, L. R. Williams, J. G. Slowik, J. P. S. Wong, J. P. D. Abbatt, W. H. Brune, N. L. Ng, D. R. Croasdale, J. P. Wright, D. R. Worsnop, P. Davidovits and T. B. Onasch (2010). Characterization of aerosol photooxidation flow reactors: heterogeneous oxidation, secondary organic aerosol formation and cloud condensation nuclei activity measurements. *Atmos. Meas. Tech. Discuss.*, **3**(6): 5211-5251.

Lambe, A. T., C. D. Cappa, P. Massoli, T. B. Onasch, S. D. Forestieri, A. T. Martin, M. J. Cummings, D. R. Croasdale, W. H. Brune, D. R. Worsnop and P. Davidovits (2013). Relationship between Oxidation Level and Optical Properties of Secondary Organic Aerosol. *Environmental Science & Technology*, **47**(12): 6349-6357.

Lammel, G., A. M. Sehili, T. C. Bond, J. Feichter and H. Grassl (2009). Gas/particle partitioning and global distribution of polycyclic aromatic hydrocarbons–a modelling approach. *Chemosphere*, **76**(1): 98-106.

Lan, Z.-J., D.-L. Chen, X. Li, X.-F. Huang, L.-Y. He, Y.-G. Deng, N. Feng and M. Hu (2011). Modal characteristics of carbonaceous aerosol size distribution in an urban atmosphere of South China. *Atmospheric Research*, **100**(1): 51-60.

Lang, Q., Q. Zhang and R. Jaffé (2002). Organic aerosols in the Miami area, USA: temporal variability of atmospheric particles and wet/dry deposition. *Chemosphere*, **47**(4): 427-441.

Laskin, A., J. Laskin and S. A. Nizkorodov (2012). Mass spectrometric approaches for chemical characterisation of atmospheric aerosols: critical review of the most recent advances. *Environmental Chemistry*, **9**(3): 163-189.

Lee, A. K. Y. and C. K. Chan (2007). Single particle Raman spectroscopy for investigating atmospheric heterogeneous reactions of organic aerosols. *Atmospheric Environment*, **41**(22): 4611-4621.

Lee, J. W. L., V. Carrascon, P. J. Gallimore, S. J. Fuller, A. Bjorkegren, D. R. Spring, F. D. Pope and M. Kalberer (2012). The effect of humidity on the ozonolysis of unsaturated compounds in aerosol particles. *Physical Chemistry Chemical Physics*, **14**(22): 8023-8031.

Leeuw, G. D. (1990). Profiling of aerosol concentrations, particle size distributions and relative humidity in the atmospheric surface layer over the North Sea. *Tellus B*, **42**(4): 342-354.

Li, X., B. Qi, L. Zeng and X. Tang (2009). Development and deployment of an instrument for measurement of atmospheric peroxy radical by chemical amplification. *Science in China Series D: Earth Sciences*, **52**(3): 333-340.

Lightfoot, P. D., R. A. Cox, J. N. Crowley, M. Destriau, G. D. Hayman, M. E. Jenkin, G. K. Moortgat and F. Zabel (1992). Organic peroxy radicals: Kinetics, spectroscopy and tropospheric chemistry. *Atmospheric Environment. Part A. General Topics*, **26**(10): 1805-1961.

Liu, D.-Y., D. Rutherford, M. Kinsey and K. A. Prather (1997). Real-Time Monitoring of Pyrotechnically Derived Aerosol Particles in the Troposphere. *Analytical Chemistry*, **69**(10): 1808-1814.

Liu, P., P. J. Ziemann, D. B. Kittelson and P. H. McMurry (1995). Generating Particle Beams of Controlled Dimensions and Divergence: II. Experimental Evaluation of Particle Motion in Aerodynamic Lenses and Nozzle Expansions. *Aerosol Science and Technology*, **22**(3): 314-324.

Liu, Y., R. Morales-Cueto, J. Hargrove, D. Medina and J. Zhang (2009). Measurements of Peroxy Radicals Using Chemical Amplification−Cavity Ringdown Spectroscopy. *Environmental Science & Technology*, **43**(20): 7791-7796.

Lyamani, H., F. J. Olmo and L. Alados-Arboledas (2010). Physical and optical properties of aerosols over an urban location in Spain: seasonal and diurnal variability. *Atmos. Chem. Phys.*, **10**(1): 239-254.

Mader, P. P., R. D. MacPhee, R. T. Lofberg and G. P. Larson (1952). Composition of Organic Portion of Atmospheric Aerosols in the Los Angeles Area. *Industrial & Engineering Chemistry*, **44**(6): 1352-1355.

Malachowski, P. J. and A. F. Goldberg (1999). *Health effects of toxic substances*, Government Institutes.

Maliszewska-Kordybach, B. (1999). Sources, concentrations, fate and effects of polycyclic aromatic hydrocarbons (PAHs) in the environment. Part A: PAHs in air. *Polish journal of environmental studies*, **8**: 131-136.

Mao, J., X. Ren, W. H. Brune, J. R. Olson, J. H. Crawford, A. Fried, L. G. Huey, R. C. Cohen, B. Heikes, H. B. Singh, D. R. Blake, G. W. Sachse, G. S. Diskin, S. R. Hall and R. E. Shetter (2009). Airborne measurement of OH reactivity during INTEX-B. *Atmos. Chem. Phys.*, **9**(1): 163-173.

Martin, S. T. (2000). Phase transitions of aqueous atmospheric particles. *Chemical Reviews*, **100**(9): 3403-3454.

McMurry, P. H. (2000). A review of atmospheric aerosol measurements. *Atmospheric Environment*, **34**(12–14): 1959-1999.

McNeill, V. F., G. M. Wolfe and J. A. Thornton (2007). The Oxidation of Oleate in Submicron Aqueous Salt Aerosols: Evidence of a Surface Process. *The Journal of Physical Chemistry A*, **111**(6): 1073-1083.

Meinwald, J. (1955). Notiz zur Anwendung der Markownikoffschen Regel auf den Verlauf der Ozonisierung. *Chemische Berichte*, **88**(12): 1889-1891.

Midander, K., K. Elihn, A. Wallén, L. Belova, A.-K. B. Karlsson and I. O. Wallinder (2012). Characterisation of nano- and micron-sized airborne and collected subway particles, a multi-analytical approach. *Science of The Total Environment*, **427–428**: 390-400.

Mihele, C. M. and D. R. Hastie (2000). Optimized Operation and Calibration Procedures for Radical Amplifier-Type Detectors. *Journal of Atmospheric and Oceanic Technology*, **17**(6): 788-794.

Mihele, C. M., M. Mozurkewich and D. R. Hastie (1999). Radical loss in a chain reaction of CO and NO in the presence of water: Implications for the radical amplifier and atmospheric chemistry. *International Journal of Chemical Kinetics*, **31**(2): 145-152.

Miñambres, L., E. Méndez, M. N. Sánchez, F. Castaño and F. J. Basterretxea (2013). Water uptake of internally mixed ammonium sulfate and dicarboxylic acid particles probed by infrared spectroscopy. *Atmospheric Environment*, **70**(0): 108-116.

Ming, Y., V. Ramaswamy, P. A. Ginoux and L. H. Horowitz (2005). Direct radiative forcing of anthropogenic organic aerosol. *J. Geophys. Res.*, **110**(D20): D20208.

Miyazaki, K., A. E. Parker, C. Fittschen, P. S. Monks and Y. Kajii (2010). A new technique for the selective measurement of atmospheric peroxy radical concentrations of HO2 and RO2 using a denuding method. *Atmos. Meas. Tech.*, **3**(6): 1547-1554.

Moffet, R., B. d. Foy, L. a. Molina, M. Molina and K. Prather (2008). Measurement of ambient aerosols in northern Mexico City by single particle mass spectrometry. *Atmospheric Chemistry and Physics*, **8**(16): 4499-4516.

Moffet, R., L. Shields, J. Berntsen, R. Devlin and K. Prather (2004). Characterization of an Ambient Coarse Particle Concentrator Used for Human Exposure Studies: Aerosol Size Distributions, Chemical Composition, and Concentration Enrichment. *Aerosol Science and Technology*, **38**(11): 1123-1137.

Moise, T. and Y. Rudich (2002). Reactive Uptake of Ozone by Aerosol-Associated Unsaturated Fatty Acids: Kinetics, Mechanism, and Products. *The Journal of Physical Chemistry A*, **106**(27): 6469-6476.

Monks, P., H. ApSimon, D. Carruthers, D. Carslaw, D. Derwent, R. Harrison, D. Laxen and J. Stedman (2012). Fine Particulate Matter (PM2.5) in the United Kingdom, Department for Environment, Food and Rural Affairs: 203.

Monks, P. S. (2005). Gas-phase radical chemistry in the troposphere. *Chemical Society Reviews*, **34**(5): 376-395.

Morawska, L., G. Johnson, Z. D. Ristovski and V. Agranovski (1999). Relation between particle mass and number for submicrometer airborne particles. *Atmospheric Environment*, **33**(13): 1983-1990.

Morrical, B. D., D. P. Fergenson and K. A. Prather (1998). Coupling two-step laser desorption/ ionization with aerosol time-of-flight mass spectrometry for the analysis of individual organic particles. *Journal of the American Society for Mass Spectrometry*, **9**(10): 1068-1073.

Morris, J. W., P. Davidovits, J. T. Jayne, J. L. Jimenez, Q. Shi, C. E. Kolb, D. R. Worsnop, W. S. Barney and G. Cass (2002). Kinetics of submicron oleic acid aerosols with ozone: A novel aerosol mass spectrometric technique. *Geophysical Research Letters*, **29**(9): 71-71-71-74.

Murphy, D. M. (2007). The design of single particle laser mass spectrometers. *Mass Spectrometry Reviews*, **26**(2): 150-165.

Myers, R. L. and W. L. Fite (1975). Electrical detection of airborne particulates using surface ionization techniques. *Environmental Science & Technology*, **9**(4): 334-336.

Na, J.-G., B. E. Yi, J. N. Kim, K. B. Yi, S.-Y. Park, J.-H. Park, J.-N. Kim and C. H. Ko (2010). Hydrocarbon production from decarboxylation of fatty acid without hydrogen. *Catalysis Today*, **156**(1–2): 44-48.

Nah, T., M. Chan, S. R. Leone and K. R. Wilson (2013). Real Time in Situ Chemical Characterization of Submicrometer Organic Particles Using Direct Analysis in Real Time-Mass Spectrometry. *Analytical Chemistry*, **85**(4): 2087-2095.

Najera, J. J., C. J. Percival and A. B. Horn (2010). Kinetic studies of the heterogeneous oxidation of maleic and fumaric acid aerosols by ozone under conditions of high relative humidity. *Physical Chemistry Chemical Physics*, **12**(37): 11417-11427.

Nash, D. G., T. Baer and M. V. Johnston (2006). Aerosol mass spectrometry: An introductory review. *International Journal of Mass Spectrometry*, **258**(1–3): 2-12.

Neeb, P., O. Horie and G. K. Moortgat (1998). The Ethene−Ozone Reaction in the Gas Phase. *The Journal of Physical Chemistry A*, **102**(34): 6778-6785.

New, A., D. Prime, S. Zomer, D. Elder, R. Donovan and E. Freney (2008). Detection and assessment of co-association in inhalable drug particles using aerosol time-of-flight mass spectrometry. *Rapid Communications in Mass Spectrometry*, **22**(23): 3873-3882.

Ng, N. L., J. H. Kroll, A. W. H. Chan, P. S. Chhabra, R. C. Flagan and J. H. Seinfeld (2007). Secondary organic aerosol formation from m-xylene, toluene, and benzene. *Atmos. Chem. Phys. Discuss.*, **7**(2): 4085-4126.

Nieto de Castro, C. A., M. J. V. Lourenço, A. P. C. Ribeiro, E. Langa, S. I. C. Vieira, P. Goodrich and C. Hardacre (2009). Thermal Properties of Ionic Liquids and IoNanofluids of Imidazolium and Pyrrolidinium Liquids†. *Journal of Chemical & Engineering Data*, **55**(2): 653-661.

Nikzadfar, K. and A. H. Shamekhi (2014). Investigating the relative contribution of operational parameters on performance and emissions of a common-rail diesel engine using neural network. *Fuel*, **125**(0): 116-128.

NIST (2011). NIST Digital Library of Mathematical Functions, Cambridge University Press.

Oliviero, L., J. Barbier Jr, D. Duprez, H. Wahyu, J. W. Ponton, I. S. Metcalfe and D. Mantzavinos (2001). Wet air oxidation of aqueous solutions of maleic acid over Ru/CeO2 catalysts. *Applied Catalysis B: Environmental*, **35**(1): 1-12.

Orlando, J. J., G. S. Tyndall and S. E. Paulson (1999). Mechanism of the OH‐initiated oxidation of methacrolein. *Geophys. Res. Lett.*, **26**(14): 2191-2194.

Ortega, A. M., D. A. Day, M. J. Cubison, W. H. Brune, D. Bon, J. A. de Gouw and J. L. Jimenez (2013). Secondary organic aerosol formation and primary organic aerosol oxidation from biomass burning smoke in a flow reactor during FLAME-3. *Atmos. Chem. Phys. Discuss.*, **13**(5): 13799-13851.

Pandis, S. N., S. E. Paulson, J. H. Seinfeld and R. C. Flagan (1991). Aerosol formation in the photooxidation of isoprene and [beta]-pinene. *Atmospheric Environment. Part A. General Topics*, **25**(5-6): 997-1008.

Pankow, J. F. (2007). An absorption model of the gas/aerosol partitioning involved in the formation of secondary organic aerosol. *Atmospheric Environment*, **41**(Supplement 1): 75-79.

Park, J., A. L. Gomez, M. L. Walser, A. Lin and S. A. Nizkorodov (2006). Ozonolysis and photolysis of alkene-terminated self-assembled monolayers on quartz nanoparticles: implications for photochemical aging of organic aerosol particles. *Physical Chemistry Chemical Physics*, **8**(21): 2506-2512.

Parrondo, R. M., P. Karafiloglou, R. R. Pappalardo and E. Sanchez Marcos (1995). Calculation of the Weights of Resonance Structures of Molecules in Solution. *The Journal of Physical Chemistry*, **99**(17): 6461-6467.

Paulot, F., J. D. Crounse, H. G. Kjaergaard, J. H. Kroll, J. H. Seinfeld and P. O. Wennberg (2009). Isoprene photooxidation: new insights into the production of acids and organic nitrates. *Atmos. Chem. Phys.*, **9**(4): 1479-1501.

Paulot, F. and D. J. Jacob (2013). Hidden Cost of U.S. Agricultural Exports: Particulate Matter from Ammonia Emissions. *Environmental Science & Technology*, **48**(2): 903-908.

Paulson, S. E., D.-L. Liu, G. E. Orzechowska, L. M. Campos and K. N. Houk (2006). Photolysis of Heptanal. *The Journal of Organic Chemistry*, **71**(17): 6403-6408.

Petters, M. D., A. J. Prenni, S. M. Kreidenweis, P. J. DeMott, A. Matsunaga, Y. B. Lim and P. J. Ziemann (2006). Chemical aging and the hydrophobic-to-hydrophilic conversion of carbonaceous aerosol. *Geophys. Res. Lett.*, **33**(24): L24806.

Pfrang, C., M. Shiraiwa and U. P¨oschl (2010). Coupling aerosol surface and bulk chemistry with a kinetic double layer model (K2-SUB): oxidation of oleic acid by ozone. *Atmos. Chem. Phys.*, **10**(10): 30.

Pfrang, C., M. Shiraiwa and U. Pöschl (2011). Chemical ageing and transformation of diffusivity in semi-solid multi-component organic aerosol particles. *Atmos. Chem. Phys. Discuss.*, **11**(4): 13003-13033.

Pope, F. D., B. J. Dennis-Smither, P. T. Griffiths, S. L. Clegg and R. A. Cox (2010a). Studies of Single Aerosol Particles Containing Malonic Acid, Glutaric Acid, and Their Mixtures with Sodium Chloride. I. Hygroscopic Growth. *The Journal of Physical Chemistry A*, ***114***(16): 5335-5341

Pope, F. D., P. J. Gallimore, S. J. Fuller, R. A. Cox and M. Kalberer (2010b). Ozonolysis of Maleic Acid Aerosols: Effect upon Aerosol Hygroscopicity, Phase and Mass. *Environmental Science & Technology*, **44**(17): 6656-6660.

Pöschl, U. (2005). Atmospheric Aerosols: Composition, Transformation, Climate and Health Effects. *Angewandte Chemie International Edition*, **44**(46): 7520-7540.

Pradeep Kumar, P., K. Broekhuizen and J. P. D. Abbatt (2003). Organic acids as cloud condensation nuclei: Laboratory studies of highly soluble and insoluble species. *Atmos. Chem. Phys.*, **3**(3): 509-520.

Prather, K. A., T. Nordmeyer and K. Salt (1994). Real-time characterization of individual aerosol particles using time-of-flight mass spectrometry. *Analytical Chemistry*, **66**(9): 1403-1407.

Pratt, K. A. and K. A. Prather (2009). Real-Time, Single-Particle Volatility, Size, and Chemical Composition Measurements of Aged Urban Aerosols. *Environmental Science & Technology*, **43**(21): 8276-8282.

Pratt, K. A. and K. A. Prather (2012). Mass spectrometry of atmospheric aerosols—Recent developments and applications. Part II: On-line mass spectrometry techniques. *Mass Spectrometry Reviews*, **31**(1): 17-48.

Prenni, A. J., P. J. DeMott and S. M. Kreidenweis (2003). Water uptake of internally mixed particles containing ammonium sulfate and dicarboxylic acids. *Atmospheric Environment*, **37**(30): 4243-4251.

Putaud, J.-P., F. Raes, R. Van Dingenen, E. Brüggemann, M. C. Facchini, S. Decesari, S. Fuzzi, R. Gehrig, C. Hüglin, P. Laj, G. Lorbeer, W. Maenhaut, N. Mihalopoulos, K.

Müller, X. Querol, S. Rodriguez, J. Schneider, G. Spindler, H. t. Brink, K. Tørseth and A. Wiedensohler (2004). A European aerosol phenomenology--2: chemical characteristics of particulate matter at kerbside, urban, rural and background sites in Europe. *Atmospheric Environment*, **38**(16): 2579-2595.

Qi, B., L. Liu, Y. Chao, Z. Wang and H. Yang (2008). Water effect on peroxy radical measurement by chemical amplification: Experimental determination and chemical mechanism. *Science in China Series B: Chemistry*, **51**(3): 282-288.

Qi, B., K. Sato, T. Imamura, A. Takami, S. Hatakeyama and Y. Ma (2006). Production of the radicals in the ozonolysis of ethene: A chamber study by FT-IR and PERCA. *Chemical Physics Letters*, **427**(4–6): 461-465.

Ranjit, B., M. R. Lynn and P. Kimberly (2010). Composition and Morphology of Individual Combustion, Biomass Burning, and Secondary Organic Particle Types Obtained Using Urban and Coastal ATOFMS and STXM-NEXAFS Measurements. *Aerosol Science and Technology*, **44**(7).

Rathouský, J., V. Kalousek, M. Kolář, J. Jirkovský and P. Barták (2011). A study into the self-cleaning surface properties—The photocatalytic decomposition of oleic acid. *Catalysis Today*, **161**(1): 202-208.

Ravishankara, A. R. (1997). Heterogeneous and Multiphase Chemistry in the Troposphere. *Science*, **276**(5315): 1058-1065.

Reichert, L., M. D. Andrés Hernández, D. Stöbener, J. Burkert and J. P. Burrows (2003). Investigation of the effect of water complexes in the determination of peroxy radical ambient concentrations: Implications for the atmosphere. *Journal of Geophysical Research: Atmospheres*, **108**(D1): 4017.

Reinard, M. S. and M. V. Johnston (2008). Ion Formation Mechanism in Laser Desorption Ionization of Individual Nanoparticles. *Journal of the American Society for Mass Spectrometry*, **19**(3): 389-399.

Ren, R., T. Hashimoto, M. Mizuno, H. Takigawa, M. Yoshida, T. Azuma and K. Kanazawa (2013). A lipid peroxidation product 9-oxononanoic acid induces phospholipase production in human blood. *Journal of Clinical Biochemistry and Nutrition*, **52**(3): 228-233.

Rengarajan, R., A. K. Sudheer and M. M. Sarin (2011). Aerosol acidity and secondary organic aerosol formation during wintertime over urban environment in western India. *Atmospheric Environment*, **45**(11): 1940-1945.

Reynolds, J. C., D. J. Last, M. McGillen, A. Nijs, A. B. Horn, C. Percival, L. J. Carpenter and A. C. Lewis (2006). Structural Analysis of Oligomeric Molecules Formed from the Reaction Products of Oleic Acid Ozonolysis. *Environmental Science & Technology*, **40**(21): 6674-6681.

Richard, C. F. (2006). Aerosol Particle Generation. *Powder Technology Handbook, Third Edition*, CRC Press.

Ripanucci, G., M. Grana, L. Vicentini, A. Magrini and A. Bergamaschi (2006). Dust in the Underground Railway Tunnels of an Italian Town. *Journal of Occupational and Environmental Hygiene*, **3**(1): 16-25.

Roberts, G. C., M. O. Andreae, J. Zhou and P. Artaxo (2001). Cloud condensation nuclei in the Amazon Basin: “marine” conditions over a continent? *Geophys. Res. Lett.*, **28**(14): 2807-2810.

Robinson, A. L., N. M. Donahue and W. F. Rogge (2006). Photochemical oxidation and changes in molecular composition of organic aerosol in the regional context. *Journal of Geophysical Research: Atmospheres*, **111**(D3): D03302.

Rogge, W. F., L. M. Hildemann, M. A. Mazurek, G. R. Cass and B. R. T. Simoneit (1993a). Sources of fine organic aerosol. 4. Particulate abrasion products from leaf surfaces of urban plants. *Environmental Science & Technology*, **27**(13): 2700-2711.

Rogge, W. F., M. A. Mazurek, L. M. Hildemann, G. R. Cass and B. R. T. Simoneit (1993b). Quantification of urban organic aerosols at a molecular level: Identification, abundance and seasonal variation. *Atmospheric Environment. Part A. General Topics*, **27**(8): 1309-1330.

Rosenfeld, D., R. Chemke, K. Prather, K. Suski, J. M. Comstock, B. Schmid, J. Tomlinson and H. Jonsson (2014). Polluting of winter convective clouds upon transition from ocean inland over central California: Contrasting case studies. *Atmospheric Research*, **135–136**(0): 112-127.

Roy, M., Harrison and V. René, Grieken (1998). *Atmospheric particles*. Chichester, John wiley & Sons Ltd.

Rudich, Y. (2003). Laboratory Perspectives on the Chemical Transformations of Organic Matter in Atmospheric Particles. *Chemical Reviews*, **103**(12): 5097-5124.

Rudich, Y., N. M. Donahue and T. F. Mentel (2007). Aging of Organic Aerosol: Bridging the Gap Between Laboratory and Field Studies. *Annual Review of Physical Chemistry*, **58**(1): 321-352.

Ryder, O. S., A. P. Ault, J. F. Cahill, T. L. Guasco, T. P. Riedel, L. A. Cuadra-Rodriguez, C. J. Gaston, E. Fitzgerald, C. Lee, K. A. Prather and T. H. Bertram (2014). On the Role of Particle Inorganic Mixing State in the Reactive Uptake of N2O5 to Ambient Aerosol Particles. *Environmental Science & Technology*, **48**(3): 1618-1627.

Sadanaga, Y., J. Matsumoto, K.-i. Sakurai, R. Isozaki, S. Kato, T. Nomaguchi, H. Bandow and Y. Kajii (2004). Development of a measurement system of peroxy radicals using a chemical amplification/laser-induced fluorescence technique. *Review of Scientific Instruments*, **75**(4): 864-872.

Sage, A. M., E. A. Weitkamp, A. L. Robinson and N. M. Donahue (2009). Reactivity of oleic acid in organic particles: changes in oxidant uptake and reaction stoichiometry with particle oxidation. *Physical Chemistry Chemical Physics*, **11**(36): 7951-7962.

Sajjad, H., H. H. Masjuki, M. Varman, M. A. Kalam, M. I. Arbab, S. Imtenan and S. M. A. Rahman (2014). Engine combustion, performance and emission characteristics of gas to liquid (GTL) fuels and its blends with diesel and bio-diesel. *Renewable and Sustainable Energy Reviews*, **30**(0): 961-986.

Sakurai, H., H. J. Tobias, K. Park, D. Zarling, K. S. Docherty, D. B. Kittelson, P. H. McMurry and P. J. Ziemann (2003). On-line measurements of diesel nanoparticle composition and volatility. *Atmospheric Environment*, **37**(9-10): 1199-1210.

Samburova, V., R. Zenobi and M. Kalberer (2005). Characterization of high molecular weight compounds in urban atmospheric particles. *Atmos. Chem. Phys.*, **5**(8): 2163-2170.

Sander, S. P., R. R. Friedl, J. R. Barker, J. B. Burkholder, D. M. Golden, C. E. Kolb, M. J. Kurylo, G. K. Moortgat, P. H. Wine, R. E. Huie and V. L. Orkin (2011). Chemical Kinetics and Photochemical Data for Use in Atmospheric Studies-Evaluation Number 17. California.

Saxena, P. and L. M. Hildemann (1996). Water-soluble organics in atmospheric particles: A critical review of the literature and application of thermodynamics to identify candidate compounds. *Journal of Atmospheric Chemistry*, **24**(1): 57-109.

Schneider, C. and T. Lippert (2010). Laser Ablation and Thin Film Deposition. *Laser Processing of Materials*. P. Schaaf, Springer Berlin Heidelberg. **139:** 89-112.

Schrobenhauser, R., R. Strzoda, M. Fleischer, A. Hartmann and M.-C. Amann (2014). Detection of the mass of fine particulate matter using light scattering and inertial filtering in a miniaturized sensor setup. *Measurement Science and Technology*, **25**(3): 035103.

Schwier, A. N., N. Sareen, T. L. Lathem, A. Nenes and V. F. McNeill (2011). Ozone oxidation of oleic acid surface films decreases aerosol cloud condensation nuclei activity. *Journal of Geophysical Research: Atmospheres*, **116**(D16): D16202.

Seaton, A., J. Cherrie, M. Dennekamp, K. Donaldson, J. F. Hurley and C. L. Tran (2005). The London Underground: dust and hazards to health. *Occupational and Environmental Medicine*, **62**(6): 355-362.

Seinfeld, J. H. and S. N. Pandis (2006). *Atmospheric Chemistry and Physics - From Air Pollution to Climate Change (2nd Edition)*, John Wiley & Sons.

Shandilya, K. K. and A. Kumar (2010). Morphology of single inhalable particle inside public transit biodiesel fueled bus. *Journal of Environmental Sciences*, **22**(2): 263-270.

She, M., D. Kim and C. P. Grigoropoulos (1999). Liquid-assisted pulsed laser cleaning using near-infrared and ultraviolet radiation. *Journal of Applied Physics*, **86**(11): 6519-6524.

Shende, R. V. and J. Levec (1999). Subcritical Aqueous-Phase Oxidation Kinetics of Acrylic, Maleic, Fumaric, and Muconic Acids. *Industrial & Engineering Chemistry Research*, **39**(1): 40-47.

Shiraiwa, M., M. Ammann, T. Koop and U. Pöschl (2011). Gas uptake and chemical aging of semisolid organic aerosol particles. *Proceedings of the National Academy of Sciences*, **108**(27): 11003-11008.

Shiraiwa, M., T. Berkemeier, K. A. Schilling-Fahnestock, J. H. Seinfeld and U. Pöschl (2014). Molecular corridors represent the multiphase chemical evolution of secondary organic aerosol. *Atmos. Chem. Phys. Discuss.*, **14**(5): 5929-5961.

Shiraiwa, M., C. Pfrang, T. Koop and U. Pöschl (2012a). Kinetic multi-layer model of gas-particle interactions in aerosols and clouds (KM-GAP): linking condensation, evaporation and chemical reactions of organics, oxidants and water. *Atmos. Chem. Phys.*, **12**(5): 2777-2794.

Shiraiwa, M., C. Pfrang and U. Pöschl (2010). Kinetic multi-layer model of aerosol surface and bulk chemistry (KM-SUB): the influence of interfacial transport and bulk diffusion on the oxidation of oleic acid by ozone. *Atmos. Chem. Phys.*, **10**(8): 3673-3691.

Shiraiwa, M., U. Pöschl and D. A. Knopf (2012b). Multiphase Chemical Kinetics of NO3 Radicals Reacting with Organic Aerosol Components from Biomass Burning. *Environmental Science & Technology*, **46** (12), pp 6630–6636

Shrestha, P., A. P. Barros and A. Khlystov (2013). CCN estimates from bulk hygroscopic growth factors of ambient aerosols during the pre-monsoon season over Central Nepal. *Atmospheric Environment*, **67**(0): 120-129.

Sierau, B., R.-W. Chang, C. Leck, J. Paatero and U. Lohmann (2014). Single-particle characterization of the High Arctic summertime aerosol. *Atmospheric Chemistry and Physics Discussions*, **14**(1): 593-649.

Silva, P. J., D.-Y. Liu, C. A. Noble and K. A. Prather (1999). Size and Chemical Characterization of Individual Particles Resulting from Biomass Burning of Local Southern California Species. *Environmental Science & Technology*, **33**(18): 3068-3076.

Silva, P. J. and K. A. Prather (2000). Interpretation of Mass Spectra from Organic Compounds in Aerosol Time-of-Flight Mass Spectrometry. *Analytical Chemistry*, **72**(15): 3553-3562.

Sinha, M. P. (1984). Laser-induced volatilization and ionization of microparticles. *Review of Scientific Instruments*, **55**(6): 886-891.

Sinha, M. P., C. E. Giffin, D. D. Norris, T. J. Estes, V. L. Vilker and S. K. Friedlander (1982). Particle analysis by mass spectrometry. *Journal of Colloid and Interface Science*, **87**(1): 140-153.

Slowik, J. G., C. Stroud, J. W. Bottenheim, P. C. Brickell, R. Y. W. Chang, J. Liggio, P. A. Makar, R. V. Martin, M. D. Moran, N. C. Shantz, S. J. Sjostedt, A. van Donkelaar, A. Vlasenko, H. A. Wiebe, A. G. Xia, J. Zhang, W. R. Leaitch and J. P. D. Abbatt (2010). Characterization of a large biogenic secondary organic aerosol event from eastern Canadian forests. *Atmos. Chem. Phys.*, **10**(6): 2825-2845.

Smith, G., E. Woods, C. DeForest, T. Baer and R. Miller (2002a). Reactive Uptake of Ozone by Oleic Acid Aerosol Particles: Application of Single-Particle Mass Spectrometry

to Heterogeneous Reaction Kinetics. *The Journal of Physical Chemistry A,* **106**(35): 8085-8095.

Smith, G. D., E. Woods, T. Baer and R. E. Miller (2003). Aerosol Uptake Described by Numerical Solution of the Diffusion−Reaction Equations in the Particle. *The Journal of Physical Chemistry A,* **107**(45): 9582-9587.

Smith, G. D., E. Woods, C. L. DeForest, T. Baer and R. E. Miller (2002b). Reactive Uptake of Ozone by Oleic Acid Aerosol Particles: Application of Single-Particle Mass Spectrometry to Heterogeneous Reaction Kinetics. *The Journal of Physical Chemistry A*, **106**(35): 8085-8095.

Smith, W. (2007). High time resolution chemical fingerprinting and source apportionment of atmospheric particulate emissions from the steel industry. School of Geography, Earth And Environmental Sciences. Birmingham, University of Birmingham. Doctor of Philosophy.

Sodeman, D. A., S. M. Toner and K. A. Prather (2005). Determination of Single Particle Mass Spectral Signatures from Light-Duty Vehicle Emissions. *Environmental Science & Technology*, **39**(12): 4569-4580.

Song, X.-H., P. K. Hopke, D. P. Fergenson and K. A. Prather (1999). Classification of Single Particles Analyzed by ATOFMS Using an Artificial Neural Network, ART-2A. *Analytical Chemistry*, **71**(4): 860-865.

Spence, J. C. H., U. Weierstall and H. N. Chapman (2012). X-ray lasers for structural and dynamic biology. *Reports on Progress in Physics*, **75**(10): 102601 (25 pp).

Spencer, M. T., J. C. Holecek, C. E. Corrigan, V. Ramanathan and K. A. Prather (2008). Size-resolved chemical composition of aerosol particles during a monsoonal transition period over the Indian Ocean. *Journal of Geophysical Research: Atmospheres*, **113**(D16): D16305.

Spencer, M. T. and K. A. Prather (2006). Using ATOFMS to Determine OC/EC Mass Fractions in Particles. *Aerosol Science and Technology*, **40**(8): 585 - 594.

Stanier, C. O., A. Y. Khlystov and S. N. Pandis (2004a). Ambient aerosol size distributions and number concentrations measured during the Pittsburgh Air Quality Study (PAQS). *Atmospheric Environment*, **38**(20): 3275-3284.

Stanier, C. O., A. Y. Khlystov and S. N. S. N. Pandis (2004b). Ambient aerosol size distributions and number concentrations measured during the Pittsburgh Air Quality Study (PAQS). *Atmospheric Environment*, **38**(20): 3275-3284.

Stockwell, W. R., C. V. Lawson, E. Saunders and W. S. Goliff (2011). A Review of Tropospheric Atmospheric Chemistry and Gas-Phase Chemical Mechanisms for Air Quality Modeling. *Atmosphere*, **3**(1): 1-32.

Stoffels, J. J. (1981). A direct-inlet mass spectrometer for real-time analysis of airborne particles. *International Journal of Mass Spectrometry and Ion Physics*, **40**(2): 217-222.

Stratmann, F., M. Bilde, U. Dusek, G. P. Frank, T. Hennig, S. Henning, A. Kiendler-Scharr, A. Kiselev, A. Kristensson, I. Lieberwirth, T. F. Mentel, U. Pöschl, D. Rose, J. Schneider, J. R. Snider, R. Tillmann, S. Walter and H. Wex (2010). Examination of laboratory-generated coated soot particles: An overview of the LACIS Experiment in November (LExNo) campaign. *Journal of Geophysical Research: Atmospheres*, **115**(D11): D11203.

Suess, D. T. and K. A. Prather (1999). Mass Spectrometry of Aerosols. *Chemical Reviews*, **99**(10): 3007-3036.

Sullivan, R. C. and K. A. Prather (2005). Recent Advances in Our Understanding of Atmospheric Chemistry and Climate Made Possible by On-Line Aerosol Analysis Instrumentation. *Analytical Chemistry*, **77**(12): 3861-3886.

Surratt, J. D., S. M. Murphy, J. H. Kroll, N. L. Ng, L. Hildebrandt, A. Sorooshian, R. Szmigielski, R. Vermeylen, W. Maenhaut, M. Claeys, R. C. Flagan and J. H. Seinfeld (2006). Chemical Composition of Secondary Organic Aerosol Formed from the Photooxidation of Isoprene. *The Journal of Physical Chemistry A*, **110**(31): 9665-9690.

Svane, M., T. L. Gustafsson, B. Kovacevik, J. Noda, P. U. Andersson, E. D. Nilsson and J. B. C. Pettersson (2009). On-Line Chemical Analysis of Individual Alkali-Containing Aerosol Particles by Surface Ionization Combined with Time-of-Flight Mass Spectrometry. *Aerosol Science and Technology*, **43**(7): 653-661.

Szmigielski, R., J. D. Surratt, R. Vermeylen, K. Szmigielska, J. H. Kroll, N. L. Ng, S. M. Murphy, A. Sorooshian, J. H. Seinfeld and M. Claeys (2007). Characterization of 2-methylglyceric acid oligomers in secondary organic aerosol formed from the

photooxidation of isoprene using trimethylsilylation and gas chromatography/ion trap mass spectrometry. *Journal of Mass Spectrometry*, **42**(1): 101-116.

Tajalli, H., A. G. Gilani, M. Zakerhamidi and P. Tajalli (2008). The photophysical properties of Nile red and Nile blue in ordered anisotropic media. *Dyes and Pigments*, **78**(1): 15-24.

Takemura, T. and T. Nakajima (2001). Single-Scattering Albedo and Radiative Forcing of Various Aerosol Species with a Global Three-Dimensional Model. *Journal of Climate*, **15**(4): 333-352.

Tao, Y. and P. H. McMurry (1989). Vapor pressures and surface free energies of C14-C18 monocarboxylic acids and C5 and C6 dicarboxylic acids. *Environmental Science & Technology*, **23**(12): 1519-1523.

Tedetti, M., K. Kawamura, M. Narukawa, F. Joux, B. Charrière and R. Sempéré (2007). Hydroxyl radical-induced photochemical formation of dicarboxylic acids from unsaturated fatty acid (oleic acid) in aqueous solution. *Journal of Photochemistry and Photobiology A: Chemistry*, **188**(1): 135-139.

Thomson, D. S., A. M. Middlebrook and D. M. Murphy (1997). Thresholds for Laser-Induced Ion Formation from Aerosols in a Vacuum Using Ultraviolet and Vacuum-Ultraviolet Laser Wavelengths. *Aerosol Science and Technology*, **26**(6): 544-559.

Thornberry, T. and J. P. D. Abbatt (2004). Heterogeneous reaction of ozone with liquid unsaturated fatty acids: detailed kinetics and gas-phase product studies. *Physical Chemistry Chemical Physics*, **6**(1): 84-93.

Tobias, H. J. and P. J. Ziemann (2000). Thermal Desorption Mass Spectrometric Analysis of Organic Aerosol Formed from Reactions of 1-Tetradecene and O3 in the Presence of Alcohols and Carboxylic Acids. *Environmental Science & Technology*, **34**(11): 2105-2115.

Topping, D. O., M. H. Barley and G. McFiggans (2011). The sensitivity of Secondary Organic Aerosol component partitioning to the predictions of component properties: part 2; determination of particle hygroscopicity and its dependence on "apparent" volatility. *Atmos. Chem. Phys. Discuss.*, **11**(3): 9019-9056.

TSI (2008). Model 3936 Scanning Mobility Particle Sizer™ (SMPS™) Spectrometer Operation and Service Manual.

Tsigaridis, K. and M. Kanakidou (2007). Secondary organic aerosol importance in the future atmosphere. *Atmospheric Environment*, **41**(22): 4682-4692.

Valorso, R., B. Aumont, M. Camredon, T. Raventos-Duran, C. Mouchel-Vallon, N. L. Ng, J. H. Seinfeld, J. Lee-Taylor and S. Madronich (2011). Explicit modelling of SOA formation from α-pinene photooxidation: sensitivity to vapour pressure estimation. *Atmos. Chem. Phys.*, **11**(3): 10121-10158.

Varutbangkul, V., F. J. Brechtel, R. Bahreini, N. L. Ng, M. D. Keywood, J. H. Kroll, R. C. Flagan, J. H. Seinfeld, A. Lee and A. H. Goldstein (2006). Hygroscopicity of secondary organic aerosols formed by oxidation of cycloalkenes, monoterpenes, sesquiterpenes, and related compounds. *Atmos. Chem. Phys.*, **6**(9): 2367-2388.

Vesna, O., M. Sax, M. Kalberer, A. Gaschen and M. Ammann (2009). Product study of oleic acid ozonolysis as function of humidity. *Atmospheric Environment*, **43**(24): 3662-3669.

Vesna, O., S. Sjogren, E. Weingartner, V. Samburova, M. Kalberer, H. W. Gäggeler and M. Ammann (2008). Changes of fatty acid aerosol hygroscopicity induced by ozonolysis under humid conditions. *Atmos. Chem. Phys.*, **8**(16): 4683-4690.

Vieceli, J., O. L. Ma and D. J. Tobias (2004). Uptake and Collision Dynamics of Gas Phase Ozone at Unsaturated Organic Interfaces. *The Journal of Physical Chemistry A*, **108**(27): 5806-5814.

Virkkula, A., R. Van Dingenen, F. Raes and J. Hjorth (1999). Hygroscopic properties of aerosol formed by oxidation of limonene, α-pinene, and β-pinene. *J. Geophys. Res.*, **104**(D3): 3569-3579.

Vivanco, M. G., M. Santiago, A. Martínez-Tarifa, E. Borrás, M. Ródenas, C. García-Diego and M. Sánchez (2011). SOA formation in a photoreactor from a mixture of organic gases and HONO for different experimental conditions. *Atmospheric Environment*, **45**(3): 708-715.

Vlasenko, A., I. J. George and J. P. D. Abbatt (2008). Formation of Volatile Organic Compounds in the Heterogeneous Oxidation of Condensed-Phase Organic Films by Gas-Phase OH. *The Journal of Physical Chemistry A*, **112**(7): 1552-1560.

Vogel, A. and V. Venugopalan (2003). Mechanisms of pulsed laser ablation of biological tissues. *Chemical Reviews*, **103**(2): 577-644.

von Hessberg, C., P. von Hessberg, U. PÃ¶schl, M. Bilde, O. J. Nielsen and G. K. Moortgat (2009). Temperature and humidity dependence of secondary organic aerosol yield from the ozonolysis of Î²-pinene. *Atmos. Chem. Phys.*, **9**(11): 3583-3599.

Wadt, W. R. and W. A. Goddard (1975). Electronic structure of the Criegee intermediate. Ramifications for the mechanism of ozonolysis. *Journal of the American Chemical Society*, **97**(11): 3004-3021.

Wallace, J. M. and P. V. Hobbs (2006). *Atmospheric Science: An Introductory Survey*. California, Academic Press.

Wang, X. and P. H. McMurry (2006). A Design Tool for Aerodynamic Lens Systems. *Aerosol Science and Technology*, **40**(5): 320-334.

Wang, X., B. Williams, Y. Tang, Y. Huang, L. Kong, X. Yang and P. Biswas (2013). Characterization of organic aerosol produced during pulverized coal combustion in a drop tube furnace. *Atmospheric Chemistry & Physics*, **13**: 10919–10932.

Washida, N., Y. Mori and I. Tanaka (1971). Quantum Yield of Ozone Formation from Photolysis of the Oxygen Molecule at 1849 and 1931 Å *Journal of Chemical Physics*, **54**(3): 1119-1122.

Weiss, V. (1905). Ueber Ozonide der aromatischen Kohlenwasserstoffe. *Justus Liebigs Annalen der Chemie*, **343**(2-3): 369-375.

Went, F. W. (1960). Blue hazes in the atmosphere. *Nature*: 641-643.

Wesely, M. L. and B. B. Hicks (2000). A review of the current status of knowledge on dry deposition. *Atmospheric Environment*, **34**(12-14): 2261-2282.

Whitten, G. Z., G. Heo, Y. Kimura, E. McDonald-Buller, D. T. Allen, W. P. L. Carter and G. Yarwood (2010). A new condensed toluene mechanism for Carbon Bond: CB05-TU. *Atmospheric Environment*, **44**(40): 5346-5355.

Willeke, B. (2001). *Aerosol Measurement: Principles, Techniques, and Applications.* . New York, John Wiley and Sons.

Wong, J. P. S., A. K. Y. Lee, J. G. Slowik, D. J. Cziczo, W. R. Leaitch, A. Macdonald and J. P. D. Abbatt (2011). Oxidation of ambient biogenic secondary organic aerosol by hydroxyl radicals: Effects on cloud condensation nuclei activity. *Geophysical Research Letters*, **38**(22): L22805.

Wood, S. H. and K. A. Prather (1998). Time-of-flight mass spectrometry methods for real time analysis of individual aerosol particles. *TrAC Trends in Analytical Chemistry*, **17**(6): 346-356.

Yadav, R., K. Saoud, F. Rasouli, M. Hajaligol and R. Fenner (2004). Study of cigarette smoke aerosol using time of flight mass spectrometry. *Journal of Analytical and Applied Pyrolysis*, **72**(1): 17-25.

Yamato, M. and H. Tanaka (1994). Aircraft observations of aerosols in the free marine troposphere over the North Pacific Ocean: Particle chemistry in relation to air mass origin. *Journal of Geophysical Research: Atmospheres*, **99**(D3): 5353-5377.

Zahardis, J., S. Geddes and G. A. Petrucci (2011). Improved Understanding of Atmospheric Organic Aerosols via Innovations in Soft Ionization Aerosol Mass Spectrometry. *Analytical Chemistry*, **83**(7): 2409-2415.

Zahardis, J., B. W. LaFranchi and G. A. Petrucci (2005). Photoelectron resonance capture ionization-aerosol mass spectrometry of the ozonolysis products of oleic acid particles: Direct measure of higher molecular weight oxygenates. *Journal of Geophysical Research: Atmospheres*, **110**(D8): D08307.

Zahardis, J., B. W. LaFranchi and G. A. Petrucci (2006). Direct observation of polymerization in the oleic acid–ozone heterogeneous reaction system by photoelectron resonance capture ionization aerosol mass spectrometry. *Atmospheric Environment*, **40**(9): 1661-1670.

Zahardis, J. and G. A. Petrucci (2007). The oleic acid-ozone heterogeneous reaction system: products, kinetics, secondary chemistry, and atmospheric implications of a model system; a review. *Atmos. Chem. Phys.*, **7**(5): 1237-1274.

Zanis, P., P. S. Monks, T. J. Green, E. Schuepbach, L. J. Carpenter, G. P. Mills, A. R. Rickard, N. Brough and S. A. Penkett (2003). Seasonal variation of peroxy radicals in the lower free troposphere based on observations from the FREE Tropospheric EXperiments in the Swiss Alps. *Geophysical Research Letters*, **30**(10): 1497.

Zeng, G., S. Holladay, D. Langlois, Y. Zhang and Y. Liu (2013). Kinetics of Heterogeneous Reaction of Ozone with Linoleic Acid and its Dependence on Temperature, Physical State, RH, and Ozone Concentration. *The Journal of Physical Chemistry A*, **117**(9): 1963-1974.

Zhang, L. and R. Vet (2006). A review of current knowledge concerning size-dependent aerosol removal. *China Particuology*, **4**(6): 272-282.

Zhang, Q., M. R. Alfarra, D. R. Worsnop, J. D. Allan, H. Coe, M. R. Canagaratna and J. L. Jimenez (2005). Deconvolution and Quantification of Hydrocarbon-like and

Oxygenated Organic Aerosols Based on Aerosol Mass Spectrometry. *Environmental Science & Technology*, **39**(13): 4938-4952.

Zhang, Q., J. L. Jimenez, M. R. Canagaratna, J. D. Allan, H. Coe, M. Alfarra, A. Takami, A. Middlebrook, Y. Sun, K. Dzepina, E. Dunlea, K. Docherty, P. DeCarlo, D. Salcedo, T. Onasch, J. Jayne, T. Miyoshi, A. Shimono, S. Hatakeyama, N. Takegawa, Y. Kondo, J. Schneider, F. Drewnick, S. Borrmann, S. Weimer, k. Demerjian, P. Williams, K. Bower, Z. Bahreini, D. Cottrell, R. Griffin, J. Rautiainen, J. Sun, Y. Zhang and D. Worsnop (2007). Ubiquity and dominance of oxygenated species in organic aerosols in anthropogenically-influenced Northern Hemisphere midlatitudes. Geophysical Research Letters, 34(13): L13801 (6 pp).

Ziemann, P. J. (2005). Aerosol products, mechanisms, and kinetics of heterogeneous reactions of ozone with oleic acid in pure and mixed particles. *Faraday Discussions*, **130**(0): 469-490.

Ziemann, P. J. (2010). Atmospheric Chemistry: Phase matters for aerosols. *Nature*, **467**(7317): 797-798.